Exploring Habitability Markers, Biosignatures, and Their False Positives Using Spectral Models of Terrestrial Exoplanets

Edward W. Schwieterman

A dissertation

submitted in partial fulfillment of the

requirements for the degree of

Doctor of Philosophy

University of Washington

2016

Reading Committee:

Victoria S. Meadows, Chair

Shawn D. Domagal-Goldman

David C. Catling

Program Authorized to Offer Degree:

Department of Astronomy

University of Washington

Abstract

Exploring Habitability Markers, Biosignatures, and Their False Positives Using Spectral Models of Terrestrial Exoplanets

Edward W. Schwieterman

Chair of the Supervisory Committee:
Professor Victoria S. Meadows
Astronomy

In the coming years and decades, we will obtain our first opportunity to spectrally characterize potentially habitable worlds outside our solar system. These planets will be at the right distance from their host star and possess the correct range of atmospheric compositions to have surfaces conducive to maintaining liquid water, the key requirement for habitability and life. For example, the James Webb Space Telescope (JWST), set for launch in 2018, could observe the transmission spectra of a handful of terrestrial planets orbiting late type stars. Direct-imaging telescopes currently in the design phases, including the Large UltraViolet Optical InfraRed (LUVOIR) Surveyor, will possess the ability to spectrally characterize planets in the habitable zones of up to hundreds of nearby planetary systems. The goal of this work is to

advance our ability to recognize whether an exoplanet can or does support life by exploring a range of spectral habitability markers and astronomical biosignatures. As our best, and currently only, example of a habitable planet, Earth provides a fiducial point for studying the possible spectral manifestation of habitability markers and biosignatures for exoplanets. This thesis includes studies in four areas related to this theme. First, I build a high fidelity, high cadence spectral Earth database from the far UV (0.1 μm) to the far Infrared (200 μm) using the VPL 3D, line-by-line, multiple scattering spectral Earth model. This database furthers our understanding of Earth as an exoplanet, illustrating spectral changes as a function of phase and rotation. Second, I demonstrate the detectability of N_2 using the $(N_2)_2$ collisional pair, which has implications for characterizing the bulk atmospheres of terrestrial exoplanets and may be a strong biosignature in combination with detection of O_2 or O_3. I use data model comparisons to show that $(N_2)_2$ produces a ~35% reduction in Earth's spectral flux at 4.1 μm. I quantify the strength of the $(N_2)_2$ feature in a variety of simulated atmospheres with different N_2 abundances with both synthetic direct-imaging and transit transmission spectra. Third, I investigate observational indicators of planetary mechanisms that may generate abiotic oxygen (O_2 or O_3) on exoplanets, leading to potential "false positives" for life. Abiotic production of O_2 from CO_2 photolysis potentially leads to detectable amounts of CO as a byproduct. Oxygen build up from massive H-loss during a runaway greenhouse could leave behind more O_2 than could be plausibly produced by biology. In this case density dependent O_4 features would be strong and potentially indicative of this process. I investigate the strength and detectability of CO (at 2.35 and 4.6 μm) and O_4 (at 0.345, 0.36, 0.38, 0.445, 0.475, 0.53, 0.57, 0.63, 1.06, and 1.27 μm) absorption for these abiotic oxygen scenarios in both transmission and direct-imaging spectroscopy. Finally, I present an interdisciplinary study of nonphotosynthetic pigments as

alternative surface reflectance biosignatures, in contrast to direct photosynthetic signatures like the vegetation red edge. This study includes reflectance measurements of a variety of pigmented organisms in the laboratory, illustrating a wide range of spectral diversity. I also model the spectra of hypothetical planets containing nonphotosynthetic pigment biosignatures including the confounding spectral effects of the atmosphere. I find that these signatures could potentially be observable in disk-averaged spectra depending on the fraction of the planet containing the signature. Organisms with nonphotosynthetic pigments will produce reflectance signatures different than that of the commonly referenced vegetation red edge, and push us to broaden our understanding of what surface biosignatures might look like on Earth-like exoplanets once remote characterization of these worlds becomes possible.

TABLE OF CONTENTS

LIST OF FIGURES

LIST OF TABLES

ACKNOWLEDGEMENTS

The completion of this dissertation required the support of a great number of individuals and organizations for whom and which I owe great debts of gratitude. Foremost, I'd like to thank my advisor, Victoria Meadows, for her support, guidance, and overall mentorship throughout my time at the University of Washington. She deserves extra acknowledgement for creating such a welcoming and productive community for scientific inquiry in the Virtual Planetary Laboratory. Also owed great thanks are the rest of my committee including Shawn Domagal-Goldman, David Catling, Roger Buick, Mark Claire, and Dale Winebrenner for their useful suggestions, friendly collaborations, and enlightening conversations. I'd like to issue a special thanks to Shawn for the unending encouragement and vigorous promotion of my work. I'd also like to extend my gratitude to the entire VPL team, its funding agency, the NASA Astrobiology Institute, the UW Astronomy Department, and the UW Astrobiology Program. Working and studying within these organizations has provided me with experiences in meaningful interdisciplinary science I could hardly imagine when I first began my graduate studies. These studies also benefited greatly from my relationships with my graduate student colleagues. They have my unending appreciation for their true friendship over the years. I can't end this section without mentioning the steadfast and loving support of my family. I thank my parents for first exposing me to the wonders of science, especially my father for taking my sister and I on exciting fossil hunting trips early in our childhoods. Finally, my biggest thanks goes to my wife, Breanna Binder, for creating so much happiness and meaning to my life. I'm looking forward to everything our partnership will bring.

DEDICATION

To Bre

Chapter 1. INTRODUCTION

This chapter provides a brief introduction to the state of exoplanet characterization and the status of the search for habitable and inhabited exoplanets. I define, review, and discuss planetary biosignatures, habitability markers, and "false positives" for life. Additionally, I outline each of the main chapters and their thematic link of using spectral models to characterize these potential signatures. In writing this dissertation I have employed the philosophy that each of the chapters should stand alone, without requiring the reader to extensively reference other sections. Each chapter has independent and extensive abstract and introduction sections. Portions of this chapter were originally published in collaboration with V.S. Meadows, S.D. Domagal-Goldman, D. Deming, G.A. Arney, C.E. Harman, A. Misra, and R. Barnes in the March 2016 edition of the *Astrophysical Journal Letters* (Schwieterman et al., 2016, ApJ, Vol. 819, L13; © 2016 American Astronomical Society), and with C.S. Cockell and V.S. Meadows in the May 2015 edition of *Astrobiology* (Schwieterman, Cockell, & Meadows. 2015, *AsBio*, Vol. 15(5), 341-361; © The authors) and are reproduced below with permission of the American Astronomical Society and the noted authors, respectively.

1.1 Motivation and Context

The search for life beyond the solar system will focus on spectral signatures of exoplanets. Thousands of exoplanets have been discovered in the last two decades (e.g., Batalha et al. 2013; Burke et al. 2014). While the vast majority of these discovered worlds are too large or too hot to support life on the planetary surface, many potentially habitable planets have already been identified (e.g., Kane et al. 2016). These worlds reside within their host star's habitable zone (HZ), which is defined as the range of distances circumscribing the star where a

planet with a sufficient atmosphere could maintain stable liquid water on its surface (Kasting et al. 1993; Kopparapu et al. 2013). Because of detection biases, the majority of the currently known potentially habitable words are larger than the Earth and orbit close to the inner edge of their HZs.

Figure 1.1 shows the known exoplanets with radii less than 10 $R_\oplus$ and semi-major axes of less than 2 AU and identifies the planets with radii less than 5 $R_\oplus$ (sub-Neptune down to Earth radii) whose atmospheres have been probed with transmission spectroscopy (Han et al. 2014), of which most are located far interior to the HZ. From statistical analyses of combined Kepler and radiative velocity data, it is known that the majority of planets with radii of more than ~1.6 $R_\oplus$ are likely to possess extensive H_2 envelopes (Rogers 2015). Currently the smallest planet known with molecular absorption features is the "warm" (T_{eq}= 878 K) mini-Neptune HAT-P-11 (R = 4.4; $R_\oplus$; Fraine et al. 2014).

The next few years will bring the opportunity to characterize many rocky planets with secondary, outgassed atmospheres. Surveys are already beginning to detect these types of worlds within the solar neighborhood (e.g., Berta-Thompson et al. 2015; Wright et al. 2016), though current observations can only rule out low molecular weight (H_2-dominated) clear sky atmospheres for the smallest planets, such as for the TRAPPIST-1 system (de Wit et al. 2016), and thus far lack the ability to detect spectral features in atmospheres with high average molecular weight, even for those atmospheres clear of high altitude condensates or hazes.

The most interesting planets from an astrobiological perspective will be rocky planets with thin N_2-H_2O-CO_2 atmospheres, analogous to Earth's atmosphere, that reside within their host star's HZ (Kopparapu et al. 2013; Seager 2013). Many of these types of planets will be found in the solar neighborhood by the upcoming Transiting Exoplanet Survey Telescope

(TESS) mission (Ricker et al. 2014; Sullivan et al. 2015). The *James Webb Space Telescope* (*JWST*), scheduled to launch in 2018, will be able to characterize the atmosphere of a handful of these worlds through transmission spectroscopy (Deming et al. 2009; Cowan et al. 2015), providing the first chance for astronomers to characterize potentially habitable planets.

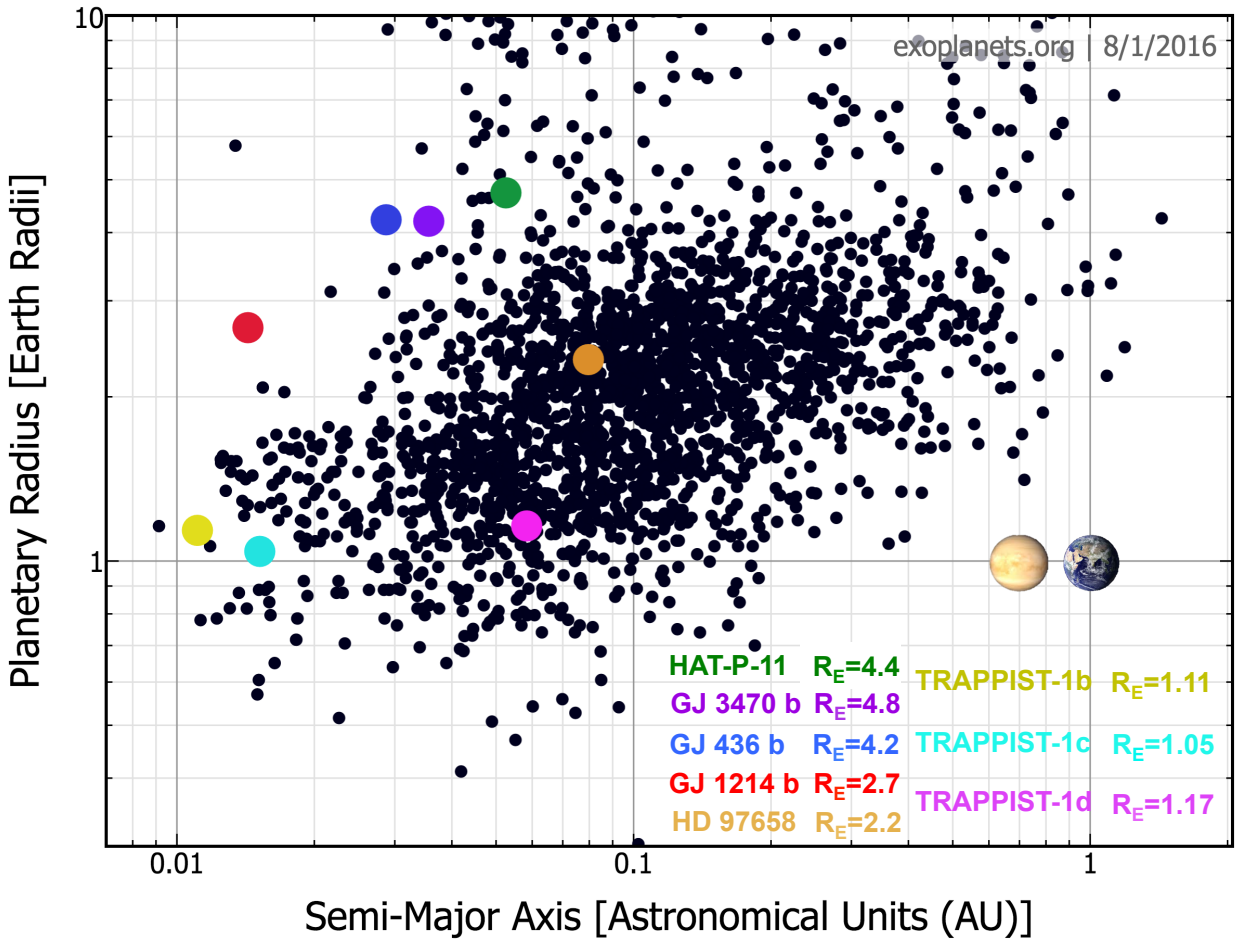

Figure 1.1. Exoplanets with $R_{Planet} < 10\ R_{\oplus}$ and $a_{planet} < 2$ AU known as of July 2016 with well-defined orbits from the Exoplanets Orbit Database[1] (Han et al. 2014). Planets with $R_{Planet} < 5\ R_{\oplus}$ that have been characterized with transmission spectroscopy are color-coded. They include GJ 3470b (R = 4.8 $R_{\oplus}$; Demory et al. 2013), HAT-P-11 (R = 4.4; $R_{\oplus}$; Fraine et al. 2014) , GJ 436b (R = 4.2 $R_{\oplus}$; Knutson et al. 2014a), GJ 1214b (R = 2.7 $R_{\oplus}$; Kreidberg et al. 2014), HD 97658 (R = 2.2 $R_{\oplus}$; Knutson et al. 2014b); and TRAPPIST-1b,c,d (R=1.11, 1.05, and 1.17 $R_{\oplus}$, respectively; Gillon et al. 2016) (1d best orbit shown). Earth and Venus shown for reference.

[1] http://www.exoplanets.org

Mission concepts that can directly image potentially habitable and inhabited planets are already in their science definition stages, such as the LUVOIR and HabEx Surveyors (Kouveliotou et al. 2014; Dalcanton et al. 2015; Rauscher et al. 2015; Seager et al. 2015). Additionally, the upcoming WFIRST-AFTA mission may possess the capability to photometrically characterize a small handful of potentially habitable planets (Spergel et al. 2015) and biosignature searches of habitable zones of nearby stars using ground-based ELTs (Extremely Large Telescopes) coming online in the 2020s have also been proposed (e.g., Kawahara et al. 2012; Snellen et al. 2013). To support the science definition, design, and future operations of these missions and observatories, it is crucial to have as complete a picture as possible about the requirements to detect habitability and life.

1.2 Astrobiology and the Search for Habitability and Life

The search for life beyond the solar system is one of the most monumental and consequential endeavors pursued by humanity and a foundational goal of the astrobiology discipline. NASA defines astrobiology as the study of the "origin, evolution, distribution, and future of life in the universe" (DesMarais & Walter 1999). Measuring the distribution of life in the universe requires both the search for habitable environments where life may thrive and the determination of whether these habitable environments in fact do host life. The common definition of planetary habitability is existence of conditions that allow the presence of surface liquid water. This can be indirectly confirmed by the analysis of the planet's position with relation to its host star (i.e., its location in the HZ), its likely temperature and pressure, and the presence of habitability markers like water vapor and carbon dioxide gas (Kaltenegger & Selsis 2007). A surface ocean may be directly confirmed by the presence of ocean glint (Williams &

Gaidos 2008; Robinson et al. 2010; Robinson et al. 2014). All of these characteristics can be explored with spectroscopic observations and are reviewed below and in the following chapters.

The characteristics of the host star can strongly affect planetary habitability due to their widely differing lifetimes and spectral energy distributions (SEDs). A host star's lifetime must be sufficiently long to allow for the origin of life. The vast majority (70%) of stars in our galaxy are M dwarf stars, which are the dimmest and reddest stars, and also possess the longest main sequence lifetimes of up to trillions of years (Laughlin et al. 1997). (In contrast, our Sun is about 4.65 Gyr and has a main sequence lifetime of ~10 Gyr, while the observable universe is 13.7 Gyr.) In the past, M dwarf stars were thought to be poor hosts for habitable planets because the habitable zone is located sufficiently close to the star that most habitable zone planets with circular orbits would be "tidally locked" and therefore subject to the freeze out of their atmosphere on the permanent "night side" (Kasting et al. 1993). However, subsequent dynamical and climate simulations have shown that this was an overly pessimistic view of the habitability of M stars (e.g., Joshi 2003; Joshi & Haberle 2012; Shields et al. 2013), though concerns about the effects of host star magnetic activity, atmospheric loss during the pre-main sequence, and the impact of high energy particle flux on the planetary atmosphere remain (e.g., Driscoll & Barnes 2015; Luger & Barnes 2015; Tabataba-Vakili et al. 2015). There is now a broad consensus that all of FGK and M stars may host habitable and inhabited planets (Tarter et al. 2007; Scalo et al. 2007), though M stars have their own unique challenges (e.g., Luger & Barnes 2015). Therefore, planets in the habitable zones of all of these stars, including M stars, are potentially interesting astrobiological laboratories.

While habitability may be confirmed by an analysis of planetary characteristics**,** the defining goal will be to determine whether the planet is *inhabited* by remote detection of

spectroscopic biosignatures. The NASA Astrobiology 2008 Roadmap (DesMarais et al. 2008) and 2015 Strategy (Hays et al. 2015) both call for searches for biosignatures in nearby planetary systems including all types of long-lived main sequence stars (2008 Roadmap Goal 7.2). Section 1.3 defines and summarizes planetary biosignatures.

1.3 Planetary Biosignatures

The search for life beyond Earth requires an understanding of the ways in which life can measurably impact its environment. The generic definition of a biosignature is "an object, substance, and/or pattern whose origin specifically requires a biological agent" (Des Marais et al. 2008). To be considered a useful biosignature, this evidence must be potentially discernable from the results of abiotic processes. This generic definition is applicable to both remote and *in situ* measurements inside and outside our solar system. The definition of a planetary biosignature, also called an astronomical biosignature, has a much higher bar to clear.

A planetary biosignature must be detectable over interstellar distances. This requires a planetary biosignature to produce a measurable impact, one that could be inferred from remote spectroscopic investigation of the whole planet. Therefore, the process generating the biosignature is likely to be global in nature, and not confined to a minor locality, the subsurface or otherwise unobservable. To be useful, the biosignature must be clearly discernable from common abiotic processes that could plausible occur given the observable or inferable planetary context (i.e., location in the HZ, bulk composition, spectra of the star, etc.). (For the rest of this text, the term "biosignature" is used interchangeably with "astronomical biosignature", unless otherwise noted.)

1.3.1 *Types of Astronomical Biosignatures*

There is currently no universally agreed upon categorization scheme for astronomical biosignatures, though efforts are being made to this end. A common approach is to classify potential biosignatures on the basis of how they would manifest themselves to an observer (e.g., Meadows 2006; Meadows & Seager 2010). In this type of scheme Earth-based biosignatures are taken as proof of concept examples for how these signatures would appear in exoplanet spectra. This approach is also aided by the heritage of existing photodissociation cross-sections, vibro-rotational line lists (e.g., HITRAN and HITEMP), and photochemical and climate models that can accurately model the impact of these gases in Earth-like atmospheres (see Chapter 2). These models and their corresponding physical and chemical data can be used to simulate climate and atmospheric chemistry on Earth-like planets orbiting stars other than the Sun (e.g., Segura et al. 2003; Segura et al. 2005; Segura et al. 2007; Segura et al. 2010; Rugheimer et al. 2013; Rugheimer et al. 2015b) and/or at various points in time in Earth's geologic history (expanding the notion of "Earth-based" beyond the modern Earth), when the planetary spectrum may have been quite different (Pilcher 2003; Meadows 2006; Kaltenegger et al. 2007; Domagal-Goldman et al. 2011; Rugheimer et al. 2015a; Arney et al. 2016).

In this system, three main classes of planetary biosignatures have been proposed (Meadows 2006), which are summarized below and in Figure 1.2.

First, there are spectral absorption features produced by biosignature gases. These are gases that are produced by, or associated with, the metabolic processes of life. Molecular oxygen (O_2) produced by photosynthesis and its photochemical byproduct ozone (O_3) are examples of gaseous biosignatures. Oxygen is considered a more robust biosignature in the simultaneous presence of a reduced gas like methane (CH_4), which establishes a clear kinetic and

thermodynamic chemical disequilibrium. Chemical disequilibrium is a higher standard often applied when defining gaseous biosignatures (Hitchcock & Lovelock 1967; Lovelock 1965; Sagan et al. 1993; Krissansen-Totton et al. 2016a).

The second class of planetary biosignatures consists of spectral reflectance features from biological matter, such as land vegetation. Reflectance is the fraction of incident light that is reflected from a surface, which will vary with wavelength depending on the optical properties of the surface (and possibly the viewing geometries of the observer). The most commonly explored spectral feature in this category is the vegetation red edge (VRE) of oxygenic photosynthesizers such as land-based plants, which produces a sharp increase in reflectance from the visible to the near infrared portions of the spectrum (Gates et al. 1965, Sagan et al. 1993; Seager et al. 2005). The VRE is used by Earth observers to map surface vegetation through the use of broadband techniques such as the Normalized Difference Vegetation Index (NDVI), capturing the brightness of planets at infrared vs. red wavelengths (Tucker 1979; Tucker et al. 2005). Surface biosignatures can be a planetary phenomenon, and potentially detectable remotely, and are therefore a complement to gaseous biosignatures.

Finally, there are temporal planetary biosignatures. These are time-dependent changes in measurable quantities such as gas concentrations or planetary albedos that are produced as a consequence of changes in biological activity (Meadows 2006). For example, seasonal periodicities observed in CO_2 and CH_4 concentrations on Earth are correlated with land-based respiration (Keeling 1960; Rasmussen & Khalil 1981; Khalil & Rasmussen 1983; Keeling et al. 1996), and seasonal variation in pigmentation can be observed in land-based vegetation.

The primary disadvantage to this Earth-based approach is that it may miss novel biosignature products from vastly different environments than exist for life on Earth, such as

planets with H_2-dominated atmospheres (Stevenson 1999; Pierrehumbert & Gaidos 2011; Seager et al. 2013b).

Other biosignature categorization schemes attempt to classify metabolic products into various categories starting from biochemical considerations. For example, in the Seager et al. (2013a) categorization scheme Type I biosignatures are metabolic products from the extraction of catabolic energy from redox gradients (e.g., CH_4 from methanogensis), Type II biosignatures are the byproducts from anabolic activity such as biomass building (e.g., O_2 from oxygenic photosynthesis), and Type III biosignatures are secondary metabolic products whose relationship to catabolism or anabolism is less clear (such as sulfur compounds like di-methyl sulfide; Domagal-Goldman et al. 2011). The focus on these types of works is usually on biosignature gases rather than surface features, which are more difficult to categorize based on this type of scheme since the surface reflectance properties of biological matter has an indirect and complex relationship with metabolism and function (see Chapter 6).

The disadvantage to this reductionist type of classification scheme is that it does not include consideration of the extent to which these gases can build up in the atmosphere or their detectability over remote distances – key requirements for any biosignature candidate - which in many cases cannot yet be determined due to a current lack of laboratory data. Therefore its use is currently limited for informing the current design of instrumentation to observe these signature gases, though it may be a useful guide for future laboratory work (Fortney et al. 2016).

Throughout this dissertation, I will adopt the first, more Earth-based framework while noting that it is not inconsistent with other frameworks, such as that of Seager et al. (2013a). For example, gaseous and surface biosignatures can be subcategorized based on functional biochemical criteria.

It is clear that due consideration must be made both to Earth-based biosignature candidates and those based on different, but physically and chemically plausible biochemistries when considering the diversity of environments that may exist on habitable worlds in the cosmos. However, the efforts here are focused on Earth-based strategies, for which arguments for plausibility, environmental context and potential false positives can be made most strongly. Alternative approaches, such as agnostically surveying the universe of small, volatile molecules (e.g., Seager et al. 2016) are in the beginning stages and the current lack of laboratory data disallows accurate modeling of the volatile stability, the expected concentrations, and the spectral signatures of most of these alternative gases in planetary atmospheres. Most practically, the Earth-based approach provides for the immediate needs of informing the initial science definition and design of habitable exoplanet characterization missions currently in progress.

1.3.2 *Oxygen as a Leading Biosignature Candidate*

By far the most commonly referenced biosignature in the context of future astronomical surveys of nearby planetary systems is atmospheric O_2 (or its photochemical byproduct O_3). Oxygen is often considered a robust astronomical biosignature on its own, even without the simultaneous detection of a reduced gas out of chemical equilibrium, because through the history of our planet life has been the dominant source of this gas. Molecular oxygen is the byproduct of photosynthetic metabolism that uses H_2O as an electron donor to generate organic matter from CO_2 (Leslie 2009). The net reaction is

$$CO_2 + H_2O + h\nu \rightarrow (CH_2O)_{org} + O_2 \quad (1.1)$$

where hv is the energy of a captured photon or photons. This is believed to be the most potentially energetic metabolism on any planet orbiting a star, due to the wide availability of both photons and H_2O as an available electron donor (Kiang et al. 2007b).

The exact mechanism(s) and timeline for the oxygenation of Earth's atmosphere is still under debate, but there is broad agreement on the fundamental causes (Lyons et al. 2014). The O_2 in Earth's atmosphere is unstable over geological timescales and would be depleted by reactions with reduced volcanic gases and through oxidation of the surface (Catling 2014), thus requiring an active source to maintain appreciable levels. On Earth, that active source exists in the form of photosynthetic production of O_2 by life, followed by burial of organic carbon, which separates the organic carbon material from atmospheric O_2, a necessary step to build up O_2 in the atmosphere (Catling 2014). Additional geochemical sinks for O_2 existed earlier in Earth's history, such as the wide availability of ferrous iron (Fe^{2+}) in the ocean, which provided a further obstacle for the eventual oxygenation of Earth's atmosphere (Kasting 2001).

The photochemical production of very small amounts of O_2 occurs on Earth from the photolysis of O-bearing molecules, but this O_2 would not build up to appreciable levels in the absence of biology due to the shape of the UV spectrum of the Sun and significant environmental sinks for O_2 (Domagal-Goldman et al. 2014; Harman et al. 2015). The O_3 in Earth's atmosphere is a result of photochemical reactions involving O_2, and the presence of large quantities of O_3 has been suggested as being an indicator of abundant, photosynthetically-generated O_2 (Leger et al. 1993; DesMarais et al. 2002; Segura et al. 2005; Léger et al. 2011). Recently, it has been calculated that the strongest disequilibrium indicator in Earth's atmosphere-ocean system in terms of free energy is the N_2-O_2-dominated atmosphere coexisting with a liquid H_2O surface ocean (Krissansen-Totton et al. 2016a). The common thread to all of these signatures is the

presence of photosynthetically produced O_2. The potential strength of oxygen as a biosignature has led to many studies of the feasibility of future ground-based and space-based observations to detect O_2 or O_3 spectral features in exoplanet atmospheres (e.g., Kawahara et al. 2012, Snellen et al. 2013; Misra et al. 2014a; Dalcanton et al. 2015).

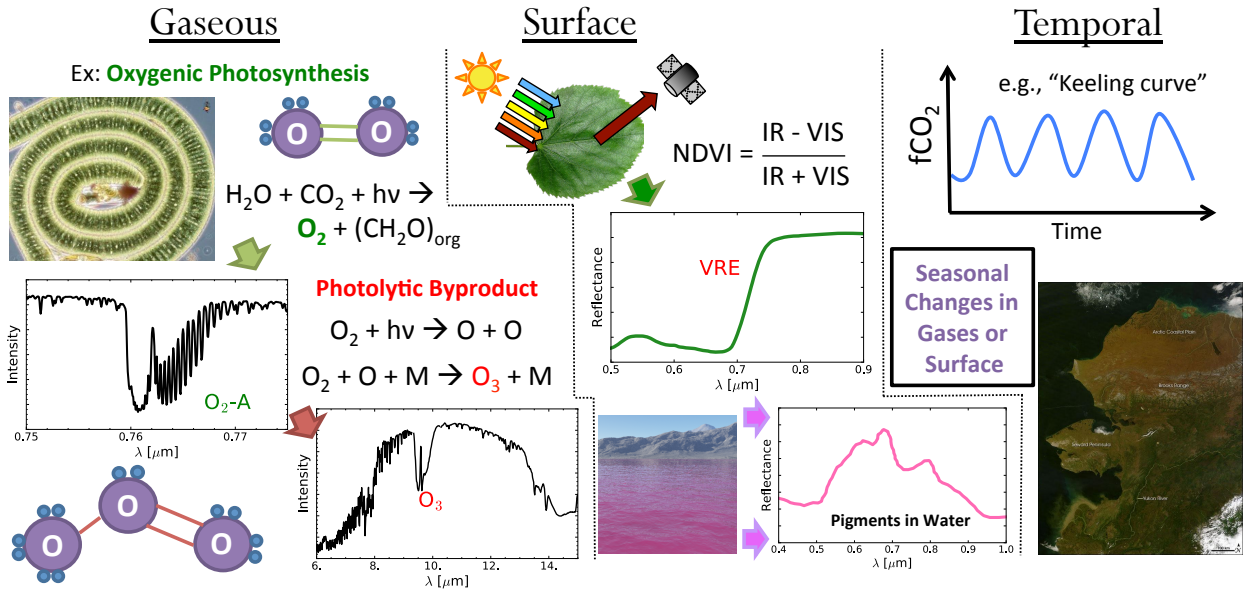

Figure 1.2. One classification scheme for planetary biosignatures: Gaseous, surface, and temporal (Meadows 2006). **Left:** Gaseous biosignatures may be directly or indirectly produced by metabolism or may be the result of photochemical processing of those gases and require spectral analysis of the planetary atmosphere to infer their presence. Molecular oxygen (O_2) from photosynthesis and ozone (O_3) are given as example gaseous biosignatures. **Middle:** The interaction of reflected light with the planetary surface can reveal surface biosignatures, which include the well-known vegetation red edge (VRE) by plants and the related Normalized Difference Vegetation Index (NDVI) used for mapping vegetated coverage by Earth observing satellites (Tucker 1979). Pigments produced by other organisms are also examples of surface biosignatures. **Right:** diurnal or seasonal changes in vegetation coverage or the abundance of gases involved in metabolism (CO_2, CH_4) could provide an indication of life (e.g, Keeling et al. 1996). Image credits: NASA & the Encyclopedia of Life (EOL)[2].

[2] http://eol.org/

1.4 Oxygen "False Positives" for Life

A decade ago the consensus view was that oxygen would be a robust signature of life if detected in the spectrum of a planet inside the habitable zone of its star (Des Marais et al. 2002). Conditions where abiotic O_2 could build up outside of the HZ have long been acknowledged. For instance, a planet undergoing a runaway greenhouse, thus necessarily closer to the star than the inner edge of the HZ, would have vast amounts of H_2O high in its atmosphere, which would be susceptible to the loss of H to space and potential buildup of O_2 (Kasting et al. 1984; Kasting et al. 1993; Schindler & Kasting 2000). How long this O_2 would remain after the oceans had been lost is disputed. Venus provides an empirical example of a planet that was presumed to lose an ocean, but retains no free O_2 in its atmosphere, though some argue this observation simply places a limit on the amount of H_2O that could have been lost (see, e.g., Chassefière 1996). On the other hand, a planet located further from the star than the HZ could potentially possess a thick, permanent ice shell, which could prevent reductants from the interior combining with the O_2 generated from the photolysis of small amounts of water vapor, allowing a tenuous O_2 atmosphere to build up (Kasting et al. 1993; Selsis 2002). Mars provides somewhat of an example of this scenario with an O_2 concentration of ~1700 ppm, which would be larger if its exposed surface did not provide a sink for O_2 (Patel et al. 2003). Planets inside the HZ are robust to these scenarios, since by definition they will not experience a runaway greenhouse or possess a permanent snowball state (although this assumes the boundaries of the HZ can be known exactly, which is likely not true, especially because those boundaries could vary as a function of planetary parameters, e.g., see Kopparapu et al. (2014).)

However, additional mechanisms for generating abiotic O_2 have been recently identified that may affect planets with different atmospheric histories than the Earth or within the HZs of

different types of host star than the Sun, which can be loosely grouped into three categories. These include: A) the photochemical production of stable concentrations of O_2/O_3 from CO_2 photolysis, which depends on the UV spectral slope of the host star and abundance of H-bearing molecules in the atmosphere (Domagal-Goldman et al. 2014; Gao et al. 2015; Harman et al. 2015; Selsis et al. 2002; Tian et al. 2014), B) massive XUV-driven H-escape and O_2-build up on planets in the HZ during the pre-main sequence, especially for planets orbiting the latest type stars (Luger & Barnes 2015), and C) abiotic O_2 buildup due to H-escape from N_2-poor atmospheres that lack tropospheric H_2O cold traps (Wordsworth & Pierrehumbert 2014). An extensive review of oxygen "false positive" mechanisms can be found in Meadows (2016). Figure 1.3 illustrates the planetary locations within the habitable zone that are susceptible to these potential abiotic O_2 scenarios.

Understanding potential false positives for O_2/O_3 biosignatures, and how to identify them, is critical and timely for informing the search for life beyond the solar system, given that the first potentially habitable planets to be characterized with transmission observations will likely orbit M dwarfs, and so will be most susceptible to O_2 biosignature impostors through CO_2 photolysis and XUV-driven hydrogen escape (mechanisms (A) and (B) above).

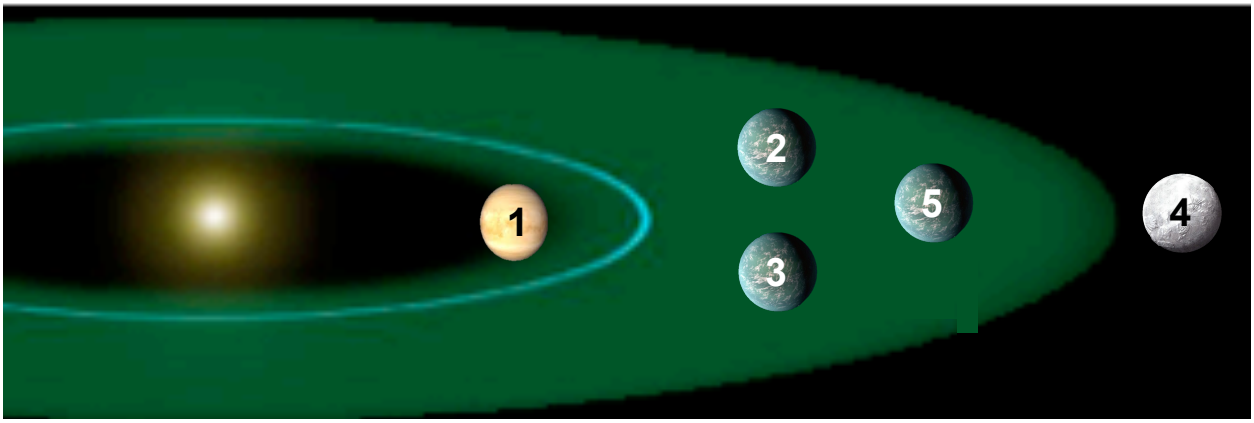

Figure 1.3. Abiotic oxygen scenarios and their locations in relation to the Habitable Zone. These are, briefly: 1) Runaway greenhouse-facilitated hydrogen escape inside the inner edge of the HZ (e.g., Chassefière 1996; Schindler & Kasting 2000); 2) Photochemical abiotic O_2 buildup in H poor atmospheres (e.g., Domagal-Goldman et al. 2014; Gao et al. 2015; Harman et al. 2015); 3) Missing cold trap from depleted N_2 (Wordsworth & Pierrehumbert 2014); 4) Frozen planet prevents reaction with surface reductants (a subset of (2); e.g., Selsis et al. 2002); and 5) massive XUV-mediated H loss in the CHZ during the pre-main sequence (a subset of (1); e.g., Luger & Barnes 2015). This figure made use of NASA images.

1.5 Outline of following chapters

As outlined earlier, the proper identification of planetary biosignatures will require a global understanding of the planetary context, not simply the knowledge that one gas is present in a planet's atmosphere. This philosophy is followed throughout this dissertation. Chapter 3 (Earth from the Moon: A Spectral Earth Database) builds upon previous work in the spectral modeling of Earth's spectral habitability markers and biosignatures by recognizing and modeling their time dependent components. Future observations of exoplanets will be made at a variety of viewing geometries, observing windows, and integration times. The study I present in Chapter 3 provides a test bed for the time-dependent information that can be recovered with future observations. Chapter 4 (Detecting N_2 in Planetary Atmospheres) is relevant both because the detection of N_2

is important for determining planetary habitability, but also because the existence of sufficient atmospheric pressure precludes scenarios for the abiotic generation of O_2, and because N_2 and O_2 together with a surface ocean represent a detectable form of chemical disequilibrium that may be indicative of life. Chapter 5 (Detecting Oxygen "False Positives" for Life) explicitly studies the strategies for identifying and discriminating against planetary mechanisms that generate abiotic O_2. Chapter 6 (Nonphotosynthetic Pigments as Potential Biosignatures) expands upon possible surface reflectance biosignatures from nonphotosynthetic pigments, which, if detected, would bolster the case of life on a planetary surface, while also acknowledging the possibility for false positives and the need for understanding planetary context. These chapters are thematically linked by the approach of using spectral models to better understand the diversity and potential detectability of habitability markers, biosignatures, and their false positives to better inform the search for life elsewhere.

The following subsections provide a more detailed outline of each subsequent chapter, including some of the major findings contained therein. Additionally, each chapter possesses a more detailed introduction including context and references for the area investigated.

1.5.1 *Chapter 2: Models and methods*

In this chapter I introduce the most significant models and methods used throughout this dissertation. These include the SMART radiative transfer model, the VPL 3D spectral Earth model, the SMART-T transit transmission radiative transfer model, a 1D radiative-convective climate model, a photochemistry model, and a model that couples the climate and photochemistry models together. SMART is a versatile radiative transfer program used to generate synthetic 1D planetary spectra. The VPL Earth model is a well-developed tool that takes as input spacecraft observations of the Earth, including realistic snow/ice and cloud cover,

to generate synthetic disk-averaged and spatially resolved spectra of the Earth from the far-UV to the far-IR. The SMART-T transmission model is used specifically to generate synthetic transit transmission spectra. The 1D radiative-convective climate model calculates self-consistent surface temperatures of hypothetical atmospheres with given greenhouse gas concentrations. The photochemistry model is used to calculate self-consistent mixing ratios of gases produced or destroyed from photolysis and chemical reactions in a planetary atmosphere.

1.5.2 *Chapter 3: Earth from the Moon: A Spectral Earth Database*

In Chapter 3 I generate a spectral library of the Earth as seen from the Moon over the course of a synodic month using the VPL Earth 3D spectral Earth model. I use this dataset to examine the phase-dependent spectral effects in Earth's simulated disk-averaged spectrum. I calculate UBVRIJHK absolute magnitudes and colors and examine the Earth's spectrophotometric variation. I find significantly reddening of the planetary spectrum near crescent phase across all UV/VIS/NIR color bands. At phases near quadrature, significant rotational variation can be recovered even with broad pass bands. I describe several applications of this synthetic dataset, including testing our ability to retrieve temporally rotationally dependent information from exoplanet spectra and spectrophotometry and data model comparisons with interplanetary spacecraft data. The subsequent chapter provides one example of this type of application.

1.5.3 *Chapter 4: Detecting N_2 in Planetary Atmospheres*

Characterizing the bulk atmosphere is important for constraining habitability. This is because the surface stability of liquid water, and therefore the habitability of a planet, is dependent not just on surface temperature but also on pressure. The modern Earth's atmosphere is dominated by N_2,

and it is likely that N_2 will be an important constituent in terrestrial planet atmospheres and yet it is extremely difficult to detect.

Here I explore the detectability of N_2 in Earth-like planetary atmospheres. I compare interplanetary spacecraft observations of the Earth from the EPOXI mission to VPL's 3D Spectral Earth model show that N_2, often considered to be a spectrally inactive gas, produces a ~35% effect on Earth's disk-averaged spectrum near 4.15 μm through N_2-N_2 collisional pairs, or $(N_2)_2$. I use radiative-convective models to construct self-consistent N_2-H_2O-CO_2 atmospheres and, using these atmosphere profiles as input to the radiative transfer model SMART, quantify the effect of $(N_2)_2$ on simulated planetary radiance spectra near 4.2 μm. I show that $(N_2)_2$ begins to produce a spectral impact strongly dependent on N_2 abundance when $pN_2 \geq 0.5$ bar, and can significantly widen the combined 4.3 μm CO_2/$(N_2)_2$ band at high pN_2. I create analytic N_2 and N_2-H_2 atmospheres and use the SMART-T transmission model to calculate the transit depth signature of $(N_2)_2$ for an Earth-size planet orbiting within the habitable zone of an M5V star with R=0.2 $R_{\odot}$, for which refraction allows deeper pressure levels in the planetary atmosphere to be probed. I demonstrate that in this case the spectral transmission signal of $(N_2)_2$ can reach 10 ppm for a pure N_2 atmosphere with no CO_2, and significantly larger for N_2-H_2 atmospheres with larger scale heights.

1.5.4 *Chapter 5: Detecting Oxygen "False Positives" for Life*

In Chapter 5 I find that the mechanisms that generate abiotic O_2 will also produce potential spectral discriminators CO and O_4. I produced self-consistent transmission spectra of these atmospheres and simulate observations of them with the *James Webb Space Telescope* (JWST). The observation of both CO (2.35, 4.6 μm) and CO_2 (1.6, 2.0, 4.3 μm) together in a transmission spectrum could indicate robust CO_2 photolysis that may generate significant abiotic O_2 or O_3. If

significant O_4 bands at 1.06 and 1.27 μm are observed in transmission, it could indicate a massive O_2 atmosphere originating from a history of significant hydrogen escape. Using JWST instrument simulation models, I find that for an Earth-size planet orbiting a nearby M dwarf star, CO at 2.35 μm, CO_2 at 2.0 and 4.3 μm, and O_4 at 1.27 μm are stronger features in transmission than O_2/O_3 and could be detected with SNRs > 3, assuming photon-limited noise. I find that massive post-runaway O_2 atmospheres could be identified in reflected light by a next generation direct-imaging telescope such as LUVOIR/HDST or HabEx with strong UV/VIS/NIR O_4 bands (at 0.345, 0.36, 0.38, 0.445, 0.475, 0.53, 0.57, 0.63, 1.06, and 1.27 μm) that would indicate an oxygen atmosphere too massive to be biologically produced.

1.5.5 *Chapter 6: Nonphotosynthetic pigments as potential surface biosignatures*

This chapter consists of an interdisciplinary study of the diversity and detectability of nonphotosynthetic pigments as biosignatures. This includes a review of the functions of biological pigments and the environments in which they are found, a lab-based study of the reflectance spectra of different pigmented organisms, and 1D and 3D spectral modeling of hypothetical, but realistic planetary environments that contained surfaces with pigmented organisms, such as a halophile-dominated ocean on an Earth-like planet with realistic clouds. I find that, given significant surface coverage, nonphotosynthetic pigments can produce significant effects on the disk-averaged spectrum of the planet. However, surface biosignatures are unlikely to be detected by broadband colors, and would require spectrally resolved data.

1.5.6 *Conclusions*

The concluding chapter includes a summary of each chapter and a short section on future work.

Chapter 2. MODELS

The subsequent chapters make wide use of various computational models for simulating aspects of planetary atmospheres. These include spectral radiative transfer models, a one-dimensional radiative-convective climate model, and a one-dimensional photochemistry model. This chapter describes the basic physical theory behind each computational model and includes standard inputs and boundary conditions for those models. I do not recapitulate every foundational detail of these complex models, but I do provide detailed references to the original and most recent publications that describe them most fully. The descriptions are ordered with respect to how widely used each model is throughout the subsequent chapters with the most widely used models in the beginning. In Section 2.1 I describe the SMART line-by-line radiative transfer model used for spectral modeling in each chapter, in Section 2.2 I describe the VPL spectral Earth model, which is used to produce high-fidelity, whole Earth spectral products in Chapters 3, 4 and 6, in Section 3.3 I describe the SMART transmission model used in Chapters 4 and 5, in Section 2.4 I describe the radiative convective climate model used in Chapters 4 and 5, and in Section 2.5 I describe the photochemistry model used in Chapter 5. I describe the coupling routines between the photochemistry and climate model in Section 2.6, which is used in Chapter 5. Small portions of this chapter (in Sections 2.1 and 2.2) were originally published in collaboration with T.D. Robinson, V. S. Meadows, A. Misra, and S.D. Domagal-Goldman in the September 2015 edition of the *Astrophysical Journal* (Schwieterman et al., 2015, ApJ, Vol. 810, 57;), and are reproduced below with permission of the American Astronomical Society.

2.1 Spectral Mapping and Atmospheric Radiative Transfer Model (SMART)

The Spectral Mapping Atmospheric Radiative Transfer (SMART) model, developed by D. Crisp, is the foundational radiative transfer program of the Virtual Planetary Laboratory (Meadows & Crisp 1996, Crisp 1997). Gaseous absorption coefficients over most relevant wavelength ranges are calculated by the companion Line-By-Line ABsorption Coefficients model (LBLABC), also developed by D. Crisp. In this subsection I describe LBLABC/SMART, which are used for spectral modeling throughout this work.

2.1.1 *Radiative Transfer Theory and SMART*

SMART is a one-dimensional, plane-parallel, line-by-line, multi-stream, multiple-scattering radiative transfer model. SMART takes as input vertical profiles of temperature, pressure, gas mixing ratios, and aerosol optical depths. With these inputs SMART calculates the monochromatic optical properties of each layer. Line absorption coefficients for gases with visible and infrared vibration-rotational transitions are calculated by LBLABC, which determines the absorption coefficients of spectrally active gases at each level of the atmosphere given a line list database.

The monochromatic optical depth of a vertical column of gas ($\tau(\nu)$) can be given in terms of the monochromatic absorption coefficient k_m, a function of altitude (z), temperature (T), wavenumber($\tilde{\nu}$), and the number density distribution of the gas, $N_m(z)$. Thus, integrating over the optical path, and summing over all gases (m) with vibrational-rotation absorption, we can write (Tinetti et al. 2006)

$$d\tau_0(\nu) = -\int \sum_{m=1}^{M} [k_m(\tilde{\nu}, z, T) N_m(z)] dz \qquad (2.1)$$

By assuming hydrostatic equilibrium (dp/dz = -ρg = -μng), where n is the number density, equation 2.1 can be written as a function of pressure *p* rather than altitude *z*

$$d\tau_0(\nu) = A_0 \int \sum_{m=1}^{M} \left[k_m(\tilde{\nu}, p, T) q_m(p) \Big/ (\mu_m g) \right] dp \qquad (2.2)$$

where $N_m(p)$ has been written in terms of the mass mixing ratio of the gas q_m, the molecular weight of the gas μ_m, the gravitational acceleration g, the temperature T, and Avogadro's number A_0. The gas absorption coefficient, k_m, is constituted from the sum of all absorption lines that contribute opacity at a given ν

$$k_m(\tilde{\nu}, p, T) = \sum_{i=0}^{N} S_i(T) f_i(\tilde{\nu} \pm \widetilde{\upsilon_{0i}}, p, T) \qquad (2.3)$$

where S_i is the strength of the ith spectral line centered at the wavenumber v_{0i}, f_i is the line profile function at a distance ($\tilde{\nu}$ - $\widetilde{\nu_{0i}}$) from the center of line i, and N is the number of lines that contribute to the absorption at wavenumber v. LBLABC evaluates Equation 2.3 to create an absorption coefficient reference file for each gas, at each pressure level, at each wavenumber, and at from one to several reference temperatures.

LBLABC uses for its line shape a Voigt line profile that includes Doppler broadening, Lorentzian (pressure) broadening, and Dicke (pressure) narrowing within a Voigt cutoff of 40 Doppler half-widths of the line-center (Meadows & Crisp 1996). At greater distances from the line center, a van Vleck-Weisskopf profile is used for all gases except for H_2O, CO_2, and O_2 (Goody & Yung 1989; pg. 100). For H_2O, the van Vleck-Weisskopf profile is altered at greater distances from line center by multiplication by an empirical wavenumber-dependent χ factor modified from Clough et al. (1989). For CO_2 a sub-Lorentzian profile is calculated based on a set of semi-empirical χ factors (Meadows & Crisp 1996). For O_2, a super-Lorentzian shape is calculated from Hirono & Nakazawa (1982) with an exponent of 1.958. LBLABC was

developed to be applicable over a wide range of temperatures (130-750 K), pressures (10^{-5} to 100 bar) and distances from the center of an absorbing line (10^{-3} to 10^{3} cm^{-1}) (Meadows & Crisp 1996). Throughout this work, when calculating gaseous absorption coefficients with LBLABC, a line cutoff of 1000 cm^{-1} is used (unless otherwise specified).

The gas absorption coefficients determined by LBLABC are read in by SMART and multiplied by the gas mixing ratios and layer thicknesses to determine the normal-incidence gas extinction optical depths (Equation 2.2). The total extinction at each layer and each spectral grid point is calculated by combining the gas extinction optical depths with those calculated for Rayleigh scattering and aerosol absorption.

SMART generates synthetic spectra of planetary atmospheres by solving the radiative transfer equation, which can be written as (Goody & Yung 1989; pg. 519)

$$\mu \frac{dI(\tau,\mu,\phi,\tilde{\upsilon})}{d\tau} = I(\tau,\mu,\phi,\tilde{\upsilon}) - S(\tau,\mu,\phi,\tilde{\upsilon}) \tag{2.4}$$

where I is the radiance, τ is again the vertical column integrated optical depth, μ is the cosine of the zenith angle (μ=cosθ_i) and ϕ is the azimuth angle. S is the source function, and it is given by

$$S(\tau,\mu,\phi,\tilde{\upsilon}) = \frac{\omega(\tau,\tilde{\nu})}{4\pi}\int_0^{2\pi} d\phi' \int_{-1}^{1} d\mu' P(\tau,\mu,\phi,\mu',\phi',\tilde{\nu}) I(\tau,\mu',\phi',\tilde{\nu}) +$$

$$[1-\omega(\tau,\tilde{\nu})]B[\tilde{\nu},T(\tau)] + \frac{\omega(\tau,\tilde{\upsilon})}{4\pi} F_{\odot} P(\tau,\mu,\phi,-\mu_{\odot},\phi_{\odot},\tilde{\nu}) e^{-\frac{\tau}{\mu_{\odot}}} \tag{2.5}$$

where $\omega(\tau,\tilde{\nu})$ is the single scattering albedo (i.e., $\omega(\tau,\tilde{\nu}) = Q_{scat}(\tau,\tilde{\nu}) / Q_{ext}(\tau,\tilde{\nu})$), $P(\tau, \mu, \phi, \mu', \phi', \tilde{\nu})$ is the scattering phase function, B[$\tilde{\nu}$,T(τ)] is the Planck function, $F_{\odot}$ is the solar (or, most generically, the illuminator) spectral irradiance at the top of the atmosphere (the calculation may run without or without an illumination source), $\mu_{\odot}$ is the solar zenith angle, and $\phi_{\odot}$ is the solar azimuth angle. The Planck function B[$\tilde{\nu}$,T(τ)] can be written as

$$B_{\tilde{\nu}}[\tilde{\nu}, T] = \frac{2h\tilde{\nu}^3 c^2}{e^{hc\tilde{\nu}/kT} - 1} \quad (2.6)$$

Figure 2.1 illustrates the geometric scheme for SMART's radiative transfer calculations. Note that for this geometric arrangement, a solar zenith angle of 90° represents the illumination source on the horizon, an angle of 0° at the zenith, and an angle of 60° approximately equal to the diurnal average. An observer azimuth angle of 0° represents the view directly towards the illumination source while a ϕ of 180° is a view directly away.

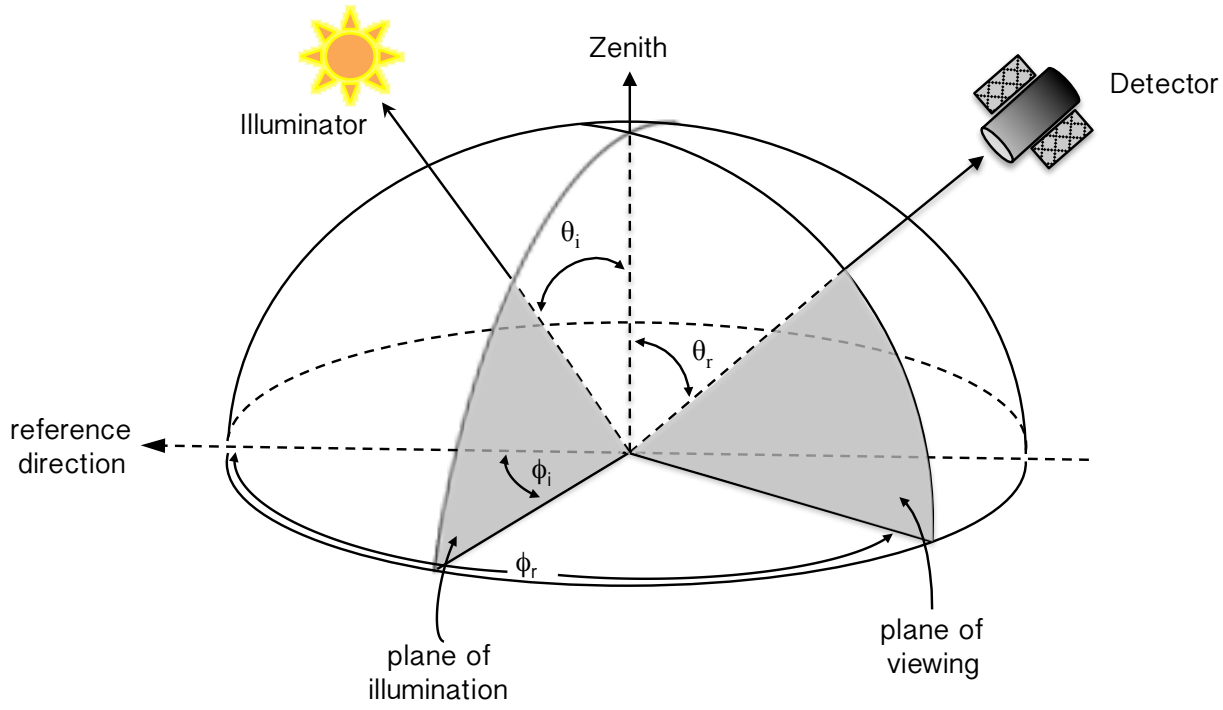

Figure 2.1. Geometric scheme for SMART radiative transfer calculations. The three input angles are: the solar zenith angle (θ_i), the observer zenith angle (θ_r), and the observer azimuth angle ($\phi_r - \phi_i$), where the illuminator azimuth angle (ϕ_i) has been chosen as the reference direction. Based on Figure 6 of Tinetti et al. (2006a).

SMART uses the discrete ordinate method to evaluate the integrals in Equation 2.5 at each level of the atmosphere (through the DISORT FORTRAN code; Stamnes et al. 1988). Each vertical layer is assumed to have constant optical properties (τ, ω, etc.) with 40-70 layers

typically used. The number of streams used for the discrete ordinate method is a tunable parameter in SMART. I used eight streams (four up, four down) for all cases of a single SMART run in this work, a parameter which has been empirically evaluated by model data comparisons of Venus's NIR spectrum (Meadows & Crisp 1996; Arney et al. 2014). The Gaussian quadrature points at 21.48°, 47.93°, 70.73°, and 86.01° are used for each of the upward and downward radiance streams. The output of the model contains the upward radiance streams and the sum of all the contributions to the disk-averaged spectrum. The streams are used directly by the VPL Earth model described below. In other cases the total (disk-averaged) radiance spectrum from a single SMART run is shown throughout this work, unless otherwise stated.

The mapping methods used by SMART greatly reduce computational time relative to strict line-by-line methods. SMART uses mapping algorithms that bin subintervals within spectral regions that have sufficiently similar optical properties (e.g., τ, ω, and P) along an optical path and then maps these subintervals into a reduced number of broader monochromatic bins. SMART then solves Equation 2.5 for just these bins (West et al. 1990). SMART can then reallocate these computed radiances back onto the original higher resolution wavenumber array, introducing radiance errors that are less than a few percent while increasing computational efficiency by two to three orders of magnitude (Meadows & Crisp 1996).

2.1.2 *Boundary conditions and standard inputs*

SMART requires atmosphere and surface parameters in order to evaluate the radiative transfer equation (eq. 2.5). These include the optical properties (τ, ω, and P) and temperature, $T(\tau)$, of each atmospheric layer. The top layer of the atmosphere is bounded by a downward thermal flux of zero and a non-attenuated downward shortwave (solar or stellar) flux set by the parent star (or generically, the illuminator) distance and appropriately scaled for the cross-sectional geometry of

the planet. The surface albedo, Av, and its reflectance function, $P_A(\mu,\mu')$, constitute the boundary conditions at the bottom layer of the atmosphere.

There are three types of atmospheric gas absorption evaluated by SMART: 1) absorption by gases with pre-computed cross-sections, 2) line absorption with temperature and pressure dependent profiles calculated by LBLABC, and 3) collisionally-induced absorption. I use cross-sections for gas absorption from electronic and pre-dissociation transitions in the UV (> 0.4 μm) throughout this work. Figure 2.2 shows UV cross sections for the major absorbing gases in Earth's atmosphere from Demore et al. (1997). Line absorption is calculated by LBLABC for rotational-vibrational transitions from the visible to far infrared wavelengths (0.4 to 200 μm). I used the HITRAN 2008 (Rothman et al. 2009) line lists in conjunction with LBLABC to calculate the absorption coefficients for the spectrally absorbing monomer gases in the Earth-Lunar spectral database presented in Chapter 3 and for the spectral products in Chapter 6. The HITRAN 2012 (Richard et al. 2012) line lists are used for the spectral products in Chapters 4 and 5. Figure 2.3 illustrates the HITRAN 2012 line intensities for these major absorbing gases in Earth's atmosphere: O_2, H_2O, CO_2, O_3, N_2O, CH_4 and CO. In the temperature, pressure, and spectral resolution regimes investigated in this work, the impact of using either HITRAN 2008 or 2012 is minimal. Collisionally induced absorption (CIA) theory (3) is relevant for gas collisions that produce temporarily induced dipoles in collision partners, or for bound van der Waals molecular complexes (dimers) that typically exist at very low temperatures (Frommhold 1993). The strength of CIA is dependent on the square of the gas density and inversely dependent on temperature. SMART can accommodate temperature-dependent CIA absorption by gases given pre-computed binary (collisional) absorption coefficients. This is relevant for the N_2-N_2, N_2-O_2,

and O_2-O_2 CIA described in Chapters 4 and 5. I include detailed formulae for the inclusion of CIA in spectral calculations in those chapters.

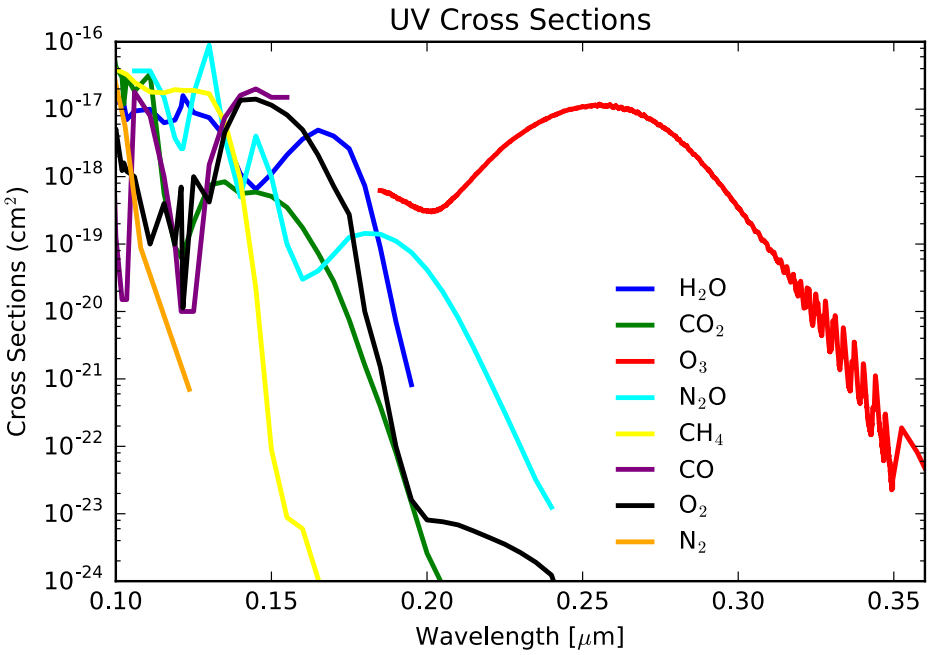

Figure 2.2. Ultraviolet (0.1-0.38 μm) cross sections (cm^2) for bulk and significant trace gases in Earth's atmosphere. Data are from Demore et al. (1997).

Scattering by molecules and aerosols is also included by SMART. The type of scattering chosen depends on the size parameter x, given by

$$x = \frac{2\pi r}{\lambda} \tag{2.7}$$

where r is the radius of the particle and λ is the wavelength. For sufficiently small x, Rayleigh scattering dominates. This is the case for gaseous molecules in the atmosphere when interacting with visible and non-dissociative UV radiation in Earth's atmosphere. The molecular cross section for Rayleigh scattering is inversely dependent on wavelength to the fourth power and is given by (Allen 1964):

$$\sigma_s = \frac{32\pi^3}{32N} \cdot \frac{(n-1)^2}{\lambda^4} \cdot \delta \qquad (2.8)$$

where σ_s is the linear scattering coefficient, N is molecular number density, n is refractive index of the atmospheric medium, and $\delta = (6+3\Delta)/(6-7\Delta)$ is the depolarization factor with $\Delta = 0.030$ for N_2 and $\Delta = 0.054$ for O_2.

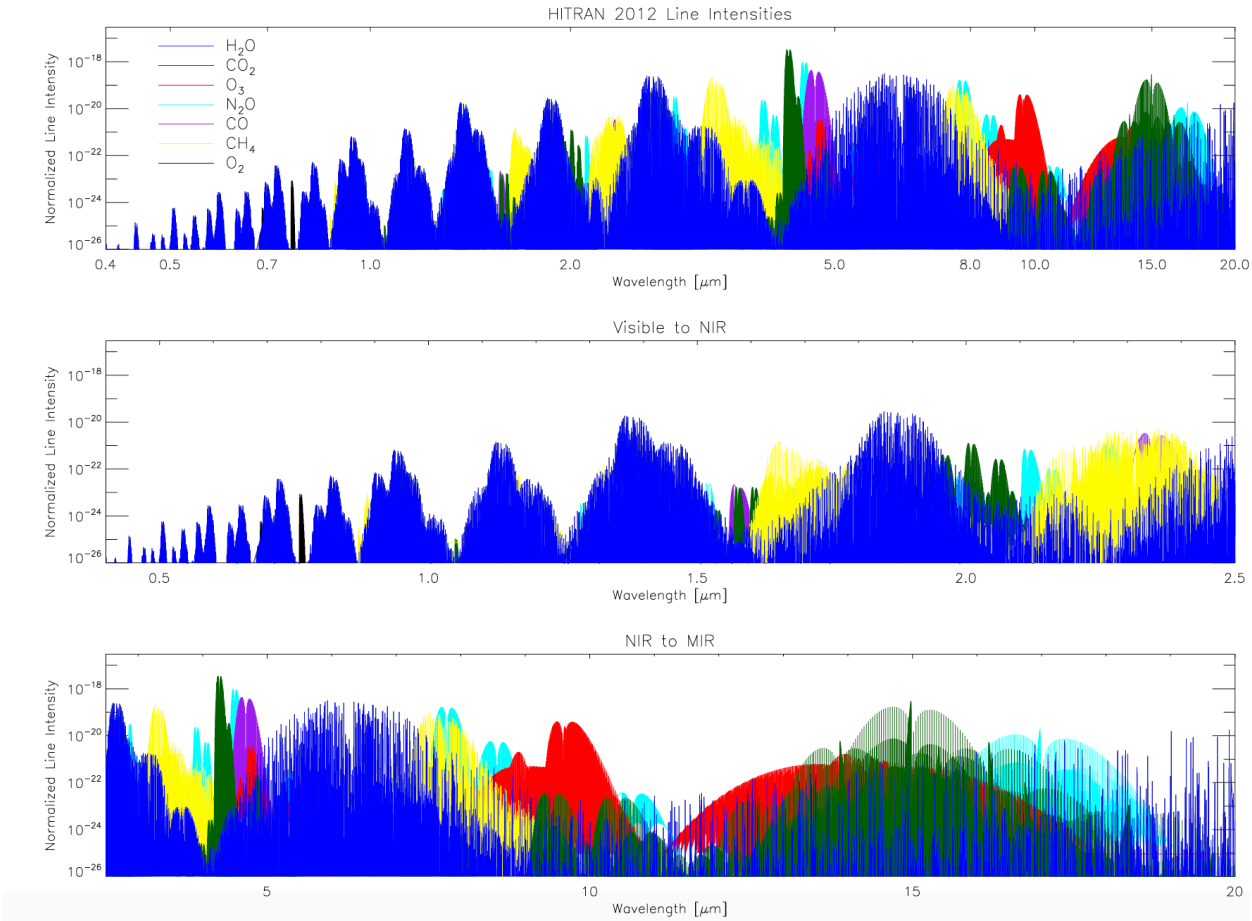

Figure 2.3. HITRAN 2012 (Richard et al. 2012) line intensities (cm^{-1}/(molecule•cm^{-2})) for each major absorbing gas in Earth's atmosphere (0.4-20 μm): H_2O, CO_2, O_3, CH_4, N_2O, CO, and O_2. Includes isotopologues whose line intensities have been scaled by their natural abundance (on Earth).

For particles with moderately large x, such as raindrops, a different scattering regime is reached. If the particles can be modeled as spheres than Mie theory can be used. For particles with non-spherical shapes, or sufficiently large x, geometrics optics must be used. SMART can include scattering by aerosols with pre-computed optical properties (e.g., Q_{ext}, Q_{scat}, g) from a Mie scattering model or a geometric optical model. A Mie scattering model (Wiscombe 1980; Crisp 1986) is used to compute the optical properties of water droplets (liquid water clouds) while ice (cirrus) clouds are modeled as distributions of hexagonal crystals and their optical properties are determined by the geometric optics approach described by Muinonen et al. (1989). For spherical particles a full Mie phase function can be used, otherwise a Henyey-Greenstein phase function is employed (Henyey & Greenstein 1941).

2.2 VPL 3D Spectral Earth Model

To generate time-dependent, high-fidelity, and well-validated disk-averaged and spatially-resolved spectra of the Earth, I use the Virtual Planetary Laboratory (VPL) three-dimensional, line-by-line, multiple scattering Earth model (Tinetti et al. 2006a; Robinson et al. 2011; Robinson 2012). This model incorporates data from Earth-observing satellites to specify Earth's atmospheric and surface state, including snow, ice, and cloud cover. The model uses these factors as input to generate synthetic, time-dependent spectra of Earth, including absorption and scattering by the atmosphere, surface, and clouds and specular reflection by the ocean (Robinson et al. 2010). The VPL Earth model has been validated against broadband visible and NIR data from NASA's *EPOXI* mission, which repurposed the Deep Impact flyby spacecraft (Livengood et al. 2011; Robinson et al. 2011), and against phase-dependent, high-resolution visible and NIR spectral data from NASA's *LCROSS* mission (Robinson et al. 2014). The temperature-pressure and gas mixing ratio profiles for each atmospheric pixel, the relative coverage of snow and

clouds for each pixel, and the wind speed and direction used to calculate specular reflectance for each ocean pixel (Cox & Munk 1954) are determined by a suite of data from Earth-observing satellites, described by Robinson et al. (2011), but summarized below. I also describe the computed spectral library and the geometric calculations used by the Earth model to create disk-averaged spectra for spatially resolved data cubes.

2.2.1 *Surface parameters*

There are five surface types used by the Earth model: grassland, forest, ice/snow, soil, and seawater. The spectral albedos for these surface types were taken from the USGS and ASTER spectral libraries (Clark et al. 2007; Baldridge et al. 2009) and are shown in Figure 2.4.

The spatial distribution of land, grassland, forest and ocean are determined from an interpolation of a yearly averaged map[3] from the Moderate Resolution Imaging Spectroradiometer (MODIS) instrumentation (Salomonson et al. 1989) aboard the NASA Aqua and Terra satellites. Snow and sea ice cover is seasonably variable and so requires a more temporarily restricted window for determining spatial distribution. Multi-day averaged snow and sea ice cover data products[4] from MODIS observations are used to assign the snow/ice (Hall et al. 1995; Riggs et al. 1999). The SeaWinds instrument on the QuickSCAT satellite (Katsaros et al. 2001) provides wind speed and direction[5], which are used as input by the Cox-Munk glint model (Cox & Munk 1954) to calculate the bidirectional reflectance distribution function (BDRF) of the wave-covered ocean[6]. Other surface types are assumed to be Lambertian reflectors (i.e., isotropic reflection).

---

[3] http://modis-land.gsfc.nasa.gov/landcover.html
[4] http://modis-snow-ice.gsfc.nasa.gov
[5] http://podaac.jpl.nasa.gov/datasetlist?ids=Measurement&values=Ocean Winds
[6] Note that QuikSCAT suffered an antennae motor failure on November 22, 2009, so wind vectors are not available for subsequent dates

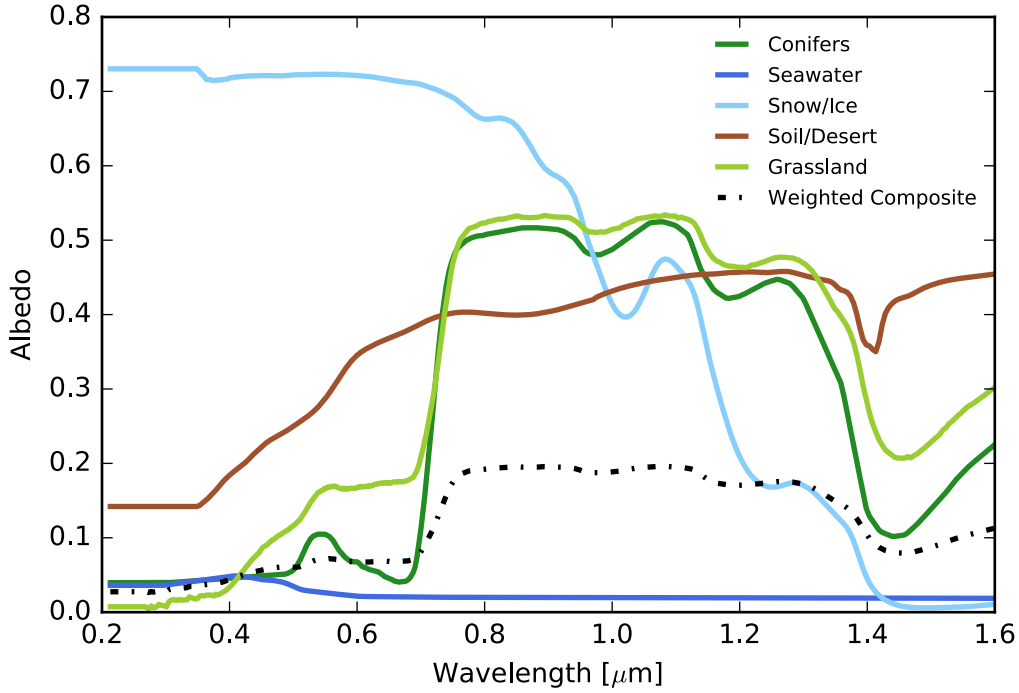

Figure 2.4. Spectral albedos for each surface type used by the VPL spectral Earth model (0.2 – 1.6 μm). The forest albedo spectrum as taken from the ASTER spectral library (Baldridge et al. 2009), while the other surface albedos were taken from the USGS spectral library (Clark et al. 2007). The seawater albedo spectrum is consistent with the albedo of an ocean averaged over all observer angles using the Cox & Munk (1954) glint model (Robinson et al. 2010, Robinson 2012). The composite spectrum (black-dash) is based on a weighted average of 65.6% seawater, 4% conifer forest, 13.6% grassland/brush, 5.5% soil/desert, and 11.3% snow/ice, based on an equatorial view during spring equinox.

2.2.2 *Atmosphere parameters*

Suites of instruments aboard Earth observing satellites inform the spatial distribution of trace gases in the atmosphere in daily averaged data products. This instrumentation includes the

Microwave Limb Sounder (MLS[7]; Waters et al. 2006) and Tropospheric Emission Spectrometer (TES[8]; Beer et al. 2001) aboard the NASA Aura satellite, and the Atmospheric Infrared Sounder (AIRS[9]; Aumann et al. 2003) aboard the NASA Aqua satellite. Table 2.1 provides a concise list of the species measured by these instruments and the dynamic range of these gases in the atmosphere (adapted from Robinson et al. (2011)). Spatially resolved temperature profiles are derived from a combination of data from MLS/Aura and AIRS/Aqua. Other major bulk and trace gases such as O_2, N_2, and CO_2 are evenly mixed in the atmosphere. See Figure 2.5 for mixing ratio and temperature profiles for a representative mid-latitude southern hemisphere profile.

Table 2.1 Earth Model Trace Gas Parameters

			Nominal Volume Mixing Ratio		
Species	Instrument	Range (Pa)	Surface	Tropopause	Stratopause
H_2O	AIRS/Aqua	10^5 - 10^4	10^{-3}-10^{-2}	3×10^{-6}	3×10^{-6}
H_2O	MLS/Aura	3×10^4 - 2×10^{-1}	-	-	-
O_3	MLS/Aura	2×10^4 – 2×10^0	10^{-8} - 10^{-7}	1×10^{-7}-1×10^{-6}	5×10^{-6}
CH_4	TES/Aura	10^{-5} - 5×10^2	10^{-6}	10^{-6}	2×10^{-7}
N_2O	MLS/Aura	10^4 – 10^1	5×10^{-7}	4×10^{-7}	2×10^{-8}
CO	MLS/Aura	10^4 - 10^2	10^{-8}-10^{-7}	10^{-8}-10^{-7}	10^{-7}

Adapted from Robinson et al. (2011) with data from Livesey et al. (2007) and Payne et al. (2009)

[7] http://mls.jpl.nasa.gov/data
[8] http://tes.jpl.nasa.gov/data
[9] http://airs.jpl.nasa.gov

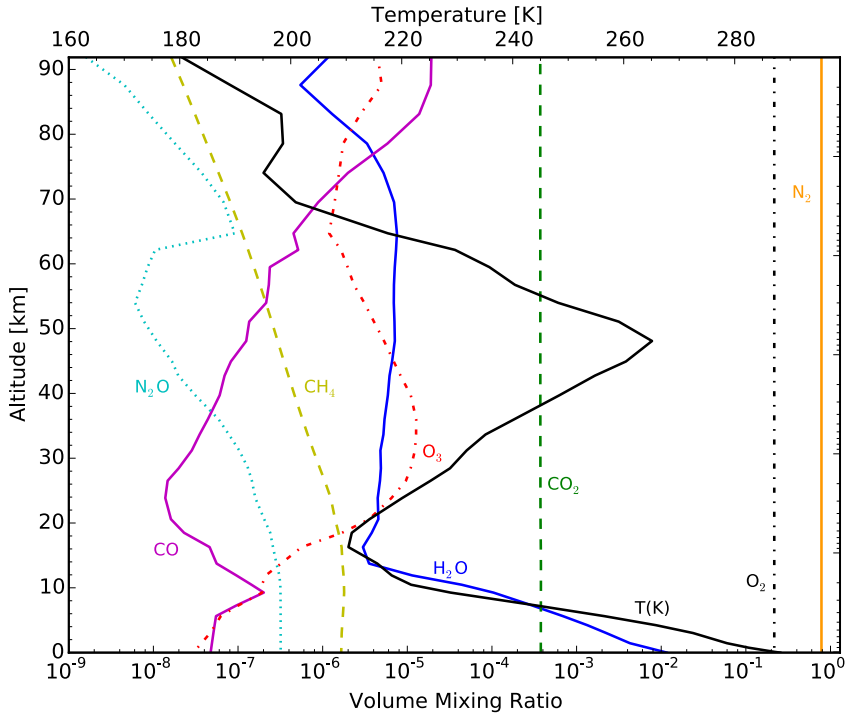

Figure 2.5. Temperature and gas volume mixing ratio profiles from a representative southern hemisphere mid-latitude Earth model atmospheric pixel (41.8° S, 23.5° W) calculated for March 19, 2008 (Schwieterman et al. 2015b; also see Chapter 3) using data products summarized in Table 2.1.

2.2.3 *Inclusion of clouds*

The Earth model determines cloud spatial locations other properties with daily averaged cloud coverage maps from MODIS[10]. The MODIS data products also indicate cloud phase (liquid, ice), cloud top pressure (a proxy for altitude), and optical depth measurements. In the model, four cloud types are chosen that give a good (observationally validated) representation of the diversity of Earth's cloud cover (Robinson et al. 2011; Livengood et al. 2011). Liquid water clouds (stratocumulus) are placed at 1.5 km (0.847 bar) while ice (cirrus) clouds are placed at 8.5 km

[10] http://modis-atmos.gsfc.nasa.gov/

(0.331 bar). Both clouds are split into moderately thick and very thick categories. Liquid water clouds have optical depths of 5 or 15, while ice clouds have optical depths of 5 or 20. These optical depths bracket well the observed range of cloud optical depths and give a good fit to validation data (Robinson et al. 2011). A Mie algorithm is used to model the scattering properties of liquid water clouds (Wiscombe 1980; Crisp 1986) , while cirrus clouds are modeled as distributions of hexagonal ice crystals with a geometric optics routine applied to determine their scattering properties (Muinonen et al. 1989; see Section 2.1.2). A full Mie phase function can be used for the spherical water droplets, while a Henyey-Greenstein (Henyey & Greenstein 1941) phase function is used for other particles.

2.2.4 *Earth model geometric calculations and SMART spectral library*

The VPL Earth model integrates the projected area weighted intensity of the planet (or a region of the planet) in the direction of the observer (Robinson et al. 2014), which can be written as

$$F_\lambda(\hat{\boldsymbol{o}}, \hat{\boldsymbol{s}}) = \frac{{R_E}^2}{d^2} \int I_\lambda(\hat{\boldsymbol{n}}, \hat{\boldsymbol{o}}, \hat{\boldsymbol{s}})(\hat{\boldsymbol{n}} \cdot \hat{\boldsymbol{o}}) d\omega \tag{2.9}$$

where $F_\lambda(\hat{o}, \hat{s})$ is the flux density measured by the observer, R_E is the radius of the Earth (6378 km), d is the distance from the planet to the observer, $I_\lambda(\hat{\boldsymbol{n}}, \hat{\boldsymbol{o}}, \hat{\boldsymbol{s}})$ is the location-dependent specific intensity directed at the observer, $\hat{\boldsymbol{o}}$ and $\hat{\boldsymbol{s}}$ are unit vectors in the direction of the observer and the Sun, respectively, $d\omega$ is an infinitesimal solid angle on the globe, and $\hat{\boldsymbol{n}}$ is a normal unit vector for the location of the planet's surface corresponding to $d\omega$. To calculate the disk-integrated spectrum, we use Equation 2.9 to integrate over the observable hemisphere (2π steradians). However, Equation 2.9 may be used to integration over small regions of the planet to create a spatially resolved spectral data cube of the Earth. This is explored further below.

The HEALpix parameterization (Gorski et al. 2005)[11] is used to pixelate the atmosphere and surface and numerically evaluate Equation 2.9. If we divide the plane into N equal-area surface pixels (Robinson et al. 2014), Equation 2.9 can be written as

$$F_\lambda(\hat{\boldsymbol{o}}, \hat{\boldsymbol{s}}) = \frac{4\pi}{N}\frac{{R_E}^2}{d^2}\sum_{i\in O} I_\lambda(\hat{\boldsymbol{n}}_i, \hat{\boldsymbol{o}}, \hat{\boldsymbol{s}})(\hat{\boldsymbol{n}}_i \cdot \hat{\boldsymbol{o}}) \qquad (2.10)$$

where $\hat{\boldsymbol{n}}_i$ is the unit vector describing the location on the sphere of surface pixel *i*, and *O* is the set of indices of all observable pixels ($\hat{\boldsymbol{n}_i} \cdot \hat{\boldsymbol{o}} > 0$). The HEALpix method divides a sphere into equal area pixels and is defined by a parameter k where the number of pixels on the sphere can be $N_{pix}=12*(2^k)^2$; however the variable 2^k is often written as N, so that the number of pixels is $12*N^2$. A key constraint is that N is limited to a series 2^k where k = 1, 2, 3, etc. For the Earth-Lunar spectral database presented in Chapter 3, I use 192 surface pixels (k=2,N=4) of mixed type (coverage weighted averages of forest, grass, desert, ocean, and snow/ice), which are nested below 48 atmospheric pixels (k=1,N=2) with 40 vertical atmosphere layers. (For a subset of this database, higher k and N are used, up to k=6, and N=64.)

For each date the Earth model is run, SMART is used to generate a spectral database for every combination of atmospheric pixel (48), surface type (5), cloud type (4, plus clear sky), solar zenith angle (0°, 15°, 30°, 45°, 60°, 75°, 80°, 85°, and 90°), observer zenith angle (the Gaussian angles 21.48°, 47.93°, 70.73°, and 86.01°), and observer azimuth angle (0°, 30°, 60°, 90°, 120°, 150°, and 180°). An illustration of the geometric angles used for each SMART calculation is shown in Figure 2.1. The size of the composite SMART spectral library is approximately 10,000 one-dimensional radiative transfer (SMART) runs, which takes approximately three weeks to generate using 100 CPUs.

[11] http://healpix.sourceforge.net/

The Earth model interpolates over this spectral library to calculate the spectrum of each surface pixel that is summed in Equation 2.10 by weighting according to the observer-planet-Sun viewing geometry and the relative coverage of each surface and cloud type for the pixel. A Kurucz model spectrum of the Sun (Kurucz 1995) is used as the input solar spectrum in the Earth model and for all other SMART runs with the Sun as the illumination source. Figure 2.6 provides an illustration of the individual spectral reflectivity contributions from each combination of surface or cloud type with a representative mid-latitude atmosphere profile (Figure 2.5) over a UV to NIR wavelength interval (0.2 – 1.6 μm). The assumed solar zenith angle is 60° and the azimuth angle is 0°.

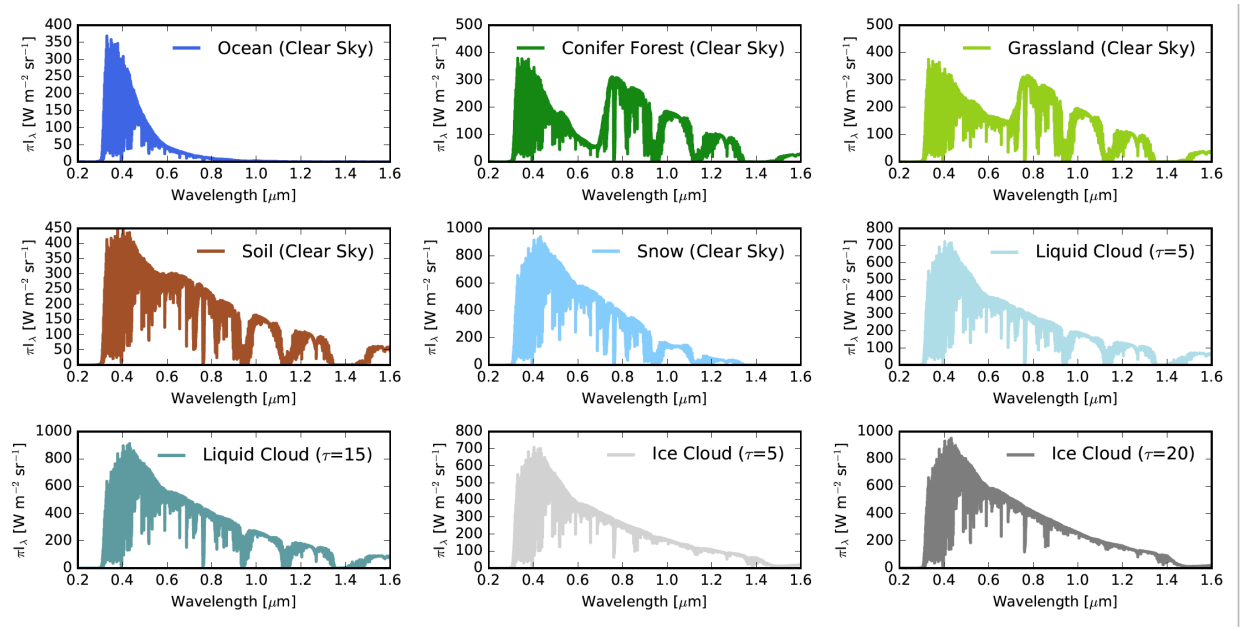

Figure 2.6. Example reflectivity spectra (planet flux/solar flux) of the VPL Earth model spectral library for each surface and cloud type. The example spectra shown were calculated using the atmosphere profile in Figure 2.5 and the albedos in Figure 2.4, assuming a solar zenith angle of 60°. The cloud types are water clouds with optical depths (τ) of 5 and 15 and ice clouds with optical depths of 5 and 20.

Spectral data cubes of each Earth view can also be generated. This consists of a data file with a spectrum corresponding to the solution to the Equation 2.8 for each pixel on the hemisphere visible to an observer with a given viewing geometry. Spectral data cubes can be used for validation observations that encompass only part of the Earth's disk (e.g., Robinson et al. 2014) and for visualization and other purposes. In Chapter 3 I present spectral data cube images of the Earth from Lunar viewing geometries.

2.3 SMART-TRANSMISSION (SMART-T)

The SMART Transmission model (SMART-T) uses the normal-incidence optical depths provided by SMART to calculate the transmission along limb-traversing paths (Misra et al. 2014a,b; Misra 2014). The transmission spectrum for each tangent altitude $h(i)$ (i.e., for each layer orthogonal to a parallel ray from the illuminating source) can be calculated with the Beer-Lambert Law by combining the optical properties determined by SMART with the path length between the adjacent atmospheric layers (Misra et al. 2014b)

$$F(\lambda, i) = e^{-\sum_j n(j)\cdot\sigma(\lambda)\cdot p(i,j)} \tag{2.11}$$

where $F(\lambda\ i)$ is the fractional flux transmitted through tangent altitude $h(i)$ at wavelength λ, $\sigma(\lambda)$ is the total extinction (absorption and scattering) cross-section at wavelength λ, $n(j)$ *is* the molecular number density at layer j, and $p(i,j)$ is the path length between neighboring layers j and $j+1$ at altitude $h(i)$, and can be written as

$$p(i,j) = \sqrt{h(j+1)^2 - h(i)^2} - \sqrt{h(j)^2 - h(i)^2} \tag{2.12}$$

The full fractional transmission through the atmosphere consists of a weighted average of Equation 2.12 that depends on the area of the planetary annulus at each altitude. It can be written as

$$F(\lambda) = \frac{\sum_i F(\lambda,i)\cdot\pi[(h(i+1)+R_P)^2-(h(i)+R_P)^2]}{\pi(\max(h)+R_P)^2} \quad (2.13)$$

where $F(\lambda)$ is the fraction of flux transmitted through the entire atmosphere at a given wavelength and R_P is the radius of the planet. The effective tangent height of at each wavelength ($R_{atm,\lambda}$) is the altitude at which less than 50% of the flux is transmitted (i.e., $F(\lambda,i) < 0.5$).

At times it is convenient to express the transmission spectrum in terms of the spectral transmission depth. The spectral transit depth can be calculated based on the effective tangent height of the atmosphere ($R_{atm,\lambda}$) with the following equation:

$$\Delta d_\lambda = \frac{\left(R_P+R_{atm,\lambda}\right)^2}{R_*^2} \times 10^6 \quad (2.14)$$

where Δd_λ is the spectral transit depth in parts-per-million, R_* is the radius of the host star, R_P is the solid radius of the planet, and $R_{atm,\lambda}$ is the wavelength dependent radius of the atmosphere, or equivalently, the effective tangent height of the atmosphere (Misra et al. 2014b).

Refraction is an important physical effect that is included in the SMART-T transmission calculation. As light originating from the star enters the planetary atmosphere from the vacuum of space, the change of medium creates a shift or bend in the path of the light. Rays that had been orthogonal to the planetary atmosphere will exit the atmosphere at an angle. This has significant consequences for an observer at an effectively infinite distance, which is the case for exoplanet observations. The primary effect of refraction is that starlight is refracted out of the beam for a distant observer during a transit (Sidis & Sari 2010). This effect sets a limit on the maximum pressure (density) that can be probed with transmission spectroscopy (García Muñoz et al. 2012; Bétrémieux & Kaltenegger 2014; Misra et al. 2014a,b). This limit is dependent on both the angular size of the star as seen by the planet (a function of stellar radius and planet-star distance) and the composition of the atmosphere. A secondary effect of refraction is that starlight can be

refracted into the observer's beam for prior to a transit, which has useful applications for characterizing planetary atmospheres (e.g., Sidis & Sari 2010; Misra et al. 2014b; Misra & Meadows 2014).

A path integration method detailed in van der Werf (2008) is used to include refraction in the transmission calculation of SMART-T. If the final angle calculated at a given tangent altitude by the path integration connects the observer to the stellar disk, then that tangent altitude can be observed with transmission spectroscopy. If the observer is not connected to the stellar disk via the final angle, that level of the atmosphere is opaque to the observer no matter what the optical properties of the layer are. Since the star will not have a constant brightness across the disk, a limb-darkening model is needed to determine the amount of flux transmitted through each layer of the atmosphere. SMART-T uses the limb darkening coefficients of Claret (2000).

The input parameters to the transit transmission model are identical to those of SMART with a two main additions. These additional inputs are: 1) the index of refraction of the surface layer of the atmosphere at standard temperature and pressure (STP) and 2) the radius of the host star in solar radii. Table 2.2 provides the indices of refraction and molecular weights for some common gases in a planetary atmosphere (matched against their HITRAN gas codes). (The index of refraction is typically measured at the wavelength of the sodium (Na) D line at 0.589 μm). SMART-T can also use a planet-star distance for geometric calculations independent of the distance used by SMART to scale stellar flux and the effects of refraction may be turned "off". Additional model details can be found in Misra et al. (2014b) and Misra (2014).

Table 2.2 Common Gas Properties

Gas	Index of Refraction[12]	Molecular Weight (amu)	HITRAN Code[13]
Air (Earth)	1.000293	28.97	-
N_2	1.000298	28.01	22
O_2	1.000271	32.0	7
CO_2	1.000445	44.0	2
H_2O	1.000256	18.02	1
O_3	-	48.03	3
CH_4	1.000444	16.04	6
N_2O	1.000516	44.01	4
CO	1.000338	28.0	5
Ar	1.000281	39.95	-
H_2	1.000132	2.02	45

2.4 1D Radiative-Convective Climate Model (CLIMA)

For climate calculations, I use a one dimensional radiative convective climate model originally developed by Kasting & Ackerman (1986) with heritage from Kasting et al. (1984) and Kasting & Pollack (1983). The climate model is used to calculate self-consistent planetary surface temperatures and atmospheric temperature profiles in Chapters 4 and 5 for various terrestrial atmosphere scenarios. This model has been substantially updated through the last few decades. The current incarnation of this climate model was recently used to calculate habitable zones for main sequence stars (Kopparapu et al. 2013), an update of the initial work by Kasting et al. (1993), and to calculate the climate of a hazy Archean Earth (Arney et al. 2016). A complete description of the climate model is outside the scope of this work, but I will briefly describe some key aspects.

The structure of the atmosphere is parameterized in the climate model as 101 layers, extending from 0 to 80 km. The troposphere temperature profile follows a wet adiabatic lapse

[12] from http://www.kayelaby.npl.co.uk/general_physics/2_5/2_5_7.html
[13] see http://www.cfa.harvard.edu/hitran/molecules.html

rate up to the stratospheric temperature (the cold trap) (Kasting 1988). The water vapor profile is based on a modified Manabe & Wetherald (1967) profile with a surface relative humidity of 80% (Kasting & Ackerman 1986). The temperature profile in the stratosphere is allowed to vary from UV heating by CO_2, O_3, and CH_4 (if present) absorption to achieve radiative equilibrium. Hydrostatic equilibrium is assumed to calculate the pressure-altitude profile. A δ2-stream multiple scattering algorithm (Toon et al. 1989) is used to account for absorbed stellar radiation in each atmosphere layer from shortwave radiation spanning 0.2 to 4.5 μm in 38 spectral bins. The main spectrally active gases are CO_2, H_2O, O_2, O_3, and CH_4. Correlated-k coefficients are used to compute absorption by these gases for net outgoing longwave infrared (IR) radiation (OLR). The correlated-k coefficients were calculated with a program called KSPECTRUM[14] using the HITRAN 2008 line lists (Rothman et al. 2009). For each gas 55 spectral intervals were used from 0 – 15,000 cm^{-1} ($\lambda > 0.67$ μm). CO_2 CIA is included based on the parameterization presented in Halevy et al. (2009).

The numerical method for calculating the thermal flux and temperature at each level are described in Appendix A of Kasting et al. (1984). Rayleigh scattering by bulk atmospheric gases N_2, O_2, CO_2 and H_2O is included in the calculation of planetary albedo. Clouds are not formally included, but are parameterized by a surface albedo (A_{surf} = 0.32) tuned to reproduce the temperature of modern Earth given empirical mixing ratio profiles and incident solar flux (Kopparapu et al. 2013). The input stellar spectrum and the overall incident flux is a tunable parameter that can vary based on the modeled planet-star distance. Additional adjustable parameters include the surface pressure and the mixing ratio of bulk and trace atmospheric gases. The 1D climate model described above is one part of the coupled photochemical-climate model Atmos, described further below in Section 2.6.

[14] http://code.google.com/p/kspectrum/

2.5 PHOTOCHEMISTRY MODEL

For modeling the photochemistry of planetary atmospheres I used a 1D diffusive photochemical code originally developed by Kasting et al. (1979), Kasting & Donahue (1980) and Kasting et al. (1989). Numerous improvements have since been made to the photochemical code to investigate a wide range of phenomena (e.g., Pavlov & Kasting 2002; Zahnle et al. 2006, Segura et al. 2007; Domagal-Goldman et al. 2011, Zerkle et al. 2012; Claire et al. 2014; Smith et al. 2014; Arney et al. 2016). The version I have used in this work has been calibrated to reproduce the modern Earth's chemical mixing ratio profiles for O_3 and other trace gas species and has been shown to be valid over a wide range of O_2 mixing ratios (Zahnle et al. 2006). It includes 48 gaseous species and 232 reactions, with the most recent heritage tracing to the study of Zahnle et al. (2006).

The photochemical code is used to calculate self-consistent gas mixing ratio profiles for high-O_2 atmospheres in Chapter 5. I will not describe the model in comprehensive detail here, but will summarize some key traits of the code and describe modifications that have been made. The model atmosphere altitude grid spans the surface to 100 km in 0.5 km intervals with a fixed tropopause height of 11 km when running independently from the climate model (but with a tropopause determined by the climate model when running in coupled mode, see Section 2.6 below). Hydrostatic equilibrium is assumed. The model includes physics that includes vertical transport by molecular and eddy diffusion, lightning, rainout, and diffusion-limited hydrogen escape (Claire et al. 2014). The fundamental equations solved are the continuity and flux equations, which are, respectively,

$$\frac{\partial n_i}{\partial t} = P_i - l_i n_i - \frac{\partial \Phi_i}{\partial z} \tag{2.15}$$

and

$$\Phi_i = -\mathrm{Kn}\frac{\partial f_i}{\partial z} - D_i n_i\left(\frac{1}{n_i}\frac{\partial n_i}{\partial z} + \frac{1}{H_i} + \frac{1+\alpha_{Ti}}{T}\frac{\partial T}{\partial z}\right) \quad (2.16)$$

where, n_i is the number density of species i, t is model time (s), z is altitude, P_i is chemical production rate (in molecules cm^{-3} s^{-1}), l_i is the chemical loss frequency (s^{-1}), Φ_i is the flux of species i, f_i is the mixing ratio of the species i (n_i/n), K is the eddy diffusion coefficient (cm^2 s^{-1}), n is the total density, D_i is the diffusion coefficient between the background atmospheres and species i. H_i is the scale height of species i (note $H = kT/m_ig$). Bank and Kockarts (1973) contains a derivation of the flux equation (eq. 2.16). These equations were integrated using a variable time-step reverse Euler method appropriate for stiff systems. This method relaxes to the steady state solution when time steps are large (e.g. 10 Gigayears). A δ2-stream algorithm (Toon et al. 1989) was used for the radiative transfer calculations that includes Rayleigh scattering by gaseous molecules. In all cases presented here, we assume a "clear sky" aerosol free atmosphere. A 50° solar zenith angle was used to compute diurnally averaged photolysis rates, though this applicable for fast-rotators only and both day and night calculations may be necessary to model a planet confirmed to be tidally locked, as is the case for retrieval of temperature profiles for hot Jupiter planets (Line et al. 2010). The model parameters can include stellar spectra of different types ranging from M dwarfs (e.g., GJ 876, an M3.5V star) to F dwarfs (e.g., Sigma Bootis, an F2V star). Minor modifications to the model have been made to increase numerical stability with high oxygen atmospheres.

2.6 Coupled Photochemical-Climate Model (Atmos)

Atmos uses an iterative process to arrive at a final atmospheric state that takes into account both photochemistry and climate in a self-consistent way. The original photochemistry-climate model

coupling routines were developed by Segura et al. (2003, 2005, 2010), and have recently been expanded upon by Arney et al. (2016) and Schwieterman et al. (2016). Briefly, the photochemistry model is first run with an initial atmospheric state with specified input parameters including gas mixing ratios or fluxes, the shape and intensity of the stellar spectrum, the total atmospheric pressure, and the pressure-temperature profiles. The photochemistry model runs to convergence, and passes the pressure-temperature-altitude and gas mixing ratio profiles to the climate model. The climate model uses this solution as an initial condition and runs to convergence. The climate model self-consistently calculates the surface temperature, temperatures of each atmosphere layer, the H_2O mixing ratio profile and troposphere altitude. These parameters are iterated back into the photochemistry code until the convergence criteria are met. The convergence criteria or criterion is usually a least change in a parameter such as the surface temperature, or the temperature at a given altitude. For most runs presented here, the convergence criterion for climate and photochemical model iteration is a change in surface temperature of $\Delta T < 0.5$ K between sets of iterations.

Chapter 3. EARTH FROM THE MOON: A SPECTRAL EARTH DATABASE

Earth is currently our only, and will always be our best, example of a living planet. Available whole disk observations of Earth by interplanetary spacecraft are limited to "snapshots" in terms of viewing geometry and Earth's dynamic surface and atmosphere state, while low Earth orbiting satellites cannot contain the whole Earth within their fields of view. It has been proposed that a dedicated Moon-based Earth observatory would be a useful platform for carrying out whole disk and time-dependent studies of Earth as an exoplanet. In this chapter I use the well-validated Virtual Planetary Laboratory 3D spectral Earth model to generate: 1) simulated disk-averaged spectra and 2) high resolution, spatially resolved spectral data cubes of Earth at viewing geometries consistent with a Lunar vantage point at wavelengths from the far UV (0.1 μm) to the far IR (200 μm). The database includes disk-averaged spectra for an entire synodic month from dates 03/19/2008 to 04/23/2008 at one-hour cadence, and full spectral data cubes for a subset of those times. These spectra are additionally used to calculate broadband UBVRIJHK magnitudes for the Earth at all phases. These data include the phase and time-dependent changes in spectral biosignatures (O_2, O_3, CH_4, N_2O, VRE) and habitability markers (N_2, H_2O, CO_2, ocean glint). The spectral and spectrophotometric database has a wide range of applications including direct use as input to instrument models for future telescopes designed to characterize Earth-like planets around other stars, informing the design of a future Lunar Earth observatory, and for testing spectral and spectrophotometric retrieval models, along with other applications. The advantages of the VPL Earth model data products over 1D spectra traditionally used for testing instrument architectures include accurate modeling of Earth's surface inhomogeneity

(continental distribution and ice caps), cloud cover and variability, pole to equator temperature gradients, obliquity, phase-dependent scattering effects, and rotation. This preliminary study is done in collaboration with V.S. Meadows, T.D. Robinson, J. Lustig-Yaeger, W. Sparks, and M. Cracraft and is currently being prepared for publication.

3.1 INTRODUCTION

Observational and modeling studies of Earth as an exoplanet has been an active field over the last decade (e.g., Tinetti et al. 2006a, 2006b; Trauger & Traub 2007; Palle et al. 2008; Arnold et al. 2009; Cowan et al. 2009; Fujii et al. 2011; Kawahara & Fujii 2011; Livengood et al. 2011; Robinson et al. 2011, 2014), which has become ever more important as the state of exoplanet characterization evolves towards the ability to study the spectral signatures of rocky terrestrial planets in the habitable zones of their stars (e.g., Dalcanton et al. 2015). Observations of the Earth can especially inform the phase and time-dependent nature of biosignatures and habitability markers for Earth-like planets.

Observations of exoplanets in orbits that are not face on ($i \neq 0°$) will have a phase-dependent component. Phase dependent information has been recognized as a key tool for exoplanet characterization (e.g., Mallama 2009; Selsis et al. 2011; Maurin et al. 2012) and this technique has already been applied to constraining the albedos and temperatures of transiting hot Jupiter planets (e.g., Crossfield et al. 2012; Knutson et al. 2012; Esteves et al. 2013). Observing the phase-dependent variability of the Earth will inform our ability to constrain the expected phase variability for Earth-like terrestrial exoplanets. One example of phase-dependent information that could be important for assessing habitability is the detection of glint at large

phase angles, which indicates the presence of an ocean (Williams & Gaidos 2008, Robinson et al. 2010; Robinson et al. 2014).

To simulate the spatially unresolved "pale blue dot" of prospective future exoplanet observations, it is important that the Earth views used as analogs include a simultaneous view of the whole planetary disk. This makes low-Earth orbiting satellites poor platforms for observing Earth as it would appear to a distant observer, because only a portion of the planet can be contained within the fields of view. This has necessitated the repurposing of interplanetary spacecraft to observe the Earth, for which their distant vantage points guarantee full-disk views (e.g., Sagan et al. 1993; Livengood et al. 2011; Hurley et al. 2014).

To solve this issue, it has been proposed that a dedicated observatory or remotely operated instrument on the Lunar surface or at an Earth-Moon Lagrange point would be an ideal platform for time-dependent studies of the Earth as an exoplanet (e.g., Sparks et al. 2010; Karalidi et al. 2012). To support this mission concept, it would be useful to possess a sequence of model spectra of the Earth as seen from the Moon through a lunar orbit to explore the nature and extent of time-dependent changes that may be observed by this potential observatory and to, in general, possess a sequence of high resolution synthetic data that simulates both Earth's rotational and phase-dependent spectral variability. While the DSCOVR spacecraft, launched in 2015, now provides continuous full phase observations of Earth from the Earth-Sun L_1 Lagrange point, it is limited to narrowband visible filter photometry and broadband radiometric observations (Burt & Smith 2012). Additionally, its viewing location does not support characterization of Earth at different phase angles.

In this chapter I present a high-fidelity spectral Earth database using the VPL's 3D, line-by-line, multiple scattering spectral Earth model. Sections 2.1 and 2.2 describe key static inputs

to this model, including the gas absorption line lists, the main surface and cloud types, and the sources of the data products that provide the gas mixing ratio profiles and coverage by main surface types and clouds. I will briefly recapitulate some of the essential properties of the simulated spectra. Each spectrum extends from the far UV (0.1 μm) to the far-IR (200 μm) with a maximum wavenumber resolution of $\Delta\nu = 1$ cm^{-1}. The radiative transfer model calculations include line-by-line gaseous absorption including natural, Doppler and pressure broadening; multiple scattering including Rayleigh scattering by gaseous molecules, Mie scattering by spherical liquid cloud droplets, and geometric scattering from hexagonal ice cloud particles; a heterogeneous surface composition including non-Lambertian reflectance from ocean surface; geographically distributed surface temperatures and altitude-dependent temperatures informed by low-Earth orbiting satellite observations; and cloud coverage, optical thicknesses, and altitudes informed by satellite data products. The radiative transfer calculations are conducted for each observable pixel, including the true solar zenith and azimuth angles in addition to the observer zenith and azimuth angles for each time interval that is simulated. The majority of the spectral products are calculated with HEALpix (Gorski et al. 2005) parameters of N_{side}=2 (k=1) for the atmosphere pixels and N_{side}=4 (k=2) for the surface pixels.

The utility of this spectral dataset extends beyond studying the feasibility of a lunar Earth observatory. The primary purpose of generating this dataset is to serve as a platform for future work, including informing the design of telescopes and instrumentation for future exoplanet observation missions and testing the retrieval models (e.g., Lustig-Yaeger et al. 2015) that will be employed to recover planetary properties from sparse spectral or spectrophotometric data (e.g., Krissansen-Totton et al. 2016b).

An outline of the remaining sections in this chapter follows. In Section 3.2 I describe the particular model inputs and observing parameters used to generate the spectral Earth database, including the simulated time range, observing geometry, the gas mixing ratios, and the surface coverage and cloud parameters. In Section 3.3, I describe main characteristics of the spectra, including the effects of phase on the spectral features and overall spectral shape in the visible, near-infrared, and mid-infrared spectral regions. I calculate UBVRIJHK broadband colors in Section 3.4 and describe their phase-dependent behavior. Future applications of this dataset are discussed in Section 3.5. I conclude with a discussion and summary in Section 3.6.

3.2 Observing Parameters and Model Inputs

3.2.1 *Modeling date range and observing geometry*

I used the VPL spectral Earth model to generate disk-averaged spectra of the Earth at one-hour cadence from 03.19.2008 00:00 UT to 04.23.2008 00:00 UT. An entire synodic month was chosen as the baseline interval to span the entire range of Sun-Earth-Moon phase angles. This specific date range was chosen for three major reasons. First, validation observations of Earth already exist from broadband visible and near-infrared spectral observations by the EPOXI mission (Livengood et al. 2011; Robinson et al. 2011; also see Chapter 4). Secondly, this date range includes the spring equinox (which occurred on 03.20.2008), which more accurately captures the seasonally averaged state of the planet than a simulated date range near a solstice, where seasonal hemispherical asymmetries are significant. Finally, some of the data products needed for the Earth model, such as wind speed data from the QuikSCAT satellite, are not available for more recent dates due to spacecraft failures. I chose a one-hour cadence so that both rotational and phase dependent changes could be accurately simulated while keeping the database to a manageable size.

Table 3.1 presents a condensed observing table of the synthetic observation Earth viewing parameters, including the Julian Date (JD+2454544), phase angle (α), illumination percentage, sub-lunar longitude ($\lambda_{\leftmoon}$), sub-lunar latitude ($\beta_{\leftmoon}$), sub-solar longitude ($\lambda_{\odot}$), sub-solar latitude ($\beta_{\odot}$), and Earth-Moon distance (Δr). Table 3.1 extends from the first observation on 03.19.2008 00:00 UT (ObsID 0) to the last observation on 04.23.2008 00:00 UT (ObsID 839) with an observing interval of 1 hour. The middle four example observations represent crescent (α = 130°), quadrature (α = 90°), gibbous, (α = 60°), and "full" (α = 4°) Earth view, in that order.

The entire observing table can be found in Appendix A, Table A.1. The JPL HORIZONS[15] ephemeris system (Giorgini et al. 1996) was used to obtain these observing parameters based on a viewpoint at Tranquility Base on the lunar surface (0.66° N, 23.5° E). This location was chosen because it is relatively centrally located on the Earth-facing side of the Moon, and possesses unobstructed Earth views at all times. I have also used the VPL Earth model to calculate Earth spectra assuming a location in a lunar polar region in work that will be presented separately (Glenar et al. 2016). It should be noted that the choice of viewing location on the Moon has only a small effect on the sub-observer latitude and longitudes of Earth, and so is applicable for a wide range of Lunar observing locations.

The simulated Earth-Moon observations here provide a range of Earth-observer phase angles analogous to the observation of an Earth-twin orbiting a solar type star with an inclination near but not exactly 90° ("edge on"), the inclination at which a planet would transit be guaranteed to transit its star. An exoplanet can have a variety of orbital inclinations and obliquities relative to a distant observer in our solar system. Of course, the obliquity of the planet need not be orthogonal with its orbital plane, as is the case for Earth with its 23.5° tilt relative to

[15] http://ssd.jpl.nasa.gov/horizons.cgi

the plane of its orbit. The Moon's orbital inclination about the Earth is 5.14° (with an eccentricity of e = 0.0549), so this observational database is more properly an analog for a very modestly inclined and modestly eccentric target system. These orbital parameters and observing window chosen limit the smallest phase angles present in the dataset to $\alpha > 4°$, but exoplanets at this and smaller phase angles will be unobservable directly due to the small planet-star separation (though they may be observed in secondary eclipse or through phase curves). Overall the choice of the Moon as the Earth viewing platform creates multiple potential applications for this synthetic dataset (see Section 3.5), including simulated exoEarth observations.

Table 3.1 Earth-Lunar Observing Table (Abbrievated)

ObsID	JD(+2454544)	α(°)	Illum(%)	$\lambda_{\leftmoon}$(°)	$\beta_{\leftmoon}$(°)	$\lambda_{\odot}$(°)	$\beta_{\odot}$(°)	Δr (×10^{-3} km)
0	0.5	147.12	8.0	331.3	13.1	182	-0.5	383.7
…	…	…	…	…	…	…	…	…
174	7.75	130.0	17.9	318.1	-24.4	91.4	2.4	403.4
…	…	…	…	…	…	…	…	…
262	11.42	90.0	50.0	123	-27	211.1	3.8	398
…	…	…	…	…	…	…	…	…
325	14.04	59.9	75.1	289.9	-18.5	345.9	4.8	385.1
…	…	…	…	…	…	…	…	…
436	18.67	3.95	99.9	119	10.3	120.6	6.6	361.8
…	…	…	…	…	…	…	…	…
839	35.46	151.93	5.9	41.2	-25.4	194.6	12.7	404.3

ObsID is the simulated observation number (the first observation is 2008-03-19 00:00 UT), **JD** is the Julian Date of the observation minus 2454544, **α** is the Sun-Earth-Moon phase angle in degrees, **illum** is the Earth's illumination percentage, $\boldsymbol{\lambda}_{\leftmoon}$ is the sub-lunar longitude, $\boldsymbol{\beta}_{\leftmoon}$ is the sub-lunar latitude, $\boldsymbol{\lambda}_{\odot}$ is the sub-solar longitude, $\boldsymbol{\beta}_{\odot}$ is the sub-solar latitude, and **Δr** is the Earth-Moon distance (×10^{-3} km). This is a condensed version of Table A.1. The middle four observations are representative of crescent, quadrature, gibbous, and "full" views, respectively.

3.2.2 *Atmosphere inputs*

I determined the spatial and vertical profiles of major spectrally active gases in the Earth's atmosphere, and the surface and temperature profiles, with a range of data products from NASA Earth observing satellites that cover the modeled time interval. These data products are summarized in Section 2.2 and Table 2.2. The two dimensional distribution of atmosphere properties was parameterized using HEALpix (Gorski et al. 2005) into 48 equal area pixels (k=1, N_{side}=2). As described in Section 2.2, a spectral library is generated for every combination of surface type, cloud type, observing zenith and azimuth angles, and solar zenith and azimuth angles for each of these 48 atmosphere pixels. However, the atmosphere parameters used in the generation of this spectra library are daily averaged data products, while the gas mixing ratios and temperature for each region on the planet will change with time over the modeled interval. To encapsulate these atmosphere changes, the spectral database was regenerated for five points in time during the model interval. These were 03.19.2008, 03.26.2008, 04.02.2008, 04.09.2008, 04.16.2008, and 04.23.2008, all at 00:00 UT. Therefore, to generate the Earth spectrum for one point in time, two spectra are initially generated, one for each fiducial spectral library that brackets that time. The final spectrum is an averaged of those two initial spectra, weighted by the final modeled time's temporal proximity to the fiducial dates. This is an appropriate approach to including the spectral changes due to changes in gas mixing ratios and temperature, since the small alterations to the mixing ratios (or temperatures) will produce a linear impact on the spectrum.

Figure 3.1 illustrates the gas mixing ratio inputs I used to create the spectral database. For two representative pixels, one if the Northern Hemisphere (19.5° N, 90° W) and one in the Southern Hemisphere (41.8° S, 23.5° W), the time-averaged median atmosphere profile is shown

for each gas (Figure 3.1a and 3.1b, respectively). The range of mixing ratios (minimum and maximum) for each gas is also shown in the lighter regions of the figure. The geographic median and range of gas mixing ratios for all 48 atmospheric pixels are shown for the 03.19.2008 fiducial date in Figure 3.1c. Figure 3.1d encapsulates both the geographic and temporal range of the gas mixing ratio profiles, illustrating the absolute minimum and maximum concentration for each gas over the modeled time interval. It is important to note that the median profile for each gas is not necessarily near the center of the range between the maximum and minimum values at each altitude layer, and in fact, may be very close to the maximum or minimum value in the range. Figure 3.2 shows the temporal and geographic range of the temperature profiles used as inputs to the spectral model. The temperature profiles have very narrow ranges for each individual pixel of the modeled time interval, but the geographic differences are significant. This is due mostly to the pole-equator temperature gradient of the planet.

3.2.3 *Surface and cloud coverage*

Surface coverage maps were generated for each one-hour observation over the simulated interval (Table 4.1 and A.1). These maps include both surface type and cloud cover information (see Sections 2.2.1 and 2.2.3, respectively for details). Snow coverage is based on an eight-day average from MODIS data products. Sea ice cover is much more sparse, sometimes with days or weeks between observations, so the sea ice is static through the modeling period and is based on an average over the entire interval. The distribution of the four cloud types is based on daily cloud map coverage data from MODIS. The distribution of surface types on the hemisphere of the planet visible to the observable is highly dynamic, dependent both on the viewing geometry of the observer and the rotation of the Earth. Figure 3.3 illustrates the relative fractional coverage of clear surface and cloud types on the illuminated portion of the hemisphere visible to a lunar

observer over the model interval. The land and ocean surface fraction shown included only land and ocean fractions not obscured by clouds. Note the 24-hour cycle due to Earth's rotation and the necessary anti-correlation of clear sky and cloud coverage. The highest volatility in coverage fraction is present near zero orbital phase (crescent) due to the small area of the illuminated portion of Earth at these times. At these times, even the otherwise smallest surface coverage constituents can dominate the illuminated crescent of the planet at certain rotational phases.

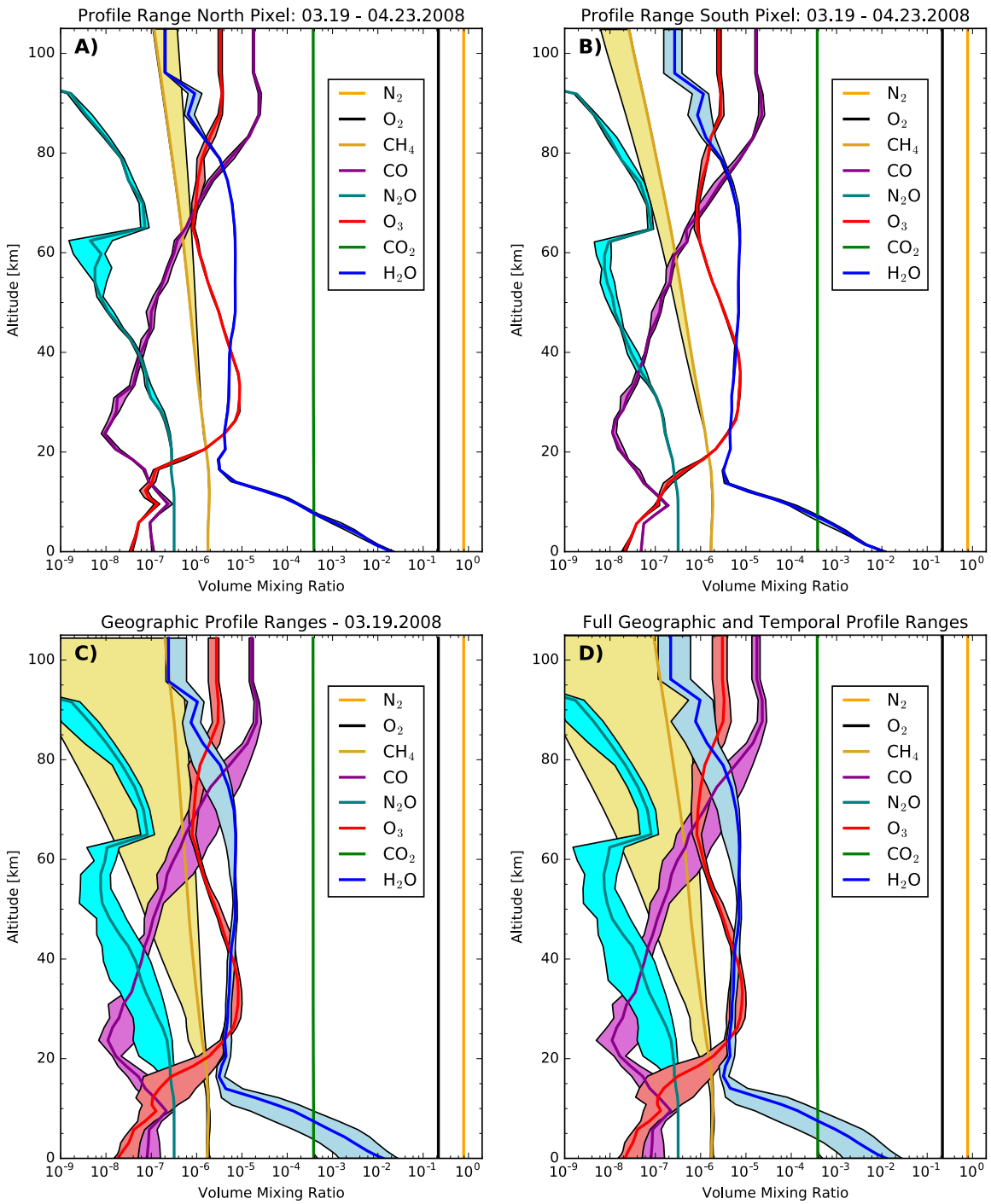

Figure 3.1 Volume mixing ratio profiles for atmospheric pixels in the VPL Earth model. Median (dark lines) and range (lighter regions) of gas concentrations as a function of altitude for A) a representative northern hemisphere pixel (19.5° N, 90° W), B) a representative southern hemisphere pixel (41.8° S, 23.5° W), C) over all 48 atmosphere pixels for modeled date 03.19.2008, D) over 48 atmospheric pixels for date range 03.19.2008 to 04.23.2008.

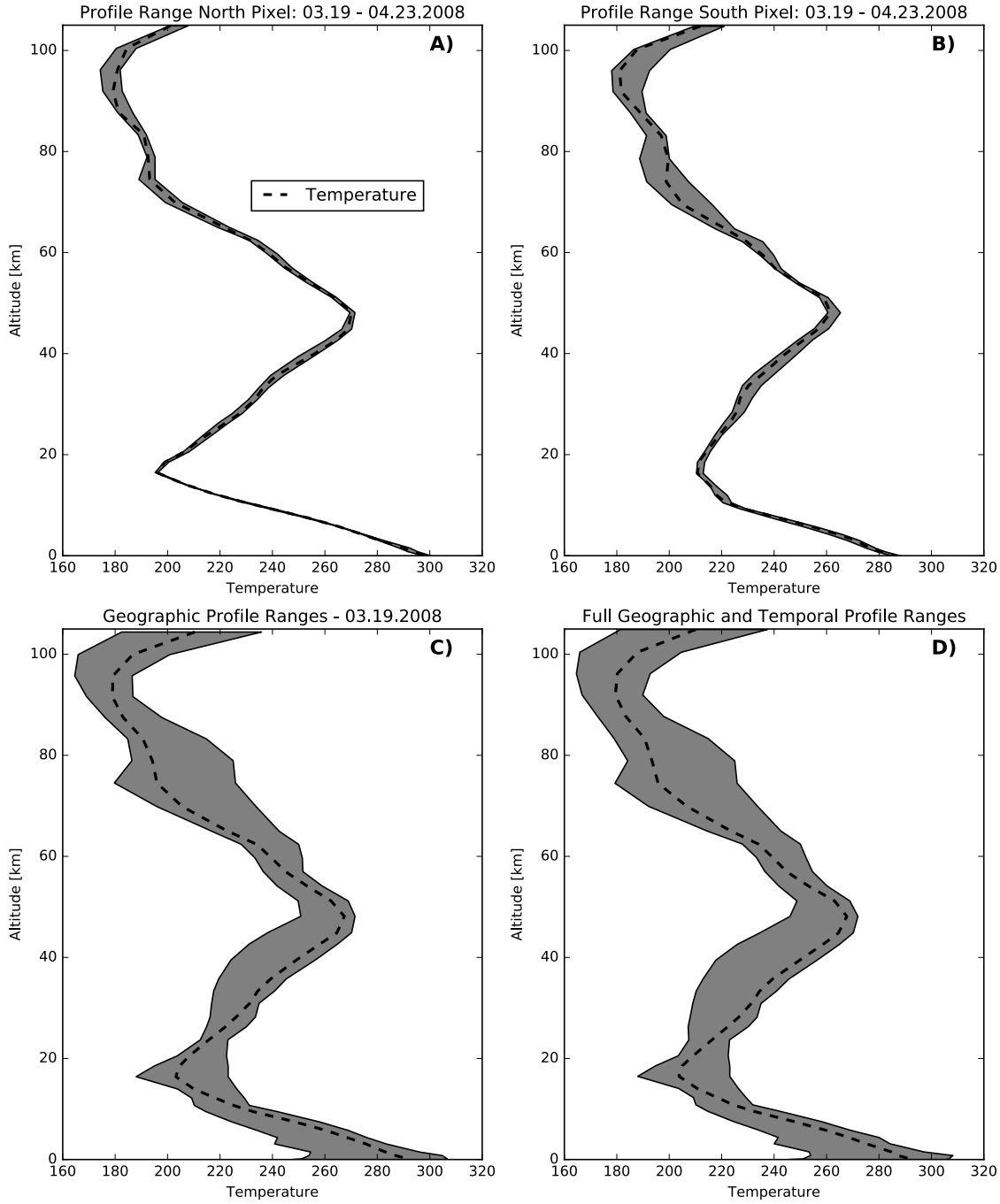

Figure 3.2 Temperature profiles for atmospheric pixels in the VPL Earth model. Median (dark dashed lines) and range (gray regions) of temperatures concentrations as a function of altitude for A) a representative northern hemisphere pixel (19.5° N, 90° W), B) a representative southern hemisphere pixel (41.8° S, 23.5° W), C) over all 48 atmosphere pixels for modeled date 03.19.2008, D) over 48 atmospheric pixels for date range 03.19.2008 to 04.23.2008.

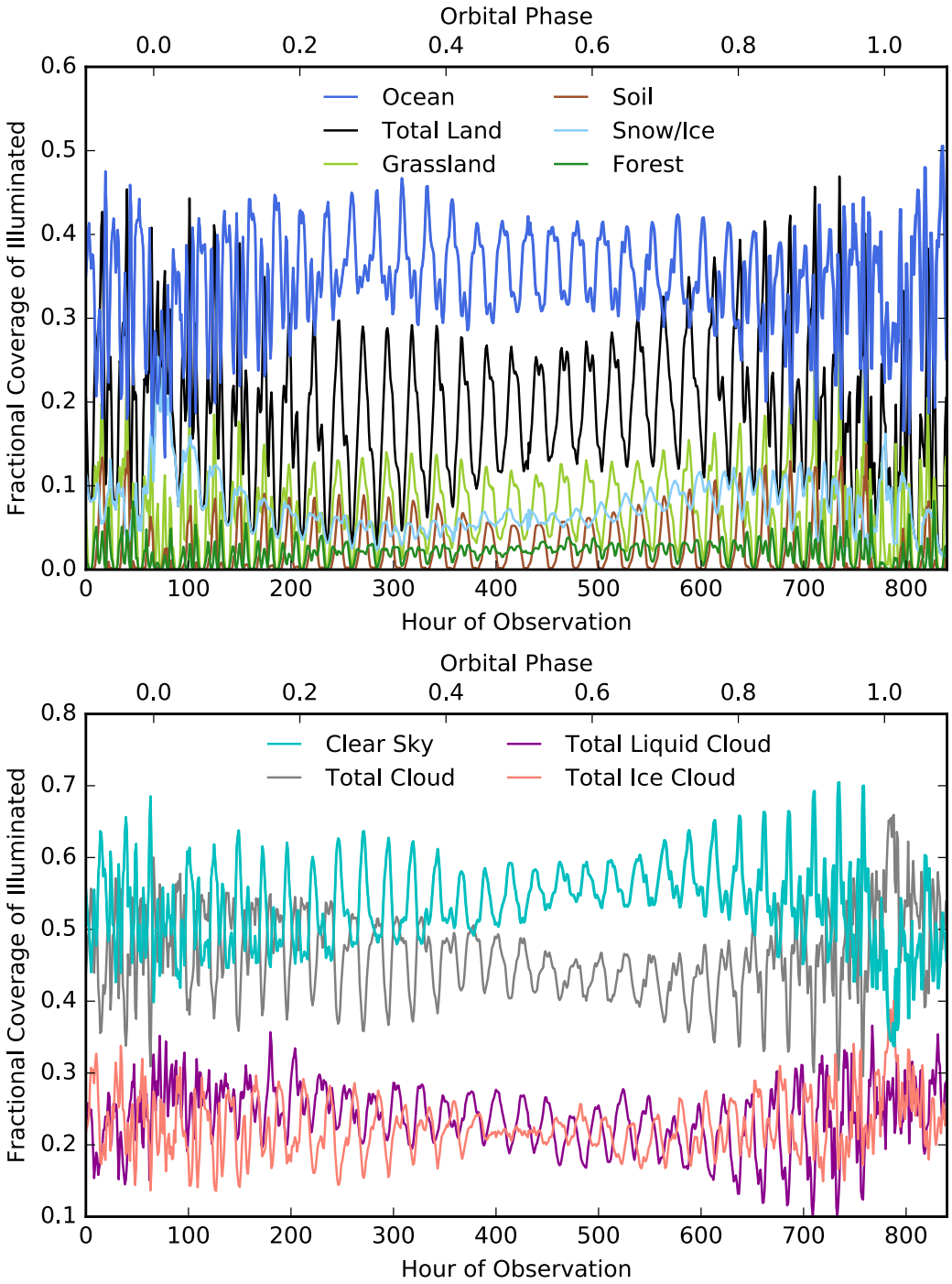

Figure 3.3 Change in fractional coverage of each major surface and cloud type. Top: fractional coverage of clear sky ocean (blue), forest (dark green), grassland (light green), soil (brown), snow/ice (light blue), and total land (black). Bottom: total fraction of clear sky surfaces (cyan), total cloud cover (gray), total liquid low cloud (magenta), and total ice high cloud (pink).

3.3 MAJOR CHARACTERISTICS OF THE SPECTRAL EARTH DATABASE

The spectral Earth database contains 840 individual disk-averaged Earth spectra that span a significant portion of the electromagnetic spectrum (0.1 – 200 μm). This spectral range includes the portions of the spectrum dominated by reflected light from the Sun and the thermal emission from the planet's surface and atmosphere. Figure 3.4 shows Earth flux (W m^{-2} sr^{-1}) spectrum at four different phases: full ((α=4°), gibbous (α=60°), quadrature (α=90°), and crescent (α=130°). These phases correspond to 100%, 75%, 50%, and 25% Earth illumination, respectively.

The major spectral features present include UV absorption from the Hartley O_3 bands (0.2-0.35 μm), Rayleigh scattering at short wavelengths (~0.35-0.55 μm), H_2O absorption throughout the visible and near-infrared (including a major band at 0.95 μm), the Chappuis O_3 bands from 0.5-0.7 μm m, O_2 absorption in the near-infrared (specifically at 0.69, 0.76, and 1.27 μm), O_3 absorption at 9.7 μm, CH_4 absorption from 7-8 μm, and significant CO_2 absorption centered at 15 μm. Additionally, surface reflectance features include greater reflectivity in the near-infrared (> 0.7 μm) due to the rising reflectivity of land surfaces from the visible to the near-infrared, including the VRE. Notable in Figure 3.4 is the drop off in flux with wavelength from the visible to the near infrared, due to the decrease in incident solar light with wavelength. The 8-12 μm region contains the Earth's thermal infrared window, where the atmosphere is relatively transparent to the thermal radiation given off by the surface. Note that the peak of Earth's thermal emission is centered around 10 μm, in the middle of the window, which represents the peak Planck wavelength for a radiating body of 288 K, Earth's seasonally and geographically averaged surface temperature.

Phase has a large impact on the reflected light spectrum of the planet. At full phase, the reflected solar light from the planet is maximized. Additionally, photons undergoing Rayleigh

scattering at this phase are scattered into the observers beam, leading to a strong Rayleigh effect at short wavelengths. At larger phase angles, this effect diminishes and begins to reverse; so that the largest phase angles (e.g., crescent phase) the Rayleigh scattering tail has disappeared, with the bluest light scattered out of the observers beam, leading to a reddened spectrum (Figure 3.4d). The depths and widths of major gas absorption bands can increase at larger phase angles (smaller illumination percentages). This is due to the higher effective atmosphere column depth in limb views, leading to stronger absorption in the Lorentzian wings of the absorption bands. Variability in the absorption depths and widths is also affected by the fractional cloud cover, since clouds can truncate the viewing path through the atmosphere, leading to smaller depths (Fujii et al. 2013).

In contrast to the reflected light spectrum, the mid-infrared (5-25 μm) spectrum, due to the thermal emission of the planet, is constant as a function of phase. This is because Earth is a fast rotator and its atmosphere allows efficient distribution of heat between day and night sides. In the model this effect is further exaggerated by the impact of the input temperature data being daily averages, so that the small changes in temperature between day and night sides that do exist are not incorporated into the spectra. The variability that does exist in the mid-infrared is primarily caused by changes in cloud cover and longitudinal temperature differences. Pole to equator temperature gradients have a small effect on the thermal-infrared of the spectra from Earth-Moon views, since sub-observer latitudes remain close to the Earth's equator, but they would be more significant in alternative viewing geometries.

Planetary rotation plays a significant role in modulating the reflected light spectrum due to the large difference in spectral albedo between the ocean and continents. The VRE effect is strongest when continental landmasses dominate the visible disk and disappears when oceans do

the same. Rotational variation is strongest (in percentage terms) at crescent phases, when different surface types or cloud cover can quickly dominate the small illuminated portion of the planet.

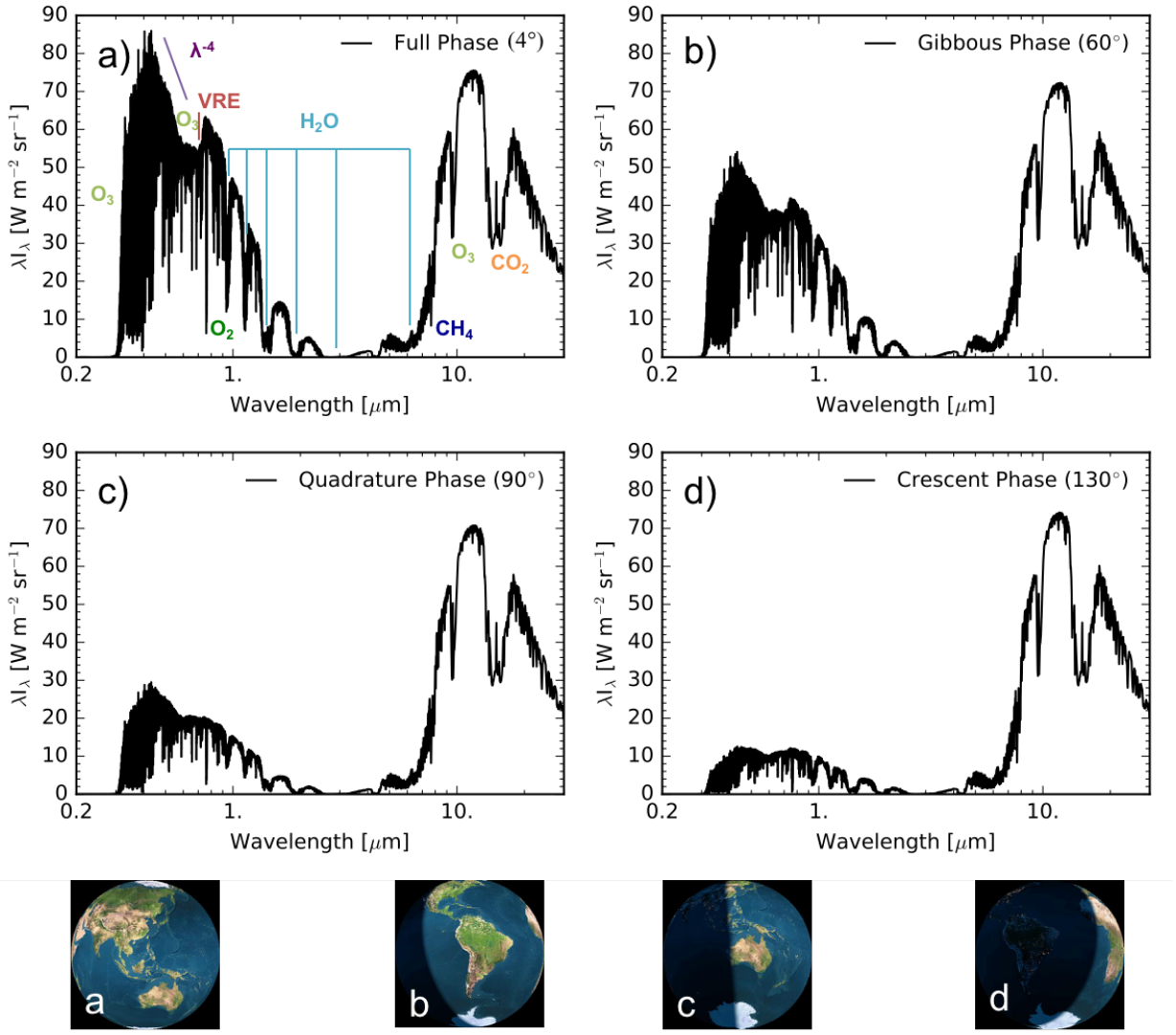

Figure 3.4. Spectral intensity (W m^{-2} sr^{-1}) as a function of wavelength with illustrations for Earth views at four phases: A) full phase (α=4°), B) gibbous phase (α=60°), C) quadrature phase (α=90°), D) crescent phase (α=130°). Major gas absorption features labeled in (A). Image insets (bottom) were generated with the Earth Moon Viewer originally developed by J. Walker (http://www.fourmilab.ch/earthview/).

The Earth-Lunar spectral database includes spectral data cubes (described in Section 2.2.4) in addition to disk-averaged spectra. The data cubes have spectral information mapped to spatial information and can be calculated for various HEALpix resolutions. Figure 3.5 shows "true color" images for Moon views of the Americas on 04.05.2008 at 17:00 UT with 0.1 μm wide filters centered on 0.45 μm, 0.55 μm, and 0.65 μm corresponding to blue, green, and red, respectively. The surface resolution is k=1,2,3,4,5,6 where the number of pixels is $N=12*(2^k)^2$, defined by the HEALPix scheme (Gorski et al. 2005). The VPL disk-averaged Earth-Lunar spectral library is calculated with an atmosphere resolution of k=1 and a surface resolution of k=2, though subsets of the database are calculated at higher resolution (k=5). This includes data cubes calculated for 24 one-hour observations at full, gibbous, quadrature, and crescent phases.

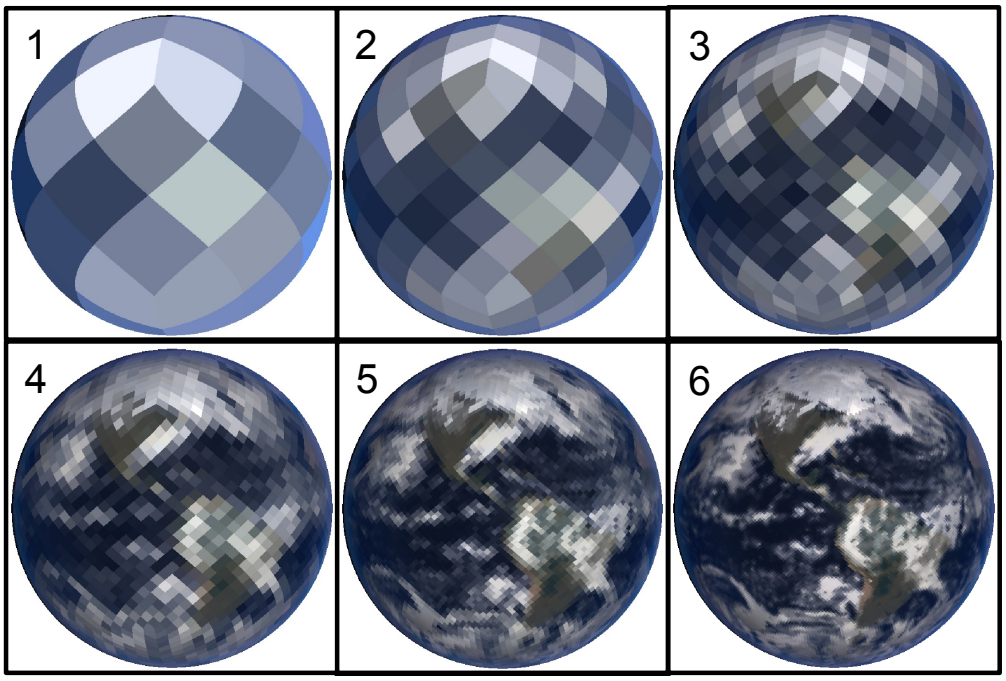

Figure 3.5. Example "true color" images from spectral data cubes generated by the VPL Earth model. Data cubes generated for Moon views of the Americas on 04.05.2008 at 17:00 UT with 0.1 μm wide filters centered on 0.45 μm, 0.55 μm, and 0.65 μm corresponding to blue, green, and red, respectively. Each pixel contains a full weighted spectrum.

3.4 MAGNITUDES & BROADBAND COLORS

3.4.1 *Calculation of magnitudes and colors*

Absolute magnitudes and colors were calculated from the simulated Earth spectra using the HST Synphot[16] package for IRAF (Laidler, et al. 2008). The filter band passes used include the Landolt U, B, V, R, and I filters (visible to near-infrared), and the Bessell J, H, and K (near-infrared) set. The Landolt UBVRI set consists of Johnson UBV (Maíz Apellániz 2006) and Cousins RI filters (Bessell 1983), while the Bessell JHK set is based on those of Bessell & Brett (1988) with modifications given in Laidler (2008). The shapes of these band passes assume a photon counting detector (in contrast to a flux). I used the STMAG system when calculating magnitudes in each band pass, which include standard color corrections (Stone 1996). STMAG magnitudes are designed so that an object with a constant flux per unit wavelength will have zero color. Recall that the absolute magnitude is the apparent magnitude for an observer at 10 parsecs.

Figure 3.6 illustrates the wavelength-dependent throughputs for the Landolt UBVRI filter set used by Synphot. Figure 3.7 shows the same for the Bessell JHK set in the near-infrared. For both Figures 3.6 and 3.7, Earth's flux spectrum (in W m^{-2} μm^{-1}) at quadrature (Table 3.1, ObsID 262) is provided to illustrate the spectral features that are encompassed by each band.

An abbreviated listing of the calculated UBVRIJHK absolute magnitudes is provided in Table 3.2. This includes the absolute magnitudes that match the observations in Table 3.1. Table A.2 has the complete listing of magnitudes for the entire dataset. Figure 3.8 plots the magnitudes of each band over the simulated observing window, illustrating the changing illumination of the Earth with phase. Note the offsets applied to each band, denoted in the figure key.

[16] http://www.stsci.edu/institute/software_hardware/stsdas/synphot

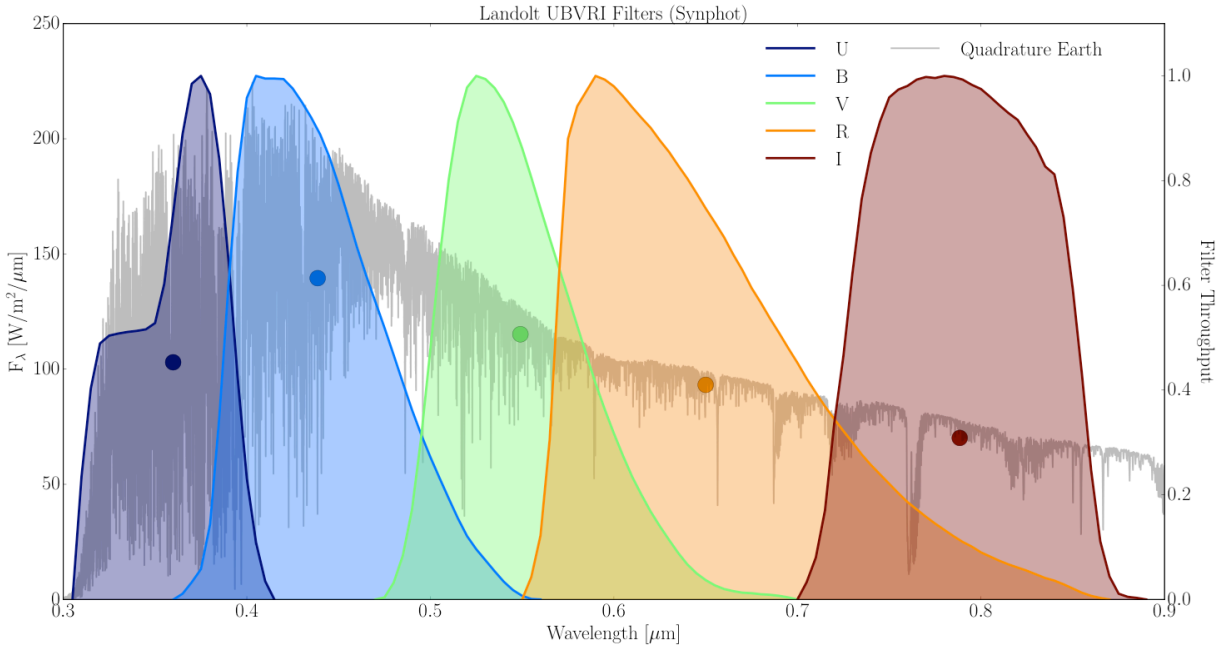

Figure 3.6. Landolt UBVRI standard filter band passes used by IRAF-HST Synphot to calculate broadband magnitudes (shaded colored regions). An Earth flux spectrum at quadrature (Table 3.1, ObsID 262) is also shown in gray. Solid points represent the convolution of the spectrum with the matching band pass response function.

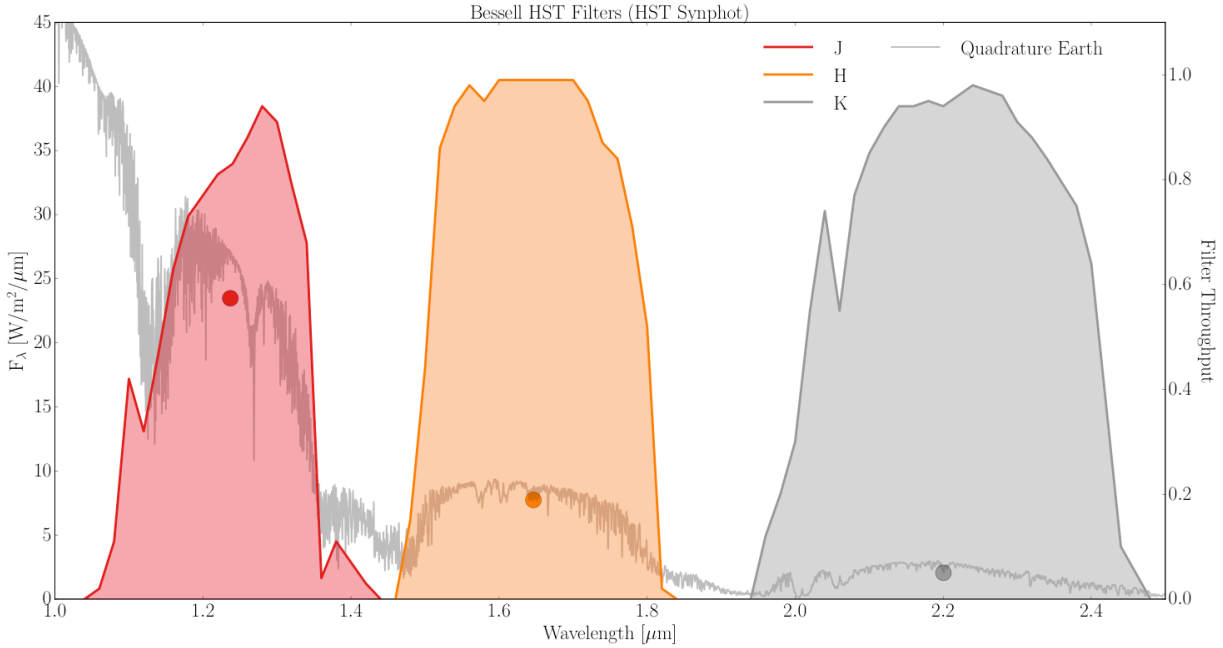

Figure 3.7. Same as Figure 3.6, but for Bessell JHK standard filter band passes used by IRAF-HST Synphot.

Table 3.2 Earth Absolute UBVRIJHK HST Standard Magnitudes (Abbreviated)

ObsID	U	B	V	R	I	J	H	K
0	31.71	30.98	31.01	31.05	31.09	32.33	32.92	34.42
…	…	…	…	…	…	…	…	…	…
174	30.95	30.33	30.42	30.60	30.80	32.09	32.90	34.38
…	…	…	…	…	…	…	…	…	…
262	29.83	29.42	29.65	29.91	30.20	31.43	32.62	34.09
…	…	…	…	…	…	…	…	…	…
325	29.15	28.76	28.96	29.20	29.42	30.68	31.77	33.26
…	…	…	…	…	…	…	…	…	…
436	28.60	28.26	28.52	28.79	28.98	30.30	31.43	33.03
…	…	…	…	…	…	…	…	…	…
839	31.98	31.19	31.16	31.16	31.17	32.36	32.96	34.42

ObsID = observation number (same as Table 4.1). Absolute HST standard (ST) magnitudes are given in the remaining columns. The UBVRIJHK band passes are shown in Figures 3.6 and 3.7.

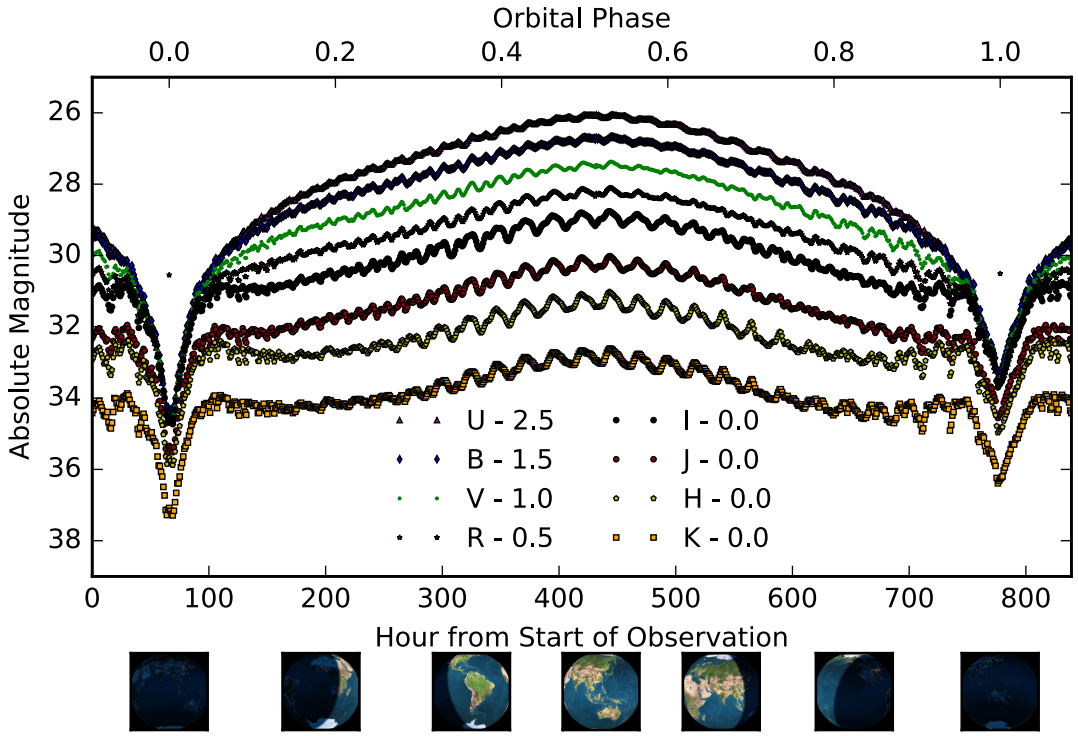

Figure 3.8. UBVRIJHK absolute HST standard magnitudes of the Earth-Lunar spectral database range. Offsets applied are indicated by the figure key. See Table A.1 for the full observing parameters. Magnitudes are also provided in tabular form in Table A.2. Both diurnal (rotational) and phase trends are evident. Image insets (bottom) were generated with the Earth Moon Viewer originally developed by J. Walker (http://www.fourmilab.ch/earthview/).

Broadband colors are the logarithmic ratios of the fluxes between two bands, with the shorter wavelength band usually given first (e.g., U-B). The smaller the number, the more dominant the flux in the first band relative to the second band. The broadband colors of each Earth spectrum are easily derivable from Table 3.2 through arithmetic operation, but are shown in Tables 3.3 (abbreviated) and A.3 (comprehensive) for completeness.

Figure 3.9 plots the U-B, B-V, V-R, and R-I colors as a function of phase. Figure 3.10 similarly shows the I-J, J-H, and H-K colors during the observing interval. These colors provide spectrophotometric information about the planetary state with different surface and atmosphere parameters affecting each band, depending on the phase of the planet. This is discussed further in the subsection below.

Table 3.3 Earth UBVRIJHK HST Standard Colors (Abbreviated)

ObsID	U-B	B-V	V-R	R-I	I-J	J-H	H-K
0	0.73	-0.03	-0.05	-0.03	-1.25	-0.58	-1.5
…	…	…	…	…	…	…	…
174	0.61	-0.09	-0.18	-0.2	-1.29	-0.81	-1.48
…	…	…	…	…	…	…	…
262	0.41	-0.23	-0.26	-0.3	-1.22	-1.2	-1.47
…	…	…	…	…	…	…	…
325	0.39	-0.2	-0.24	-0.21	-1.27	-1.09	-1.49
…	…	…	…	…	…	…	…
436	0.34	-0.26	-0.27	-0.18	-1.33	-1.12	-1.61
…	…	…	…	…	…	…	…
839	0.79	0.03	0	-0.01	-1.19	-0.6	-1.47

ObsID = observation number (same as Table 4.1). These colors are derived from the absolute HST standard (ST) magnitudes given in Table 4.2. Table A.3 contains the complete listing of colors for each spectrum in the database.

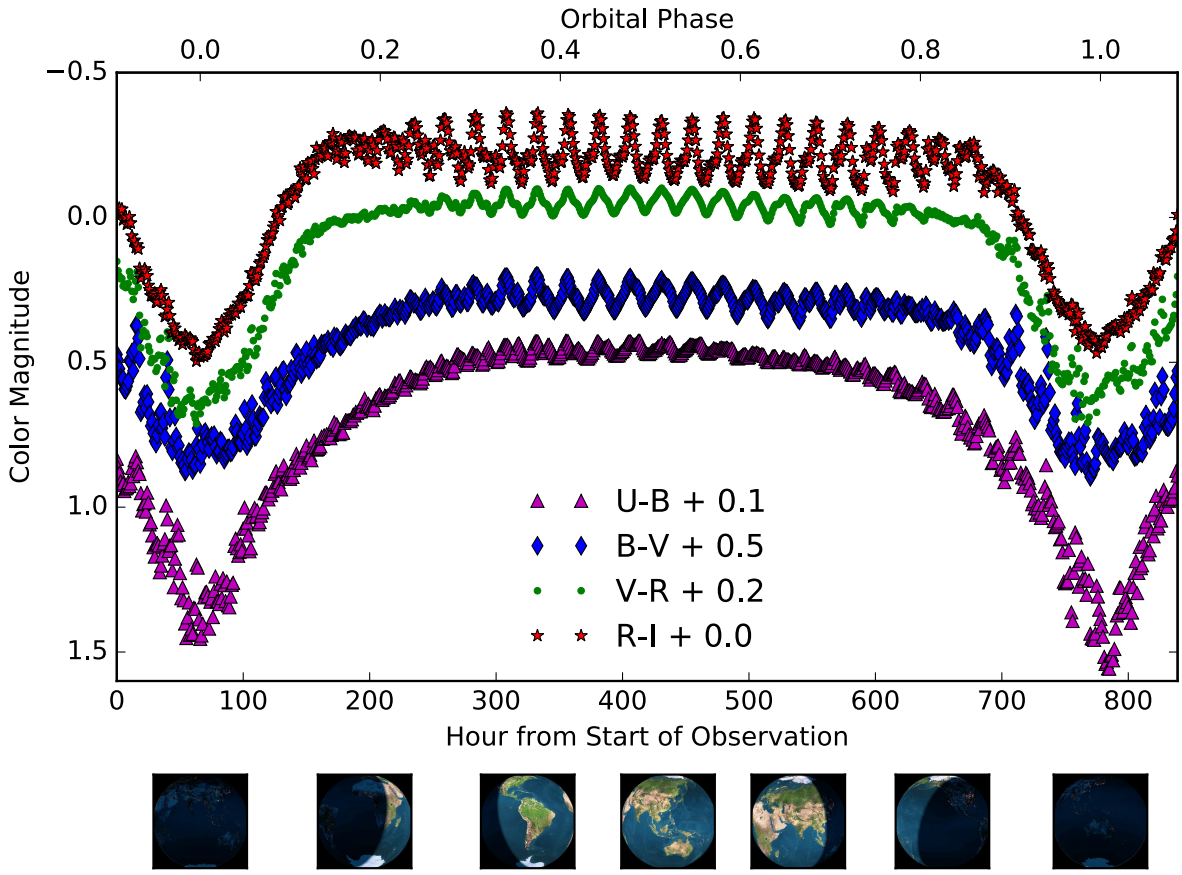

Figure 3.9. UBVRI colors from HST standard magnitudes of the Earth-Lunar spectral database range. Offset applied are indicated by the figure key. See Table A.1 for the observing parameters. Colors are also provided in tabular form in Table A.3. Both diurnal (rotational) and phase trends are evident. Image insets (bottom) were generated with the Earth Moon Viewer originally developed by J. Walker (http://www.fourmilab.ch/earthview/).

3.4.2 *Characteristics of time-dependent magnitudes and colors*

Here I will briefly describe the main time-dependent characteristic of the spectrophotometric information presented in Tables 3.2 and 3.3 and Figures 3.8 to 3.10. The dominant effect is from the changing phase (illumination percentage) of the planet from crescent phases (orbital phase zero, $\alpha = 180°$) to full phase (orbital phase 0.5, $\alpha = 0°$). Near crescent phase, the overall brightness in reflected light is low due to the small portion of the planet that is illuminated; leading to large

observed magnitudes (Figure 3.8). The UBVRI magnitudes near crescent phase reach a minimum of 35. The planet reaches maximum brightness near full phase with UBVRI magnitudes of near 30. Therefore, the change in planetary brightness between full and crescent phases in reflected light is near a factor of 100.

In addition to the obvious impact on the overall brightness of the planet, the changing phase introduces an impact on the colors (Table 3.3, Figures 3.9 and 3.10). At crescent phase the atmospheric column of the illuminated portion of the planet becomes dominated by the limb, which produces a larger effective atmospheric column and increases the effect of Rayleigh scattering versus fuller phases. At large phase angles most of the scattered light is directed out of the observer's beam, leading to significant observed reddening present in the colors. Rayleigh scattering is strongly inversely wavelength-dependent, so the impact is significantly larger for the shorter wavelength band passes (e.g, U-B, B-V, becoming almost negligible at the longest wavelength H-K colors (see Figure 3.10). Figure 3.4 can be referenced for the overall effect of the change of phase on the shortwave planetary spectrum.

Planetary rotation introduces 12 and 24 hour modulations in the color and absolute magnitude variations outside of crescent phase. These modulations are due to the changing fraction of viewable land and ocean (see Figure 3.3) and the different reflectance properties (wavelength-dependent albedos) of each surface type. (At crescent phase Rayleigh scattering opacity masks the amplitude of these modulations). Note that the centroid of the Eurasian-Africa landmass is centered almost 180° away from the centroid of the North and South American landmass, creating a 12-hour alias in the "true" 24 hour rotation signal. The color amplitude seen due to the planetary rotation is dependent on the filter bands used in the color calculation. The U band pass has high scattering opacity even at full phase, so the U-B colors show less regular

amplitude variation with rotation. However, the other bands are more transparent to scattering opacity and so show larger variations. The R-I color shows the largest amplitude as a function of changing land and ocean fraction due to the large increase in continental brightness in the I band, partly due to the presence of the vegetation red edge (VRE) effect (see Figures 2.4 and 2.6). This wavelength region is also effected the least by Rayleigh scattering opacity (save for the JHK bands).

The changing depth and width of spectral features can also create a change in the observed colors (Fujii et al. 2013), though this effect is secondary to the primary effects listed above. The intersection between spectral features and the filter band passes is illustrated in Figure 3.6. The traditional UBVRIJHK filter bands employed in this study were originally designed to characterize the temperatures of stars using ground-based observatories that must look through Earth's own atmosphere. Therefore, the band passes are by intention centered on relatively transparent portions of the atmosphere in wavelength space. However, some bands do possess significant overlap with key absorption features. Both the R and I bands intersect with the relatively narrow 0.76 μm O_2-A band. All of the UBVR bands include some impact from the 0.5-0.7 μm Chappuis O_3 band, while the U band includes a small portion of the O_3 UV Hartley bands. The most significant effects come from the overlap of the J band with the 1.1 and 1.4 μm H_2O bands, and the H band with the 1.4 and 1.6 μm H_2O bands. These overlaps with H_2O features make the J and H bands particularly sensitive to (stochastic) cloud cover, since the H_2O bands will be much stronger in clear sky views with viewing paths into the wet troposphere. Additionally, the H_2O bands will be significantly larger at crescent phases, where the increased effective atmospheric column will enlarge the size of the bands (see Figure 3.4d). This can be seen as volatility in the short cadence I-J and J-H color data in Figure 3.10.

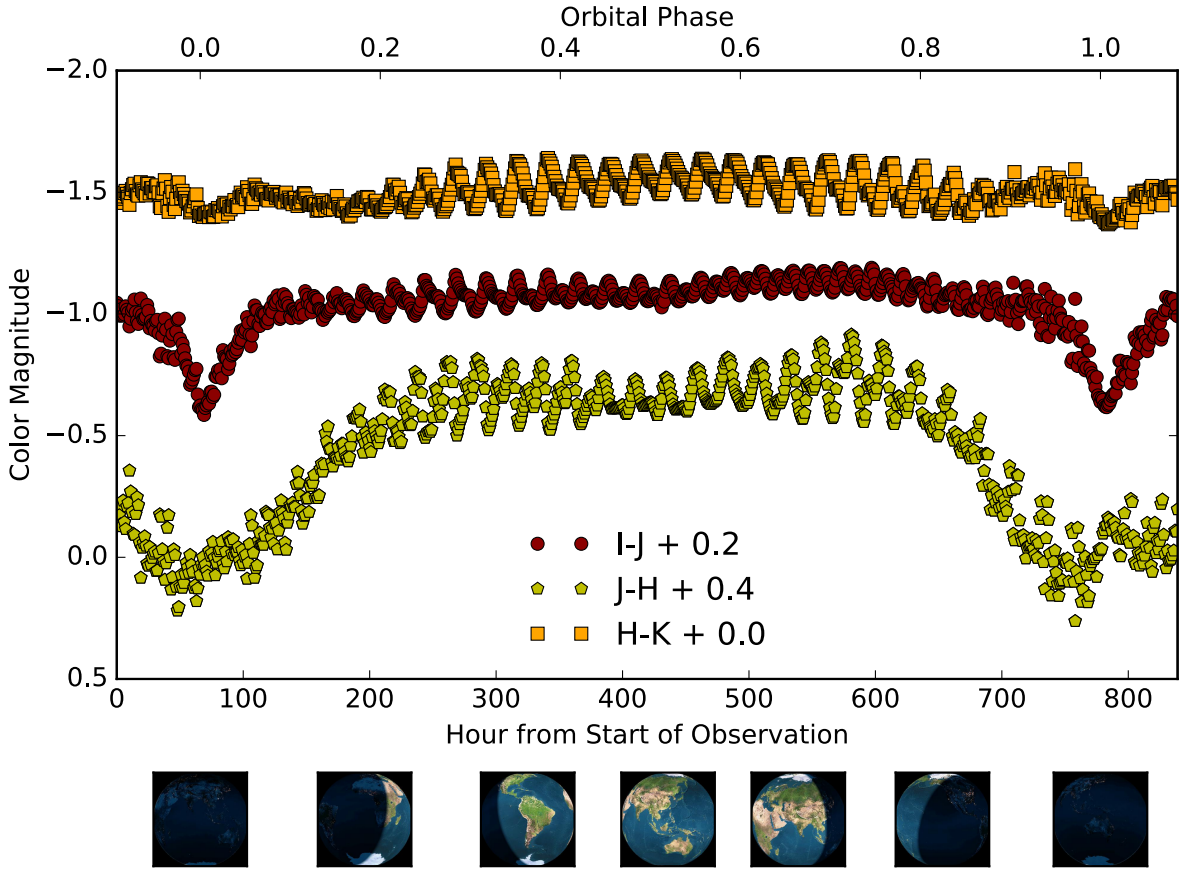

Figure 3.10. IJHK colors from HST standard magnitudes of the Earth-Lunar spectral database range. Offset applied are indicated by the figure key. See Table A.1 for the observing parameters. Colors are also provided in tabular form in Table A.3. Both diurnal (rotational) and phase trends are evident. Image insets (bottom) were generated with the Earth Moon Viewer originally developed by J. Walker (http://www.fourmilab.ch/earthview/).

3.5 APPLICATIONS

The disk-averaged spectra and spectral data cubes presented in this chapter have myriad uses, some of which are already in the process of implementation. Below I briefly describe some of these applications.

3.5.1 *Informing telescope design and testing instrument models*

Currently several space-based telescope missions that may characterize Earth-like planets around other stars are in their design phases with Science and Technology Definition Teams now in place. This includes the LUVOIR Surveyor[17] (Kouveliotou et al. 2014; Dalcanton et al. 2015; Postman et al. 2010) and HabEX[18] (Swain et al. 2015) concepts in the UV to near-infrared wavelength regimes ($0.2 < \lambda < 5.0$ μm), and the Far-Infrared Surveyor[19] at wavelengths > 10 μm (Kouveliotou et al. 2014). The disk-averaged spectra that constitute this database are useful inputs to instrument models (e.g., Robinson et al. 2016) that will test the feasibility of these concept missions to detect atmospheric or surface spectral features. This is particularly important for selecting the wavelengths and operating temperatures necessary for instruments to meet important science targets.

The time-dependent spectra presented in this database have several advantages as test cases over synthetic spectra of a static planet at a particular viewing geometry and atmosphere, surface state. The spectral database includes phase-dependent scattering effects, planetary rotation, surface inhomogeneity (continental distribution and ice caps), realistic changes in cloud cover and cloud fraction, spatial gradients in temperature, and non-zero obliquity. This is

[17] http://cor.gsfc.nasa.gov/studies/luvoir.php
[18] http://www.jpl.nasa.gov/habex/
[19] http://asd.gsfc.nasa.gov/firs/

especially important because integration times for rocky exoplanet spectral observations will be long (hours or more). Observations will also be made at various phase angles, especially in the case of target planets with unknown initial inclinations.

The calculated broadband colors or binned spectra can additionally be used to predict the spectrophotometric accuracy and ideal band passes required to distinguish an Earth-like planet from other planetary types (Krissansen-Totton et al. 2016). Similarly, this information can be used to distinguish a directly imaged planet from a faint background star (Krissansen-Totton et al. 2017, in prep).

3.5.2 *Testing the ability of spectral retrieval models to recover planetary parameters*

Time-dependent broadband and spectral information can be decomposed into including albedo maps and cloud cover data (Cowan et al. 2009; Cowan et al. 2011; Cowan & Strait 2013). Time-dependent broadband data can also be used to infer planetary obliquity (Schwartz et al. 2016; Kawahara 2016). Typically, complex spectral retrieval models are tested on singular observations to determine properties like gas abundance. Time-dependent information is extracted from simpler broadband models that do not encapsulate detailed spectral information or other complications like realistic changes in cloud cover, retreat and advance of snow, or spatial variation in gas mixing ratio profiles. These shortcuts are taken due to the time and expense required for full spectral modeling. In contrast, the spectral Earth database will be a community resource appropriate for both types of investigations with very high fidelity and realistic physics informed by actual, validated observations of the real Earth.

3.5.3 *Modeling Earthshine on the Moon*

Recently the spectral Earth database has been used to investigate the impact of Earthshine on the radiation environment of permanently shadowed regions at the lunar poles (Glenar et al. 2016). Permanently shadowed crater regions never see the Sun, but do experience irradiation from the Earth's disk. This radiation field is most accurately modeled when spatial and rotational heterogeneity is taken into account. This research has implications both for the stability of ice in the shadowed lunar regions and accurate modeling of the light field relevant to planning for future remote sensing and in situ exploration purposes.

3.5.4 *Other uses*

Other uses of the spectral Earth database can include, but are not limited to: third-party model validation, data model comparisons for future interplanetary spacecraft or lunar observatories, and spacecraft instrument calibration. An example of the last case is the use of an earlier Earth model dataset to discover an instrument calibration error discovered for the visible spectrometer on the Lunar CRater Observation and Sensing Satellite (LCROSS; see Robinson et al. 2014). The VPL Earth model spectra were used to derive a wavelength-dependent correction factor that can be applied to the archival observed spectra. Additionally, the following chapter, which explores the detectability of N_2 in Earth's atmosphere, is further illustrative of the range of problems that can be investigated with this and similar synthetic Earth datasets using the VPL Earth model.

3.6 SUMMARY

In this chapter I presented the Virtual Planetary Laboratory's Earth from the Moon Spectral Earth Database. The database includes disk-averaged spectra (0.1 – 200 μm) of the Earth as seen from the Moon during an entire synodic month at one-hour cadence with a spatially heterogeneous planetary atmosphere. Spectral data cubes are available for a subset of those times. The effects of Earth's surface inhomogeneity (continental distribution and ice caps), cloud cover and variability, spatial temperature gradients, obliquity, phase-dependent absorption and scattering effects, and rotation are included in the model. I describe main characteristics of the spectra including the effects of phase on the spectral features and overall spectral shape in the visible, NIR, and MIR spectral regions. I calculate UBVRIJHK absolute magnitudes and colors from this dataset and describe their time-dependent behavior. Some future applications of the data set are explored including informing instrument design for future exoEarth observing missions, testing retrieval models and techniques, and modeling the Earthshine environment on the Moon. The next chapter is illustrative of the kind of problems that may be investigated with this or similar data sets.

Chapter 4. DETECTING N_2 IN PLANETARY ATMOSPHERES

In this chapter I investigate the detectability of N_2 in planetary atmospheres through $(N_2)_2$ collisional pairs, also known as N_2-N_2 collisionally induced absorption (CIA). While N_2 dominates the composition of Earth's atmosphere, it is difficult to detect spectrally because it lacks normal absorption features. I use data-model comparisons between spectra from NASA's *EPOXI* mission and synthetic data from the VPL 3D spectral Earth model, described in Chapter 2, to show that $(N_2)_2$ absorption produces a ~35% decrease in flux in Earth's disk-averaged spectrum near 4.15 μm. I used a 1D radiative convective model CLIMA to produce self-consistent N_2-CO_2-H_2O profiles of atmospheres with different amounts of N_2, but with realistic CO_2 and H_2O contents. I then used the radiative transfer model SMART to produce synthetic spectra of these planetary atmospheres and included $(N_2)_2$ absorption to investigate the strength of N_2 absorption with increasing N_2 abundance. I find that $(N_2)_2$ absorption in the wings of the 4.3 μm CO_2 band is strongly dependent on pN_2 above 0.5 bar and can significantly widen this band in thick N_2 atmospheres. I create analytic N_2-CO_2, N_2-H_2, and N_2-H_2-CO_2 atmospheres that are used as input into the transit transmission model SMART-T to test the spectral strength of $(N_2)_2$ absorption in transit transmission observations. I find that for an Earth-size planet in the habitable zone transiting an M5V star with $R_* = 0.2\ R_\odot$, the $(N_2)_2$ spectral transmission signal is up to 10 ppm, and could be significantly greater for atmospheres with both significant N_2 and H_2 mixing ratios. Portions of this chapter were originally published in collaboration with T.D. Robinson, V. S. Meadows, A. Misra, and S.D. Domagal-Goldman in the September 2015 edition of the *Astrophysical Journal* (Schwieterman et al., 2015, ApJ, Vol. 810, 57; © 2015 American

Astronomical Society), and are reproduced below with permission of the American Astronomical Society.

4.1 INTRODUCTION

Molecular nitrogen (N_2) comprises the bulk of Earth's modern atmosphere, is an important constituent in the atmospheres of Venus and Mars, and dominates the atmosphere of Saturn's icy moon Titan. Because of its geochemical stability, N_2 has constituted the largest fraction of Earth's atmosphere throughout its history, though its total abundance may have varied over time (Goldblatt et al. 2009; Som et al. 2012; Marty et al. 2013; Johnson & Goldblatt 2015). While N_2 is the most abundant gas in Earth's atmosphere, it is extremely difficult to detect remotely, because it is a symmetric homonuclear molecule with no transitional dipole moment and therefore does not produce spectral features throughout the visible and near-infrared portions of the spectrum. N_2 has a significant dissociation cross section in the Extreme Ultraviolet (EUV), $\lambda < 0.1$ μm (Samson et al. 1987; Stark et al. 1992), but the planetary flux at these wavelengths is likely to be low both due to a lack of EUV light from the incident stellar spectrum and significant absorption in the planet's atmosphere. Similarly, N_2-N_2 collisionally-induced absorption (CIA) in the far infrared ($\lambda > 40$ μm) (Borysow & Frommhold 1986) will be difficult to discern from many planetary spectra because it can be masked by water vapor absorption. However, N_2-N_2 collisions create short-lived N_2-N_2 pairs, also written as $(N_2)_2$, which are spectrally active at shorter wavelengths. $(N_2)_2$ has an absorption feature near 4.3 μm, nearly coincident with the 4.3 μm CO_2 band, but with broader wings at Earth-like N_2 abundances. The $(N_2)_2$ absorption in this wavelength region is dominated by CIA, but N_2 quadrupole line absorption, and absorption by true $(N_2)_2$ van der Waals molecules also contributes (Long et al. 1973). The temperature and

wavelength-dependent absorption coefficients for this primarily collisional feature have been measured empirically (Farmer & Houghton 1966; Lafferty et al. 1996), and $(N_2)_2$ absorption has been observed in solar occultation (transmission) observations by Earth-observing satellites (Rinsland 2004), but it has never before been considered in the context of planet characterization from full-disk or transit transmission observations.

A comprehensive study of a planetary atmosphere would require determination of its bulk properties, such as atmospheric mass and composition, which are crucial for ascertaining surface conditions. Because $(N_2)_2$ is detectable remotely, it can provide an extra tool for terrestrial planet characterization. For example, the level of $(N_2)_2$ absorption could be used as a pressure metric if N_2 is the bulk gas, and break degeneracies between the abundance of traces gases and the foreign pressure broadening induced by the bulk atmosphere. If limits can be set on surface pressure, then the surface stability of water may be established if information about surface temperature is available. The technique of using collisional pairs (or dimers) to determine atmospheric pressure in the reflection and transmission spectra of exoplanets was first described by Misra et al. (2014a), who considered $(O_2)_2$ features specifically. The absorption by CIA or dimer molecules is quadratic in number density, while it is linear for monomers, making CIA or dimers especially sensitive to different maximum gas densities. Misra et al. (2014a) considered the strength of $(O_2)_2$ absorption features at 1.06 μm and 1.27 μm specifically as pressure discriminators. However, for almost half (Kump 2008), or possibly more (Planavsky et al. 2014), of Earth's geologic history, there was little O_2 present in the atmosphere, as oxygenic photosynthesis had not yet evolved or geochemical sinks for O_2 had not yet been exhausted (Buick 2008). For a substantial fraction of this time period life existed on the Earth (Wacey et al. 2011; Brasier et al. 2015). Therefore, if Earth is taken as an informative example, there may be many habitable and

inhabited planets with no detectable O_2. For these worlds pressure determination with $(O_2)_2$ will be impossible and some other metric must be employed, such as quantifying $(N_2)_2$.

Additionally, it has been shown that atmospheres with low abundances of non-condensable gases such as N_2 and argon (Ar) are more susceptible to the abiotic accumulation of O_2, creating a potential false positive for life (Wordsworth & Pierrehumbert 2014). This occurs when the surface temperature is high enough, and the non-condensable gas abundance low enough, for water vapor to dominate the lower atmosphere. A water dominated atmosphere lacks a cold trap, allowing water to more easily diffuse into the stratosphere and become photodissociated, leaving free O_2 to build up over time. Direct detection of N_2 (through $(N_2)_2$) could rule out abiotic O_2 via this mechanism and, in tandem with detection of significant O_2 or O_3, potentially provide a robust biosignature. Moreover, the simultaneous detection of N_2, O_2, and a surface ocean would establish the presence of a significant thermodynamic chemical disequilibrium (Krissansen-Totton et al. 2016) and further constrain the false positive potential. Finally, $(N_2)_2$ overlaps significantly with the 4.3 μm CO_2 band, which may be used in future exoplanet observations to quantify CO_2 abundances. This retrieval would be biased unless the absorption in the wings from $(N_2)_2$ is considered. This effect is accounted for by Earth-observers using solar occultation limb sounding to measure vertical CO_2 profiles (e.g., Rinsland et al. 2010; Sioris et al. 2014).

Here I explore the detectability of $(N_2)_2$ in terrestrial planetary atmospheres using modern Earth as an exoplanet analog. In Section 4.2 I describe the inclusion of N_2-N_2 and N_2-O_2 CIA absorption in the VPL spectral Earth model described in Chapter 2. In Section 4.3, I report the detection of $(N_2)_2$ in Earth's disk-integrated spectrum using comparison data from *EPOXI* and perform a series of sensitivity tests to conclusively demonstrate the origin of the reported

absorption. Additionally, I quantify the maximum transit transmission signal produced by $(N_2)_2$ for an Earth-Sun analog. In Section 4.4, I quantify the effect of $(N_2)_2$ in synthetic emission spectra of planets using self-consistent atmosphere-climate models. In Section 4.5, I simulate the transit transmission signal of $(N_2)_2$ for both a modern Earth analog and planets with N_2-H_2 atmospheres orbiting in the habitable zone (HZ) of a late type star. I discuss the implications of these results further in Section 3.

4.2 Addition of $(N_2)_2$ and N_2-O_2 Absorption to the Earth Model and SMART

The $(N_2)_2$ and N_2-O_2 absorption included in our models is treated mathematically as collisionally-induced absorption (CIA). In general, the temperature- and wavenumber-dependent CIA absorption coefficients of a pure mixture of a collisionally absorbing gas A can be given as

$$\alpha(\nu, T, d_A) = B_{A-A}(\nu, T) d_A^2 \tag{4.1}$$

where $\alpha(\sigma, T, d_A)$ is the absorption coefficient (with units of cm^{-1}) for a given temperature (T), wavenumber (ν), and density (d_A, in units of amagat), and $B_{A\text{-}A}$ is a density-normalized CIA coefficient, usually given in cm^{-1} $amagat^{-2}$. For a binary mixture of gases A and B, where B is spectrally inactive in the wavelength range of interest and is considered only as a collision partner to A, Equation (4.1) becomes

$$\alpha(\nu, T, d_A) = [d_A B_{A-A}(\nu, T) + d_B B_{A-B}(\nu, T)] d_A \tag{4.2}$$

Lafferty et al. (1996) present a simple empirical model to calculate the wavenumber and temperature-dependent normalized CIA coefficients for a mixture of pure N_2

$$B_{N_2-N_2}(\nu, T) = B_{N_2-N_2}{}^0(\nu) \exp\left[\beta_{N_2-N_2}{}^0(\nu)\left(\frac{1}{T_0} - \frac{1}{T}\right)\right] \tag{4.3}$$

where ${B_{N_2-N_2}}^0(\nu)$ and ${\beta_{N_2-N_2}}^0(\nu)$ are wavenumber-dependent empirical reference parameters given in Lafferty et al. (1996) (their Table 1), and T_0 is a reference temperature of 296 K. The empirically derived normalized CIA coefficients from this model are valid for a temperature range of 190-300 K. Figure 4.1 illustrates the normalized CIA coefficients (as a function of wavenumber or wavelength) calculated from Equation (4.3) for a variety of different temperatures. Lafferty et al. 1996 found the efficiency of N_2-O_2 absorption relative to N_2-N_2 absorption to be approximately independent of wavenumber, and given by

$$E_{O_2/N_2}^{N_2}(T) = \frac{B_{N_2-O_2}(\nu,T)}{B_{N_2-N_2}(\nu,T)} \cong \left[1.294 - 0.4545\left(\frac{T}{T_0}\right)\right] \tag{4.4}$$

Therefore, according to Equations (4.2, 4.3, and 4.4) the wavenumber- and temperature-dependent absorption coefficients due to CIA from a mixture of N_2 and O_2 gas can be calculated as

$$\alpha(\nu, T, d_{N_2}, d_{O_2}) = B_{N_2-N_2}(\nu, T)\left[d_{N_2} + E_{O_2/N_2}^{N_2}(T) d_{O_2}\right] d_{N_2} \tag{4.5}$$

Lafferty et al. (1996) give their absorption coefficients in wavenumbers. Note that I convert from wavenumber (cm^{-1}) to wavelength units (μm) for the model results presented throughout this work. I assume the CIA absorption in the 3.7-4.7 μm region is due entirely to N_2-N_2 and N_2-O_2 CIA, though CIA from other collision partners such as N_2-Ar will contribute a small, but insignificant, amount to the absorption, due to the small mixing ratios of these partners. It should be noted that there is a weaker $(N_2)_2$ band near 2.15 μm, a harmonic of the 4.3 μm band. However, the binary absorption coefficients for this band are more than 100 times weaker than those of the 4.3 μm band and poorly characterized (Shapiro & Gush 1966). While this weaker band is observable in N_2 ices (solids) in the outer solar system (e.g., Grundy & Fink 1991), it

would be substantially more difficult to detect in gaseous phase than the 4.3 μm $(N_2)_2$ band. I do not discuss the 2.15 μm $(N_2)_2$ band further here.

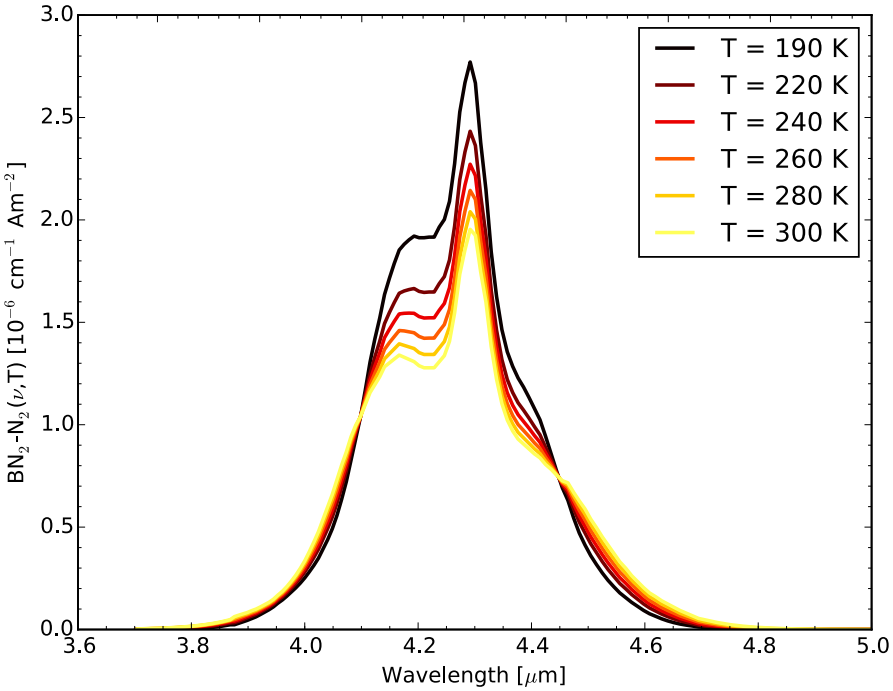

Figure 4.1. Density-normalized wavelength and temperature-dependent $(N_2)_2$ absorption coefficients. The normalized absorption coefficients are calculated from Equation (5) and reference parameters given in Table 1 of Lafferty et al. (1996) for a gas of temperature T = 190 K (black), 220 K (dark red), 240 K (red), 260 K (dark orange), 280 K (light orange), and 300 K (yellow). The wavenumber (or wavelength) and temperature dependent absorption coefficients of a mixture of N_2 and O_2 gas can be calculated using Equation (4.5) given in the text.

4.3 Detecting $(N_2)_2$ in Earth's Disk-Averaged Spectrum

4.3.1 *EPOXI Earth observations*

Our comparison observations consist of 1.0-4.5 μm disk-integrated NIR spectra taken of the Earth by the HRI instrument on the *Deep Impact* flyby spacecraft (Hampton et al. 2005; Klaasen et al. 2008) as part of NASA's *EPOXI* mission, which was a repurposing of the *Deep Impact*

spacecraft. I present data model comparisons for four observations taken from 2008-March-18 through 2008-March-19 that span a full rotational cycle. These observations were made at a spacecraft to planet distance of 0.18 AU when Earth was at a phase angle of 57.7° (~77% illumination). Table 4.1 provides a summary of observations. Measured spectral irradiances were converted to distance-independent spectral radiances for data model comparison. The *EPOXI* Earth spectra are publicly available on the Planetary Data System (PDS) archive[20] and described in more detail in Livengood et al. (2011).

Table 4.1. A Summary of *EPOXI* Observations

Midpoint time of observation (UT)	Sub-spacecraft latitude (°N)	Sub-spacecraft longitude (°W)	Sub-solar latitude (°S)	Sub-solar longitude (°W)
2008-03-18 18:39:11	1.7	154.6	0.6	97.1
2008-03-18 22:39:11	1.6	214.6	0.5	157.1
2008-03-19 04:36:50	1.6	304.4	0.4	246.8
2008-03-19 12:36:50	1.5	64.6	0.3	6.8

4.3.2 *Comparisons of models and observations*

Simulated Earth model spectra were generated with a resolution of 1 cm^{-1} and then degraded to the *EPOXI*/HRI resolution using a Gaussian convolution with FWHMs equal to the spectral bin size reported by the PDS for each spectral interval (for λ = 4.15 μm, this is $\Delta\lambda \sim 0.013$ μm). Figure 4.2 compares NIR observations of the spectral radiance of the Earth with the synthetic Earth model data. The model cases where $(N_2)_2$ absorption is included provide a much better match to the data in the 4.0 – 4.15 μm range. The differences between the data and the model without collisional $(N_2)_2$ and N_2-O_2 absorption reach 31-40% at 4.15 μm, whereas the residuals

[20] http://pds.nasa.gov/

between the data and the model with $(N_2)_2$ or with $(N_2)_2$ and N_2-O_2 absorption is less than 5%. The $(N_2)_2$ feature is robust and relatively constant (residuals within a few percent) through rotational phase, implying that the sensitivity of the spectral flux to surface features is small in this wavelength range.

There does remain a sharply peaked residual at the edge of the CO_2 band even when accounting for $(N_2)_2$ and N_2-O_2 absorption. The offset I observe between the EPOXI and Earth model spectra at the bottom of the 4.3 um CO_2 band, and the difference in line shape at the edge of the band, could be explained by non-LTE emission of CO_2 in the upper atmosphere, which is not accounted for in our model. Non-thermal emission by CO_2 near 4.3 μm is a well-studied phenomenon, seen in limb soundings of the atmospheres of Earth (e.g., López-Puertas & Taylor 1989), Venus (e.g., Gilli et al. 2009), and Mars (e.g., López-Valverde et al. 2005). Non-LTE models predict a peak radiance near 4.28 μm (~2337 cm^{-1}) (e.g., López-Valverde et al. 2011), which is the wavelength where the largest offset between our model spectra and the EPOXI data is observed within the bottom of the band. Disk-integrated observations of Earth (such as the EPOXI observations presented here) include limb paths, where non-LTE contributions can be relatively large due to path length effects. Non-thermal CO_2 emission varies as a function of altitude, latitude, and solar zenith angle, and recent calculations indicate that non-LTE emission from CO_2 can account for the offset between our model and the data at the bottom of the 4.3 um CO_2 band (López-Valverde et al. 2011). Importantly, at wavelengths shortward of 4.15 μm where the effect of $(N_2)_2$ is observed, the atmospheric transmission is relatively high and insensitive to the temperatures in the upper atmosphere. I conduct a series of sensitivity tests in Section 4.3.3 to show the peaked residuals or the absorption that is attributed to $(N_2)_2$ and N_2-O_2

does not originate from simple differences between the width of the CO_2 band in the data and the model.

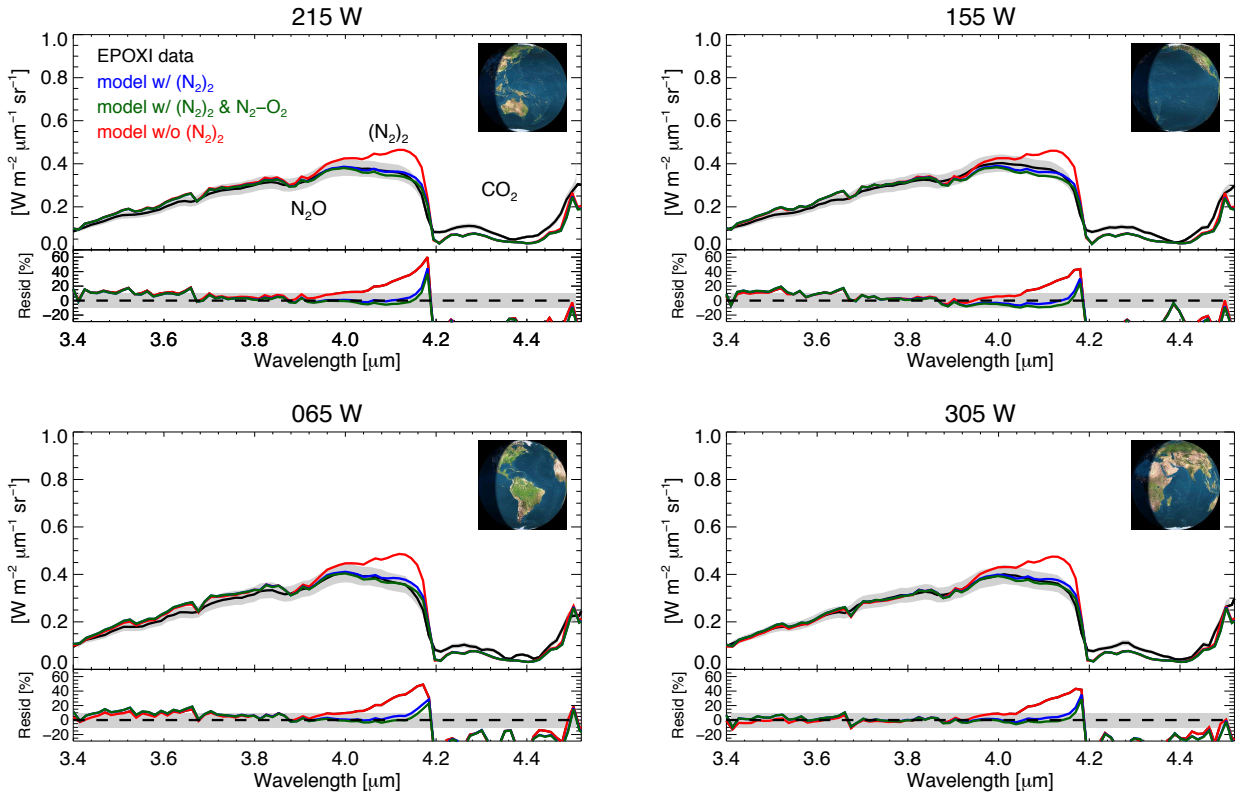

Figure 4.2. Detection of $(N_2)_2$ absorption in Earth's NIR spectra. Spectral radiances of the Earth as measured by the *EPOXI* NIR spectrograph (black), as generated by the VPL three-dimensional Earth Model without $(N_2)_2$ absorption (red), with $(N_2)_2$ absorption (blue), and with both $(N_2)_2$ and N_2-O_2 absorption (green). Titles provide the sub-spacecraft longitudes (also given in Table 1). The gray band is the calibration uncertainty for the NIR data (Klaasen et al. 2008). *Insets:* Illustrations of Earth's illumination as seen by the *EPOXI* spacecraft during each observation. Insets were generated with the Earth Moon Viewer originally developed by J. Walker (http://www.fourmilab.ch/earthview/).

To my knowledge, this is the first time N_2 has been demonstrated in Earth's disk-averaged radiance spectrum. Spectra of Earth from other studies, including *Galileo*/NIMS spectra (Sagan et al. 1993; their figure 1c), *Mars Express*/OMEGA[21] IR spectra (Tinetti et al. 2006; their figure 10), and spatially resolved *ROSETTA*/VIRTIS spectra (Hurley et al. 2014; their figure 3) show a 4 um "roll off" on the short wavelength side of the CO_2 band with a similar spectral shape to the $(N_2)_2$ feature presented here. However, these studies do not attribute this feature to $(N_2)_2$. It should be noted that a disk-averaged *ROSETTA*/VIRTIS spectrum presented in Irwin et al. (2014; their figure 3) does not appear to show the same shape as seen in Figure 4.2. However, the shape of their measured spectrum is also not consistent with the other studies mentioned above. Comparison synthetic spectra presented by Irwin et al. (2014) are also poor fits to their measured data in the 2.2-5 μm spectral range, except for the core of the 4.3 μm CO_2 band.

4.3.3 *Sensitivity tests*

To demonstrate that the spectral "roll off" seen near 4 μm is due to collisional $(N_2)_2$ absorption and not an artifact or the influence of other gaseous absorption, I conducted a series of sensitivity tests. In my first test, I examined the sensitivity of the residuals between the *EPOXI* spectral data and the synthetic Earth model comparisons to the assumed FWHM used to degrade the high-resolution synthetic spectra. As stated in Section 4.3.2, I degraded the synthetic spectra to the same spectral resolution as the *EPOXI* measurements using a Gaussian convolution with FWHMs equal to the spectral bin size reported in the PDS for each wavelength. I determined the effect of the assumed FWHM on the shape of the data-model residuals by degrading one set of synthetic spectra (top left panel in Figure 4.3; sub-spacecraft longitude of 215° W) with 1, 2, and

[21] http://sci.esa.int/mars-express/31033-objectives/?fbodylongid=661

4 times the FWHM at 4.15 μm (0.013 μm). Figure 4.3 shows the result. While a FWHM of 0.052 μm (4 × 0.013 μm) decreases the residuals somewhat shortward of 4.16 μm, it leads to an increase in the residuals longward of 4.2 μm and an overall poorer fit to the spectral shape.

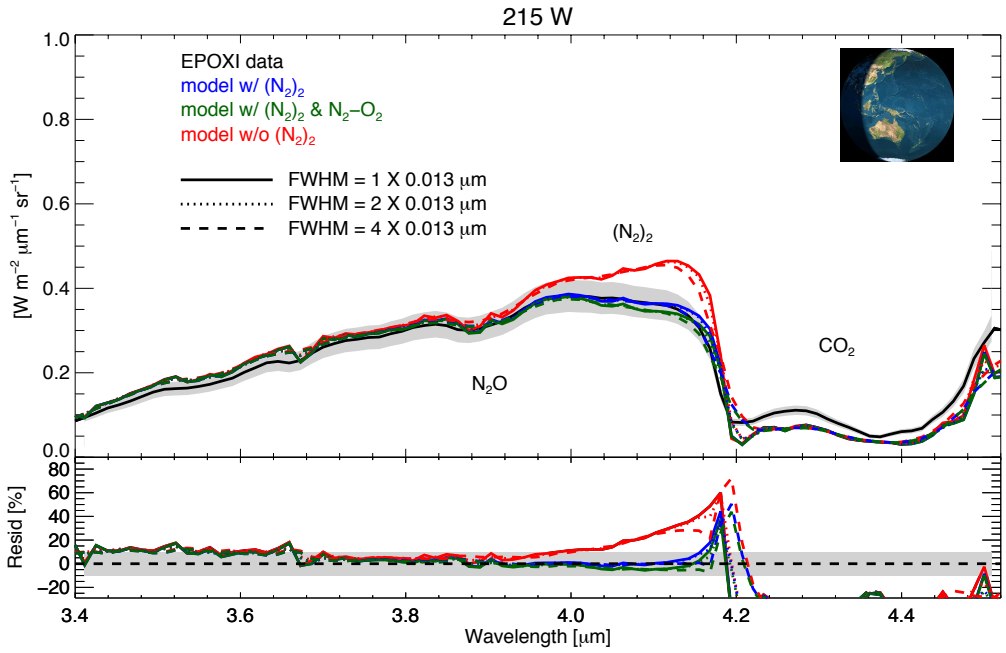

Figure 4.3. Spectral resolution sensitivity tests. The data are the same as in the upper left panel of Figure 2. Lines indicate Gaussian spectral convolution with different FWHMs in factors of 1 (solid line), 2 (dotted line), 4 (dashed line) × 0.013 um (the spectral bin size at λ = 4.15 μm reported by PDS).

Next I used a series of one-dimensional SMART runs to compare the absorption of $(N_2)_2$ and N_2-O_2 to absorption by CO_2 and N_2O, which are also spectrally active in this wavelength region. Besides helping to demonstrate the detection of $(N_2)_2$ in Earth's spectrum, these sensitivity tests are also useful guides to the robustness of $(N_2)_2$ absorption in atmospheres with slightly different compositions. For each of these SMART runs, I used a temperature and gas mixing ratio profile from one of the retrieved profiles used in the VPL Earth Model (Figure 2.5).

I assumed the surface was an ocean (McLinden et al. 1997) with no clouds, a surface temperature of T_{surf} = 288.2 K, a solar zenith angle of 60° and an azimuth angle of 0°. Figure 4.4 illustrates the results of these tests.

In Figure 4.4a, I show one-dimensional clear sky SMART spectra with and without $(N_2)_2$ and N_2-O_2 absorption, which looks similar to comparisons of the data and model without $(N_2)_2$ and N_2-O_2 absorption in Figure 4.2 (though the one-dimensional SMART spectra are not directly comparable to the three-dimensional disk-integrated Earth model spectra). In the remaining tests I do not include collisional N_2 absorption. In Figure 4.4b, I show the effect of doubling or halving the CO_2 mixing ratio, demonstrating this saturated band is relatively insensitive to differences in CO_2. In Figure 4.4c, I experiment with different line cutoffs used in LBLABC to generate our absorption coefficients (see Section 2.1). This panel shows that line cutoffs larger than 100 cm^{-1} would be adequate to model the 4.3 μm CO_2 band. For all other cases I used line cutoffs of 1000 cm^{-1}, which is larger than the width of the plot window (a $\Delta\nu$ of 1000 cm^{-1} is a $\Delta\lambda$ of ~1.76 μm at λ = 4.2 μm). Finally, in Figure 4.4d I show the effect of doubling and halving the N_2O concentration. While N_2O absorbs between 4.0-4.2 μm, its effect is negligible. In each of the panels of Figure 4.4, the *EPOXI* spectrum of the Earth with a sub-spacecraft longitude of 215° W (see Figure 4.2 and Table 4.1) is added for contrast. Note that the EPOXI spectrum of the disk-integrated Earth and the 1-D SMART synthetic spectra of a single sounding are not directly comparable. This is because the observed Earth contains clouds, heterogeneous surfaces including land as well as ocean, and a distribution of solar zenith and observer angles, which are not present in the simple synthetic spectra - with an ocean surface and no clouds - generated to show sensitivity to a given atmospheric constituent or line cutoff assumption (see Figure 4.2 for the directly comparable synthetic spectra).

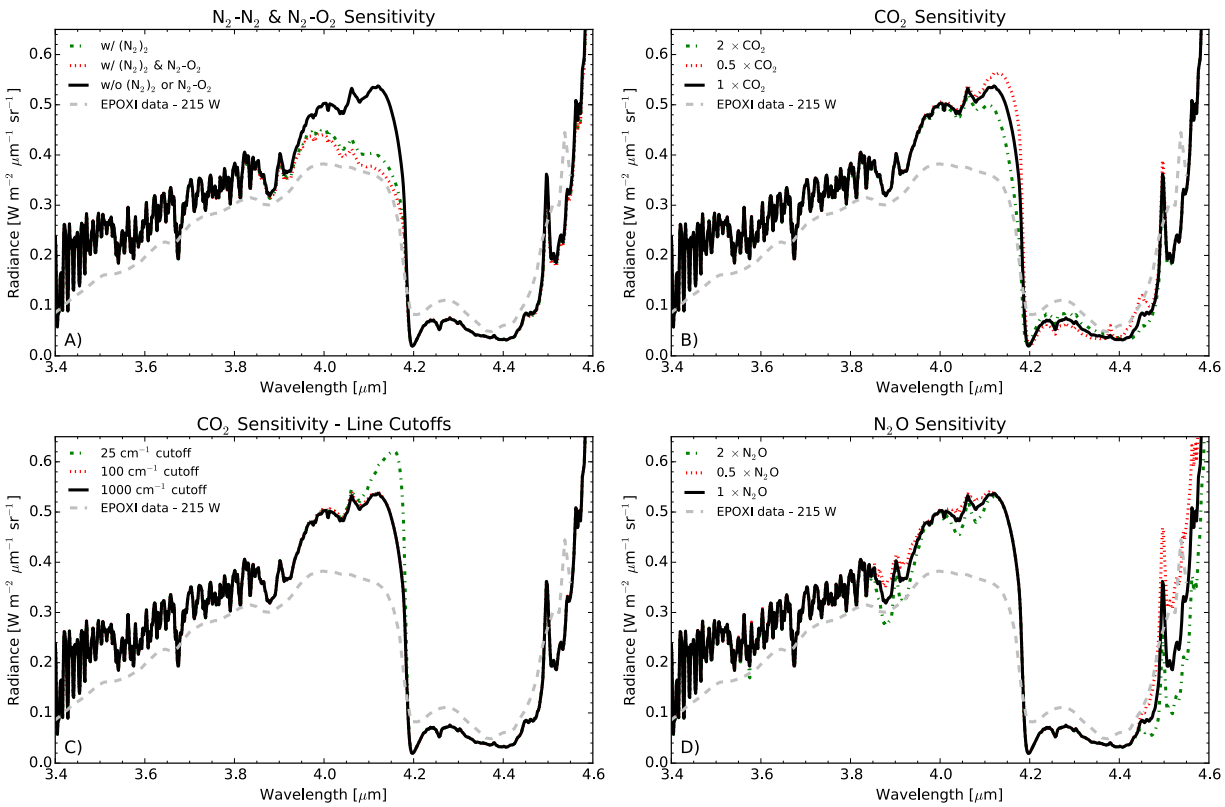

Figure 4.4. Sensitivity to molecular absorption by key species. Cloud-free spectra are generated by SMART with a solar zenith angle of 60°, an azimuth angle of 0°, and a Lambertian ocean surface. None of the synthetic spectra contain N_2-N_2 and N_2-O_2 absorption besides those in the top left panel. **A)** Model spectra without $(N_2)_2$ and N_2-O_2 absorption (black solid), with $(N_2)_2$ absorption only (green dash-dot), with $(N_2)_2$ and N_2-O_2 absorption (red dotted). **B)** Model spectra with 1 × standard CO_2 (black solid), 2 × standard CO_2 (green dash-dot), and 0.5 × standard CO_2 (red dotted). **C)** Model spectra with 1000 cm^{-1} line cutoff for CO_2 absorption coefficients (black solid), with a 100 cm^{-1} line cutoff (red dotted), and with a 25 cm^{-1} line cutoff (green dash-dot). **D)** Model spectra with 1 × standard N_2O (black solid), 2 × standard N_2O (green dash-dot), and 0.5 × standard N_2O (red dotted). Mixing ratio profiles assumed for CO_2 and N_2O can be found in Figure 1. The *EPOXI* Earth spectrum with a sub-spacecraft longitude of 215° W (see Figure 3 and Table 1) is added to each panel for illustration (gray dashed), though it is not directly comparable with sensitivity spectra presented here.

4.3.4 *Simulated transmission spectrum of the Earth-Sun with $(N_2)_2$ absorption*

To investigate the detectability of $(N_2)_2$ in Earth's transmission spectrum and inform future observations of Earth-Sun analogs, I used the VPL one-dimensional transmission model, which includes the effects of refraction and has been validated for Earth observations (Misra, Meadows & Crisp 2014). I assumed the same temperature and mixing ratio profiles as given in Figure 2.5 (including absorbing gases O_2, H_2O, CO_2, O_3, N_2O, CH_4 and CO) and no clouds or aerosols. The spectral resolution for the simulated transit transmission spectrum is $\Delta\lambda = 0.005$ μm. Due to refraction only the top ~0.2 bars of the atmosphere can be probed for a distant observer with the Earth-Sun geometry (García Muñoz et al. 2012; Bétrémieux & Kaltenegger 2013). Figure 4.5 shows the largest effect $(N_2)_2$ could have on the transmission spectrum of an Earth-Sun analog. The maximum signal is < 0.1 ppm due to the limiting tangent pressure (defined as the pressure above which only 50% or less of light is transmitted) of < ~0.2 bar and the strong density dependence of collisional pair and/or dimer absorption (Misra et al. 2014a). While N_2 absorption would be undetectable in an Earth-Sun analog due to high limiting tangent altitudes from refraction, circumstances are more favorable for planets orbiting within the habitable zone of lower mass stars where refraction allows lower altitudes to be probed (Bétrémieux & Kaltenegger 2014; Misra et al. 2014b). I investigate this further in Section 4.5.

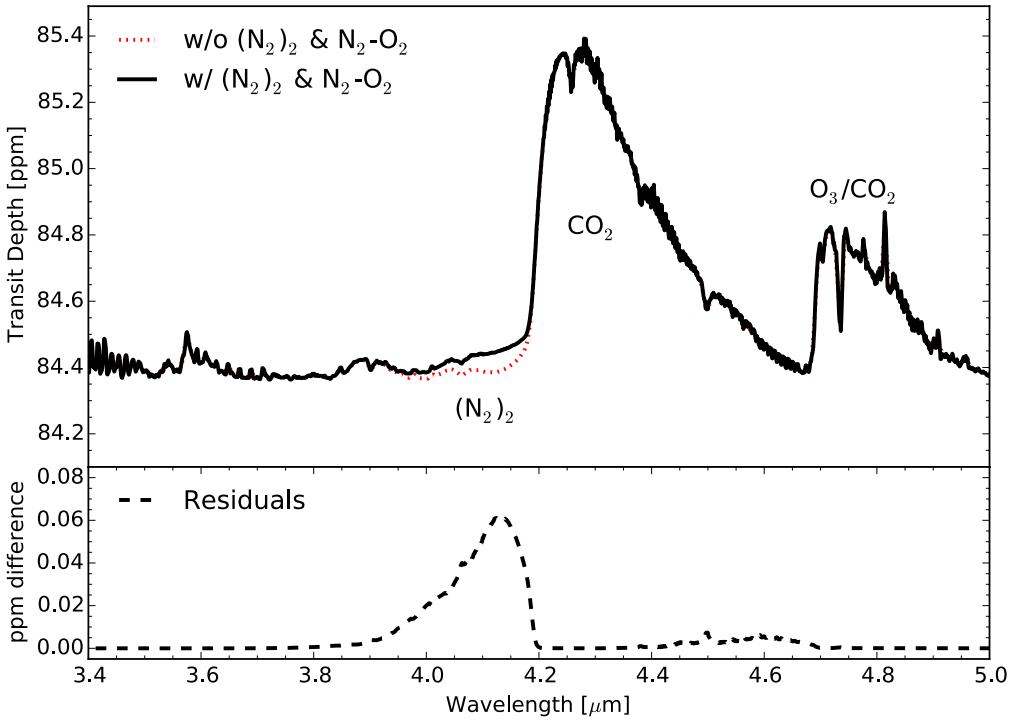

Figure 4.5. Transmission spectrum for an Earth transiting a Sun with (solid black) and without (dashed red) $(N_2)_2$ absorption in units of ppm. The spectral resolution is $\Delta\lambda$ = 0.005 μm. The bottom panel shows the difference between the model with and without $(N_2)_2$ absorption. The temperature and gas mixing ratio profiles assumed were the same as in Figure 1. Note the very small difference in transit depth is due to high limiting tangent altitudes for Earth-Sun geometries due to refraction, such that these spectra do not probe the deepest parts of the atmosphere where $(N_2)_2$ absorption is most significant (García Muñoz et al. 2012; Bétrémieux & Kaltenegger 2013; Misra et al. 2014).

4.4 RADIANCE SPECTRA OF $(N_2)_2$ IN N_2-CO_2-H_2O ATMOSPHERES

4.4.1 *Self-consistent* N_2-CO_2-H_2O Atmospheres

To explore the general case of $(N_2)_2$ absorption in the emission spectra of terrestrial planets, I used a modified version of a publicly available[22] radiative-convective model (Kasting et al. 1993; Segura et al. 2005; Haqq-Misra et al. 2008) to construct self-consistent temperature-pressure and water vapor mixing ratio profiles of pure N_2-CO_2-H_2O atmospheres to use as input for SMART. Atmospheres that have CO_2 and H_2O concentrations consistent with their surface temperatures are useful because of the possible degeneracy between CO_2 absorption and $(N_2)_2$ absorption in the wings of the 4.3 μm CO_2 band. In contrast, I could have explored cases with increased N_2 but with constant CO_2, while maintaining the same surface temperature (which sets the magnitude of the thermal flux), but this would be unrealistic because the planet's CO_2 concentration would be inconsistent with its temperature and thermal flux. Pure N_2-CO_2-H_2O atmospheres are chosen to provide terrestrial planet base cases without complicating assumptions about the origin of major or trace gases that may be due to life (such as O_2 from photosynthetic organisms), and the development of trace gases from photochemistry that may also be greenhouse absorbers (such as O_3 from O_2). The gray surface Bond albedo of the planet was chosen such that in an Earth-like scenario with modern (pre-industrial) mixing ratios of CO_2, H_2O, O_3, N_2O, N_2, and CH_4 the surface temperature converged to 288 K. This albedo (A_B =0.238) was used for each surface pressure and temperature scenario. This is effectively a tuning parameter that allows a one-dimensional climate model to match Earth's modern surface temperature for calibration (Kasting et al. 1993).

[22] http://vpl.astro.washington.edu/sci/AntiModels/models09.html

I assumed the same incident solar flux as Earth currently receives and adjusted the CO_2 concentration until the surface temperature of the planet converged to the desired value. The water vapor mixing ratios were calculated using a relative humidity profile with a surface relative humidity of 80% (Manabe & Wetherald 1967). The CO_2 mixing ratio profile was constant with altitude. N_2 constituted the remaining atmospheric volume of each layer after CO_2 and H_2O were accounted for. Six pressure scenarios were considered, with P_{surf} = 0.2, 0.5, 1.0, 2.0, 5.0, and 10.0 bars. Three temperature scenarios were calculated with a solar input spectrum: 273 K, 288 K, and 300 K. A similar set of atmospheric profiles were calculated for a 288 K surface temperature planet with the incident spectrum of AD Leo, an M3.5 dwarf with an effective temperature of 3390 K (Rojas-Ayala et al. 2012). I used the same AD Leo spectrum as in Segura et al. (2005, 2010), which was scaled from the Earth-Sun flux equivalent distance by an albedo correction factor (A_{fac}) of 0.9 to correct for the absorption of redder stellar radiation by an Earth-like atmosphere. This distance from the star to the planet was calculated as r = 1 AU $[(L/L_{\odot})/A_{fac}]^{1/2}$, following Segura et al. (2005). This produced a distance of r = 0.16 AU and a normalized flux of 1225 W/m^2 for the AD Leo cases, compared to an incident flux of 1360 W/m^2 for the Earth-Sun scenarios. AD Leo was chosen to represent the category of stars with effective temperatures less than that of the Sun, where a larger number of habitable zone planets may be found (Dressing & Charbonneau 2013; Kopparapu 2013). AD Leo is often used in the study of the atmospheres of planets orbiting different spectral classes of star because a complete, calibrated spectrum of this star is available from the UV to the MIR (Segura et al. 2010; von Paris et al. 2013; Domagal-Goldman et al. 2014).

To study the potential for CO_2-dominated (i.e., Mars-like) atmospheres to mimic the $(N_2)_2$ feature, a set of temperature-pressure and gas mixing ratio profiles were calculated using

the same radiative-convective model as described above, but for atmospheres dominated by CO_2. This allows comparison between the change in band intensity and shape for self-consistent atmospheres with CO_2 (broadened by N_2) plus $(N_2)_2$, and self-consistent atmospheres with only CO_2. For these atmospheres, the volume fraction of CO_2 was fixed at 96%, equivalent to Mars' CO_2 mixing ratio, with small amounts of N_2 constituting the remaining volume after accounting for H_2O. Instead of using the CO_2 fraction (f_{CO2}) as the dial to converge the model to the desired surface temperatures, the surface pressure was adjusted.

The properties of each atmosphere are given in Table 4.2 (N_2-CO_2-H_2O atmospheres) and Table 4.3 (CO_2-dominated atmospheres) and their temperature-pressure profiles are shown in Figure 4.6. There are two competing factors that set the CO_2 mixing ratio. As the surface pressure (equivalently atmospheric mass for constant surface gravity and temperature) increases, the total amount of CO_2 (and H_2O) also increases, forcing the CO_2 mole fraction to be tuned downwards. However, as the atmospheric mass increases, the planetary albedo also increases because of enhanced Rayleigh scattering to space. This cools the surface (by reducing the amount of incident solar radiation) and necessitates more CO_2. (It should also be noted that CO_2 is also much more efficient at Rayleigh scattering than N_2 and for this reason, along with the saturation of CO_2 absorption bands, there are diminishing returns for adding more CO_2). The temperature-pressure profiles are affected by the mole fraction of CO_2 in the upper atmosphere. More CO_2 enhances the radiative cooling in these upper layers, and because the CO_2 mixing ratio is constant with altitude for each scenario, this results in the radiative cooling in the upper atmosphere being more effective for the atmospheres with lower total surface pressure and thus larger CO_2 mixing ratios. It is important to note that because the absorption by $(N_2)_2$ is highly density dependent and weakly temperature dependent, our results are insensitive to the

temperature profiles of the upper atmosphere. Segura et al. (2005) showed that a lower integrated stellar flux is required from M dwarfs to achieve the same planetary surface temperature, due to the lower planetary albedo caused by gaseous absorption of more plentiful incoming IR radiation. I follow the convention suggested by Segura et al. (2005), and use a lower integrated stellar flux for our AD Leo planets. However, the pressures and compositions of our atmospheres differed from Segura et al. (2005). As a result, more CO_2 was required for the $P_{surf} \leq 1$ bar AD Leo cases to achieve the same surface temperature (T_{surf}=288 K) as the Earth-Sun cases, as these cases have less efficient albedo augmentation due to the lack of absorbing gases other than H_2O and CO_2. For the AD Leo cases with $P_{surf} \geq 2$ bar, the combination of the redder spectrum of AD Leo and the greater total H_2O content of the atmospheres (see Table 4.2), necessitated lower CO_2 fractions than for the equivalent Earth-Sun cases. Note that for a surface pressure of $P \leq 0.2$ bars, a surface temperature of 300 K assuming a solar spectrum and a surface temperature of 288 K with an AD Leo spectrum are inconsistent with even a pure CO_2 atmosphere, so I have not included those scenarios in Figure 4.6, Table 4.2, or subsequent figures.

Table 4.2. Parameters for N_2-CO_2-H_2O atmospheres

P_{surf} [bar]	f_{CO2}	Total CO_2 [bar]	Total H_2O [bar]	Max f_{H2O}	Planetary Albedo
T_{surf} = 273 K (Sun)					
0.2	7.90e-5	1.58e-5	2.32e-4	2.35e-2	0.223
0.5	1.90e-6	9.60e-7	4.41e-4	9.54e-3	0.238
1.0	1.10e-6	1.10e-6	7.43e-4	4.81e-3	0.260
2.0	1.05e-6	2.10e-6	1.31e-3	2.40e-3	0.291
5.0	6.50e-6	3.25e-6	3.00e-3	9.62e-4	0.353
10.0	1.10e-4	1.10e-3	5.82e-3	4.82e-4	0.412
T_{surf} = 288 K (Sun)					
0.2	9.95e-2	1.99e-2	8.37e-4	6.25e-2	0.208
0.5	3.15e-3	1.58e-3	1.66e-3	2.62e-2	0.223
1.0	6.40e-4	6.40e-4	2.75e-3	1.33e-2	0.245
2.0	3.65e-4	7.30e-4	4.66e-3	6.72e-3	0.276
5.0	5.00e-4	2.50e-3	1.01e-2	2.70e-3	0.337
10.0	9.30e-4	9.30e-3	1.90e-2	1.35e-3	0.398
T_{surf} = 288 K (AD Leo)*					
0.5	1.26e-2	6.30e-3	1.66e-3	2.62e-2	0.140
1.0	1.30e-3	1.30e-3	2.75e-3	1.33e-2	0.145
2.0	1.38e-4	2.76e-4	4.66e-3	6.71e-3	0.146
5.0	7.80e-6	3.90e-5	1.01e-2	2.70e-3	0.156
10.0	2.95e-6	2.95e-5	1.90e-2	1.35e-3	0.173
T_{surf} = 300 K (Sun)**					
0.5	7.70e-2	3.85e-2	4.27e-4	5.32e-2	0.211
1.0	9.95e-3	9.95e-3	7.00e-3	2.75e-2	0.232
2.0	3.35e-3	6.70e-3	1.17e-2	1.40e-2	0.263
5.0	1.77e-3	8.85e-3	2.40e-2	5.65e-3	0.325
10.0	1.77e-3	1.77e-2	4.38e-2	2.85e-3	0.386

* For $_{Psurf}$= 0.2 bar no N_2-CO_2-H_2O atmosphere is possible; maximum CO_2 fraction produces T_{surf}= 287.0K.

**For $_{Psurf}$ = 0.2 bar no N_2-CO_2-H_2O atmosphere is possible; maximum CO_2 fraction produces T_{surf}= 284.5 K.

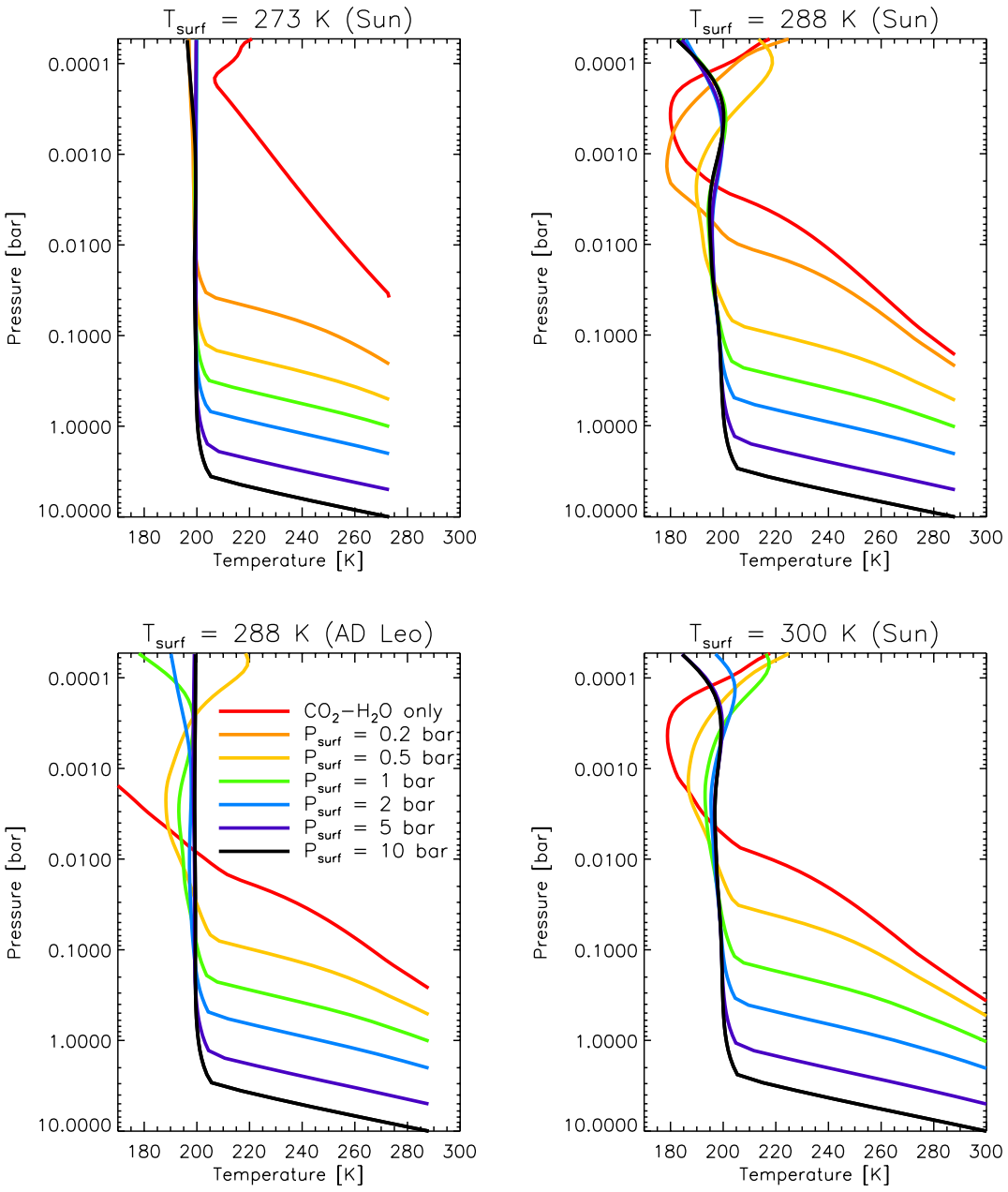

Figure 4.6. Self-consistent N_2-CO_2-H_2O and CO_2-dominated atmosphere temperature-pressure profiles. The colors represent total surface pressures of 0.2 bar (orange), 0.5 bar (yellow), 1.0 bar (green), 2.0 bars (blue), 5 bars (purple), and 10 bars (black). The CO_2-dominated atmospheres that produce the same surface temperature are in red. More atmosphere parameters can be found in Table 2 and Table 3.

Table 4.3. Parameters for CO_2-H_2O atmospheres

P_{surf} [bar]	f_{CO2}	CO_2 [bar]	H_2O [bar]	Max f_{H2O}	Planetary Albedo
T_{surf} = 273 K (Sun)					
0.032	9.60e-1	3.07e-2	6.28e-5	1.38e-1	0.216
T_{surf} = 288 K (Sun)					
0.148	9.60e-1	1.42e-1	6.66e-4	8.21e-2	0.213
T_{surf} = 288 K (AD Leo)					
0.213	9.60e-1	2.04e-1	8.91e-4	5.90e-2	0.141
T_{surf} = 300 K (Sun)					
0.332	9.60e-1	3.19e-1	3.07e-3	7.77e-2	0.213

4.4.2 *Simulated radiance spectra*

For each of the self-consistent N_2-CO_2-H_2O temperature pressure and mixing ratio profiles described in section 4.4.1, I generated spectra using SMART. One series of spectra assumed only thermal emission, shown in Figure 4.7. In these cases, the spectral albedo in the 3.4-5.0 μm range was set to zero and the emissivity was set to 1 to isolate thermal emission, because reflected stellar light contributes much less than thermal emission to the total spectral flux from the planet, but will depend on the surface spectral albedo and cloud emissivities and altitudes. The albedo in this wavelength range contributes very little to the Bond albedo of the planet, so this assumption is not inconsistent with Section 4.4.1. The resulting spectra demonstrate strong dependence on N_2 abundance for surface pressures exceeding 1 bar with the flux being reduced in the wings of the 4.3 μm CO_2 band by up to 100% for sufficiently high N_2 abundances. The results from the one-dimensional model spectra are consistent with the *EPOXI*-VPL Earth model comparison. For the P_{surf} =1 bar, T_{surf} = 288 K synthetic spectrum from the one dimensional model, the $(N_2)_2$ absorption has a maximum effect of 35% on the spectral flux, which is similar to that observed by *EPOXI* for Earth's disk-averaged spectrum. The effect of $(N_2)_2$ absorption decreases for self-consistent scenarios with higher surface temperatures. This is because the higher temperature

planets require more CO_2 to warm their surfaces, and thus the width of the 4.3 μm CO_2 band increases and masks $(N_2)_2$ absorption.

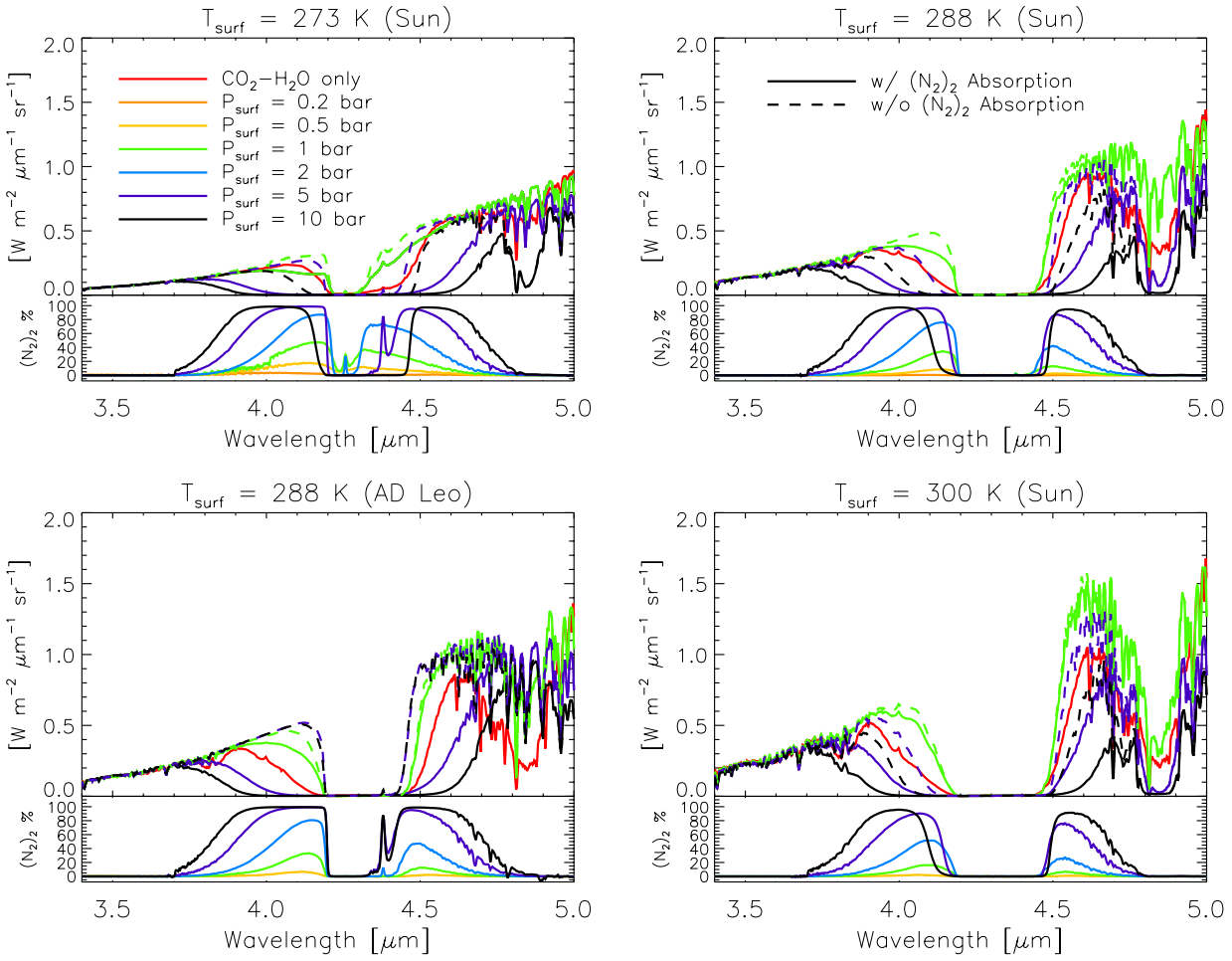

Figure 4.7. Thermal-only radiance spectra of model Earth-like planets showing $(N_2)_2$ absorption in the NIR. The temperature-pressure profiles used for these spectra are shown in Figure 4.6. In the top sub-panels only the P_{surf} = 1, 5, and 10 bar, and the CO_2-dominated spectra are shown. The bottom sub-panels plot the wavelength-dependent percentage difference between the cases with $(N_2)_2$ absorption (solid) and without it (dashed) for all pressure scenarios given in the figure key.

I generated another series of spectra that include reflected light, shown in Figure 4.8. In these cases, the spectral albedo of the planet was set to 10% for the 3.4-5.0 μm wavelength range. The spectrum used to model the incident light from the Sun is a Kurucz model (Kurucz 1995), and the spectrum used for AD Leo is the same used in Section 4.4.1 (Segura et al. 2005; Segura et al. 2010). The increase in the total spectral flux is especially notable for AD Leo, whose SED is shifted more strongly into the NIR compared to the Sun due to its lower effective temperature. The peak relative $(N_2)_2$ contribution is similar for the scenarios that include reflected light (Figure 4.8) and the scenarios that do not include reflected light (Figure 4.7), though the differences for the cases with reflected light are greater at shorter wavelengths where there is more incident flux from the star. The inverse problem is not attempted here, but note that accounting for $(N_2)_2$ absorption could potentially provide leverage to constrain N_2 abundances with future retrieval algorithms when applied to direct-imaging spectra of planets with substantial atmospheres (e.g., Benneke & Seager 2012; Line et al. 2013; von Paris et al. 2013).

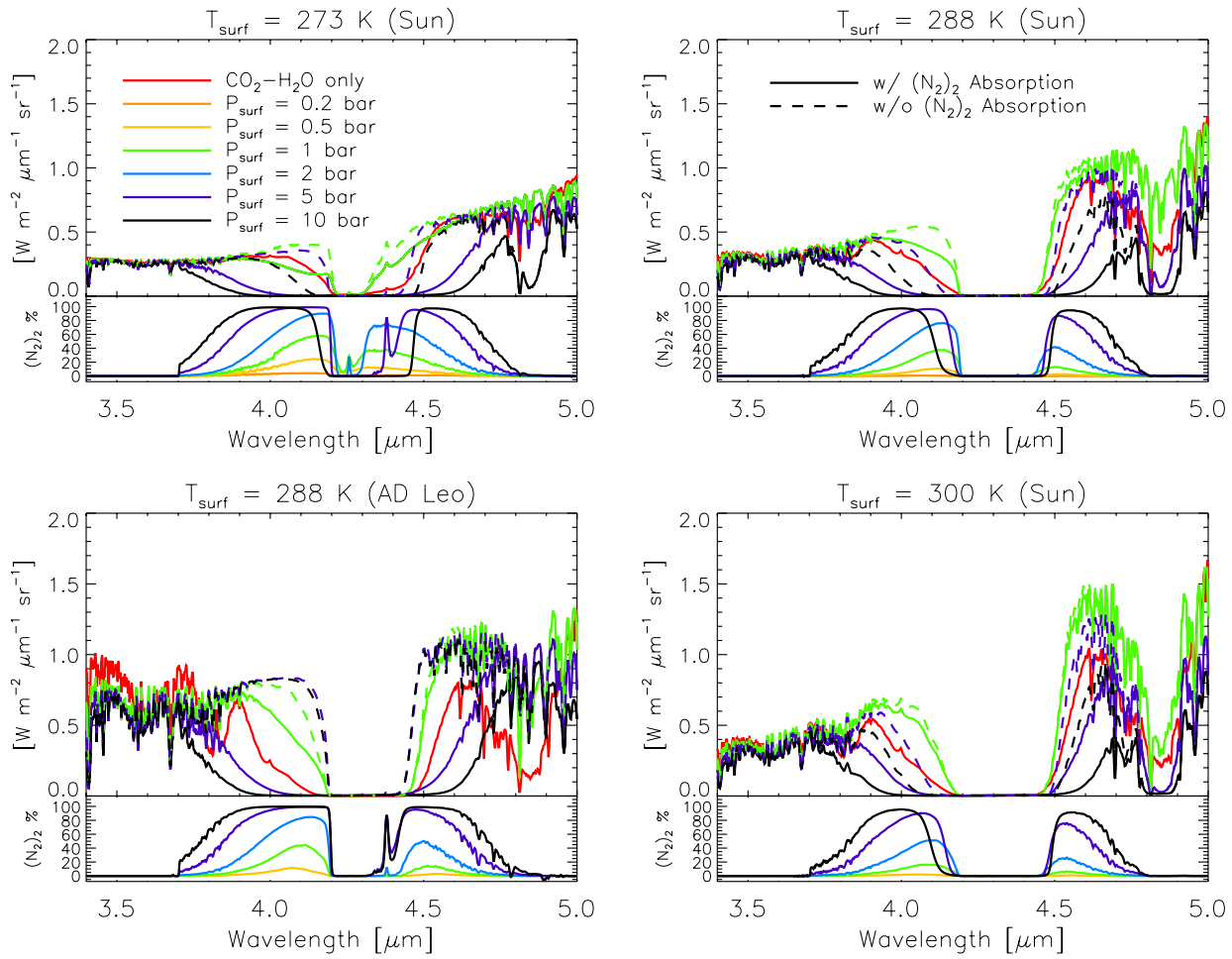

Figure 4.8. Same as Figure 4.7 except including both thermal emission and reflected light. The surface albedo is assumed to be 10% and constant over the wavelengths shown here. The incident stellar spectrum is either that of AD Leo (bottom left panel) or the Sun (all other panels).

4.5 Transmission Spectra of Planets with N_2 Atmospheres Orbiting Late Type Stars

Transit transmission observations will be more favorable for planets orbiting the HZ of late type stars, where the lower atmosphere may be probed because geometric refraction limits approach pressures greater than (or equivalent altitudes lower than) ~1 bar for N_2-dominated atmospheres (Bétrémieux & Kaltenegger 2014; Misra et al. 2014b). Additionally, JWST may have the

opportunity to characterize one or more super-Earths in the habitable zones of late type stars (Deming et al. 2009), increasing the importance of studying these cases. I generated a synthetic transit transmission spectrum of an Earth orbiting in the HZ of an M5V star (a = 0.05 AU, R = 0.2 $R_\odot$) using the model described in Misra et al. (2014b). The conservative and optimistic inner edge limits for the habitable zone of a T_{eff} = 2800 K, L = 0.0022 $L_\odot$ M5V star are a = 0.049 AU and a = 0.039 AU, respectively (Kopparapu et al. 2013)[23]. I assumed the same set of temperature and gas mixing ratios in Figure 2.5. Figure 4.9 shows the effect of $(N_2)_2$ in this test case. The maximum spectral transmission depth is ~3 ppm, which is almost two orders of magnitude greater than that seen for the Earth-Sun analog (Figure 4.5). This difference is primarily due to the smaller radius of the M5V host star relative to that of the Sun. An additional contribution comes from the combination of refraction - which permits deeper altitudes to be probed for a planet orbiting in the habitable zone of an M5V star - and the strong density dependence of $(N_2)_2$ absorption. However, this is still less than the anticipated noise level for JWST/NIRSPEC observations of an M5V host star at 4.1 μm, which Misra et al. (2014b) calculate as ~5 ppm (see their Figure 13) assuming all transits in a five year period are observed.

Figure 4.9 does not represent the most ideal scenario for detecting $(N_2)_2$. The spectral impact of $(N_2)_2$ is also function of the atmospheric scale height, the mean molecular weight of the atmosphere, and the concentrations of CO_2 and N_2O, since both gases have overlapping absorption features. To demonstrate the maximum plausible detectability of $(N_2)_2$ with transit transmission spectroscopy, I calculated transmission spectra of atmospheres dominated by mixtures of N_2 and H_2 with different trace fractions of CO_2 and N_2O. The addition of a low molecular weight component (H_2) will increase the scale height and consequently the transit

[23] See the VPL HZ calculator based on Kopparapu et al. (2013): http://depts.washington.edu/naivpl/content/hz-calculator

height variations (or, equivalently, spectral transit depths) due to the spectrally absorbing gases (Miller-Ricci et al. 2009). Below I describe the model atmospheres and the synthetic transmission spectra generated.

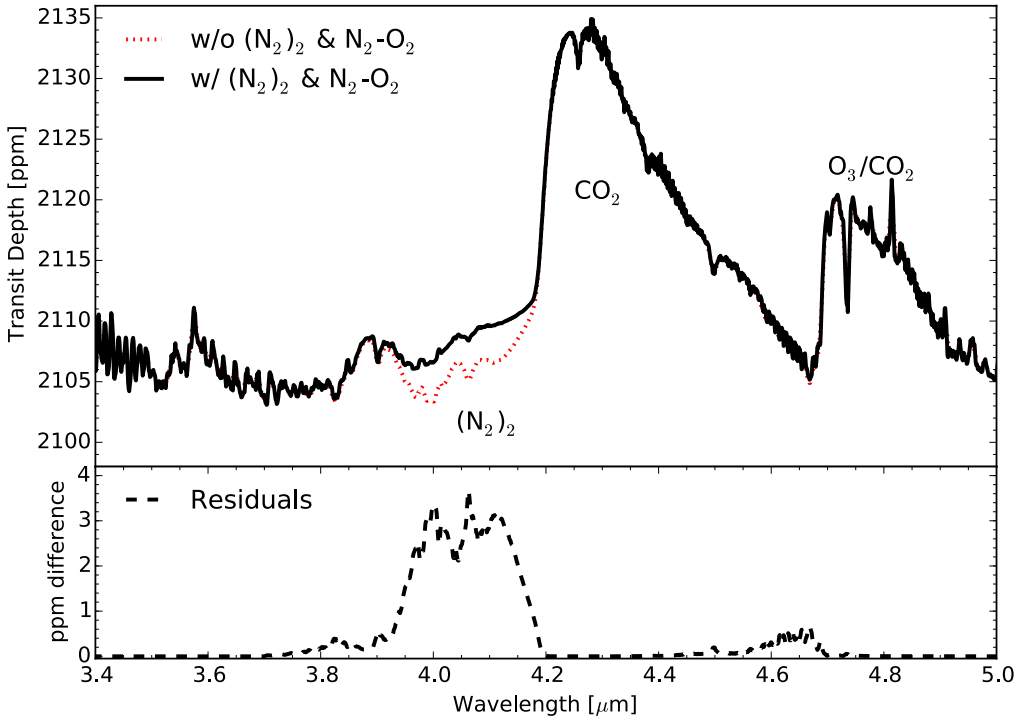

Figure 4.9. Transmission spectrum for an Earth transiting an M5V star (R = 0.2 $R_\odot$; a = 0.05 AU) with (solid black) and without (dashed red) $(N_2)_2$ absorption in units of ppm. The spectral resolution is $\Delta\lambda$ = 0.005 μm. The bottom panel shows the difference between the model with and without $(N_2)_2$ absorption. The temperature and gas mixing ratio profiles assumed were the same as in Figure 2.5.

4.5.1 *Analytic N_2-H_2 Atmospheres*

I employed a simple model for calculating the temperature-pressure-altitude structure of an atmosphere that consists of pure mixtures of one or more gases. I assumed a surface pressure of 1

bar, a surface temperature of T_{surf} = 288 K, and an isothermal stratospheric temperature of T_{strat} = 200 K, which is used when simulating atmospheres without stratospheric UV absorbers (Schindler & Kasting 2000; Haqq-Misra et al. 2008; Domagal-Goldman et al. 2011). I used the thin layer approximation, so the gravity remained constant with altitude. The altitude grid extended from 0 km to 1000 km in intervals that increased with altitude from 3-100 km, though I found the results were insensitive to the altitude intervals used. The temperature changed at each altitude below the stratosphere based on the lapse rate. The lapse rate of the atmosphere was calculated as:

$$L = \frac{dT}{dz} = -\frac{g}{c_p} \tag{4.6}$$

where L is the dry adiabatic lapse rate, g is the surface gravity, and c_p is the heat capacity of the gas mixture at constant pressure. The heat capacity is a weak function of temperature, which is ignored in this simple treatment. The temperature at each altitude level below the tropopause is calculated as:

$$T = T_{surf} + L * Z \tag{4.7}$$

where Z is the altitude point in the array and T_{surf} is the input surface temperature. For all values of $T < T_{strat}$ the temperature is set to T_{strat}. To calculate the pressure below the stratosphere, the barometric equation is used:

$$P = P_{surf}\left(\frac{T_{surf}}{T}\right)^{\left(\frac{g}{RL}\right)} \text{ for } T > T_{strat} \tag{4.8}$$

Here, P is the pressure at a grid point, P_{surf} is the surface pressure, and R is the gas constant of the mixture. The pressure above the troposphere is calculated as:

$$P = P_{strat} * e^{-\left[\frac{(Z - Z_{strat})}{H_{strat}}\right]} \tag{4.9}$$

where Z_{strat} is the altitude where the temperature lapses to the stratospheric temperature, P_{strat} is the pressure at that altitude as calculated by (10), and H_{strat} is:

$$H_{strat} = \frac{k_B T_{strat}}{\mu g} \quad (4.10)$$

where k_B is the Boltzmann constant, and μ is the mean molecular mass of the atmosphere. The properties μ (N_2=28.02 $\frac{g}{mol}$, H_2=2.06 $\frac{g}{mol}$), c_p (N_2=1040 $\frac{J}{kg \cdot K}$, H_2=14320 $\frac{J}{kg \cdot K}$), and R (N_2=296.8 $\frac{J}{kg \cdot K}$, H_2= 4124 $\frac{J}{kg \cdot K}$) are given in terms of mass quantities for individual gases; I therefore weight according to mass mixing ratio when calculating these variables. I used the above equations to calculate the temperature-pressure-altitude structure for gas mixtures of 100% N_2, 75% N_2, 50% N_2, and 0% N_2 with the remaining percentages consisting of H_2.

4.5.2 *Transmission spectra of N_2-H_2 atmospheres*

I modeled the transmission spectra of the analytic N_2-H_2 atmospheres described above, including $(N_2)_2$ absorption (Lafferty et al. 1996). Since the $(N_2)_2$ feature substantially overlaps with the 4.3 μm CO_2 band, I modeled scenarios including different concentrations of CO_2 (Rothman et al. 2009): 0 ppm, 1 ppm, 10 ppm, 100 ppm, and 1000 ppm. Figure 4.10 shows the effect of $(N_2)_2$ in the transmission spectrum for the cases described from 3.5 – 5.0 μm. The only sources of opacity for these simple synthetic spectra are CO_2 and $(N_2)_2$ absorption. I find that with a 100% N_2 atmosphere, the maximum spectral transit signal produced for the Earth-sized planet is 10 ppm, while the 25% N_2/ 75% H_2 case produces a spectral transmission signal of about 50 ppm at 4.3 μm (with no CO_2). For the 50% N_2/50% H_2 cases with trace CO_2 concentrations, the peak spectral transmission depths due to $(N_2)_2$ range from 20 ppm (0 ppm CO_2) to 8 ppm (1000 ppm CO_2). The transit depth variations would be smaller for super-Earth atmospheres containing the

same mixing ratios of N_2, H_2, and CO_2 due to a smaller scale height, though super-Earths are more likely to retain larger fractions of H_2 (Miller-Ricci et al. 2009).

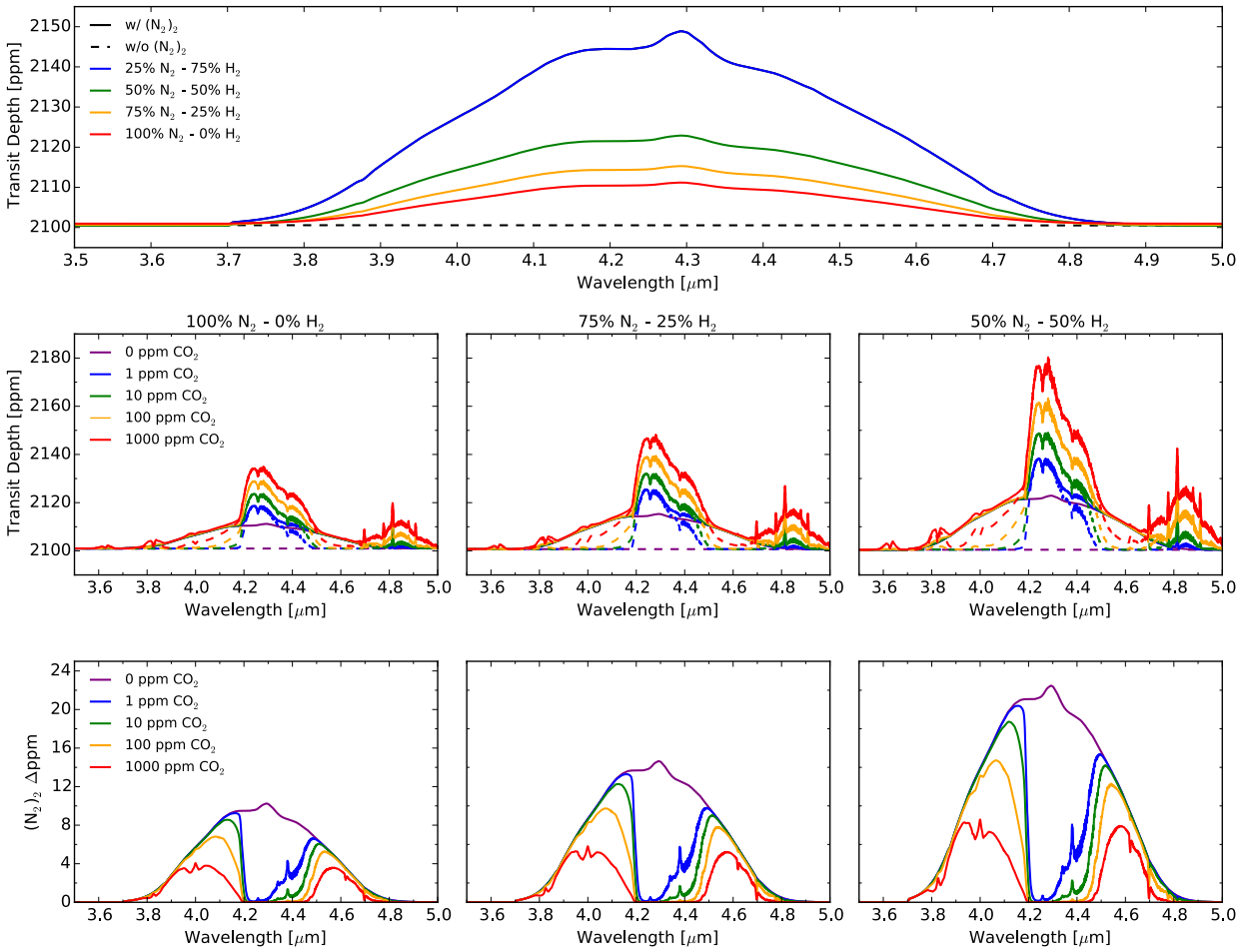

Figure 4.10. $(N_2)_2$ absorption in transmission for analytic N_2 and N_2-H_2-dominated atmospheres. Top panel: $(N_2)_2$ transmission depths for atmospheres that are pure N_2-H_2 mixtures (no CO_2). Middle panels: Transmission spectra for 100% N_2 (left), 75% N_2 (middle), and 50% N_2 (right) atmospheres with CO_2 concentrations of 0 ppm (purple), 1 ppm (blue), 10 ppm (green), 100 ppm (orange), and 1000 ppm (red) including $(N_2)_2$ absorption (solid lines) and without $(N_2)_2$ (dashed lines). Bottom panels: differences in transmission depths due to $(N_2)_2$ matched to spectra in the middle panel. The geometry assumed is a star with 20% the radius of the Sun, a planet-star distance of 0.05 AU and an impact parameter of 0.

Because N_2O also absorbs in this wavelength range (see Figure 4.4d), here I illustrate the sensitivity of $(N_2)_2$ absorption in transit transmission to different N_2O abundances. The introduction of N_2O would provide opacity at these wavelengths preventing an observer from probing the lower altitudes where $(N_2)_2$ can most impact the spectrum. I generate transmission spectra for a 75% N_2, 25% H_2 atmosphere with 100 ppm CO_2 and 0 ppb, 10 ppb, 100 ppb, 1000 ppb, and 10000 ppb N_2O (Figure 4.11). For comparison, the pre-industrial concentration of N_2O in Earth's atmosphere is ~265 ppb (Flückiger et al. 2002) and the atmospheric concentration of this biogenic gas likely varied greatly on Earth over geologic time (Buick 2007). With 100 ppm CO_2, 75% N_2, 25% H_2 and trace N_2O, peak spectral transmission depth variations due uniquely to $(N_2)_2$ range from just under 10 ppm (0 ppb N_2O) to just under 6 ppm (10000 ppb N_2O). The integrated $\Delta(N_2)_2$ residuals of the spectral transmission depths from 3.7 μm to 4.8 μm decrease more strongly with increased N_2O mixing ratios than the peak spectral transmission depths.

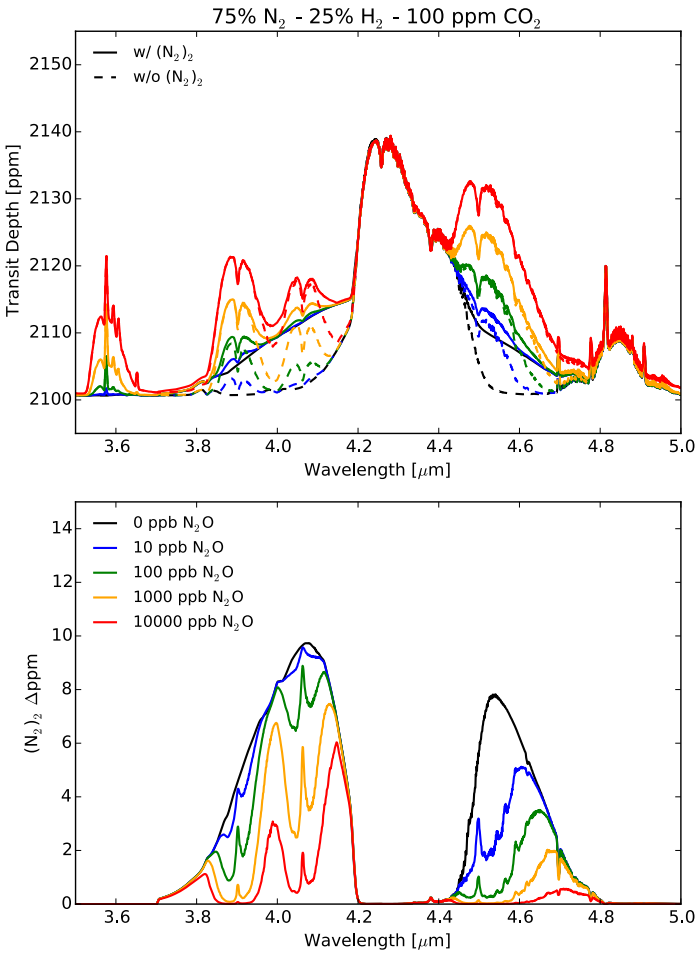

Figure 4.11. Sensitivity of $(N_2)_2$ absorption to different N_2O abundances in transit transmission spectra. The atmosphere assumed is 75% N_2 and 25% H_2 with 100 ppm of CO_2 and 0 ppb (black), 10 ppb (blue), 100 ppb (green), 1000 ppb (orange), and 10000 ppb (red) of N_2O (see Section 4). The spectral resolution is $\Delta\lambda$ = 0.005 μm. Top panels show the transmission spectra with $(N_2)_2$ (solid) or without $(N_2)_2$ (dashed) absorption. Bottom panels show differences in transmission depths due to $(N_2)_2$ matched to spectra in the top panel. The 0 ppb N_2O case is identical to the 100 ppm CO_2 case in the lower middle

4.6 DISCUSSION

4.6.1 *Detecting bulk gases to establish habitability*

Here I have shown that the absolute flux differences at the relevant wavelengths for $(N_2)_2$ absorption are significant (~30-35%) for Earth-analog cases, potentially allowing for the detection of N_2 in exoplanet atmospheres. Characterizing the bulk atmosphere of a terrestrial exoplanet will allow for the determination of the atmospheric mass, and therefore the surface pressure if the surface gravity is known. Liquid water stability, the common definition of habitability, depends on both temperature and pressure. To establish habitability, it is not necessary to quantify the pressure exactly, but to constrain it to be above the stability criterion for water within a known temperature range for the planet. I have demonstrated that $(N_2)_2$ would not create a measurable effect at the low surface pressures that preclude surface water stability for habitable temperatures.

4.6.2 *Biosignature confirmation with $(N_2)_2$*

Detection of $(N_2)_2$ could also help discriminate whether the presence of O_2 is more or less likely to be due to life. It has been postulated that the abiotic buildup of O_2 could occur on planets with a limited abundance of non-condensable gases (Wordsworth & Pierrehumbert 2014) that would allow the atmosphere of those planets to become H_2O-dominated. For each possible surface temperature a minimum non-condensable gas partial pressure is required to generate a cold trap and stabilize an atmosphere against rapid H loss through H_2O photolysis in the stratosphere and consequent O_2 buildup. An N_2 surface pressure of above a few percent of modern day Earth's is required to prevent the upper atmosphere of a planet with $T_{surf} = 288$ K from becoming rich in H_2O (Wordsworth & Pierrehumbert 2014). I find that the effect of $(N_2)_2$ on the spectral flux does

not become significant (exceeding 5%) in emission spectra unless the surface pressure is greater than 0.5 bar. Therefore, direct detection of $(N_2)_2$ would imply a non-condensable gas partial pressure larger than that required to rule out this abiotic O_2 scenario and bolster the case that detected O_2 is biological in origin. While H loss due the lack of a cold trap is not the only possible source of abiotic O_2 in a terrestrial planet atmosphere (e.g., Domagal-Goldman et al. 2014; Luger & Barnes 2015), it is the only mechanism that has thus far been proposed that could operate at all locations of the habitable zone for all spectral classes of host star.

4.6.3 *Detecting $(N_2)_2$ in transit transmission*

I have demonstrated that $(N_2)_2$ absorption can create spectral transmission depths of about 50 ppm for N_2-H_2 atmospheres without CO_2 and 10 ppm for N_2 atmospheres without CO_2. The detection of $(N_2)_2$ in the transit transmission spectrum of an N_2-doimated atmosphere would require an atmosphere to be predominately cloud-free down to a ~0.5 bar pressure level. The requirement to probe deep altitudes is potentially problematic because long path lengths through an atmosphere in transit transmission mean that even tenuous clouds or hazes can be optically thick at high altitudes (Fortney 2005). The flat transmission spectra of GJ 1214b (Kreidberg et al. 2014) and GJ 436b (Knutson et al. 2014) demonstrate that high-altitude clouds might be commonplace in close-in exoplanets. However, NIR transmission spectrum of the "warm Neptune" HAT-P-11 from WFC3 on *Hubble* demonstrates the presence of water vapor and indicates the planet's atmosphere is cloud-free at least down to the 1 mbar level and perhaps to levels where pressure are larger than 1 bar (Fraine et al. 2014). Thus, at least some planetary atmospheres may be characterizable at the pressure altitudes where N_2 collisional absorption would become detectable.

4.7 SUMMARY

I have shown that $(N_2)_2$ is detectable in disk-integrated observations of the Earth from interplanetary spacecraft, creating a ~35% effect on the spectrum of the Earth at 4.15 μm. This significant because N_2 has often been presumed to be a spectrally inactive molecule with no potentially detectable absorption features, though detecting $(N_2)_2$ will still be difficult due to the low planetary flux at its spectrally active wavelengths. I calculated the strength of the $(N_2)_2$ collisional pair on the emission spectra of self-consistent N_2-H_2O-CO_2 atmospheres and find a strong spectral response for N_2 abundances greater than 0.5 bar. A detectable amount of N_2 would imply surface pressures high enough to support liquid water and rule out the production of abiotic O_2 due to the lack of a cold trap in rarefied atmospheres with small amounts of non-condensable gases. I find that $(N_2)_2$ absorption could produce transmission depths of 8-10 ppm at 4.1 μm in the spectra of planets orbiting in the habitable zones of late type stars with N_2-dominated atmospheres and transit depths several factors larger, up to 50 ppm, for N_2-H_2 atmospheres with larger scale heights. I demonstrated that for both direct imaging and transit transmission spectroscopy, $(N_2)_2$ could significantly widen the width of the 4.3 μm CO_2 band in thick N_2 atmospheres. The detection of N_2 would provide critical contextual information about planetary atmospheres and may be relevant to future exoplanet observing missions.

Chapter 5. IDENTIFYING OXYGEN "FALSE POSITIVES" FOR LIFE

Atmospheric oxygen is the most commonly referenced target biosignature gas for future observations of potentially habitable exoplanets. However, multiple mechanisms that may abiotically produce molecular oxygen (O_2), or its photochemical byproduct ozone (O_3), have been described in the literature. Understanding the contexts in which these "false positives for life" may occur, and how we may uniquely identify abiotic and biotic origins of oxygen, is crucial for the search for life beyond the solar system. In this chapter I investigate the ways mechanisms for abiotic O_2 or O_3 generation may modify the planetary environment in potentially identifiable ways. I describe specific spectroscopically observable discriminants for abiotic O_2/O_3 in a planetary atmosphere: CO and O_4. I present explicit, self-consistent simulations of these spectral discriminants as they may be seen by the *James Webb Space Telescope* (JWST). *JWST* is set to launch in 2018 and is our first chance to probe the atmospheres of potentially habitable planets. I find that if the *JWST* NIRISS and/or NIRSpec instruments observe CO (2.35, 4.6 μm) in conjunction with CO_2 (1.6, 2.0, 4.3 μm) in the transmission spectrum of a terrestrial planet it could indicate robust CO_2 photolysis and suggest that a future detection of O_2 or O_3 might not be biogenic. I show that these features are much more easily detectable in transmission than reflected light observations, and that to detect CO in reflected light, wavelength coverage to 2.5 μm would likely be required. I further find that strong O_4 bands seen in transmission at 1.06 and 1.27 μm could be diagnostic of a post-runaway O_2-dominated atmosphere from massive H-escape. I find that for these "false positive" scenarios, CO at 2.35 μm, CO_2 at 2.0 and 4.3 μm, and O_4 at 1.06 and 1.27 μm would be stronger features in transmission than O_2/O_3 and could be detected with SNRs $\gtrsim$ 3 for an Earth-size planet orbiting a nearby M dwarf star with as few as 10 transits, assuming photon-limited noise. I propose that

detection of strong O_4 bands in UV/VIS/NIR reflected light (at 0.345, 0.36, 0.38, 0.445, 0.475, 0.53, 0.57, 0.63, 1.06, and 1.27 μm) by next generation direct-imaging telescopes would indicate an oxygen atmosphere too massive to be biologically produced. I explore the strength of the UV/VIS/NIR O_4 bands in transmission and reflected light over a grid of total O_2 pressures. Portions of this chapter were originally published in collaboration with V.S. Meadows, S.D. Domagal-Goldman, D. Deming, G.A. Arney, C.E. Harman, A. Misra, and R. Barnes in the March 2016 edition of the *Astrophysical Journal Letters* (Schwieterman et al., 2016, ApJ, Vol. 819, L13; © 2016 American Astronomical Society), and are reproduced below with permission of the American Astronomical Society. Additionally, results and analysis, but not copyrighted figures or text, are described from Harman, C.E., Schwieterman, E.W., Schottelkotte, J.C., Kasting, J.F. ApJ, Vol. 812, 137; © 2015 American Astronomical Society).

5.1 INTRODUCTION

Several planetary mechanisms that may allow for the abiotic accumulation of oxygen in terrestrial planet atmospheres have been identified and are reviewed in Section 1.2. Two of the most potentially confounding mechanisms are 1) the buildup of abiotic O_2 from photolysis reactions in H poor atmospheres (Domagal-Goldman et al. 2014; Gao et al. 2015; Harman et al. 2015; Tian et al. 2014), which is highly dependent on the UV spectrum of the host star, and 2) the accumulation of oxygen left behind by massive H escape during a runaway greenhouse, which can occur early in the history of planets in the habitable zones of late type stars (Luger & Barnes 2015; Tian 2015). Because oxygen remains a valuable target biosignature gas, it is important to consider how future observers may discriminate against these processes.

Possible discriminants for false positive mechanisms have previously been discussed in the literature. For instance, identifying the byproducts of CO_2 photolysis, such as

CO, using direct imaging was discussed in recent papers that described this false positive mechanism (Domagal-Goldman et al. 2014; Harman et al. 2015). N_2-depleted atmospheres without a cold trap (mechanism (3)) may be identified via the absence of pressure-sensitive N_2-N_2 CIA features (Schwieterman et al. 2015b; also see Chapter 4). However, previous studies have not quantified the potential spectral signal from these indicators, addressed identification of CO_2 photolysis with transmission spectroscopy, or addressed identification of the O_2-dominated atmospheres that result from massive H-escape.

This is significant because the production of CO from CO_2 photolysis is much more potentially observable in transmission spectroscopy than in reflected light observations. This is partly because CO absorbs strongly at long wavelengths where the reflected light signal will be weak (2.35 and 4.6 μm) and partly due to the increased effective path through the atmosphere for transmission observations, allowing gases with weaker intrinsic absorption coefficients, but distributed high in the atmosphere, to have a significant impact.

The potentially very high O_2 pressures for planets with significant oxygen buildup from massive H-loss could constitute a separate and discernible regime from biologically produced O_2 in atmospheres of living worlds. This is because the atmospheric O_2 abundance on Earth has been limited by negative environmental feedbacks to $\lesssim 0.3$ bar (in Earth's ~1 bar atmosphere) due to the chemical instability of higher O_2 abundances with organic matter (Kump 2008).

In the following sections of this chapter, I examine the detectability, in simulated *JWST* transmission spectra, of CO from CO_2 photolysis as an indicator for abiotically generated O_2/O_3 for terrestrial HZ planets. I also examine the detectability of highly pressure-dependent O_2-O_2 (O_4) collisionally induced absorption (CIA) features in transmission and reflectance spectroscopy. These features would be indicators of massive, post-runaway, abiotic

O_2 atmospheres. This examination builds on earlier work by (Misra et al. 2014) that analyzed the capacity of the NIR (1.06 and 1.27 μm) O_4 bands to determine pressure in O_2-rich atmospheres, which were presumed to be photosynthetically generated (that work did not include the UV/VIS O_4 bands). In Section 5.2, I describe the additional model modifications for this work, including the addition of O_2-O_2 (O_4) absorption coefficients in SMART (Chapter 2), and the JWST noise model. In Section 5.3, I show how abiotic O_2/O_3 generation from the photolysis of CO_2 may be spectrally identified in transmission and reflected light. In Section 5.4, I present transmission and reflected light spectra of high-O_2 atmospheres ($pO_2 \geq 1$ bar), and show how O_4 can be used to identify these atmospheres. I discuss some implications of these results in Section 5.5 and summarize my findings in Section 5.6.

5.2 Additional Models and Model Modifications

5.2.1 *Addition of O_2-O_2 (O_4) absorption*

All spectra in this chapter have been calculating using SMART (Crisp 1997; Meadows & Crisp 1996; Misra et al. 2014b; see Chapter 2). I have included O_4 absorption (O_2-O_2 CIA) in all modeled spectra, although O_4 only produces a strong spectral impact in the cases with O_2-dominated atmospheres. Weak O_4 bands are present in Earth's disk-averaged spectrum (Tinetti et al. 2006; Turnbull et al. 2006) and are observable through Earth's atmosphere from ground-based observations of the Moon and scattered sunlight (Wagner et al. 2002). O_4 absorption has been found to be only very weakly temperature-dependent, suggesting that O_2-O_2 CIA dominates over true van der Waals molecule absorption (Thalman & Volkamer 2013). The CIA absorption from O_4 varies quadratically with density, and the absorption coefficients can be given as:

$$\alpha(\lambda, T, d_{O2}) = B_{O2-O2}(\lambda, T) d_{O2}^2 \sim \ B_{O2-O2}(\lambda) d_{O2}^2 \qquad (5.1)$$

where α is the absorption coefficient, d_{O2} is the density of O_2 molecules, and $B_{O2\text{-}O2}$ is a density-normalized CIA coefficient. We use the density-normalized O_4 coefficients from C. Hermans[1] for the 0.333-0.666 μm spectral range (Hermans et al. 1999), and the values from Greenblatt et al. (1990) and Maté et al. (1999) for the 1.06 and 1.27 μm features, respectively. Figure 5.1 shows the combined O_4 binary absorption coefficients for the 0.3-1.4 μm (UV/VIS/NIR) spectral range.

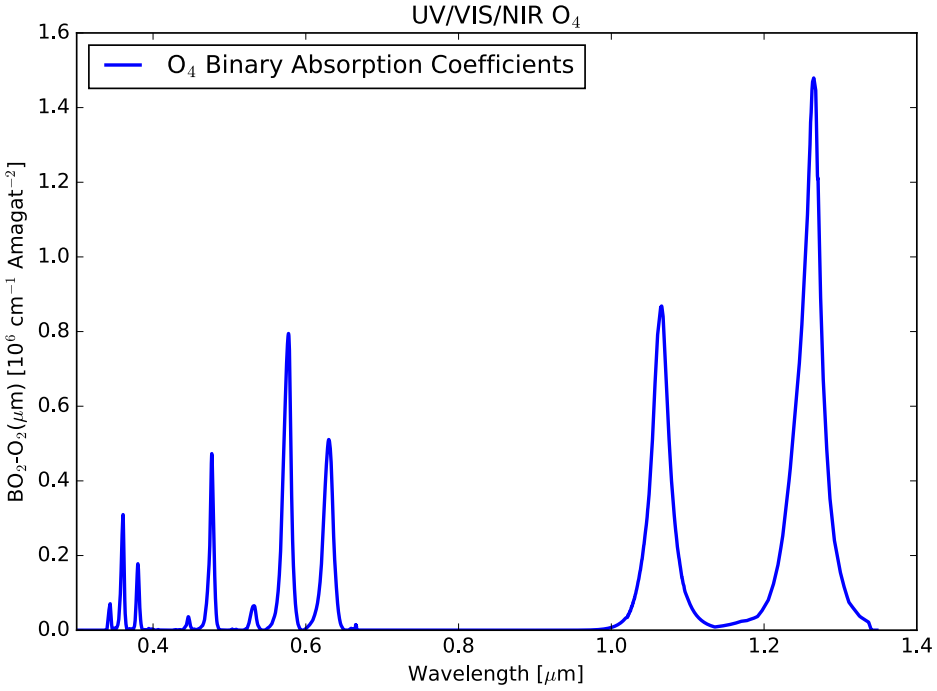

Figure 5.1. Collisional absorption coefficients for O_4 (O_2-O_2 CIA) in the UV to NIR (0.3 – 1.4 μm) spectral range. These coefficients are relevant for the high-O_2 atmosphere transmission and reflection spectra show below.

[1] http://spectrolab.aeronomie.be/o2.htm

5.2.2 *JWST NIRISS & NIRSpec noise model*

We calculated the synthetic *JWST* observations as described by Deming et al. (2009) with some updates. The total throughput of the Near-InfraRed Imager and Slitless Spectrograph[2] (NIRISS; Doyon et al. 2014) and the Near InfraRed Spectrograph[3] (NIRSpec; Ferruit et al. 2014)) instruments, including the telescope, were taken from Albert (2015, private communication) and from http://www.cosmos.esa.int/web/jwst/nirspec-pce, respectively. Thermal and zodiacal background were included as described by Deming et al. (2009), but the background only becomes significant longward of approximately 4 μm. There is very little overhead for NIRISS transit spectroscopy (Albert 2015, private communication), so an observing efficiency of unity was adopted for NIRISS. For NIRSpec, the observing efficiency was calculated assuming a 2048 × 32 subarray (Tumlinson 2010), and adopted a number of groups in an integration (ngrp) of 4 from Karakla et al. (2010). For both instruments, the observations are close to saturation, but we assume that saturation can be avoided by slightly dithering or scanning the telescope perpendicular to dispersion. For these simulations, photon-limited noise is adopted, dropping the hypothetical instrument systematic noise used by Deming et al. (2009). Recent HST experience has demonstrated close to photon-limited performance for bright stars (Kreidberg et al. 2014). The star is represented in the noise simulator using a Phoenix model atmosphere (Allard & Hauschildt 1995). For all of the transmission noise calculations presented in this chapter, 65-hour integrations with photon-limited noise are assumed.

[2] http://www.stsci.edu/jwst/instruments/niriss
[3] http://www.stsci.edu/jwst/instruments/nirspec

5.3 IDENTIFYING ABIOTIC O_2/O_3 FROM PHOTOLYSIS OF CO_2

The first set of "O_2 false positive" atmosphere scenarios I consider are habitable, but lifeless, planets with N_2-CO_2-H_2O clear sky atmospheres, orbiting in the habitable zone of their host stars and susceptible to the abiotic accumulation of O_2 and CO through CO_2 photolysis:

$$CO_2 + h\nu\ (\lambda < 175\ \text{nm}) \rightarrow CO + O \quad (5.2)$$

where hν represents photons of sufficient energy to dissociate CO_2. Photochemically liberated O will lead to the formation of both O_2 and O_3 through the Chapman scheme, reviewed in Domagal-Goldman et al. (2014), and provided below.

$O_2 + h\nu\ (\lambda < 240\ \text{nm}) \rightarrow O + O$
$O + O_2 + M \rightarrow O_3 + M$
$O_3 + h\nu\ (\lambda < 340\ \text{nm}) \rightarrow O_2 + O$
$O + O_3 \rightarrow O_2 + O_2$

Harman et al. (2015) considered abiotic O_2/O_3 buildup on habitable, but uninhabited Earth-like (e.g., $R_p=R_\oplus$; $M_p=M_\oplus$) planets orbiting F, G, K, and M stars (see Table 5.1 for stellar parameters) using a 1D photochemical model (with mostly the same heritage as that described in Section 2.5). The focus of that work was quantifying the amount of O_2/O_3 generated assuming a prebiotic Earth-like atmosphere. My focus here is to explore the spectral detectability of the O_2/O_3 "biosignature impostors" and the spectral discriminators ($CO + CO_2$) that show the O_2/O_3 results from an abiotic process. In Figure 5.2, I show gas-mixing ratio and temperature profiles from Harman et al. (2015) for hypothetical planets orbiting the stars in Table 5.1. The most permissive boundary conditions for building up abiotic O_2/O_3 is assumed for all stars but "GJ 876 – low O_2". In these cases, the ocean is assumed to be saturated in O_2 and the O_2 deposition and rainout terms are set to zero. For the last, least permissive case for generating abiotic O_2

("GJ 876 – low O_2"), CO_2 and O_2 are assumed to react directly in solution, and the deposition velocities are set to be their maximum, piston-limited values. See Table 5 in Harman et al. (2015) for more details on the boundary conditions of these model atmospheres.

Table 5.1. Stellar Parameters for photochemical "false positive" atmospheres

Star	Spectral Type	T_{eff} (K)	Luminosity ($L_\odot$)	Stellar Radius ($R_\odot$)	Distance (pc)	Semi-major Axis (AU)
GJ 876	M4V	3129	0.012	0.38	4.7	0.15
AD Leonis	M3.5Ve	3390	0.023	0.39	4.9	0.21
Epsilon Eridani	K1V	5039	0.32	0.74	3.2	0.76
Sun	G2V	5780	1	1	0	1.3
Sigma Bootis	F4V	6435	3.15	1.431	15.8	2.31

The values given above are based on Table 2 in Harman et al. (2015) and references therein. The spectra of these stars used by Harman et al. (2015) and in this work originate from France et al. (2013; for GJ 876) and appropriate scaling of the stellar spectra from Segura et al. (2005; for the remaining stars).

Note that the O_2 and O_3 mixing ratios are the highest for M stars GJ 876 and AD Leonis and lowest for the Sun. That abiotic O_2/O_3 would be generated most efficiently through photolysis on planets orbiting late type (K and M) stars is shown consistently between different model studies (Domagal-Goldman et al. 2014; Harman et al. 2015; Tian et al. 2014).

5.3.1 *Transmission spectroscopy*

I use the SMART transmission model (Chapter 2; Misra et al 2014b) to show that O_3 could potentially be detectable for a range of these photolytic abiotic O_2/O_3 atmospheres. Figure 5.3 shows the effective transit height in the UV through visible (0.15 – 1.0 μm) for each atmosphere described in Table 5.1 and Figure 5.2. The resolution for this figure is $\Delta\lambda = 0.001$ μm.

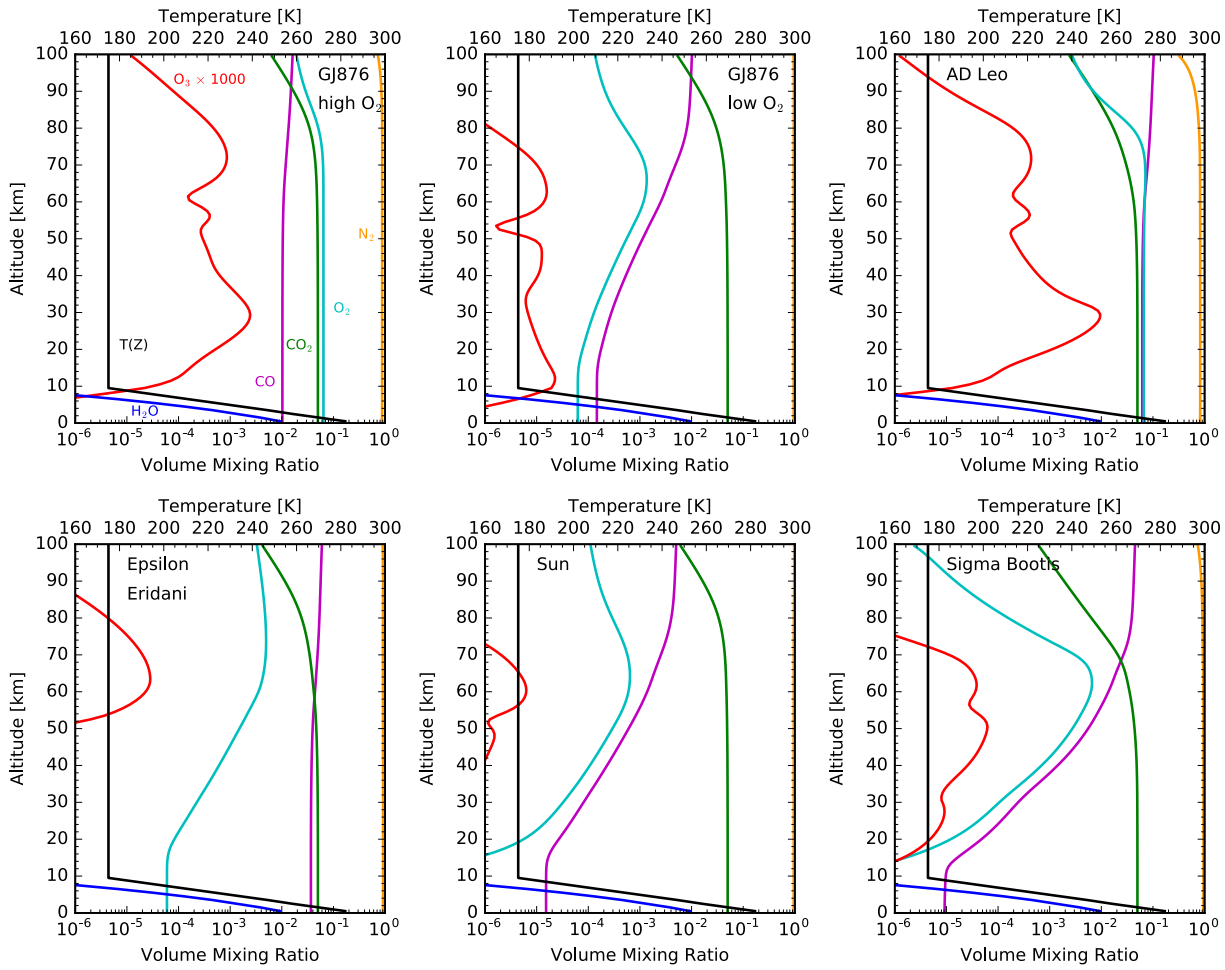

Figure 5.2. Gas mixing ratio and temperature profiles for the abiotic photochemical O_2/O_3 "false positives" examined in this section. These gas mixing ratios were calculated in Harman et al. (2015) with stellar and planetary parameters given in Table 5.1.

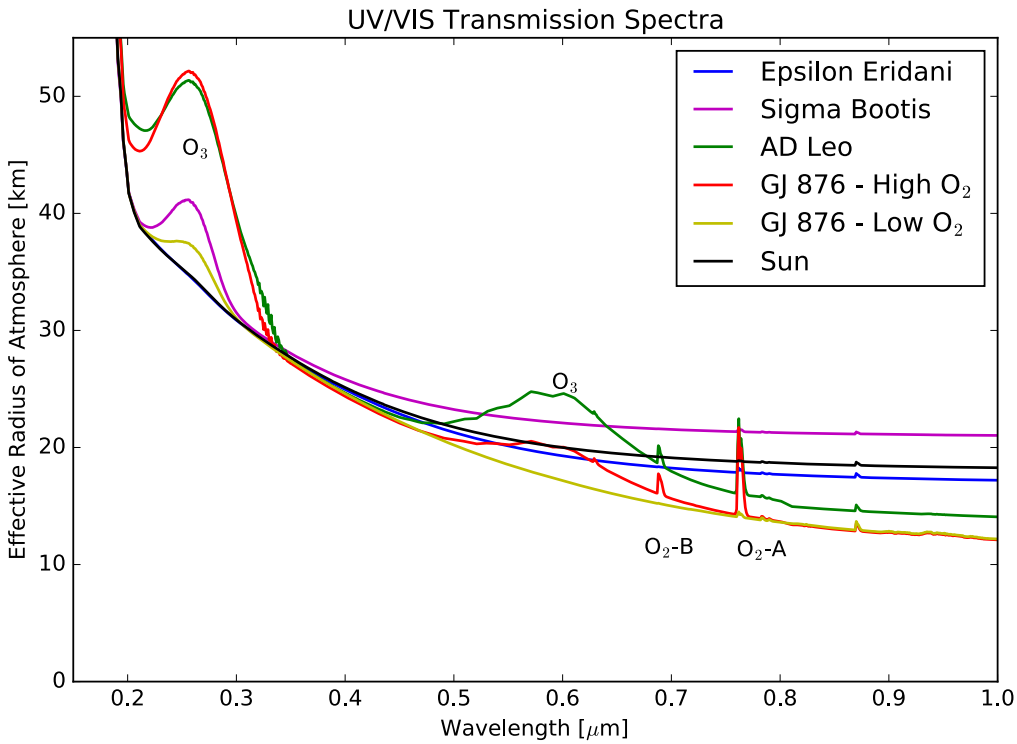

Figure 5.3. UV to visible transmission spectrum (0.15 – 1.0 μm) of each "false positive" atmosphere given in Table 5.1 and Figure 5.2. The O_3 and O_2 features are labeled. The y-axis shows the effective tangent height, to put the atmospheres on the same vertical scale.

Figure 5.3 shows that the O_3 Hartley bands (0.2-0.3 μm) are significant for GJ 876 (M4V), AD Leo (M3.5), and Sigma Bootis (F4V). The Chappuis O_3 bands (0.5 – 0.7 μm) are significant for AD Leo and the high-O_2 GJ 876 scenario. The significance of these O_3 bands would be problematic for some proposed targeted observing missions that would search nearby, potentially habitable terrestrial exoplanets for UV O_3 absorption, such as the Occulting Ozone Observatory (O3) concept (Pravdo et al. 2010; Savransky et al. 2010; Domagal-Goldman et al. 2014). Current modeling shows that a search for only UV O_3 absorption as an indicator of photosynthetic life would be susceptible to being fooled by photochemical false positives. However, *JWST,* potentially our first chance to characterize the transmission spectrum of a habitable zone world, will only have spectral sensitivity longward of 0.6 μm, and it is likely that

near to intermediate future transit transmission observations would have access to the NIR wavelength range. Figure 5.4 shows a simulated transmission spectrum in the NIR (1.0 – 5.0 μm), within the spectral range of the *JWST* NIRISS/NIRSpec instruments (Deming et al. 2009). Access to the NIR would allow the detection of both CO_2 (1.6, 2.0, and 4.3 μm) and CO (2.35 and 4.6 μm) that could indicate CO_2 photolysis was ongoing and a dynamic equilibrium with high levels of photolytic products O_2 and CO had been achieved in the atmosphere.

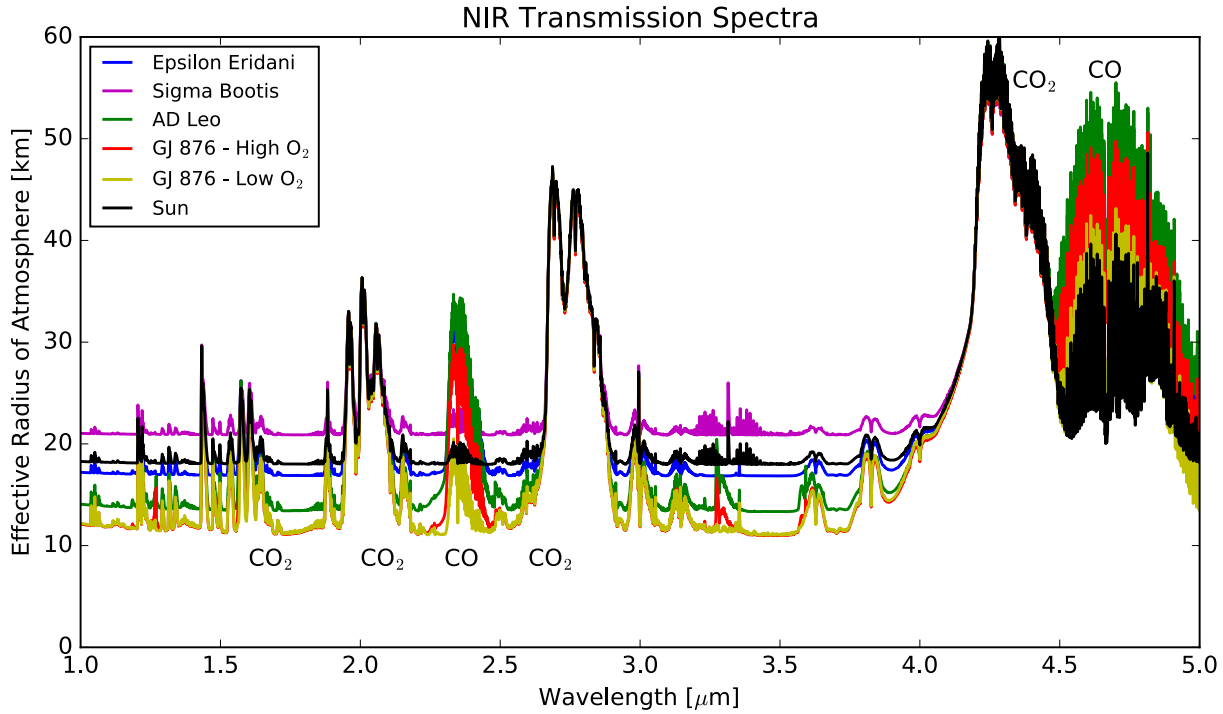

Figure 5.4. NIR transmission spectrum (1.0 – 5.0 μm) of each "false positive" atmosphere given in Table 5.1 and Figure 5.2. The CO and CO_2 features are labeled. The y-axis shows the effective tangent height, to put the atmospheres on the same vertical scale. The resolution for this figure is $\Delta\lambda$ =0.01 μm, which corresponds to a spectral resolving power of R = 300 at 3.0 μm.

Indeed, Figure 5.4 demonstrates that the CO spectral features at 2.35 and 4.6 μm becomes strongest for the GJ 876 "high-O_2", AD Leo, and Epsilon Eridani end member abiotic O_2/O_3 scenarios, while the features are weak to non-existent for the GJ 876 "low-O_2", solar, and Sigma

Bootis atmospheres. Thus there is an overall correlation of the strength of the CO and O_3 features in transmission observations, with two notable exceptions. The F star (Sigma Bootis) has a somewhat substantial O_3 UV feature (though weaker than those of the GJ 876 "high-O_2" and AD Leo cases), but no CO feature in transmission, partially due to the distribution of O_3 at high altitudes in the F star atmosphere (Harman et al. 2015). The K star (Epsilon Eridani) has substantial CO, but little O_3. Ultimately, the UV SEDs of these stars control both the rate of CO_2 photolysis, and the lifetime and therefore the steady state concentration of photochemically produced O_3.

To quantitatively examine the detectability of spectral descriminators through transmission spectroscopy with *JWST*, I input the "high-O_2" atmosphere profile for GJ 876 (Table 5.1) from Harman et al. (2015) and Figure 5.2 to the *JWST* instrument simulator described in Section 5.2.2 (Deming et al. 2009; Schwieterman et al. 2016). Note that this N_2-dominated atmosphere contains 5% CO_2, 6% O_2 and 2% CO. Ten transits and 65 hours of total integration time are assumed for the target with photon-limited noise. Figure 5.5 shows the calculated spectral transmission depths and simulated observations for this case in the *JWST* NIRISS (0.6-2.5 μm) and NIRSpec (2.9-5.0 μm) bands (left panel). The noise calculations show that the 2.0, and 4.3 μm CO_2 bands can be detected with a SNR > 3 (4.3 and 8.0, respectively) when binned across the absorption bands and compared to the continuum level. The 2.35 μm CO band has a SNR of 3.7 while the 4.6 μm CO band has an SNR of 2.6. The combined CO + CO_2 bands at 1.65 μm have an SNR of 3.1. Other absorption bands have SNRs $\lesssim$ 1. The simultaneous detection of both CO_2 and CO could indicate CO_2 photolysis in the planet's atmosphere. Note that for the integration time used here, the relatively narrow O_2-A band (0.76 μm) and weaker O_2 features would not be detectable. On the right side panel of Figure 5.5 we show a spectrum of

modern Earth orbiting GJ 876 using atmosphere profiles from Figure 1 of Schwieterman et al. (2015b) (also, Figure 2.5), but with otherwise the same geometric transit parameters as the left panel. This spectrum is provided for comparison.

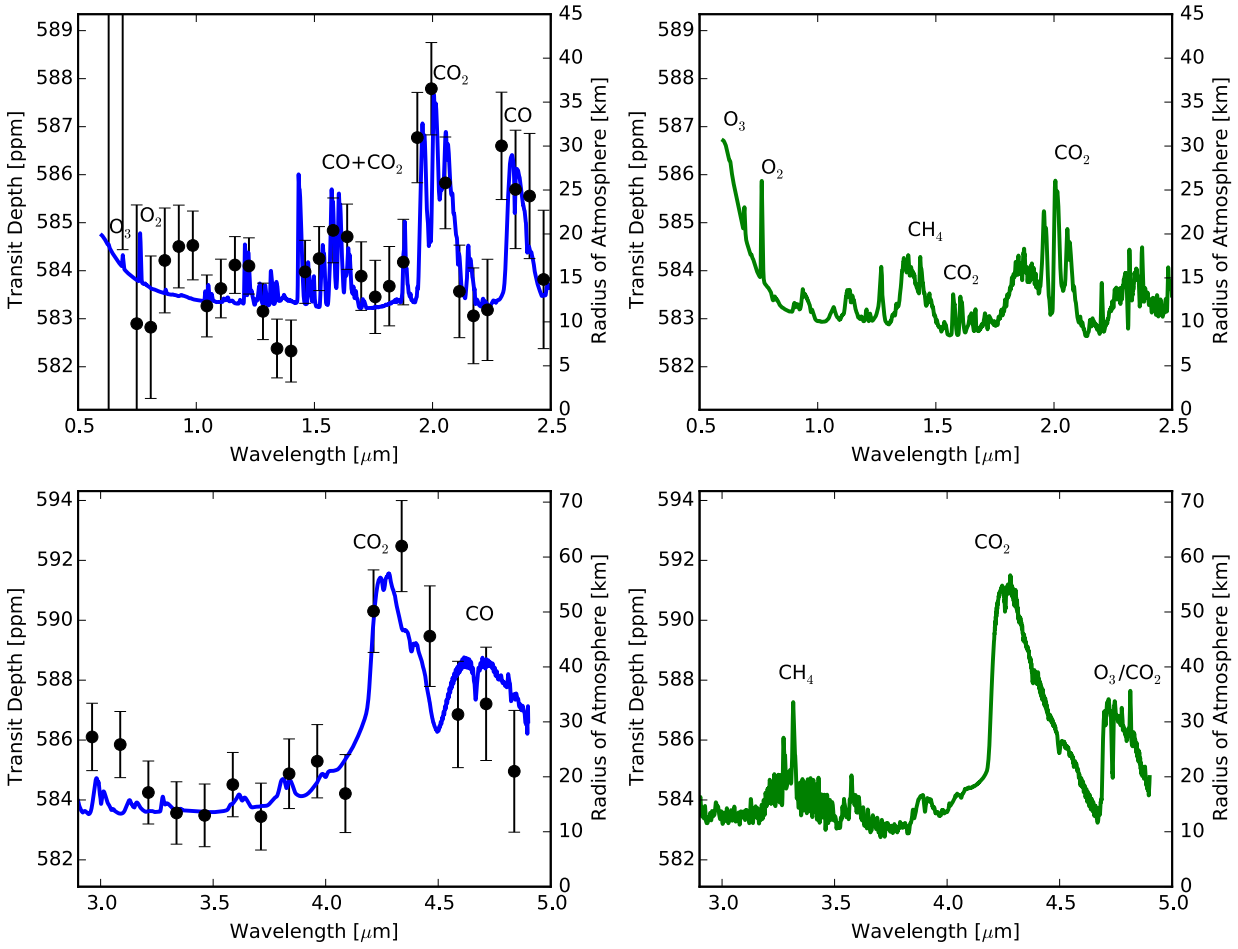

Figure 5.5. Left: Spectrum (blue) of photochemical high-O_2/CO GJ 876 atmosphere from Figure 5.2 (Harman et al. 2015) in the *JWST*-NIRISS band (top) and in the *JWST*-NIRspec band (bottom)). Data points and 1σ error bars were generated with the *JWST* instrument simulator (Section 5.2.2; Deming et al. 2009) assuming 65-hour integrations (10 transits of GJ 876) and photon-limited noise. Right: Comparable model spectrum (green) of Earth orbiting GJ 876 using atmosphere profiles taken from Figure 2.5 (also Figure 1 of Schwieterman et al. (2015b)).

5.3.2 *Direct-imaging spectroscopy*

Future space-based direct-imaging telescope concepts such as the HDST, LUVOIR (D ~ 10-12 meters) or the smaller HabEx (D ~ 4 meters) missions will have the capability to directly image terrestrial planets in the habitable zones of their stars (Stark et al. 2014; Dalcanton et al. 2015; Rauscher et al. 2015; Swain et al. 2015). It is therefore useful to investigate the strength of the "biosignature impostor" O_3 and O_2 bands and their abiotic spectral discriminants (CO + CO_2) in synthetic direct-imaging spectra. Figure 5.6 shows the UV O_3 Hartley bands (0.2 – 0.3 μm) for each of the photochemical false positives in Table 5.1 and Figure 5.2.

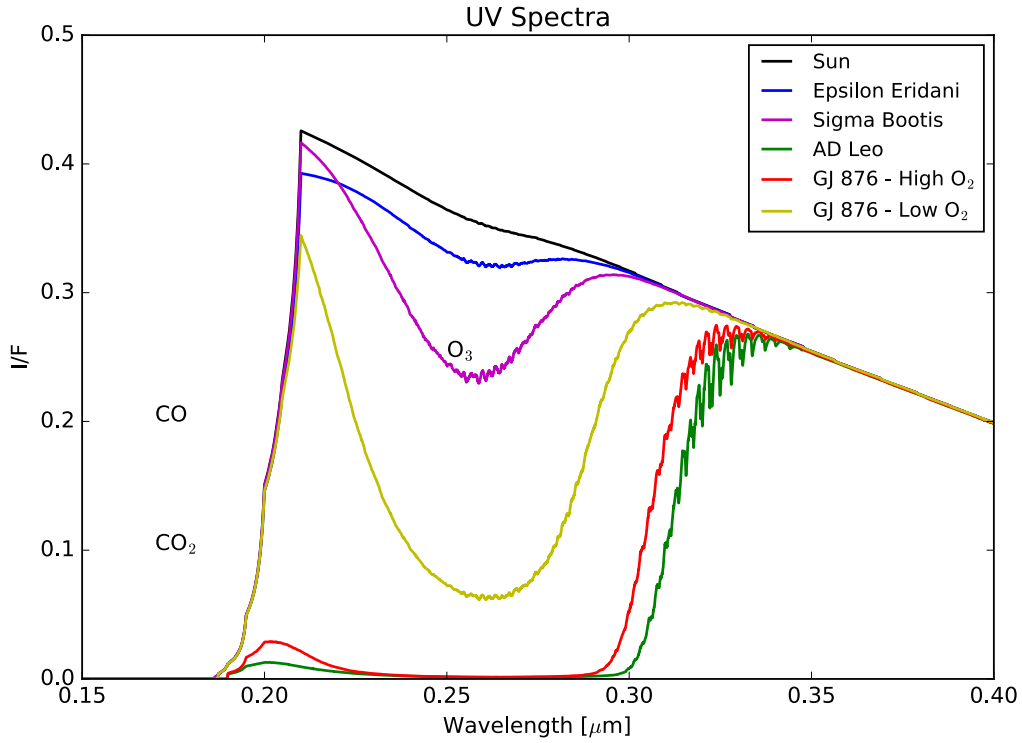

Figure 5.6. UV spectrum (0.15- 0.4 μm) of each photochemical "false positive" atmosphere given in Table 5.1 and Figure 5.2. The O_3 band absorption is apparent for all cases but the solar (G2V) case. The y-axis shows the reflected light over the incident light from the star.

Figure 5.6 shows that the O_3 UV absorption for the M-star cases are most significant, comparable in terms of reflectivity to the Hartley O_3 absorption band in Earth's atmosphere (Robinson et al. 2014). Figure 5.7 shows the same photochemical false positive atmospheres, but in the visible (0.4 – 1.0 μm) range. This figure demonstrates that only for the late M star cases would the O_2-A (0.76 μm) or O_2-B (0.69 μm) bands be potentially detectable due to the high (~6%) O_2 contents (though it should be emphasized that these cases are the worst case scenarios for abiotic O_2 buildup in the presence of a surface ocean).

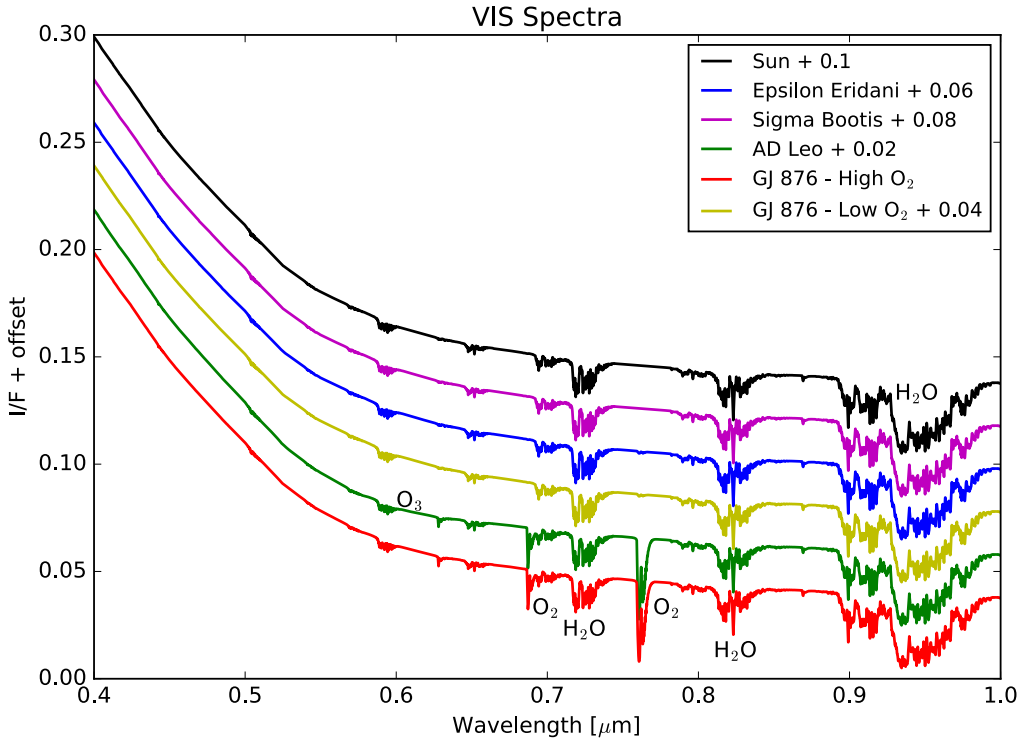

Figure 5.7. Visible spectrum (0.4 - 1.0 μm) of each photochemical "false positive" atmosphere given in Table 5.1 and Figure 5.2. The O_2-A, O_2-B, and O_3 Chappuis band absorption is apparent for the AD Leo and GJ 876 – High O_2 cases. The y-axis shows the reflected light over the incident light from the star plus an offset in reflectivity indicated in the figure legend for each spectrum. The spectral resolution is 1 cm^{-1} with a boxcar smoothing factor of 10 applied for illustration purposes.

A common wavelength range given for the Large, Ultra-Violet, Optical, and InfrarRed (LUVOIR) telescope is 0.2 – 2.0 μm, though instrument designs and wavelength coverage ranges are still in preliminary design stages (e.g., Dalcanton et al. 2015; Rauscher et al. 2015, Werner et al. 2016). However, without active cooling it is unlikely that wavelength coverage will extend beyond 2.0 μm. Therefore, the search for abiotic O_2/O_3 descriminators such as CO + CO_2 and O_4 may be limited to this wavelength range. In Figure 5.8, I show sensitivity tests for molecular absorption in the NIR (1.0 – 2.0 μm) top of atmosphere flux (in $W/m^2/\mu m^{-1}$) for the Sun, Epsilon Eridani, AD Leo, GJ 876 – low O_2, and GJ 876 – high O_2 photochemical false positive atmospheres in Figure 5.2. The sensitivity tests remove, one at a time, the spectral contributions of water (H_2O), CO_2 (magenta), CO (goldenrod), and O_2 (green), illustration the wavelength regions affected by each molecule. The only potentially detectable absorption band for CO in this wavelength range is at 1.6 μm, which overlaps substantially with the CO_2 bands near 1.6 μm. Figure 5.9 shows the same series of sensitivity tests, but further into the near-infrared (2.0 – 5.0 μm). The flux decreases sharply with increasing wavelength due to the drop off in stellar light reflected by the planet. However, these plots show a significant CO "shoulder" feature centered around 2.35 μm. To fully detect this feature, LUVOIR's maximum wavelength sensitivity would have to extend to at least 2.5 μm, and other considerations such as signal-to-noise, integration times, inner-working-angle constraints, and exo-zodiacal dust emission must also be considered (Stark et al. 2014, Robinson et al. 2015). Overall, Sections 5.3.1 and 5.3.2 together show that the CO + CO_2 abiotic O_2/O_3 spectral discriminator is much less potentially detectable in direct-imaging spectroscopy than in transmission spectroscopy for the CO abundances predicted in Harman et al. 2015.

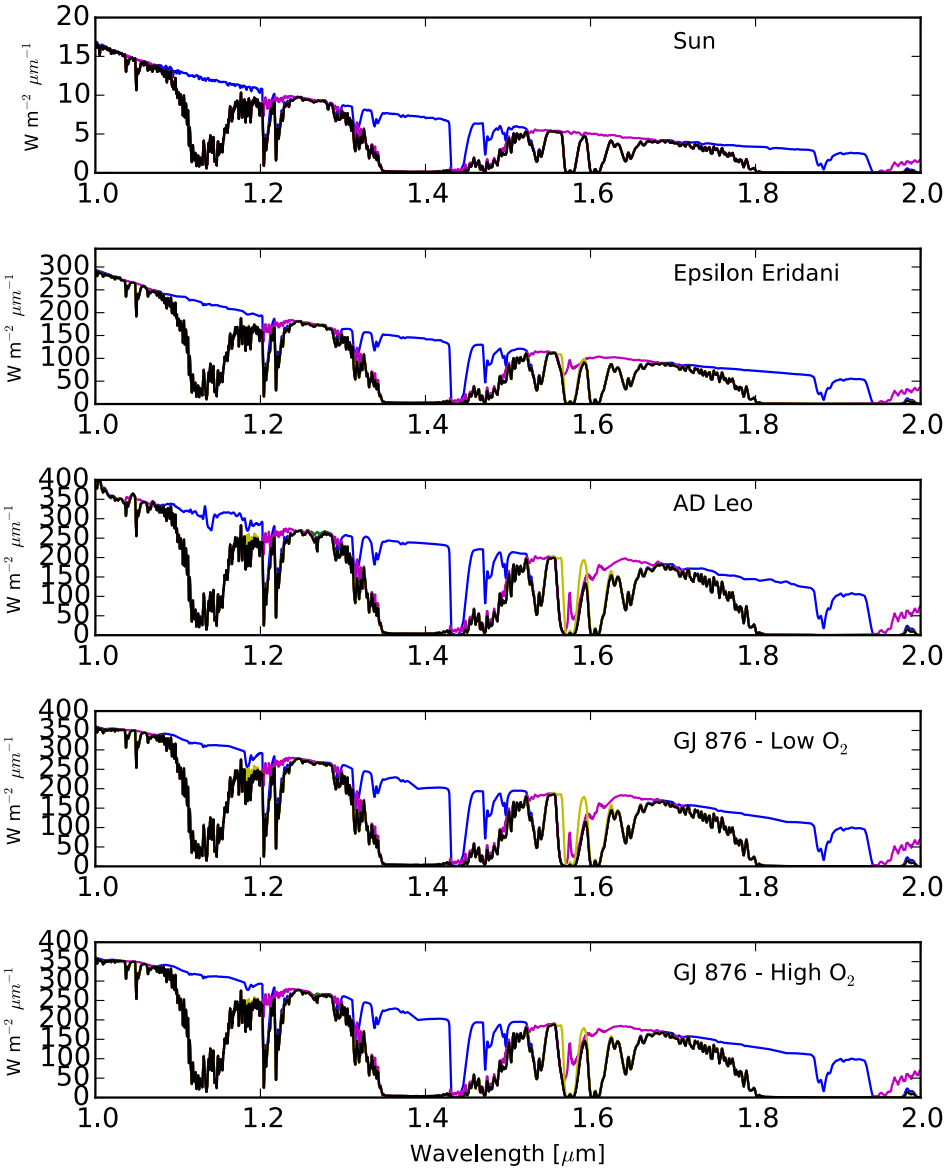

Figure 5.8. NIR spectrum (1.0 – 2.0 μm) in terms of top-of-atmosphere flux (in W/m^2/μm^{-1}) of each photochemical "false positive" atmosphere given in Table 5.1 and Figure 5.2, except for Sigma Bootis (F star), which has low abiotic O_2 and CO abundances. The sensitivity tests remove, one at a time, the spectral spectra contributions of water (blue), CO_2 (magenta), CO (goldenrod), and O_2 (green), showing the wavelength regions affected by each molecule. The spectral resolution is 1 cm^{-1} with a boxcar smoothing factor of 10 applied for illustration purposes, equivalent to a spectral resolving power of R ~ 625 at 1.6 μm.

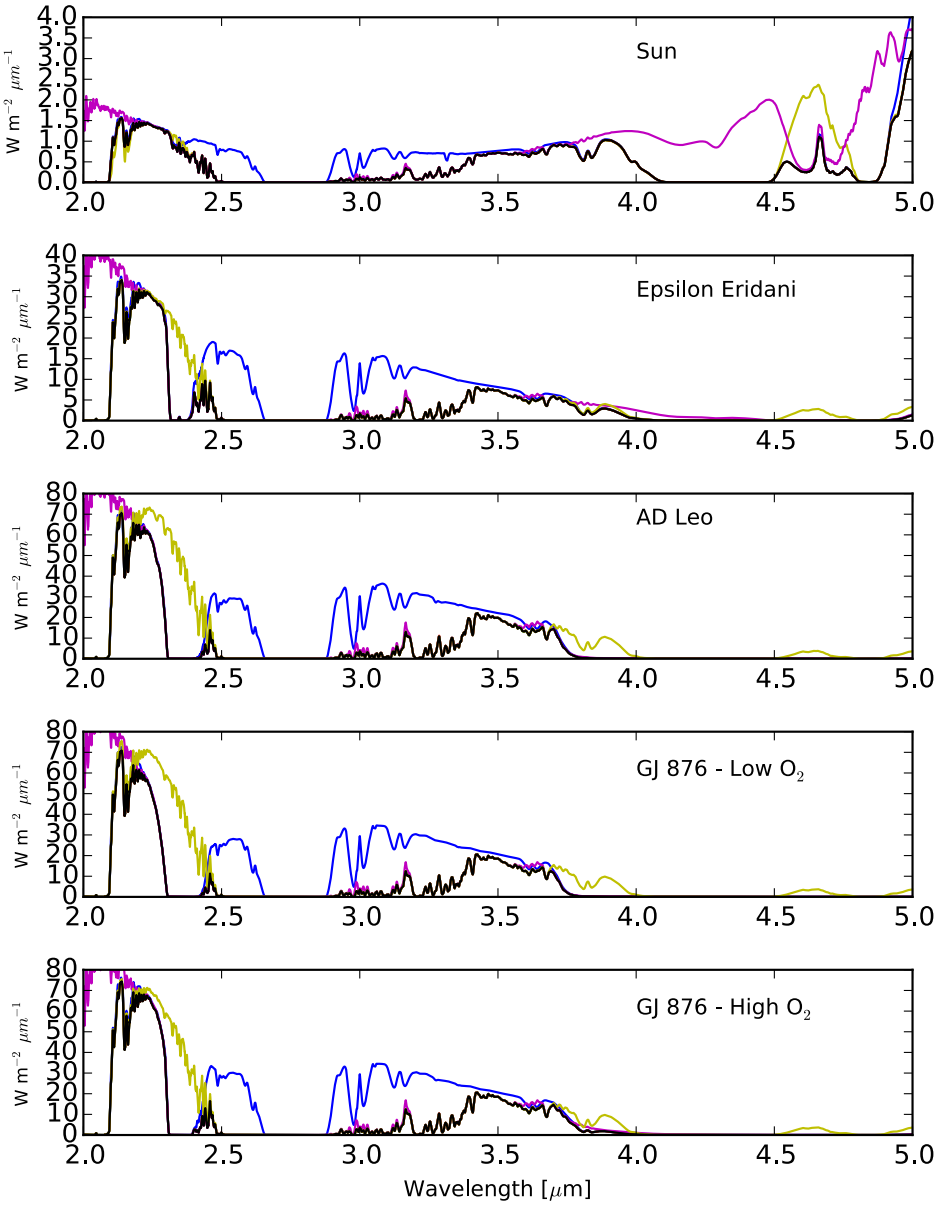

Figure 5.9. Same as Figure 5.8, but further into the NIR (2.0 – 5.0 μm). Note the decrease in reflected light compared to Figure 5.8, due to the fall off of reflected stellar light for each case, which is not counterbalanced by the increasing thermal contribution at longer wavelengths. The spectral resolution is 1 cm^{-1} with a boxcar smoothing factor of 10 applied for illustration purposes, equivalent to a spectral resolving power of R ~ 285 at 3.5 μm.

5.4 IDENTIFYING ABIOTIC O_2/O_3 FROM MASSIVE H ESCAPE

Luger & Barnes (2015) calculate that up to thousands of bars of abiotic O_2 can be generated by XUV-driven H-escape during the pre-main sequence phase of the planet's host star. This depends on a number of factors, including the starting H_2O inventory. One useful fiducial references it that losing the H from one Earth ocean leaves behind up to 240 bars of O_2, assuming none of the O is lost due to hydrodynamic escape (Chassefière 1996). Some of this O_2 would oxidize the surface; but eventually there would be a point where the oxidization of the planetary surface is complete and O_2 remains stable in the atmosphere (e.g., Chassefière 1996; Luger & Barnes 2015). Even if geological processes slowly draw down this remaining O_2, much could remain for extended time periods, limited by the rate of mantle overturn and available sinks. Since many parameters determine how much (if any) abiotic O_2 would remain behind on these planets when they are observed, here I investigate the spectral signatures and climate of O_2-dominated atmospheres in the HZ of a Sun-like and M-type star (GJ 876; Table 5.1) with a prescribed range of pressures. Since the O_2 content of Earth's atmosphere has self-limited to $P_0 \leq$ 0.3 bar (Kump 2008; Lyons et al. 2014), my focus here is on spectrally detectable signatures that an atmosphere has accumulated more O_2 than may be possible from biology, as a way to potentially identify these hypothetical atmospheres and provide future observational confidence about "true" O_2 astronomical biosignatures. In the following subsections I describe the generation of the O_2-dominated atmosphere profiles (5.4.1), the surface temperatures of these simulated planets (5.4.2), their spectral futures in simulated transmission observations (5.4.3), and simulated direct-imaging spectra (5.4.4).

5.4.1 *Oxygen-dominated atmosphere profiles*

To self-consistently calculate temperature and ozone profiles for simulated O_2-dominated, post-runaway atmospheres, I used a version of the coupled photochemical-climate mode *Atmos* (Arney et al. 2016; Chapter 2) based on photochemical and climate models originating with the Kasting group (Kasting & Donahue 1980; Segura et al. 2005, Haqq-Misra et al. 2008; Domagal-Goldman et al. 2014), which I upgraded to handle high-pressure O_2-dominated atmospheres (Chapter 2). For these scenarios I assume (a) completely desiccated planets (no H_2O) and (b) planets with an H_2O reservoir remaining even after substantial H-loss (Luger & Barnes 2015), orbiting at the inner edge of the HZ the Sun (with a = 1.0 AU; S_{eff} = 1.0 $S_{\odot}$) and a star with identical properties to GJ 876 (with a = 0.12 and 0.13 AU; and S_{eff} = 1.0 and 0.866 $S_{\odot}$, respectively). Self-consistent temperature-pressure and gas mixing ratio profiles were calculated for prescribed surface pressures (P_0) ranging from 0.2 to 100 bar, with O_2 fractions of 90-95% and with CO_2 contents of f_{CO2} = 360 ppm (similar to modern Earth), 0.1%, 0.5%, and 1%. For each combination of surface pressure, CO_2 fraction, and O_2 fraction the coupled climate-photochemical model was run to equilibrium. For the cases with an assumed surface ocean reservoir, a Manabe & Wetherald (1967) profile is assumed with a surface relative humidity of 80%. An O_2 fraction of 90% was chosen in most cases due to the instability of the 1D climate model in cases with both high O_2 (>90%) and a high surface water vapor pressure (non-desiccated cases). I calculated an identical series of desiccated cases with 90% O_2 so they would be directly comparable to the scenarios where H_2O remains. N_2 is assumed to be a filler gas and constitutes the remaining atmospheric volume after accounting for O_2, CO_2, H_2O, CO, and O_3. I show the calculated surface temperatures (climates) for all of these cases in Section 5.4.2. Figure 5.10 shows the chemical and temperature altitude profiles for the desiccated GJ 876 P_0= 0.2, 0.5,

1, 2, 10, and 100 bar atmospheres with 90% O_2 and fCO_2 = 3.6e-4. Figure 5.11 shows the chemical and temperature altitude profiles for the "wet" (H_2O reservoir remaining) GJ 876 atmospheres with otherwise the same parameters as Figure 5.10. From these series of profiles direct-imaging and transit transmission spectra are generated in Sections 5.4.3 and 5.4.4.

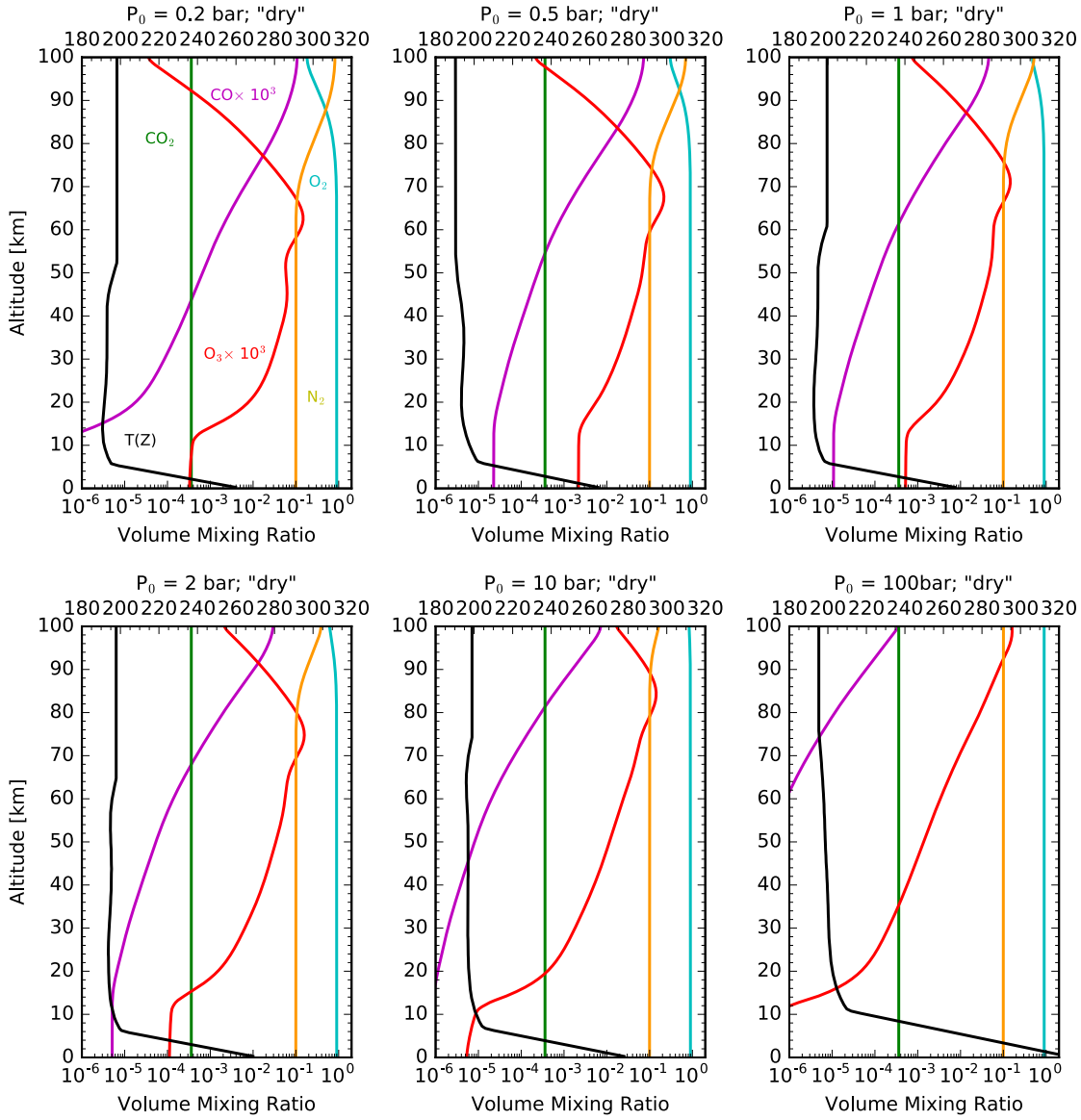

Figure 5.10. Desiccated abiotic O_2-dominated atmosphere profiles from coupled *Atmos* climate-photochemistry runs for Earth-sized planets (Luger & Barnes 2015) orbiting GJ 876 with S_{eff} = 0.866 $S_{\odot}$.

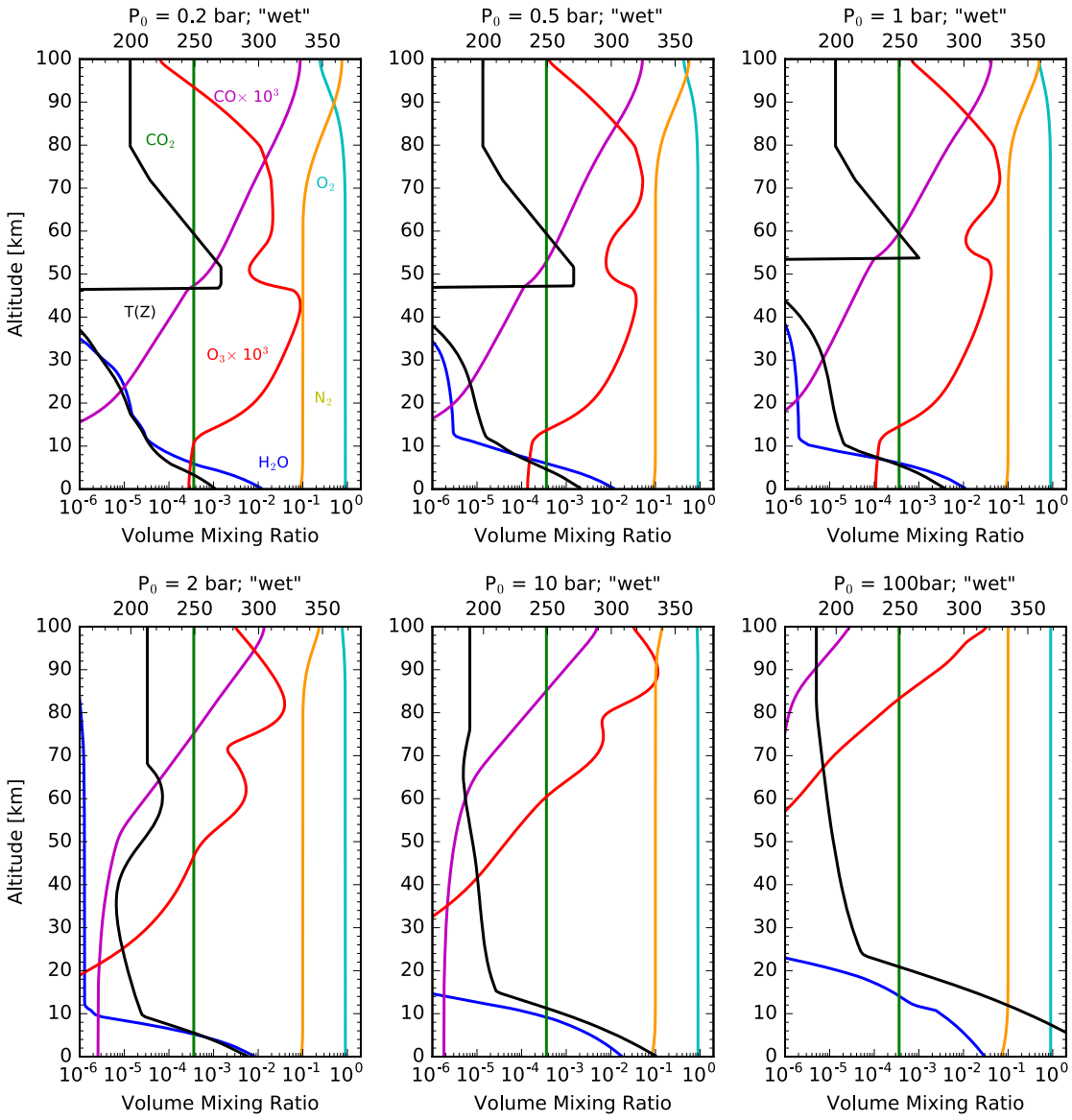

Figure 5.11. "Wet" abiotic O_2-dominated atmosphere profiles from coupled *Atmos* climate-photochemistry runs for Earth-sized planets (Luger & Barnes 2015) orbiting GJ 876 with S_{eff} = 0.866 $S_{\odot}$ with a surface ocean remaining.

5.4.2 *Climates*

Here I present the surface temperatures for the grid of hypothetical O_2-dominated planetary atmospheres described in Section 5.4.1. It is outside the scope of this work to completely

circumscribe the habitable zone for these high-O_2 planets. Rather I explored conditions near the inner edge of the traditional habitable zone (Kopparapu et al. 2013) where the conditions that lead to oxygen-rich, post-runaway atmospheres and the potential for confusion with inhabited planets are most likely (Luger & Barnes 2015). Figure 5.12 shows the surface temperatures of these hypothetical atmospheres. The tabular data are given in Table 5.2.

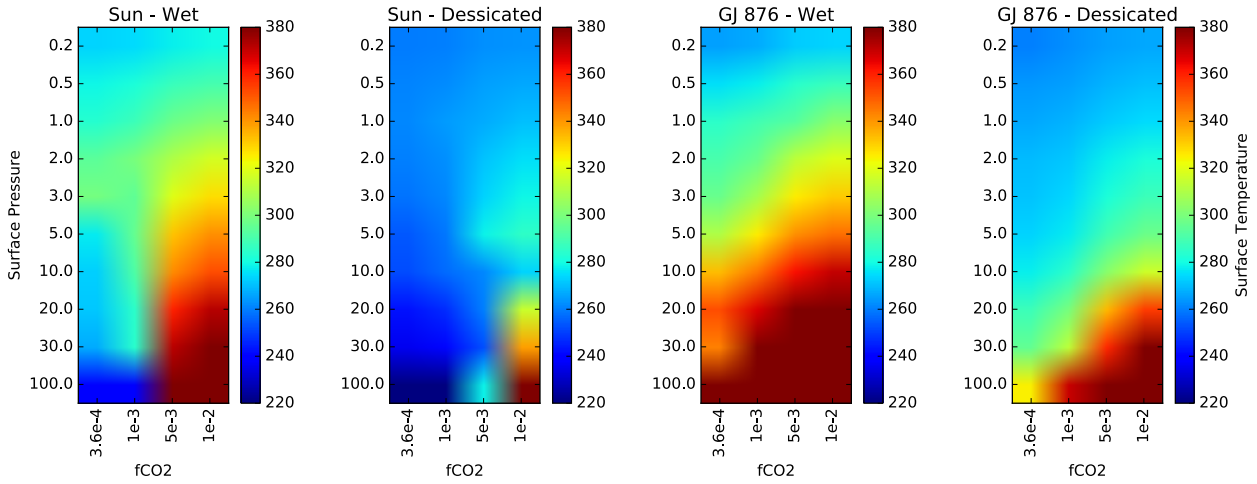

Figure 5.12. Surface temperatures from coupled *Atmos* climate-photochemistry runs for abiotic O_2-dominated Earth-sized planets (Luger & Barnes 2015) orbiting the Sun at 1 AU with a surface H_2O reservoir remaining (left) and desiccated (right); orbiting GJ 876 with S_{eff} = 0.866 $S_\odot$ with an H_2O reservoir remaining (left) and desiccated (right). See tabular data in Table 5.2.

There are two factors that drive the surface temperatures shown in Figure 5.12 and Table 5.2. Increases in total CO_2 content generally lead to more greenhouse absorption, and therefore higher temperatures. For a fixed pressure and increased CO_2, the surface temperature will always increase. Additional, since the CO_2 fraction is always fixed in the scenarios presented here, an increase in total pressure is also a commensurate increase in total CO_2 abundance, and therefore generally leads to a temperature increase. However, the increase in total pressure also increases the planetary albedo through enhanced Rayleigh scattering, which is a competing effect. While

this effect is generally small when increasing surface pressures by just fractions of a bar (Goldblatt & Zahnle 2011), it becomes significant when increasing the atmospheric mass by the equivalent of several or tens of bars. Therefore, at high pressures (i.e., large overall atmospheric masses) and low CO_2 fractions, high albedos can produce low temperatures. These competing effects lead to some interesting structure in Figure 5.12.

Despite the complexity, Figure 5.12 shows that "habitable" (273 K – 373 K) surface temperature are achievable for a range of total O_2 abundances and (sufficiently low) CO_2 fractions. The traditional view of the habitable zone assumes a carbonate-silicate weathering feedback keeps CO_2 values low near the inner edge of the HZ (Walker et al. 1981; Kasting et al. 1993). Kopparapu et al. (2013) found that while the runaway greenhouse threshold is not affected by CO_2, a CO_2 fraction ten times greater than modern Earth's would trigger a moist greenhouse, which is consistent with our results. I note here the caveat that the precondition that these atmospheres have gone through a runaway greenhouse may guarantee that substantially greater concentrations of CO_2 would be present in the atmosphere (e.g., Venus) than assumed here, at least for the desiccated cases where the lack of an ocean would deprive the planet of a weathering feedback for returning atmospheric CO_2 to the crust and mantle. However, for the cases where H_2O remains it is reasonable to assume that carbonate-silicate weathering might continue to regulate planetary climate and buffer CO_2 concentrations to these somewhat low values (Walker et al. 1981). Additionally the presence of a significant hydrological cycle from a remaining ocean reservoir would limit the lifetime of highly soluble sulfur species in the atmosphere, which would rain out (Giorgi & Chameides 1985). The likelihood of a Venus-like sulfur aerosol haze and consequent anti-greenhouse effect is therefore reduced for the non-desiccated scenarios.

Table 5.2. Surface temperatures for O_2-dominated atmospheres

Star: Sun, condition: wet; Surface Temperature [K]				
Pressure [bar]	f_{CO2} = 3.6e-4	f_{CO2} = 1.0e-3	f_{CO2} = 5.0e-3	f_{CO2} = 1.0e-2
P_0=0.2	273.2	274.9	278.0	279.7
P_0=0.5	278.9	281.6	287.0	289.7
P_0=1.0	283.4	288.0	297.1	301.3
P_0=2.0	294.0	299.7	310.5	317.4
P_0=3.0	299.0	294.9	319.6	327.6
P_0=5.0	277.0	295.8	332.2	340.8
P_0=10.0	273.1	291.3	341.7	352.0
P_0=20.0	271.6	284.7	359.4	371.9
P_0=30.0	267.2	284.2	371.3	385.5
P_0=100.0	239.5	238.2	415.0	432.3
Star: GJ 876, condition: wet; Surface Temperature [K]				
P_0=0.2	265.2	267.4	272.2	273.3
P_0=0.5	275.0	278.1	284.0	286.9
P_0=1.0	284.6	289.0	293.0	303.0
P_0=2.0	290.0	296.8	313.0	319.1
P_0=3.0	296.8	308.5	325.6	331.1
P_0=5.0	310.6	325.1	340.9	346.7
P_0=10.0	333.6	345.4	363.0	370.0
P_0=20.0	352.0	366.9	388.2	396.5
P_0=30.0	343.7	381.4	405.3	408.2
P_0=100.0	414.4	437.6	460.3	468.4
Star: GJ 876, condition: dry; Surface Temperature [K]				
P_0=0.2	260.3	262.6	265.2	266.5
P_0=0.5	263.9	265.6	268.7	270.2
P_0=1.0	266.6	268.6	272.3	274.5
P_0=2.0	269.4	271.6	277.5	281.6
P_0=3.0	271.1	273.8	281.8	287.5
P_0=5.0	273.6	277.4	289.2	297.2
P_0=10.0	277.8	284.4	303.0	315.8
P_0=20.0	287.5	299.4	334.0	355.2
P_0=30.0	295.5	312.6	358.4	386.9
P_0=100.0	324.4	369.8	447.4	473.7
Star: Sun, condition: dry; Surface Temperature [K]				
P_0=0.2	259.7	260.3	262.5	263.5
P_0=0.5	261.0	262.4	265.1	266.5
P_0=1.0	261.8	264.5	267.1	270.0
P_0=2.0	260.6	262.7	270.9	275.0
P_0=3.0	258.4	261.8	273.6	279.0
P_0=5.0	253.9	258.8	278.2	285.4
P_0=10.0	252.3	257.3	261.4	273.3
P_0=20.0	243.1	247.2	260.0	315.3
P_0=30.0	235.8	241.2	253.0	338.5
P_0=100.0	217.4	211.8	278.4	406.0

5.4.3 *Transmission spectra*

Using the SMART transit transmission model (Misra et al. 2014a,b), I have calculated the simulated transmission spectra of the high-O_2 atmospheres discussed earlier in this section. I have incorporated O_4 absorption (Section 5.4.1) and show how the strength of the O_4 features changes with increasing O_2 abundance. Transit depth is calculated assuming a star of the radius of GJ 876 (Table 5.1) at 0.13 AU and a planet of Earth radius ($R_\oplus$=6371 km) transiting with an impact parameter of b = 0. I have not calculated transmission spectra for transits of a Sun-like star, due to the low much lower transit depths for an Earth-Sun case (< 1 ppm for the strongest absorption features due mostly to the smaller relative area of the planet's disk compared to the star's). Refraction is included in these transmission spectra assuming an index of refraction at standard temperature and pressure of n=1.000272, which is consistent with an O_2-dominated atmosphere.

Figure 5.13 shows the visible to near-infrared (0.4 – 2.5 μm) transmission spectra of the desiccated O_2-dominated atmospheres (Figure 5.10) with surface pressures of 0.2, 0.5, 1, 2, 10, and 100 bars. The transmission spectra show the Chappuis O_3 bands (~0.5-0.7 μm), the narrow O_2-A (0.76 μm) and O_2-B (0.69 μm) bands, CO_2 bands centered at 1.6 and 2.0 μm, and O_4 bands at 1.06 and 1.27 μm. The UV/Visible O_4 bands (0.33-0.66 μm) do not produce significant features in transmission even for very high total O_2 abundances. Note that the 1.27 μm O_4 band overlaps with the narrower $a\ ^1\Delta_g$ O_2 band near 1.27 μm (Lafferty et al. 1998). This figure shows that the 1.06 and 1.27 μm O_4 bands are insignificant for total O_2 abundances of about 0.2 bars (i.e., Earth-like abundances), but increase with increasing surface pressure until plateauing between 2 and 10 bars. The detection of strong O_4 bands would indicate a very massive O_2 atmosphere free of aerosols at high altitudes.

The increasing transit depth of the continuum in Figure 5.13 results from refraction setting a minimum tangent height in the atmosphere (or equivalently, a maximum pressure), which will also set a limit on the transit depth due to any atmospheric absorption feature, including O_4 (Misra et al. 2014a,b). Figure 5.14 is the same as 5.13, except for the high-O_2 atmospheres with a surface ocean remaining (see Figure 5.11 for atmosphere profiles), and so contains some weak H_2O features at 1.4 and 1.8 μm.

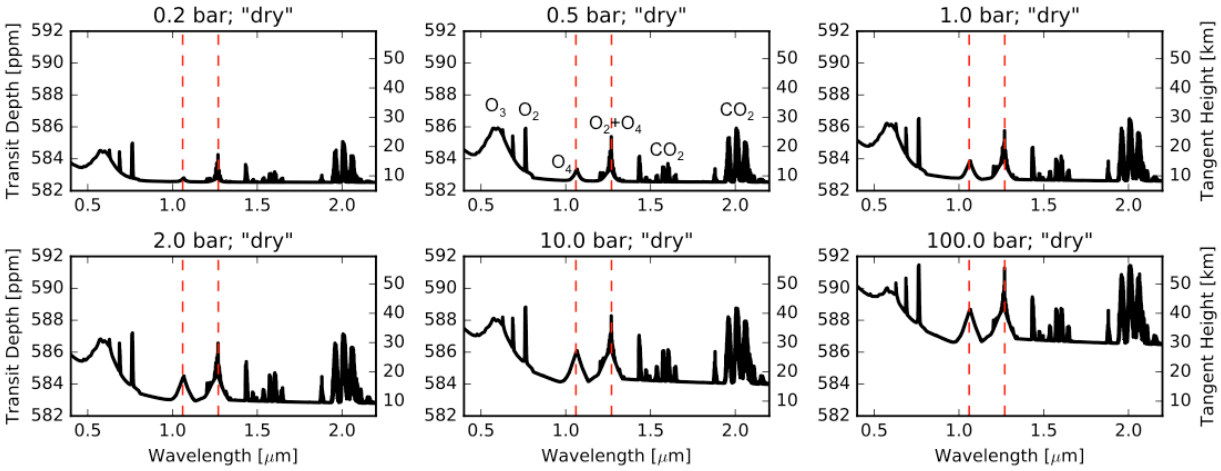

Figure 5.13. Visible to near-infrared (0.4 – 2.5 μm) transmission spectra of desiccated high-O_2 atmospheres shown in Figure 5.10. The tangent depth in pars-per-million (ppm) in indicated on the right y-axis, and the tangent height of the atmosphere on the left y-axis. The 1.06 and 1.27 μm O_4 features are indicated with a dashed vertical red line.

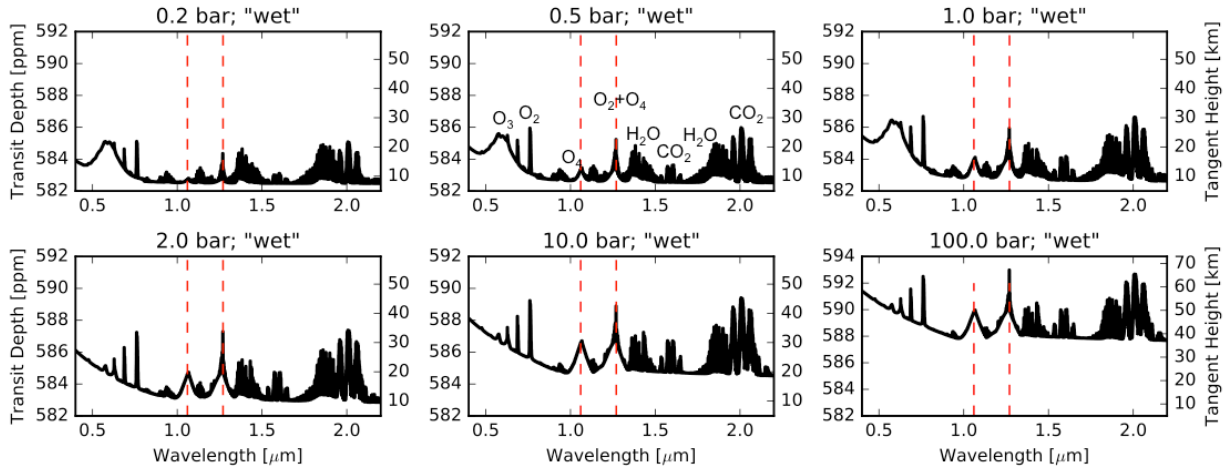

Figure 5.14. Same as Figure 5.12 but for the high-O_2 atmospheres with surface water whose profiles are shown in Figure 5.11.

We explored the detectability of these features in transit transmission observations with JWST using the instrument noise model described in Section 5.2.2 and used in Figure 5.5. Figure 5.15 shows the calculated spectral transit depths of a P_0=100 bar, desiccated high-O_2 planet orbiting GJ 876 (a = 0.12 AU) using the JWST instrument simulator described in Section 5.2.2. A total integration time of 65 hours (10 transits) is assumed, as is an impact parameter of b=0. The input atmosphere profile is similar to that in Figure 5.10, except that the O_2 concentration is 95% instead of 90%. The signal-to-noise ratios (S/Ns) of the 1.06 and 1.27 μm O_4 bands are 2.8 and 3.1, respectively. Note that the assumed instrument parameters are identical to those assumed for Figure 5.5. Therefore, assuming photon-limited noise, O_4 bands could be reasonably detectable within 3σ for a high-O_2 atmosphere transiting a late type star in the solar neighborhood.

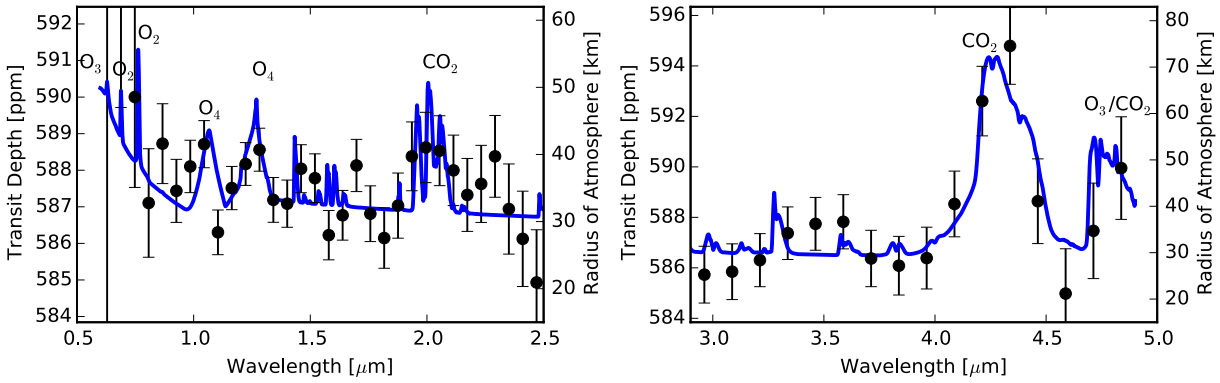

Figure 5.15. Spectra (blue) of 100 bar post-runaway 95% O_2 atmosphere in *JWST*-NIRISS band (left) and in the *JWST*-NIRSpec band (right). Data points and 1σ error bars were generated with the *JWST* instrument simulator (Deming et al. 2009) assuming 65 hr integrations (10 transits of GJ 876) and photon-limited noise. See right (top and bottom) panels of Figure 5.5 for a comparable Earth spectrum.

5.4.4 *Direct-imaging spectra*

In this section I show simulated reflectance (direct-imaging) spectra of O_2-dominated atmospheres (P_0=1, 10, and 100 bar) seen at quadrature (solar zenith angle of 60°) using SMART (Chapter 2; Meadows & Crisp 1996). I use the chemical profiles shown in Section 5.4.1. A gray surface albedo of A_B = 0.15 is assumed. Figure 5.16 shows the spectra for the desiccated, high-O_2 atmospheres orbiting GJ 876 from Figure 5.10 with P_0=1, 10, and 100 bar. For comparison I include the spectrum of an Earth atmosphere (Schwieterman et al. 2015b; Chapter 2). The O_4 bands at 0.345, 0.36, 0.38, 0.445, 0.475, 0.53, 0.57, 0.63, 1.06, and 1.27 μm (see Figure 5.1) are labeled, with the NIR bands saturating at the highest O_2 abundance. Figure 5.17 is the same as 5.16 except using the atmosphere profiles from Figure 5.11 that include a surface ocean reservoir and water vapor in the atmosphere. The presence of water vapor effects the altitude-dependent concentration of O_3 through photochemistry, especially the destruction of ozone by hydroxyl

(OH-) ions that are the product of the photolysis of water. Figure 5.18 shows the same information contained in Figure 5.16 and 5.17, but includes sensitivity spectra that show the contribution of each gas (O_2/O_4, O_3, and H_2O) the overall spectrum.

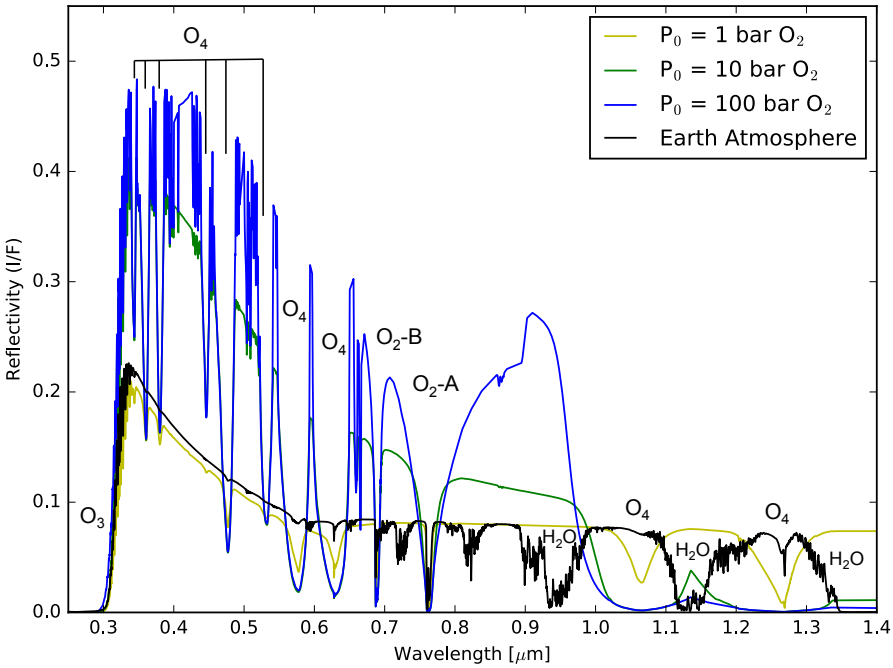

Figure 5.16. Synthetic reflectance spectra of desiccated P_0=1, 10, and 100 bar high-O_2 atmospheres from Figure 5.10 (yellow, green, and blue, respectively) with O_2 and O_4 bands identified. A comparable Earth spectrum is shown in black.

These simple tests cases demonstrate that if the high-O_2 atmospheres proposed by Luger & Barnes (2015) exist, the O_4 absorption band strength in those planetary spectra would rival or exceed that of the monomer O_2 bands. These spectra are qualitatively different than modern-Earth's spectrum, even in the 0.3-1.0 μm range, with a different shape, broader O_2 features, and additional features from O_4. These are all signs of a much higher O_2 abundance than the Earth's atmosphere – environmentally controlled by negative feedbacks - has ever achieved.

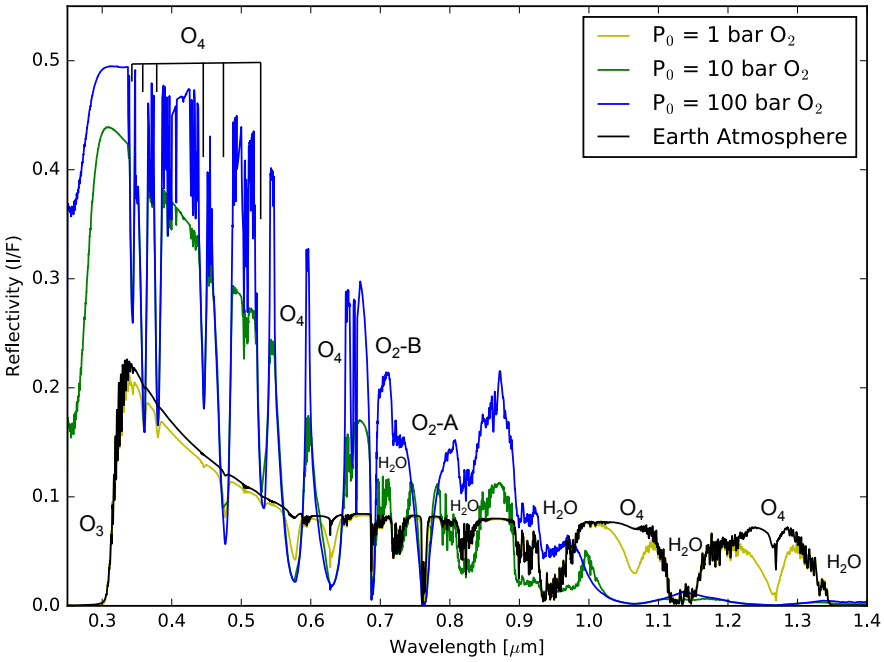

Figure 5.17. Same as Figure 5.17 but for high-O_2 atmospheres from Figure 5.11 with a surface ocean. Note the H_2O absorption in the high-O_2 atmosphere spectra for these cases.

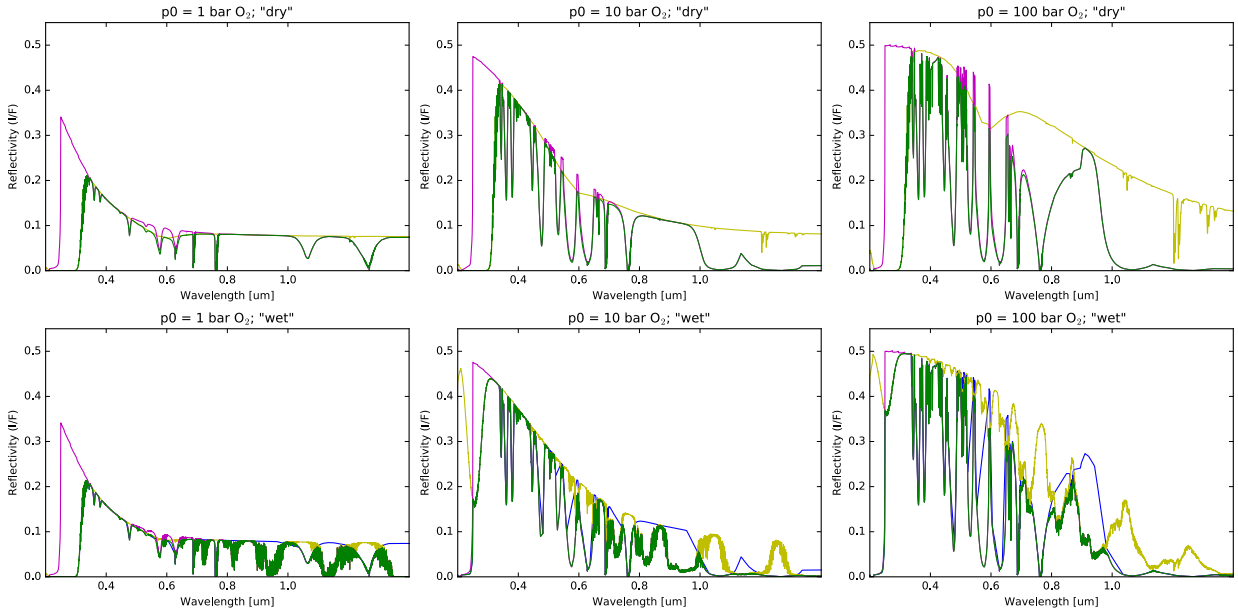

Figure 5.18. Sensitivity spectra. P_0=1, 10 and 100 bar high-O_2 (90%) atmosphere spectra for desiccated (top) and cases with a surface ocean remaining (bottom). Shown are the full composite spectra (green), spectra with O_3 removed (magenta), spectra with O_2 and O_4 removed (yellow), and with H_2O removed (blue).

I use a coronagraph noise model (Robinson et al. 2015b; Robison 2016 private communication) to quantitatively demonstrate the potential detectability of the visible O_4 bands in an observation of a planet with a large O_2-dominated atmosphere orbiting a nearby late type star. For this test case, I assume the planet is orbiting at the inner edge of the habitable zone of Lalande 21185 (a = 0.149 AU), an M2V star with an effective temperature of T_{eff} = 3,828 K that is 2.5 pc distant from Earth (Cenarro et al. 2007). I assume a telescope diameter (D) of 12 m, an inner working angle (IWA) of 3 λ/D, an outer working angle (OWA) of 30 λ/D, no active cooling (T_{system} = 300 K), one exozodi, and a spectral resolving power of R = 70. These parameters are consistent with current design proposals for HDST/LUVOIR (Dalcanton et al. 2015; Rauscher et al. 2015). Figure 5.19 shows the simulated data and noise for a ten-hour integration on a planet with a 10 bar, desiccated, post-runaway O_2 atmosphere (see Figure 5.10 and Figure 5.16) orbiting Lalande 21185.

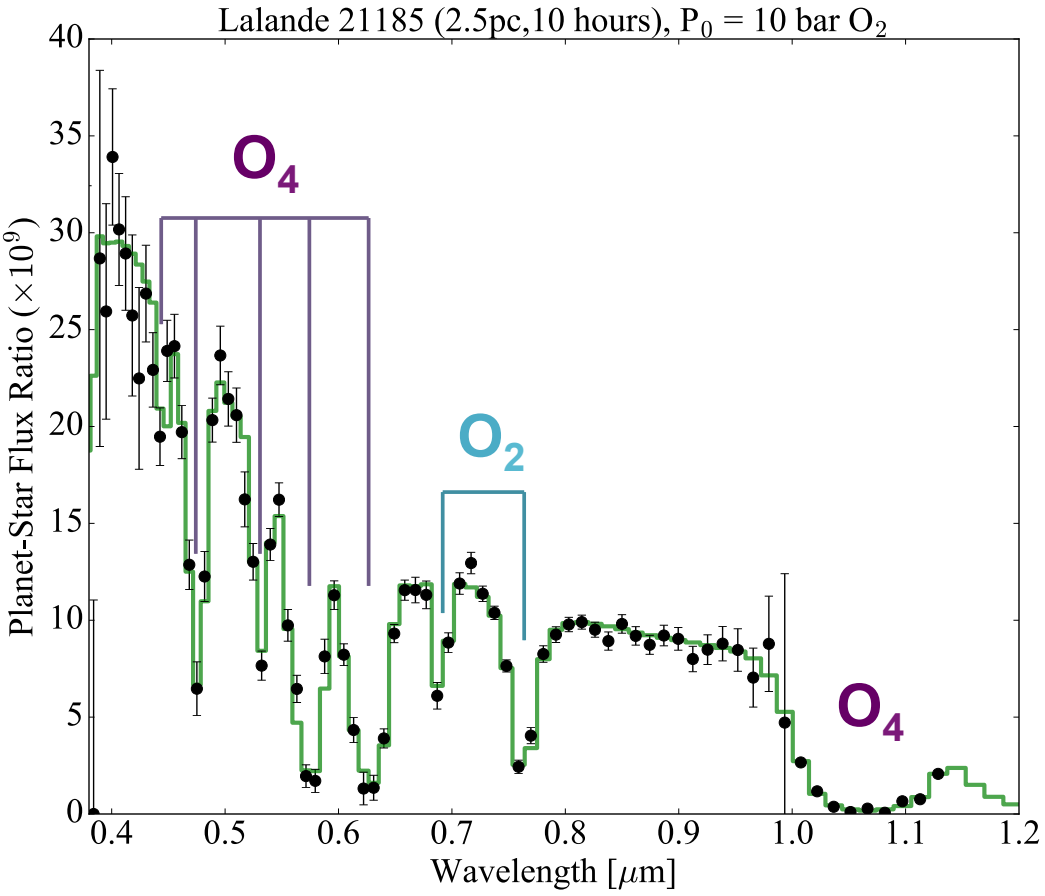

Figure 5.19. Simulated spectrum and noise of a desiccated 10 bar, high-O_2 atmosphere orbiting the nearby M2V star Lalande 21185 at the inner edge of the HZ (d = 2.5pc, a = 0.149 AU). The y-axis indicates the planet/star flux ratio in reflected light. Labels indicate O_4 and O_2 bands.

The O_4 and O_2 bands in Figure 5.19 would be detectable with signal-to-noise ratios of substantially greater than 5σ with a ten-hour integration. It is important to note that the IWA and OWA, together with the distance to the star and the position of the planet relative to the star, set the maximum and minimum wavelength cutoff, respectively. The maximum wavelength in Figure 5.19 is ~1.1 μm, thereby excluding a large portion of the NIR spectrum. Observations of other target planet-star combinations will have access to different portions of the spectrum than

those presented here, though, in general, planets orbiting most nearby M stars will be limited to wavelength cutoffs of < 1 μm due to inner working angle (IWA) constraints (assuming a telescope-coronagraph configuration; a starshade occulter (e.g., Cash 2006) could potentially remove the IWA constraint).

5.5 DISCUSSION

The first potentially habitable terrestrial planet atmospheres to be characterized via transmission spectroscopy by *JWST* or large ground-based observatories will likely be orbiting near the inner edge of the HZ of late type stars (Deming et al. 2009; Sullivan et al. 2015). This is due to the detection biases of planet transit searches and the shorter orbital periods of HZ planets around late type stars, allowing greater potential to integrate over multiple transits for characterization. Unfortunately, according to current modeling studies (e.g., Harman et al. 2015; Luger & Barnes 2015) these planets are the worlds in which "biosignature impostors"- abiotic O_2 and O_3 - are most likely. Furthermore, this potential for false positives for life is even greater for the extended inner habitable zone for dry planets (Abe et al. 2011), which have an even greater probability of being characterized earliest. The development of observing strategies to mitigate the potential for false positive biosignature detection is thus relevant now, when the missions that will have the capability to detect astronomical biosignatures are in their early design phases. I have demonstrated here that the detection of significant CO and CO_2 could indicate robust CO_2 photolysis, which can produce abiotic O_2/O_3 through photochemistry. I have also shown that strong O_4 bands would be potentially detectable for a massive O_2 atmosphere, and indicative of an oxygen atmosphere too massive to be biological. Thus CO_2/CO and O_4 are potentially powerful spectral discriminators against abiotic O_2/O_3 in future potentially habitable exoplanet observations.

In the cases presented here, the spectral discriminators against abiotic O_2/O_3 are more detectable with a hypothetical *JWST* transit transmission observation than the O_2 or O_3 signatures themselves. In the presented *JWST* example transmission spectra, neither O_2 nor O_3 would be directly detectable with just 10 transits (65 hours of integration), but the abiotic discriminators CO/CO_2 and O_4 could be. This provides an opportunity to maximize the utility of observing time if the ultimate goal is to characterize planets where true biosignatures are obtainable. If spectral indicators for biosignature impostors are detected with reasonable confidence, the community may wish to reallocate the remaining time to other promising targets, rather than integrate further. Additionally, it may also be the case that O_2 or O_3 may be identified in the same targets via other observing strategies at a concurrent or future date. For example, it has been proposed that O_2 may be found via ground-based Extremely Large Telescope (ELT) observations of the 0.76 μm O_2-A (Snellen et al. 2013). Observations by space-based telescopes such as *JWST* or a future LUVOIR telescope operating in transit mode on a favorable target could detect or rule out these indicators before significant observing time is expended by ELTs on promising targets. If an ELT observation of a potentially habitable planet is conducted, these potential spectral discriminators could be characterized in addition to the target band (e.g., the O_2-A band).

It is important to note that the strength of an absorption band in transmission, unlike in reflected light, is not dependent on the mixing ratio of the gas at the surface or the absolute column abundance of the gas. Rather, the strength is mostly dependent on the altitude at which the gas produces an optical depth near unity, and thus the distribution of the gas in the atmosphere is extremely important. Direct imaging of CO_2 and CO spectral signatures on an Earth twin is potentially problematic because they are weak and narrow shortward of 2.0 μm, they overlap with other strong absorption bands, and the reflected/emitted planetary flux at the

wavelengths where the absorption is relatively strongest (e.g., the 4.3 μm CO_2 band) is low (Robinson et al. 2014; Schwieterman et al. 2015b). The work presented here shows these CO and CO_2 bands are much stronger in transmission spectroscopy. Thus transmission spectroscopy is complementary to potential future direct-imaging characterization missions, and in particular for characterizing potential biosignature impostors. Transmission spectroscopy is also more sensitive to Earth-like CH_4 abundances than direct-imaging. Detection of CH_4 with O_2/O_3 would help confirm a true biosignature, as modeling predicts extremely low CH_4 abundances in cases of abiotic O_2/O_3 generation (Domagal-Goldman et al. 2014).

Next-generation space-based direct-imaging telescope concepts such as ATLAST/LUVOIR, HDST, and HabEx would be able to directly image planets in the HZ (Rauscher et al. 2015; Dalcanton et al. 2015; Swain et al. 2015), and thus potentially characterize biosignature gases in exoplanet atmospheres. Detection of strong O_4 bands in UV/VIS/NIR reflected light would indicate a large O_2 atmosphere originating from massive H-escape. While planets in the conservative HZ of G and F type stars would be high priority for these missions and are less susceptible to an extended history of runaway H-loss and O_2-buildup, planets orbiting between the optimistic (recent Venus) and conservative (runaway greenhouse) inner edge of the HZ, potentially brighter targets for direct imaging, would also be susceptible to this process (Luger & Barnes 2015). Additionally, many nearby M and K type stars will likely be characterized by LUVOIR/HDST (Stark et al. 2014, Dalcanton et al. 2015; Seager et al. 2015), where the entire HZ could potentially be contaminated by "biosignature impostors" from massive H-escape and consequent O_2 build up (Luger & Barnes 2015). Using a coronagraph model, I have shown here that if this the case, the O_4 bands that indicate these atmospheres have

too much O_2 to have resulted from biology would be detectable with LUVOIR with high signal-to-noise ratios (S/N > 5σ) and reasonable integration times (~hours for the nearest stars).

5.6 SUMMARY

Recently proposed mechanisms for developing abiotic O_2/O_3 in terrestrial exoplanet atmospheres would produce spectral discriminators that are potentially identifiable with future telescope observations, including *JWST*. These discriminants are more detectable than O_2 or O_3 in transmission observations. CO seen at 2.35 μm or 4.6 μm with CO_2 at 2 or 4.3 μm would indicate robust CO_2 photolysis and suggest a high likelihood of abiotic O_2/O_3 generation. I find that CO in a realistic exoplanet atmosphere orbiting a late type star could be seen with a S/N > 3 at 2.35 μm in *JWST*-NIRISS with as few as 10 transits. O_4 bands seen in transmission or direct-imaging can be diagnostic of high-O_2 post-runaway atmospheres that have experienced a history of H-escape. The 1.06 and 1.27 μm O_4 bands in a massive, O_2-dominated atmosphere without high-altitude aerosols would be potentially detectable with a S/N $\gtrsim$ 3 with as few as 10 transits with *JWST*-NIRISS, assuming photon-limited noise. LUVOIR would be able to detect visible and near-infrared O_4 bands (at 0.345, 0.36, 0.38, 0.445, 0.475, 0.53, 0.57, and 0.63 μm, 1.06, and 1.27 μm) in the spectra of high-O_2 planets orbiting in the HZ of the nearest late type stars with integration times of order ten hours or less. The detection of these strong O_4 bands would indicate an O_2 atmosphere too massive to have been biologically produced. Taken together these proposed spectral discriminants against "biosignature impostors" provide strategies that will assist us in identifying true evidence for life beyond the solar system.

Chapter 6. NONPHOTOSYNTHETIC PIGMENTS AS POTENTIAL SURFACE BIOSIGNATURES

This chapter describes a multi-faceted, interdisciplinary study of the potential of non-photosynthetic pigments to be astronomically detectable surface biosignatures. Previous studies of potential astronomical biosignatures have focused on gaseous biosignature gases such as O_2, O_3, and CH_4, or analogs to surface features of photosynthetic life on Earth, such as the vegetation "red edge". However, pigmentation has evolved for many purposes other than the collection of photons for energy to adapt organisms to their environment. The diversity of these functions leads to spectral breaks and features for non-photosynthetic pigments to occur at different visible and UV wavelengths than those for photosynthetic pigments such as chlorophyll. Here I investigate the diversity and detectability of non-photosynthetic pigments as biosignatures. First, I review the reasons why and in what cases nonphotosynthetic pigments may be important remotely biosignatures. Then I describe a lab-based study where I cultured and measured the reflectance spectrum of a collection of pigmented organisms. I then use SMART and the VPL spectral Earth model to investigate the spectral effect of non-photosynthetic pigments on the disk-averaged spectrum of a planet when including full radiative transfer through an Earth-like planetary atmosphere. I find that, given sufficient surface coverage, nonphotosynthetic pigments can, like the vegetation red edge, significantly impact the disk-averaged spectrum of a planet. I also find that broadband colors alone are not able to identify planets with significant coverage of biologically produced pigment and that spectrally resolved data would be required. Portions of this chapter were originally published open access in collaboration with C.S. Cockell and V.S. Meadows in the May 2015 edition of *Astrobiology* (Schwieterman, Cockell, & Meadows. 2015,

AsBio, Vol. 15(5), 341-361; © The authors), and are reproduced below with permission of the authors. The research contained in this chapter was conducted in part to fulfill the research rotation requirements of the University of Washington Astrobiology Dual PhD Program.

6.1 INTRODUCTION

Chapter 1 reviewed three plausible categories of planetary biosignatures: 1) gaseous biosignatures such as O_2 resulting from photosynthesis, 2) surface biosignatures such as the "vegetation red edge" (VRE), and 3) temporal biosignatures resulting from seasonal changes in biologically modulated gases or surface biosignatures. This chapter focuses specifically on surface biosignatures in (2) from nonphotosynthetic processes. In contrast, the most commonly considered biosignatures are products of photosynthesis, or are phenomena otherwise associated with photosynthetic organisms. Photosynthesis is a method of primary production (turning CO_2 to biomass) that uses photons from the Sun (or in general, a host star or stars) as a source of energy and a reductant, such as H_2, H_2S, Fe^{2+}, or H_2O, as a source of electrons (Hohmann-Marriott & Blankenship 2012). Oxygenic photosynthesis, which uses H_2O as a reductant and generates O_2 as a waste product, is by far the most productive metabolism by orders of magnitude on modern Earth (Kiang et al. 2007b). It is often reasoned that the organisms with the most productive metabolism will be the most plentiful and therefore will generate the most detectable signatures, and those signatures will be related to their primary metabolism. However, oxygenic photosynthesis may not have always dominated the detectable biosphere in the past. Geological evidence suggests that biofilms or microbial mats of anoxygenic photosynthesizers may have generated the most prevalent surface signatures of life for several hundred million years before the development of oxygenic photosynthesis. This is inferred from the gap between the earliest stromatolite fossils near 3.5 Ga (Schopf 1993; Wacey et al. 2011; Brasier et al. 2015)

and the earliest (mostly) undisputed geochemical evidence for oxygenic photosynthesis at 2.7 Ga (Buick 2008).

There are currently no known remotely detectable gaseous biosignatures strictly associated with anoxygenic photosynthesis (though this is currently being investigated; N. Parenteau, private communication), and there are also many chemosynthetic metabolisms that do not produce waste gases in chemical disequilibrium with their environments (Des Marais et al. 2002). In the absence of gaseous biosignatures, surface reflectance features would be the only possibly detectable biosignatures. Anoxygenic photosynthesizers and chemosynthetic pigment-bearing species would have generated their own surface reflectance biosignatures by reflecting more strongly at wavelengths where their pigment absorption was least efficient.

Future spaced-based telescopes may have the ability to directly image Earth-sized planets in the habitable zones of their host stars (Des Marais et al. 2002; Cockell et al. 2009; Levine et al. 2009; Postman et al. 2010; Seager et al. 2014; Stapelfeldt et al. 2014; Dalcanton et al. 2015; Rauscher et al. 2015). To support the design and operation of these next generation telescopes, it is important to better understand the possible diversity of planetary biosignatures, including surface biosignatures. Several authors have investigated the effects of photosynthetic vegetation or microbial mats on the disk-averaged spectrum of the Earth or Earth-like planets (Seager et al. 2005; Montanes-Rodriguez et al. 2006; Tinetti et al. 2006b, 2006c; Sanromá et al. 2013), and Sanromá et al. (2014) investigated the spectrum and temporally varying broadband colors of an Earth substantially covered with anoxygenic purple bacteria. Hegde & Kaltenegger (2013) explored whether broadband filter photometry can serve as a first step to characterizing the surfaces of Earth-like exoplanets, and argued that visible spectrum broadband colors could be used to identify certain environments or significant coverage by specific types of extremophiles,

lichens, or bacterial mats. However, this initial study did not consider the effects on the resulting broadband colors due to reflected radiation transmitted through the atmosphere.

I argue here that nonphotosynthetic pigments could provide alternative biosignatures to those generated by photosynthesis. In particular, this may be the case for highly productive chemosynthetic biospheres that have evolved pigmentation to cope with extreme environments, or for photosynthetic biospheres where the spectral reflectance is dominated by a non-photosynthetic pigment. In support of this argument, I detail below a range of environments on Earth where non-photosynthetic pigments dominate the spectral reflectance. While my focus is on applications to remotely detectable surface biosignatures on exoplanets, pigmented organisms may also be searched for in limited environments within our own Solar System such as in the martian subsurface or Europa's ocean (Dalton et al. 2003).

There is empirical evidence from several environments on modern Earth that even in the presence of photosynthetic primary producers, the dominant reflectance biosignature can be from biologically produced pigments that developed to provide functions other than light capture for photosynthesis. For example, halophilic archaea such as *Halobacterium salinarum* and bacteria such as *Salinbacter ruber* dominate the spectral reflectance of hypersaline lakes and saltern crystallizer ponds with their non-photosynthetic pigments (DasSarma 2006; Oren 2009; Oren 2013). The pink coloration of the northern portion of the Great Salt Lake, Utah, USA, has been visible in photographs from the International Space Station. Owens Lake, California, USA, and the saltern crystallizer ponds of San Francisco, USA, are further examples of the macroscopic coloration effect from these pigmented organisms (see Figure 6.1a, 6.1b, and 6.1c). Other environments where pigmented halophiles dominate the spectral reflectance include Lake Hillier in Australia, the Sivash in Ukraine/Russia, and Lake Retba in Senegal. These halophilic

organisms contain substantial amounts of carotenoids such as bacterioruberin resulting in red, pink, or orange coloration to water above threshold salinities. Although the photosynthetic primary producers in hypersaline environments are often green algae like *Dunaniella salinarum,* which also contain carotenoid pigments, Oren et al. (1992) and Oren & Dubinsky (1994) found that the visible coloration of hypersaline lakes is dominated by the (smaller but more abundant) halophilic archaea and bacteria. This is due to the even distribution of pigments in the archaeal cells, which provides them with more surface area per volume and allows them to effectively shade the more concentrated pigments in the *Dunaniella* cells (Oren et al. 1992).

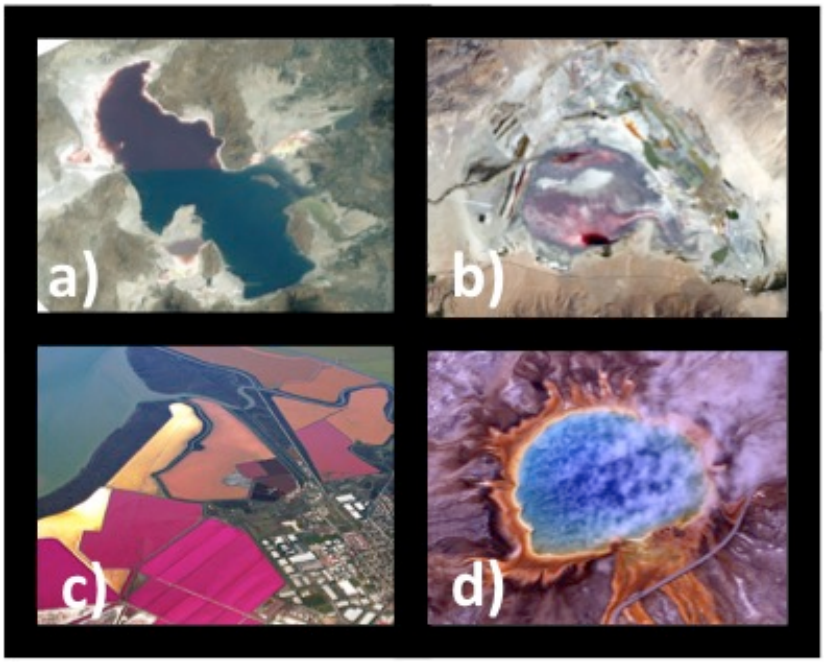

Figure 6.1. Macroscopic surfaces where carotenoid type pigments dominate the spectral reflectance. **A)** The Great Salt Lake, Utah, USA, seen from the International Space Station (credit: NASA). The Great Salt Lake is approximately 120 km long, 45 km wide and 4.9 m deep on average. **B)** Owens Lake in California, USA (credit: NASA). Owens Lake is 28 km long, 16 km wide, and 0.9 m deep on average. **C)** Salt ponds in San Francisco, California, USA (credit: dro!d, Atlanta, Georgia). **D)** The Grand Prismatic Spring in Yellowstone National Park, Wyoming, USA (credit: National Park Service). The spring is 90 m long by 80 m wide and approximately 50 m deep.

Another example where nonphotosynthetic pigments dominate the spectral reflectance comes from extremophiles (including chemotrophic thermophiles) at the edges of hot springs, where temperatures can exceed the 73 °C temperature limit for photosynthesis (Meeks & Castenholz 1971). Thermophiles such as *Thermus aquaticus* (Brock & Freeze 1969), whose pigmentation may be an adaptation to oxidative stress, generates the inner ring of yellow seen in the Grand Prismatic Spring in Yellowstone National Park, USA (Figure 6.1d). Pigmented thermophilic chemotrophs, together with carotenoid-bearing cyanobacteria, form a visible color gradient across the spring (Dartnell 2011). "Watermelon snow" is a designation given to the visible red or pink coloration of snow caused by the green algae *Chlamydomonas nivalis* (Painter et al. 2001; Williams et al. 2003). This organism thrives in high altitudes and polar regions during the summer with the aid of the red carotenoid pigment astaxanthin, which helps protect it from UV radiation and warms the cell by absorbing more incident solar radiation than the surrounding snow.

Many types of vegetation alter their spectral appearance (color) seasonally, illustrating another case where nonphotosynthetic pigments can dominate the visible reflectance spectrum. The red and orange autumn coloration of leaves is due to carotenoid pigments that are unmasked as chlorophyll degrades, while red pigmentation is due to anthocyanin, a pH-dependent pigment that is produced *de-novo* in autumn foliage, perhaps to provide photoprotection (Archetti et al. 2009).

Nonphotosynthetic pigments can serve a variety of functions, many of which help the organism adapt to stressors in the environment. These compounds can be used for photoprotection (Proteau et al. 1993, Williams et al. 2003, Solovchenko & Merzlyak 2008; Archetti et al. 2009) and as quenching agents for protection against free radicals (Saito et al.

1997). Desiccation and ionizing-radiation resistant organisms such as *Deinococcus radiodurans* and *Rubrobacter radiotolerans* contain carotenoid pigments that are thought to function primarily as anti-oxidants (Saito et al. 1994; Cox & Battista 2005; Tian et al. 2008). Some pigments serve as biocontrol mechanisms to slow growth as resources are exhausted (Venil & Lakshmanaperumalsamy 2009) or to facilitate interactions between bacterial cells in colonies or aggregates through a phenomenon known as "quorum sensing" (McClean et al. 1997; Williams et al. 2007). Such pigments are often associated with pathogenic bacteria, as invading a host exposes these organisms to extremes in terms of temperature and in many cases an immune system attack (Liu & Nizet 2009). "Siderophore" pigments are used as Fe^{3+} bonding agents in iron-limited conditions (Meyer 2000). Plants and animals use pigments in signaling to other organisms (Chittka & Raine 2006), as is the case for pigments used in flowers for attracting pollinators.

The spectral properties of many biological pigments are decoupled from the light environment to varying degrees. While some non-photosynthetic pigments are adapted to be sensitive to small portions of the electromagnetic spectrum, such as UV screening pigments, others are hosted by organisms in zero light conditions (Kimura et al. 2003). Organisms possessing non-photosynthetic pigments are not necessarily closely related genetically to photosynthetic species, and the phylogenetic diversity of pigment-producing species in general is much broader than that of photosynthetic species (Klassen 2010). Table 6.1 shows a list of functions that pigment molecules perform other than light harvesting, and provides specific examples of pigments that carry out these functions, and the organisms in which they are found. It should be noted that some carotenoids can have a light-harvesting function in anoxygenic phototrophs and cyanobacteria, but predominantly function as protectants against photo-

oxidative stress (Cogdell et al. 2000; Glaeser & Klug 2005; Ziegelhoffer & Donohue 2009). For the purposes of this chapter, I consider these carotenoids as photoprotectants and antioxidants, and thus as nonphotosynthetic pigments.

Table 6.1. The diverse functions of biological pigments

Function	Pigment Type(s)	Example Pigments	Example Organism(s)
(1) Photosynthesis	Chlorophylls, Bacteriochlorophylls	Chls a, b; Bchls a, c, g	Cyanobacteria, anoxygenic phototrophs
(2) Other light capture; other phototrophy	Some rhodopsins, some carotenoids	Xanthorhodopsin; bacteriorhodopsin	*Salinbacter ruber*; *Halobacterium salinarum*
(3) Sunscreen	cyclized β-ketoacid	Scytonemin	Cyanobacteria
(4) Antioxidant	Carotenoids	Bacterioruberin, Deinoxanthin	*Halobacterium salinarum*; *Deincoccus radiodurans*
(5) Protection against temperature extremes	Tyrosine derivative	Melanin	Cryptococcus neoformans
(6) Acquisition of nutrients such as iron	Siderophore	Pyoverdine	*Pseudomonas putida*
(7) Regulation of growth (cytotoxicity)	Prodiginine	Prodigiosin	*Serratia marcescens*
(8) Protection against competition or grazing (antimicrobial)	Indole derivative	Violacein	*Janithobacterium lividum*
(9) Signaling Other Organisms	Carotenoids, anthocyanins, betalains	Cryptoxanthin	Narcissus psuedonarcissus
(10) Bioluminescence	Luciferin	Dinoflagellate luciferase	Dinoflagellates

References: [1] (Hohmann-Marriott & Blankenship 2012; Clayton 1966), [2] (Boichenko et al. 2006; Oren 2013; Grote & O'Malley 2011), [3] (Proteau et al. 1993), [4] (Lemee et al. 1997; Saito et al. 1997; Shahmohammadi et al. 1998), [5] (Dadachova et al. 2007; Liu & Nizet 2009), [6] (Meyer 2000), [7] (Bennett & Bentley 2000; Hejazi & Falkiner 1997), [8] (Kimmel & Maier 1969; Schloss et al. 2010; Durán et al. 2007), [9] (Tanaka et al. 2008; Chittka & Raine 2006; Valadon & Mummery 1968), [10] (Haddock et al. 2010)

To expand the study of remotely detectable surface biosignatures beyond those associated with photosynthesis, this chapter explores the nature, diversity, and detectability of nonphotosynthetic pigments. This study is broken into four components. First, I measure the reflectance spectra of a diverse collection of pigmented organisms on Earth. These organisms may be considered as analogs to the possible biologically pigmented surfaces that may be present on other planets. Second, I generate synthetic spectra with SMART (see Chapter 2) that simulates ideal cases where single surface types dominate planetary surfaces and are viewed through a planetary atmosphere. I compare scenarios with nonphotosynthetic pigment surfaces to those with other dominant surface types. I include in these simulations both the spectral reflectances measured in the first, experimental portion of the study and spectral reflectances of biotic and abiotic surfaces from literature. Third, I use a comprehensive 3D spectral model of an Earth-analog planet where the oceans are dominated by pigmented halophiles at the same densities found in high salinity ponds on Earth, and include the effects of an atmosphere, clouds, and a heterogeneous surface. Finally, I examine the utility of broadband colors in identifying and characterizing a diversity of biological and abiotic surface types when full consideration of atmospheric effects is made.

6.2 LAB METHODS

Below I describe the methods and the models for both the experimental and spectral modeling components of this study.

6.2.1 *Choice of cultured organisms*

I cultured and measured the spectral characteristics of a variety of pigmented bacteria (and one archaea) that represent various colorations, metabolisms, and phylogenies. For practical reasons,

I preferentially selected fast-growing, easily culturable strains. Table 6.2 lists the species, phylum, color, primary pigment, metabolism, and environment of the selected organisms. Below I briefly describe each organism.

Table 6.2. Data for cultured organisms (section 6.2.1)

Species	Phylum	Visual	Pigment(s)	Metabolism(s)	Environment(s)
(1) Brevibacterium aurantiacum	Actinobacteria	Orange	3,3-dihydroxy-Isorenieratene or canthaxanthin	Aerobic Heterotroph	Food products, rice plots, industrial waste
(2) Chlorobium tepidum	Chlorobi	Green	Bchls a,c; Chlorobactene	Anaerobic Photolithotroph	Anoxic zones of eutrophic lakes
(3) Deinoccocus radiodurans	Deinococcus-Thermus	Red-orange	Deinoxanthin	Aerobic Heterotroph	Deserts, desiccating environments
(4) Halobacterium salinarium	Euryarchaetoa	Pink-red	Bacterioruberin; bacteriohodopsin	Aerobic photoheterotroph	Hypersaline lakes, salterns
(5)Janthinobacterium lividum	Proteobacteria	Dark-violet	Violacein	Aerobic heterotroph	Soils, tundra
(6) Micrococcus luteus	Actinobacteria	Yellow	Canthaxanthin (a β-carotene); α-carotenes	Aerobic heterotroph	Soil, air, water
(7) Phaeobacter inhibens	Proteobacteria	Brown	Unknown	Aerobic heterotroph	Sea water
(8) Rhodobacter sphaeroides	Proteobacteria	Brown-green	Bchl a, b; spheroidenone; neurosporene	Anaerobic Photoautotroph, Aerobic chemoheterotroph	Deep lakes, stagnant waters
(9)Rhodopseudomonas palustris	Proteobacteria	Red-purple	Bchl a, neurosporene	Various – photoautotrophic, photoheterotrophic, chemoheterotrophic, chemoautotrophic	Pond water, coastal sediments
(10) Rubrobacter radiotolerans	Actinobacteria	Red	Bacterioruberin, monoanydrobacterioruberin	Aerobic heterotroph	Desert soil
(11) Serratia marcescens	Proteobacteria	Red	Prodigiosin	Aerobic heterotroph	Soils, household surfaces, animal tissue

References: [1] (Gavrish et al. 2004), [2] (Wahlund et al. 1991), [3] (Cox & Battista 2005; Tian et al. 2008), [4] (DasSarma 2006; Oren 2009; Shahmohammadi et al. 1998), [5] (Kimmel & Maier 1969; Schloss et al. 2010), [6] (Ungers & Cooney 1968; Greenblatt et al. 2004), [7] (Porsby et al. 2008; Martens et al. 2006; Dogs et al. 2013), [8] (Pfennig & Truper 1971; Mackenzie et al. 2007; Wiggli et al. 1999; Glaeser & Klug 2005), [9] (Larimer et al. 2004; Bosak et al. 2007), [10] (Saito et al. 1994; Schabereiter-Gurtner et al. 2001; Chen et al. 2004), [11] (Hejazi & Falkiner 1997; Bennett & Bentley 2000; Schuerger et al. 2013; Haddix et al. 2008).

***Brevibacterium aurantiacum* –** an orange Gram-positive actinobacterium that has been isolated from food products, rice plots, and industrial waste. The production of orange carotenoid pigmentation is observed to be induced by blue (~400 nm) light (Gavrish et al. 2004; Takano et al. 2006)(Gavrish et al. 2004; Takano et al. 2006).

Chlorobium tepidum – a green sulfur Gram-negative bacterium that grows photoautotrophically or photoheterotrophically under anaerobic conditions. *C. tepidum* was isolated from an acidic (pH4.5 – 6.0) hot spring containing high concentrations of sulfide (Wahlund et al. 1991). *Chlorobium* species are often found in anoxic zones of eutrophic lakes (Prescott et al. 2005). Molecular fossils (biomarkers) indicate *Chlorobium* blooms were present in high numbers during the end-Permian mass extinction event (Cao et al. 2009).

***Deinococcus radiodurans* –** a well-known polyextremophile that stains Gram-positive (although its cell wall has Gram-negative characteristics), which can survive exposure to large amounts of ionizing radiation and desiccating conditions (Cox & Battista 2005). The primary pigment produced by *D. radiodurans* is the carotenoid deinoxanthin, which gives colonies a red-orange coloration.

Halobacterium salinarum – a Gram-negative halophilic Archaea that contains the red carotenoid pigment, bacterioruberin, and achieves photoheterotrophy with bacteriorhodopsin. Bacterioruberin has been shown to assist *H. salinarum* in resisting damage to DNA by ionizing radiation and UV light (Shahmohammadi et al. 1998). Halobacterium species are of interest to astrobiologists because they are polyextremophiles and occupy a niche populated by few other

organisms (DasSarma 2006). *H. salinarum* was chosen in his work to represent the pigmented halophiles that give hypersaline lakes and ponds their pink or red color.

***Janthinobacterium lividum* -** a Gram-negative aerobic proteobacterium commonly found in soils, freshwater, and tundra. *J. lividum* produces the dark violet pigment violacein and can aggregate in dense colonies or biofilms (Kimmel & Maier 1969; Pantanella et al. 2007; Schloss et al. 2010). The pigment violacein is involved in "quorum sensing," which can facilitate interactions between cells in a colony (McClean et al. 1997; González & Keshavan 2006; Williams et al. 2007).

***Micrococcus luteus* –** a Gram-positive, yellow-pigmented aerobic actinobacterium. The yellow pigmentation is due to the carotene derivative canthaxanthin (Ungers & Cooney 1968).

***Phaobacter inhibens* –** a Gram-negative brown-pigmented proteobacterium isolated from seawater. *P. inhibens* produces an uncharacterized brown pigment and displays antimicrobial properties (Porsby et al. 2008; Dogs et al. 2013).

***Rhodobacter sphaeroides* –** a Gram-negative purple nonsulfur anoxygenic photosynthetic proteobacterium. *R. sphaeroides* has a diverse array of metabolic pathways, growing by aerobic or anaerobic respiration, photosynthesis or fermentation (Mackenzie et al. 2007). Carotenoids produced by *R. sphaeroides* have been shown to reduce photo-oxidative stress against singlet oxygen (Glaeser & Klug 2005) and are the cause of the orange-brown coloration the organism exhibits in anaerobic cultures. The *R. sphaeroides* strain in this study was grown photoheterotrophically in anaerobic conditions.

Rhodopseudomonas palustris – a Gram-negative purple anoxygenic photosynthetic proteobacterium. Like *R. sphaeorides*, *R. palustris* is metabolically versatile, able to grow photoautotrophically, photoheterotrophically, chemoautotrophically, or chemoheterotrophically (Larimer et al. 2004). This diverse array of metabolisms allows the organisms to survive in a variety of environments. *R. plaustris* is especially interesting as it has been shown to precipitate calcite in solutions rich in calcium carbonate, serving as a model to illuminate how ancient anoxygenic photosynthetic stromatolites may have been constructed (Bosak et al. 2007). The *R. palustris* strain in this study was grown photoheterotrophically in anaerobic conditions.

Rubrobacter radiotolerans – a Gram-positive red pigmented actinobacterium that is isolated from desert soil. *R. radiotolerans* is highly radioresistant and can survive radiation doses higher than other radioresistant bacteria including *Deinococcus radiodurans* (Saito et al. 1994). *R. radiotolerans* contains bacterioruberin and other pigments typically found in halophilic bacteria (Saito et al. 1994).

Serratia marcescens – a common Gram-negative environmental proteobacterium that produces the red pigment prodigiosin (Venil & Lakshmanaperumalsamy 2009). *S. marsensas* is often found growing as a thin pink film on bathroom surfaces and has been known to cause infections (Hejazi & Falkiner 1997; Haddix et al. 2008). A related organism, *Serratia liquefaciens*, which also produces prodigiosin, has been shown to grow in an anoxic, CO_2-enriched 7 mbar (Mars-like) atmosphere at 0 °C (Schuerger et al. 2013).

6.2.2 *Growth and harvesting of cells*

Each organism in Table 6.2 was acquired from Deutsche Sammlung von Mikroorganismen und Zellkulturen (DSMZ[27]) in the form of either a live culture or a freeze-dried pellet in a vacuum-sealed glass ampoule. Standard culturing procedures were followed after assembling the recommended growth medium for each organism (see Table 6.3). All species were grown in oxic conditions with the exception of the anaerobic anoxygenic photosynthesizers *Chlorobium tepidum*, *Rhodobacter sphaeroides*, and *Rhodopseudomonas palustris*, which were grown anaerobically in light. Cells were harvested for reflectance spectra measurements in one of two ways:

1) Liquid cultures were transferred to 50 mL Falcon tubes and centrifuged for 10 minutes at 2700 × g to pelletize the intact cells. The supernatant was removed and replaced with deionized water. The tube was agitated to rinse the cells of the growth media and then centrifuged again for 10 minutes at 2700 × g to re-isolate the cells as a pellet. A sterilized small metal spatula was used to transfer the cleaned cell pellet to black filter paper in a Petri dish (black paper was chosen to minimize the scattering of light during subsequent reflectance spectra measurements).

2) Plate-spread cultures were allowed to proliferate until a substantial percentage of the plate was covered with growth. A sterilized metal spatula was then used to gently scrape the surface of the growth media until a thick paste of cells was gathered. This was transferred to filter paper in a Petri dish.

In both (1) and (2), the sample was allowed to dry for one hour to remove any film of water on the surface of the sample that could cause specular reflection. The resulting cell mass was at least

[27] https://www.**dsmz**.de/

0.5 x 0.5 cm and opaque. See Figure 6.2 for an example. Growth media and dead cell matter were removed because these factors varied from strain to strain, and would complicate the direct comparison of one organism to another. Their removal ensured that the spectral features observed in the subsequent reflectance spectra measurements originated from the pigmented cells.

Table 6.3. Data for cultured strains.

Species	DSMZ Strain ID #	DSMZ Media #	Culture Type[1]
Brevibacterium aurantiacum	20426	92	Aerobic; plated
Chlorobium tepidum	12025	29	Anaerobic in light; liquid
Deinoccocus radiodurans	20539	53	Aerobic; plated
Halobacterium salinarium	22414	97	Aerobic (37 °C); plated
Janthinobacterium lividum	1522	1, 1a	Aerobic; plated
Micrococcus luteus	20030	1	Aerobic; liquid
Phaeobacter inhibens	16374	514	Aerobic; liquid
Rhodobacter sphaeroides	158	27	Anaerobic in light; liquid
Rhodopseudomonas palustris	8283	651	Anaerobic in light; liquid
Rubrobacter radiotolerans	5868	535	Aerobic; liquid
Serratia marcescens	30121	1	Aerobic; liquid

Table Details: Data for cultured strains. Aerobic cultures were grown in the presence of oxygen, whereas anaerobic cultures were grown in airtight bottles evacuated of oxygen. Further detailed information regarding strain type and culture media can be found online at https://www.dsmz.de/.

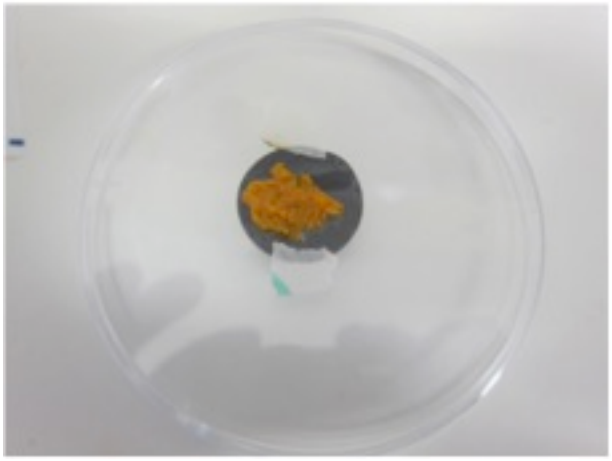

Figure 6.2. A sample of *Brevibacterium aurantiacum* before measurement with the Ocean Optics Spectrometer.

6.2.3 *Spectral reflectance measurements*

Spectral reflectance measurements were made of a monoculture of each species to determine the wavelength-dependent features of the organism's reflectance spectrum without environmental effects. Specifically, I aimed to quantify the location and strength of major spectral features. I assumed the samples were sufficiently thick to be diffuse reflectors due to multiple scattering within the cellular layers (see e.g., Broschat et al. 2014). The light environments are similarly diffuse above microbial mats mixed within a sediment matrix (Decho et al. 2003; Jorgensen & Des Marais 1988; Kühl et al. 1997).

Reflectance spectra measurements were made with an Ocean Optics USB2000+ UV/VIS spectrometer (Ocean Optics grating #3) with 2048 pixel channels, a dispersion of 0.32 nm per pixel and an optical resolution of 4.12 nm. The spectrometer was attached to a reflectance probe (Ocean Optics R400-7) via a 400-μm diameter SMA 905 fiber optic cable. The reflectance probe contained one read fiber and six illuminating fibers arranged in a circular pattern around the read

fiber. An Ocean Optics HL-2000 Tungsten-Halogen light source was joined to the fiber optic cable. A similar experimental configuration was described by Decho et al. (2003).

The reflectance probe was secured by an adjustable clamp attached to a vertical ring stand. Samples were placed on a custom holder on a level surface below the reflectance probe. The probe's position was maintained 30 mm from the surface of the sample with a 0° (perpendicular) orientation. The entire sampling apparatus was contained within a custom built dark box to exclude ambient light. This box was coated in matte black paper to minimize scattering of light from the light source.

The wavelength-dependent radiance reflectance ($R(\lambda)$) was calculated according to the following equation:

$$R(\lambda) = \frac{C(\lambda)_{sample} - C(\lambda)_{dark}}{C(\lambda)_{standard} - C(\lambda)_{dark}} \times \frac{t_{standard}}{t_{sample}} \times k(\lambda)_{WS1} \qquad (6.1)$$

where $C_{sample}(\lambda)$ is the counts from the sample measurement, $C_{dark}(\lambda)$ is the dark count with no illumination, $C_{standard}(\lambda)$ is the counts measured from the standard, t_{sample} is the integration time of the sample, $t_{standard}$ is the integration time of the standard, and $k(\lambda)_{WS\text{-}1}$ is the wavelength-dependent calibration factor for the WS-1 diffuse reflectance standard. The factor $k(\lambda)_{WS1}$ varies between 0.992 and 0.993 for the wavelength range measured in this work (tables with the wavelength-dependent calibration factors are available on the Ocean Optics website[28]).

Calibrations for reflectance measurements were made as follows. The light source was turned on several minutes before calibration measurements were made. The Spectralon WS-1 diffuse reflectance standard was placed in the sample position 30 mm below the reflectance probe. A series of 100-500 calibration spectra with integration times of 1 millisecond were collected from the illuminated reflectance standard. These calibration spectra were averaged and

[28] http://www.oceanoptics.com/

stored to computer memory. To measure the dark current, the light was blocked from entering the fiber with a switch-operated internal shutter, and a complementary series of calibration spectra were taken and stored to memory. New dark and reflectance calibration spectra were taken before each new sample measurement set.

Three to five spectral sets were recorded for each organism sample. Each set was a series of 100-500 spectral scans encompassing the 0.4-0.85 μm wavelength range. Each scan had an integration time of 1 millisecond, chosen to achieve maximum signal-to-noise without saturating the detector. The series of spectral scans were then averaged to produce a composite spectrum. This procedure was repeated 3-5 times at different locations on the sample surface to produce a spectral set. The location of the sample under the fiber was adjusted for each composite spectrum in the set, such that the sensor viewed a smooth area of the sample to minimize the effect of surface roughness on the reflectance of the isolated cells. The final spectrum for each organism was computed by taking the median value at each wavelength point of the averaged composite spectra in the spectral set. This setup yields spectra with high signal-to-noise for the 0.4 – 0.85 μm spectral range. The standard deviation for any wavelength in the composite spectra was less than 5%. Although the fiber-spectrometer combination had spectral sensitivity from 0.35-0.85 μm, shorter wavelengths were inaccessible because the Tungsten-Halogen fiber optic light source does not produce significant UV light.

6.3 Measured Reflection Spectra and Model Inputs

6.3.1 *Reflection spectra measurements*

The reflectance spectrum for each organism measured in the laboratory is shown in Figure 6.3. The wavelength-dependent spectral reflectance of a conifer forest, obtained from the ASTER spectral library (Baldridge et al. 2009), is provided for comparison. The strength of spectral break features such as the vegetation red edge (VRE) can be quantified by measuring the reflectance change between the maximum reflectance and the nearest local minimum in reflectance, given here as:

$$\Delta R = R_{\lambda_{max}} - R_{\lambda_{min}} \tag{6.2}$$

where $R_{\lambda_{max}}$ is the maximum reflectance and $R_{\lambda_{min}}$ is the reflectance at the nearest local minimum. Another way to quantify the strength of the spectral feature is to calculate the change in reflectance factor ($f_{\Delta R}$) over a wavelength interval:

$$f_{\Delta R} = \frac{R_{\lambda_{max}} - R_{\lambda_{min}}}{R_{\lambda_{min}}} = \frac{\Delta R}{R_{\lambda_{min}}} \tag{6.3}$$

Table 6.4 reports the locations of notable spectral features in the measured reflectance spectra and the strength of those features as defined above. The strength of the red edge for a conifer forest, an increase in reflectance from 0.69 to 0.77 μm of $\Delta R \sim 0.5$ and $f_{\Delta R} \sim 12$ is in the upper range of red edge strength. Other vegetation and photosynthetic organisms may have substantially weaker red edges (Kiang al. 2007a). As shown in the figure and table, there is a diverse range of spectral features in the measured organisms, including edge features that are well within a factor of two of the conifer forest red edge strength. Especially notable is *H.*

salinarum, which has $\Delta R \sim 0.3$ and $f_{\Delta R} \sim 4$ over a wavelength interval comparable to the conifer forest red edge rise.

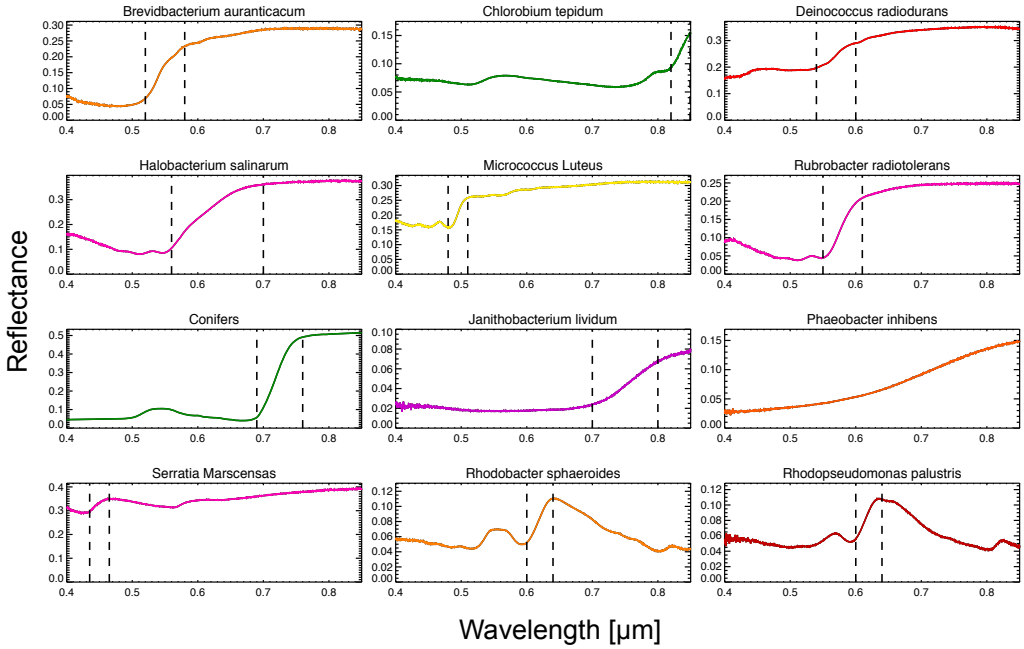

Figure 6.3. Spectra of all 11 pigmented microorganisms studied in this work organized and grouped into the categories given in Table 4. The seventh panel is the reflectance spectrum of a conifer forest taken from the ASTER spectral library (Baldridge et al. 2009). Spectra were taken from 0.4-0.85 μm. The dashed lines bracket the wavelength region containing the strongest spectral feature (listed in Table 6.4). Note that the vertical axes have different scales in order to show the spectral features of all organisms.

The spectra were split into three categories based on the strength and location of major spectral features (also shown in Table 6.4). The first category includes spectra with a strong spectral break or reflectance increase into the red or near infrared. This category includes the red-edge producing conifers and the bacterioruberin-containing *Halobacterium salinarum* and *Rubrobacter radiotolerans*. The second category includes spectra that show a shallow or gentle rise into the near infrared, including *Janithobacterium lividum and Phaobacter inhibens*. The

final category includes spectra with strong features in the visible spectrum (<0.7 μm) that are also absorptive in the near infrared, in contrast to categories 1 and 2. The members of this category of organisms are the anoxygenic photosynthesizers *Rhodobacter sphaeroides and Rhodopseudomonas palustris*, which possess bacteriochlorophylls that absorb at near infrared wavelengths, but also show spectral features in the visible spectrum due to carotenoid pigments.

Table 6.4. Empirically Measured Spectral Edges and Features 0.4-0.85 μm

Organism	"Edges" or Spectral Breaks [μm]	Absorption Features [μm]	Maximum Reflectance Change (ΔR)	Maximum Change in Reflectance Factor ($f_{\Delta R}$)
Category 1 – Strong Spectral Break and Reflective in the NIR				
B. aurantiacum	0.52-0.58	0.40-0.50	0.248	5.70
C. tepidum	0.82-0.86	0.52, 0.77	0.096	1.65
D. radiodurans	0.54-0.58	0.51-0.55	0.197	1.26
H. salinarium	0.56-0.70	0.48-0.55	0.298	3.70
M. luteus	0.49-0.510	0.45, 0.485	0.158	1.01
R. radiotolerans	0.56-0.60	0.51, 0.55	0.213	5.64
Conifers	0.69-0.76	0.40-0.50, 0.60-0.68	0.473	11.71
Category 2 – Gradual Rise into the NIR				
J. lividum	0.70-0.80	0.40-0.70	0.064	3.90
P. inhibens	-	-	0.127	5.77
S. Marscensas	0.44-0.46	0.41-0.43, 0.57	0.107	0.37
Category 3 – Strong Features in Visible and Absorptive in NIR				
R. sphaeroides	0.54-0.57, 0.61-0.64	0.52, 0.60, 0.805, 0.85	0.07	1.75
R. palustris	0.54-0.57, 0.61-0.64	0.52, 0.60, 0.805, 0.85	0.067	1.61

Table Details: Spectral features in measured organisms. "Edges" or spectral breaks (column 2) refer to sharp changes in reflectivity over a small wavelength range. Absorption features can be seen as negative excursions in reflectance.

6.3.2 *Spectral model inputs and parameters*

In the realistic case of a disk-averaged planetary observation, a pigmented surface will be viewed through an atmosphere, and therefore a remote observation of a planetary spectrum will include atmospheric absorption and scattering effects by gaseous molecules and clouds. To explore the effects of the atmosphere on the detectability of reflectance from surface pigments, I use SMART (Chapter 2) to calculate top-of-atmosphere spectra for both abiotic and biotic surfaces observed through an Earth-like atmosphere. I use the abiotic surfaces to compare spectra where surface biosignatures are present to those cases where they are not present.

I use the reflectance spectra measured in Section 6.3.1 as input surface reflectances for one series of simulated spectra. Another series of spectra uses spectral reflectances obtained from the literature and encompasses a wavelength range that is larger than our experimental spectra. Figure 6.4 shows the wavelength dependent reflectances of kaolinite soil, basaltic loam, gypsum, limestone, halite, snow, ocean water, a conifer forest, grass, a bacterial mat, red algae coated water, and a halophile-dominated saltern evaporation pond. The reflectance spectrum for the halophile-dominated pond (see Fig. 6.1c) was taken from the work of Dalton et al. (2009), which provides reflectance spectra of the San Francisco salt ponds measured *in situ* and therefore includes the spectral effects of both the pigmented organisms contained within the pond and the overlying layers of water. The other surface reflectances are from the USGS and ASTER spectral libraries (Clark et al. 2007; Baldridge et al. 2009). The conifer forest and the halophile-dominated pond provide a comparison between surfaces dominated by photosynthetic and non-photosynthetic organisms that are known to exist on Earth. The organisms that constitute these biological surfaces contain pigments that cause reflectance peaks at different wavelengths and thus may be distinguishable from each other.

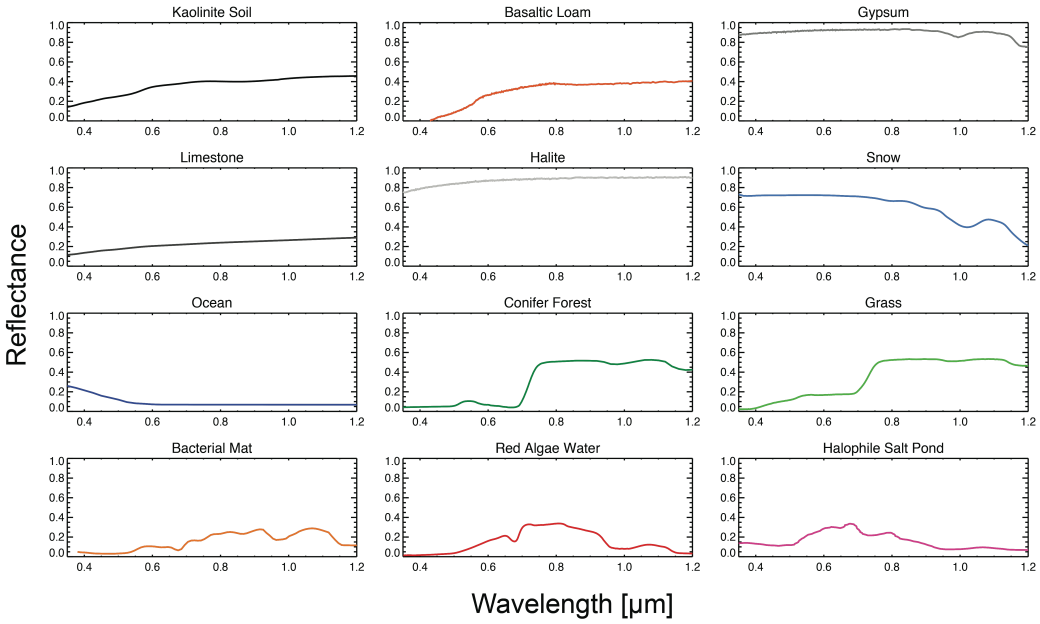

Figure 6.4. Spectral reflectances of abiotic and biotic surfaces from the USGS (Clark et al. 2007); and ASTER (Baldridge et al. 2009) spectral libraries from 0.35-1.2 μm. The halophile salt pond's spectral reflectance is from work by (Dalton et al. 2009). Note the water absorption features in the bacterial mat, red algae water, and halophile salt pond cases.

6.4 Incorporation into Spectral Models

I used SMART (1D) to generate a spectrum of a planet dominated by each of the surfaces listed above under an Earth-like atmosphere in a clear sky (no cloud) scenario. I then use the 3D spectral Earth model with clouds to explore a more realistic scenario comparing the modern (simulated) Earth with a plausible Earth-like planet (with clouds) containing a salty ocean dominated by non-photosynthetic pigmented organisms.

6.4.1 *1D SMART model spectra*

In this case, I consider a planetary surface dominated by a single surface type possessing either the experimentally measured spectral reflectances, or previously known spectral reflectances from literature. I use SMART (Meadows & Crisp 1996; Crisp 1997) to model the resulting spectra of these surfaces under an annually averaged mid-latitude Earth-like atmosphere and an incident stellar spectrum identical to the Sun's. I assume the surfaces are diffuse reflectors, which has been demonstrated to be an adequate assumption when comparing synthetic spectra to validation data for Earth at gibbous phases (Williams & Gaidos 2008; Robinson et al. 2010; Cowan & Strait 2013). I assume an Earth-like atmosphere including average temperature-pressure and gas mixing ratio profiles (Earth-like atmospheres are assumed because each biological and non-biological surface exists on modern Earth). The spectrally active (absorptive) gases included are H_2O, CO_2, O_3, O_2, N_2O, CO, and CH_4. In this case, the HITRAN 2008 (Rothman et al. 2009) line lists were used to calculate the absorption cross-sections for each spectrally active gas. The resolution of the spectral grid in the model was 1 cm^{-1}, which corresponds to a wavelength resolution of $\Delta\lambda = 2.5 \times 10^{-5}$ μm at $\lambda = 0.5$ μm. A single solar zenith angle of 60 degrees was used, which approximates the illumination observed in a planetary disk average (Segura et al. 2005) and consider cases with no cloud cover. This mimics a clear sounding through the atmosphere, and is only achievable for a partially cloud-covered planet when the observation has adequate spatial resolution. Realistically, some level of cloud cover is expected, and while obtaining longitudinally resolved observations of terrestrial exoplanets may be possible with adequately time-resolved photometry from future space-based telescopes (Cowan 2009; Cowan et al. 2011; Cowan & Strait 2013), the spatial resolution obtainable will span a significant fraction of the planet, and so will likely still include clouds. While this will

affect absolute detectability of surface reflectance biosignatures, it will not introduce spurious wavelength-dependent features in the spectrum because clouds are approximately gray (i.e. they have largely wavelength-independent reflectivity) in the visible regime. The spectrum of a partially cloud-covered planet will be a linear combination of spectra from clear soundings and spectra from fully and partially cloud-covered soundings. The effect on the planetary spectrum of spatially inhomogeneous clouds are more fully captured in the 3D Earth model runs described below.

6.4.2 *3D Earth model spectra*

To better assess the detectability of the most promising non-photosynthetic pigmented organism in a plausible context, and to compare with spatially resolved models of inhabited Earth-like planets in the literature (e.g., Tinetti et al. 2006a,b; Robinson et al. 2011; Sanromá et al. 2013, 2014), I produced more comprehensive whole-planet spectra that contain the confounding effects of spatially resolved clouds and different surface types. To do this I use the Virtual Planetary Laboratory's 3-D spectrally resolved Earth model, described in Chapter 2 and Robinson et al. (2011). For the model runs presented here, the atmospheric parameters varied spatially over 48 atmospheric pixels with 40 vertical layers, and the surface was approximated as 192 pixels. The surface reflectance of each surface pixel was calculated as a linear combination of five surface types (ocean, soil, snow, forest, and grassland). The modern Earth continental arrangement is used for the land and ocean spatial distribution. It is assumed that the observer is viewing the disk-averaged planet from an approximately sub-equatorial latitude (1.6° N) and a Sun-planet-observer phase angle of 57.7° over a 24 hour period from March 18-19. This date was chosen because the VPL Earth model has already been validated on this date with observed near-infrared and broadband visible spectra taken during the EPOXI mission by the Deep Impact Spacecraft

(Cowan et al. 2011; Livengood et al. 2011). The disk-integrated spectrum of the planet produced by the model was divided by a solar spectrum corrected for phase (i.e., partial illumination of the planet) with a Lambertian phase function, to produce the whole-disk planetary spectral albedo (hereafter referred to as the "albedo"). It has been shown that Earth's phase function only deviates significantly from a Lambertian function near crescent phase (phase angles near zero) where glint (specular reflection from the ocean) and cloud forward scattering becomes important (Williams & Gaidos 2008; Robinson et al. 2010).

To explore the potential detectability of a non-photosynthetic pigment with as comprehensive a model as possible, I used the 3D spectral Earth model to compare the spectrum of a realistic Earth with a similar model case in which the spectral reflectance of the oceans has been replaced by that of the halophile-dominated saltern pond. This environment was chosen for further modeling because the halophile spectrum produced a strong spectral signature that was comparable in strength to that of photosynthetic plants (e.g., the conifer forest), and so had a higher probability of being detectable in the disk-average. This simulation approximates a scenario in which an Earth-like planet contains a very salty, shallow ocean populated by pigmented halophile organisms at the same density found in the San Francisco saltern ponds with the highest salinity (Dalton et al. 2009), but with the same cloud and snow/ice cover of modern Earth. This "halophile Earth" case presents a best-case end member scenario for the surface coverage of pigmented halophile organisms on an Earth-like planet.

6.5 Spectral Model Results

6.5.1 *1D SMART model spectra*

Figure 6.5 shows the simulated spectral reflectivity (the top-of-atmosphere irradiance divided by the incident solar irradiance) for sunlight transmitted through an Earth-like atmosphere and

reflected from surfaces that have the same diffuse spectral reflectance properties as the experimentally measured microbes. Dashed vertical lines indicate the wavelength region containing the strongest spectral feature in the experimental reflectance spectra. Table 6.5 lists the maximum fractional reflectivity change in the synthetic spectra over these wavelength regions by using equation (6.3). Because the spectra were generated assuming the average solar zenith angle for a planet observed at quadrature, the reflectivity given in Figure 6.5 is not on the same absolute scale as the reflectance in Figure 6.3 and 6.4.

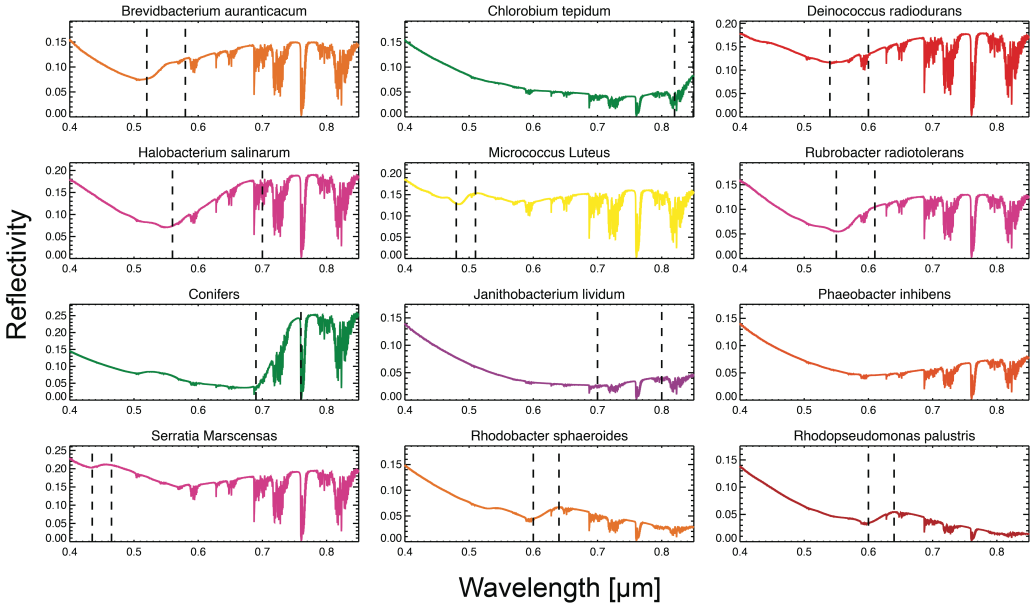

Figure 6.5. Resulting top-of-atmosphere spectral reflectivity of planets with surfaces dominated by the pigmented microbes described in Sections 6.2.1 and 6.3.1 and shown in Figure 6.3. The microbe surfaces are modeled as diffuse reflectors. The average solar zenith angle is assumed to be 60°. The reflectivity is calculated as the modeled top-of-atmosphere spectral irradiance divided by the spectral irradiance of the Sun and not corrected for solar zenith angle. The dashed lines bracket the wavelength region containing the strongest feature seen in the measured reflectance spectrum (listed in Table 6.4). For the purpose of illustration, the spectra have been smoothed with a moving 5-point statistical mean.

Table 6.5. 1D Synthetic spectra feature strengths.

Surface Organism	Wavelengths of Strongest Spectral Feature [μm]	Maximum Change in Reflectance Factor ($f_{\Delta R}$)
Category 1 – Strong Spectral Break and Reflective in the NIR		
B. aurantiacum	0.52-0.58	0.53
C. tepidum	0.82-0.86	1.17
D. radiodurans	0.54-0.58	0.35
H. salinarium	0.56-0.70	2.35
M. luteus	0.49-0.510	0.21
R. radiotolerans	0.56-0.60	0.21
Conifers	0.69-0.76	6.96
Category 2 – Gradual Rise into the NIR		
J. lividum	0.70-0.80	1.88
P. inhibens	-	-
S. Marscensas	0.44-0.46	0.05
Category 3 – Strong Features in Visible and Absorptive in NIR		
R. sphaeroides	0.54-0.57	0.53
R. palustris	0.54-0.57	0.60

Table Details: The strengths of surface spectral reflectance features from pigmented organisms as seen through an Earth-like atmosphere. See Section 6.4.1 for a description of the 1D synthetic spectra.

Figure 6.6 shows the resulting top-of-atmosphere spectral reflectivity for cases of planets with Earth atmospheres and underlying surfaces dominated by kaolinite soil, basaltic loam, gypsum, limestone, halite, snow, ocean water, conifer forest, grass, bacterial mat, red algae coated water, and a halophile-dominated saltern evaporation pond (surface spectral reflectances shown in Figure 6.4). These spectra are presented to show the best-case scenario for detection of that surface type through an Earth-like atmosphere. Figure 6.7 shows, for direct comparison, the spectra of the conifer forest, halophile salt pond, and ocean case from Figure 6.6. The red-edge feature of the forest case is apparent through the cloud-free atmosphere. The spectrum from the halophile salt pond case preserves the ~0.68 μm spectral reflectance peak (a 40% increase from a

local minimum at 0.57 μm) and is much more reflective, by a factor of ~3, than the ocean case from 0.6-0.7 μm.

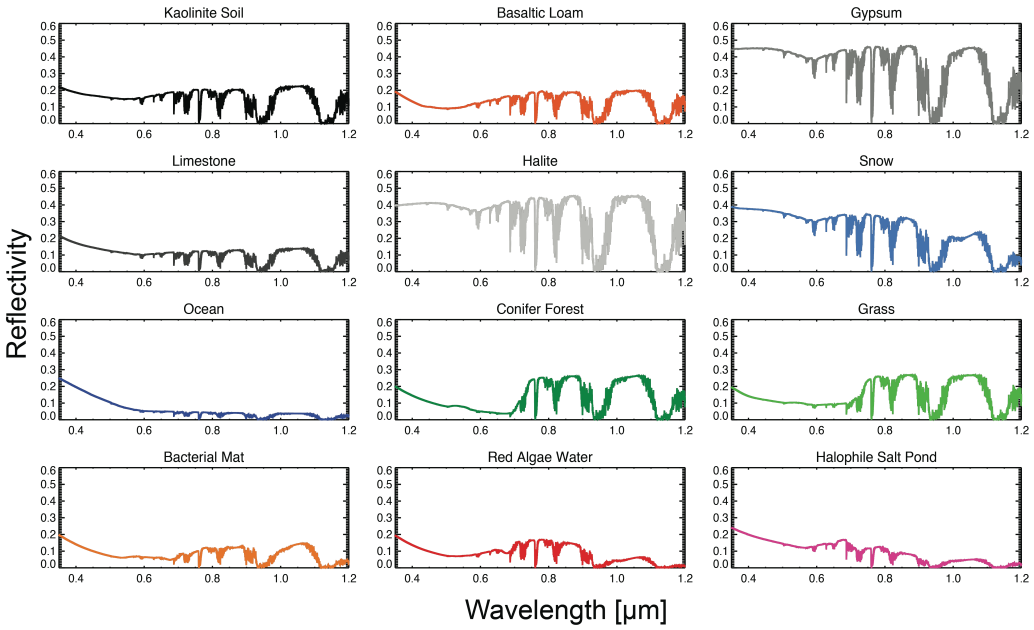

Figure 6.6. Resulting top-of-atmosphere spectral reflectivity of planets dominated by the abiotic and biotic surfaces described in Section 6.3.2 and whose spectral reflectances are shown in Figure 6.4. The average solar zenith angle is assumed to be 60°. The reflectivity is calculated as the modeled top-of-atmosphere spectral irradiance divided by the spectral irradiance of the Sun and not corrected for solar zenith angle. For the purpose of illustration, the spectra have been smoothed with a moving 5-point statistical mean.

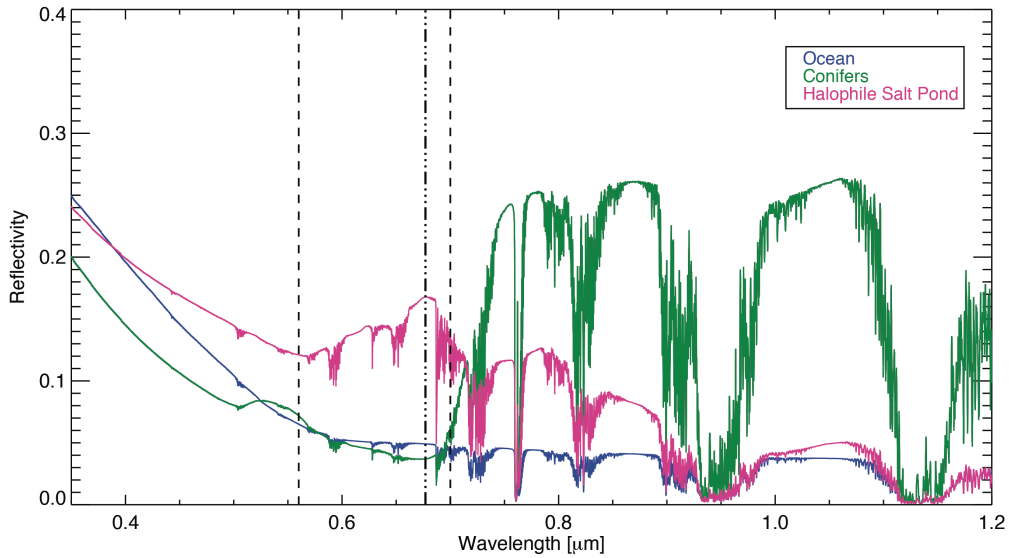

Figure 6.7. Reflectivity spectra of the conifer forest, hypersaline pond, and ocean planet from Figure 6.6 are shown together for contrast. The dashed line brackets the wavelength region containing the largest feature seen in the reflectance spectrum of *Halobacterium salinarum*, which contains similar pigments to the biota in the San Francisco salt ponds. The dot-dash line corresponds to the local maximum reflectivity of the halophile salt pond at ~0.68 μm. For the purpose of illustration, the spectra have been smoothed with a moving 5-point statistical mean.

6.5.2 *3D model spectra with realistic clouds*

I present below the 3D Earth model synthetic spectra of the realistic Earth and the Earth with halophile-dominated oceans as described in Section 6.4.2. I provide the 24-hr diurnally averaged spectra in addition to a subset of the time-dependent longitudinally resolved spectra.

Figure 6.8 shows the phase-corrected spectral albedo of the modeled planet from 0.4-1.4 μm. The diurnally averaged top-of-the-atmosphere spectral albedo of the "halophile planet" is up to a factor of two times more reflective than the realistic Earth case from 0.55-0.85 μm, and produces a characteristically different spectrum. The halophile Earth spectrum shows an increase in albedo of 25% from a local minimum at 0.5 μm to the reflectance peak at 0.68 μm, just

shortward of a water band. The difference in albedo from the 3D halophile planet spectrum and the 1D halophile surface spectrum result both from the introduction of clouds and the inclusion of multiple surface types in the 3D model. The local minimum in the Earth's spectrum at ~0.6 μm is the result of absorption from the broad Chappuis ozone band (0.5-0.7 μm). However, in the halophile ocean planet spectrum, the minimum is instead seen at 0.5 μm due to the combination of increasing reflectivity with wavelength of the halophile pigments on the surface and the atmospheric absorption due to the ozone band.

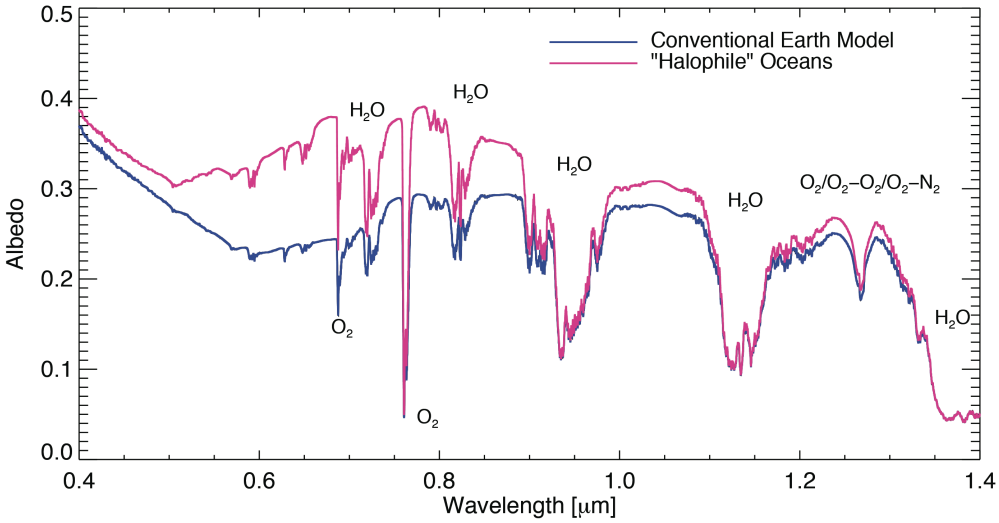

Figure 6.8. Diurnally averaged spectral albedos from the VPL 3D Earth model for March 18-19, 2008, under a realistic scenario (blue) from Robinson et al. (2011) and a scenario that is identical with the exception that the spectral reflectance of the ocean surface has been replaced by the spectral reflectance of a pigmented halophile-dominated saltern pond from work by Dalton et al. (2009) (pink). Major gaseous absorption features are labeled. For the purpose of illustration, the spectra have been smoothed with a moving 20-point statistical mean.

Figure 6.9 shows the spectral albedo of the disk-averaged "halophile planet" at disk views with sub spacecraft longitudes of 160° W and 20° E. These correspond to times when the planet is dominated by the Pacific Ocean (160° W) and the African and parts of the European and Asian continents (20° E). Unsurprisingly, the nonphotosynthetic halophile pigmentation is more detectible when it constitutes a larger fraction of the surface. The halophile-dominated ocean is more reflective at most visible wavelengths than the continents, which is the opposite of modern Earth's spectral contrast between land and ocean. The magnitude of this change at 0.68 μm is ~13%. In near-infrared wavelengths, the land is more reflective than the halophile-dominated ocean, which is similar to Earth's ocean and land contrast. These effects would combine to produce unique spectral and time dependent behavior as a function of rotational phase. This heterogeneity would allow the use of time-dependent broadband colors to determine the planetary rotation period and reconstruction of the longitudinal land distribution (Cowan et al. 2011; Cowan et al. 2009; Cowan & Strait 2013).

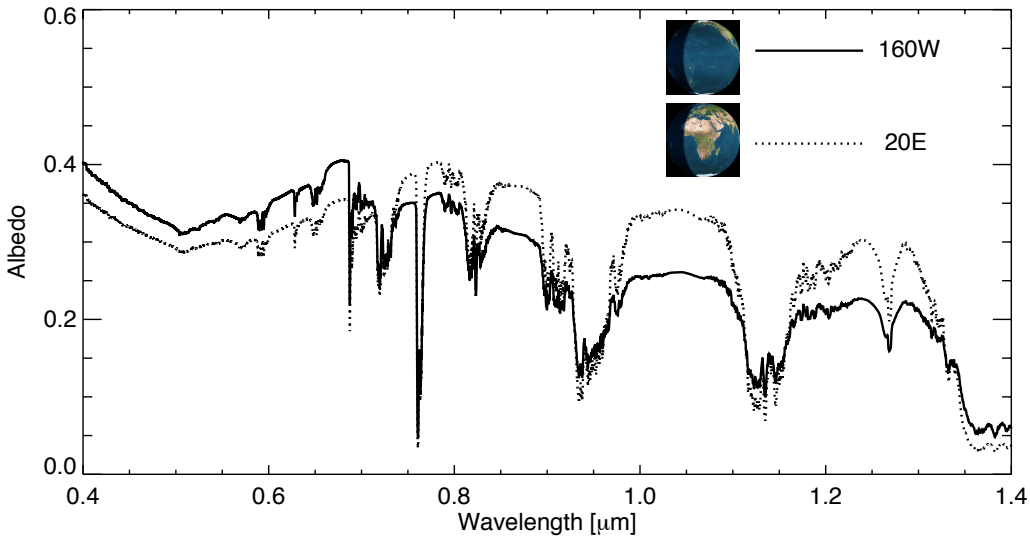

Figure 6.9. Spectra from the halophile ocean version of the Earth model at two discrete sub-observer longitudes: 160° W (over the Pacific Ocean) and 20° E (centered over the African Continent and Eurasia). Note the difference in the reflectance peak at ~0.68 μm produced by the halophiles' carotenoid pigments suspended in water. Insets were generated with the Earth Moon Viewer (http://www.fourmilab.ch/earthview/). For the purpose of illustration, the spectra have been smoothed with a moving 20-point statistical mean.

6.6 Broadband Color Calculations and Results

Broadband colors were calculated to investigate their usefulness in identifying exoplanet surface types via astronomical observations and to search for possible patterns when comparing the colors produced by biotic or abiotic surfaces. I show and compare broadband colors with and without effects from an overlying atmosphere. Broadband color in this context is the difference in brightness between two bands. In astronomical observations, this is reported as a logarithm. To compare two bands X and Y, the following equation is used:

$$C_{XY} = X - Y = -2.5 * \log_{10}\left(\frac{r_X}{r_Y}\right) \quad (6.4)$$

where r_X is the reflectivity in band X and r_Y is the reflectivity in band Y. I define reflectivity here as the irradiance from the planet in a given band divided by the irradiance of the incident solar spectrum. Typically in astronomical observations color is a difference in observed flux between bands, which will vary as a function of the host star's spectrum when the flux from the target object is composed of reflected light from the star. Here, reflectivity is used only in calculating broadband colors and assume that the host star's spectrum, which will be known, has been divided out of the observed planet flux. I first calculate broadband colors of the experimentally measured reflectance spectra shown in Figure 6.3 and the biotic and abiotic surfaces from spectral libraries shown in Figure 6.4, neglecting the effects from atmospheric absorption and scattering. Colors and then calculating using the simulated spectra that account for the effects of viewing a surface through a planetary atmosphere (Figures 6.5, 6.6, and 6.8). I define three bands: B*= Blue= 0.4-0.5 μm, V*= Visible= 0.5-0.7 μm, and I*= Infrared= 0.7-0.85 μm. These bands are modeled after the Johnson-Cousins BVI bands, but differ in that they have perfect transmission through the entire idealized filter band-pass for comparison with other studies of broadband colors of planetary surfaces (e.g., Hegde & Kaltenegger 2013). The infrared band additionally has a smaller width and terminates at a shorter wavelength (0.85 μm vs. ~0.9 μm) due to limitations on our measurements from the Ocean Optics spectrometer.

6.6.1 *Broadband colors of pigmented surfaces without atmospheric effects*

A color-color plot of the idealized broadband colors of the spectra shown in Figure 6.3 is shown in Figure 6.10. These surface-only colors could be considered "no atmosphere" scenarios or cases where the effects of the atmosphere have been perfectly removed. The colors occupy a wide range in color-color space with the scatter meeting or exceeding that for abiotic surface types shown here, though seawater, red algae water (from the USGS spectral library), and the

conifer forest present clear outliers. The forest presents a stronger red edge than grass or a bacterial mat, giving it a redder B*-I* index.

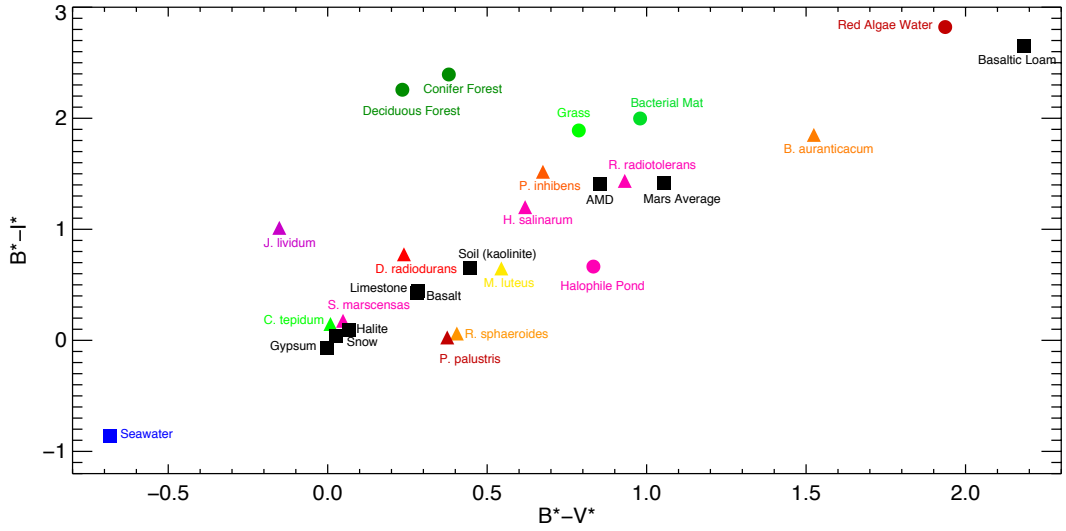

Figure 6.10. Color-color plot of pigmented microorganisms from this work and biotic and abiotic surfaces from spectral databases. Triangles represent colors of organisms derived from reflectance spectra measured for this work; squares are abiotic reflectances from spectra taken from the USGS spectral library (Clark et al. 2007); circles are biotic reflectances from the USGS spectral library or the ASTER spectral library (Baldridge et al. 2009).

6.6.2 *Broadband colors of pigmented surfaces as seen through an atmosphere*

Figure 6.11 shows the broadband colors of abiotic and biological surfaces from the USGS and ASTER spectral libraries, and colors resulting from the normalized spectral reflectivities or albedos of the 1D and 3D spectral models. The colors of the 1D (no clouds) and 3D (heterogeneous surface and clouds) model spectra include the effects of scattering and absorption in the atmosphere, while the two 3D model spectral colors additionally include the effects of realistic clouds. As expected, the effect of Rayleigh scattering makes the colors of the clear sky spectra almost uniformly bluer. Red algae water, basaltic loam, and trees, apparent outliers when

considering only the surface reflectance function in the color calculation, begin to populate similar areas in B*-V* vs. B*-I* color space when the effects of scattering in a planetary atmosphere are included. The presence of an atmosphere therefore reduces the spread in the distribution of surface colors. This is consistent with work by (Sanromá et al. 2013), which included fewer surface types in their analysis but noted a similar trend. For the two cases where heterogeneous surface distributions are assumed and cloud cover is included, that is, the ocean-dominated realistic Earth case and the halophile-dominated oceans case, colors are redder than the 1D clear sky cases, but still bluer than seen for the airless, pure surface spectra cases. This reddening in comparison to the clear sky cases is due to the effects of clouds, which truncate the atmospheric column, thereby decreasing Rayleigh scattering, while also behaving as gray scatterers.

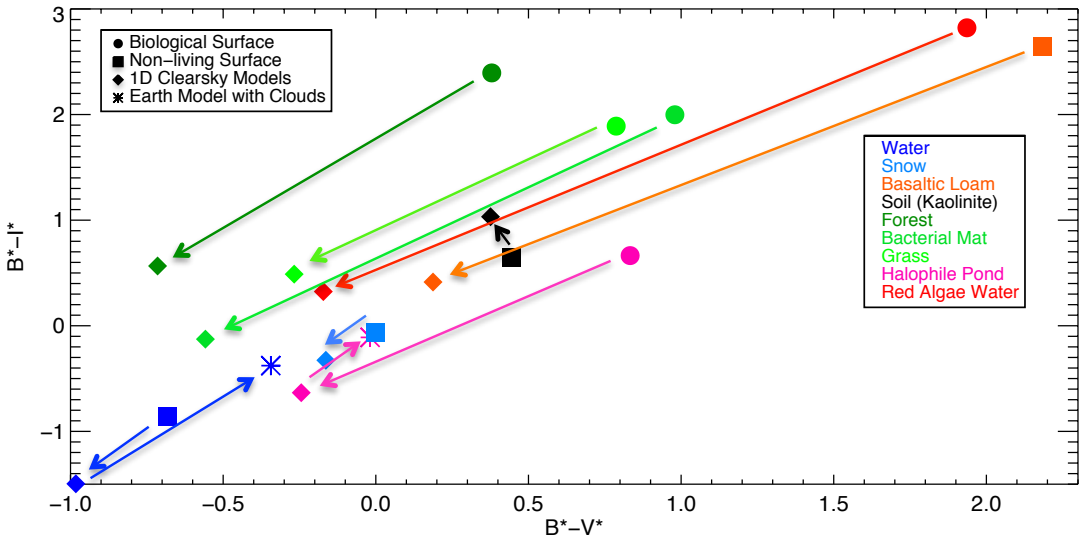

Figure 6.11. Color-color plot comparing the normalized colors of lifeless surfaces (squares), pigmented biological surfaces (circles), these surfaces under an earth-like cloudless atmosphere (diamonds), and two cases that are diurnal averages of a heterogeneous planet with realistic clouds (asterisks). Arrows are drawn from the colors with no radiative effects from the atmosphere included, to the colors including effects from the atmosphere.

In Figure 6.12, I show the broadband colors of the simulated planet spectra with the experimentally measured surfaces viewed through an Earth-like atmosphere (from Figures 6.5 and 6.6). Similar to the cases shown for Figure 6.11, the colors become bluer with the addition of spectral effects from the atmosphere.

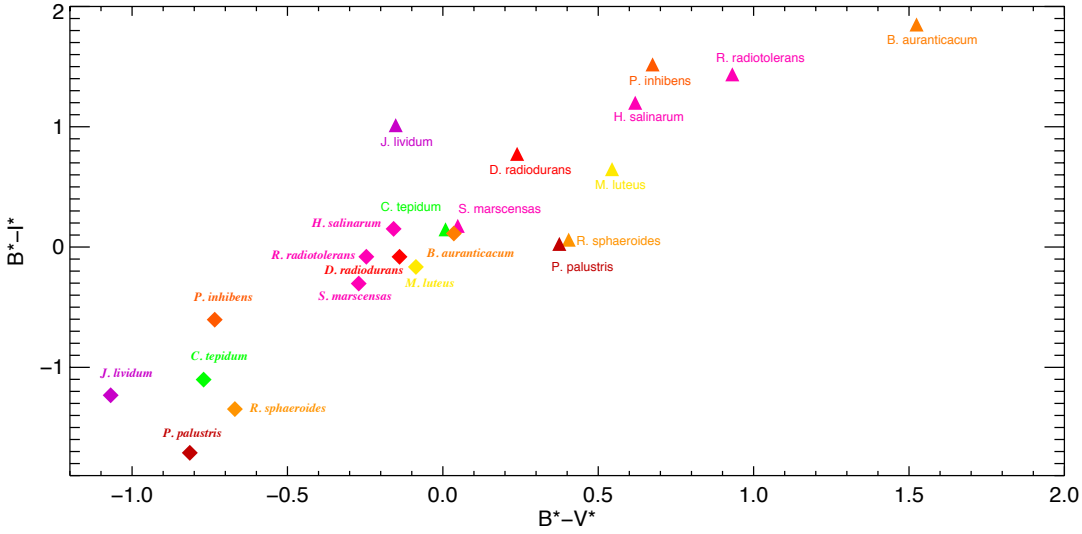

Figure 6.12. Color-color plot comparing the normalized colors of experimentally measured microbial spectral reflectances (triangles, non-italicized text labels) and those of surfaces dominated by these pigmented organisms under an Earth-like cloudless atmosphere (diamonds, italicized text labels). Note that the colors for pigmented microbial surfaces shown here are the same for Figure 6.10, but the axis limits are different to accommodate the spectral model colors.

6.7 Discussion

In this study, I explored non-photosynthetic pigments as potential biosignatures and found that non-photosynthetic organisms display a rich diversity of spectral features. Within the example set of non-photosynthetic organisms investigated in this work, significant spectral breaks (>~10% change in reflectance) are found throughout the visible spectrum from 0.44 to 0.7 μm. In

contrast, Kiang et al. (2007a) showed that red-edge breaks for photosynthetic vascular plants, lichens, moss, algae, and seagrass clustered between 0.69-0.73 μm. Additionally, I find that for some visibly pigmented organisms, such as *Phaeobacter inhibens*, no significant spectral-break features are present.

6.7.1 *Challenges in identifying biological reflectance spectra signatures*

It is shown here that pigmented organisms do not occupy a unique region of visible broadband color-color space and that the broadband colors of biological and abiotic surfaces are altered significantly when viewed through a planetary atmosphere. Previous work has been done to calculate the visible broadband colors of biotic and abiotic surfaces, but that work did not include the effects of an overlying atmosphere (Hegde & Kaltenegger 2013). The atmosphere's effect on the observed colors is due primarily to Rayleigh scattering, which drives colors to bluer regions of color-color space, although absorption from water vapor and ozone also modify the colors inferred from the surface alone. A planet dominated by even a single surface type could exhibit a variety of broadband colors depending on the overlying atmosphere's level of Rayleigh scattering and cloud cover. Rayleigh scattering is modulated by the thickness of the atmospheric column, and may be difficult to determine, as some atmospheric and surface absorbing species can mask the presence of Rayleigh scattering even for planets with substantial atmospheres (Crow et al. 2010). Realistically, planets will have a variety of surface types, atmospheric compositions and masses, and cloud composition and fractional coverage. The observed colors will therefore be highly degenerate, with similar colors being produced by a large variety of possible planetary environments.

The surface reflection signal of any possible surface biota will also be a component of a larger, complex planetary environment, which will have its own effects on the reflectance

spectrum. This will make attributing specific spectral features to life implausible without information about the planetary context. If the dominant pigments for the organisms are non-photosynthetic, there is a large range of possible wavelengths where significant spectral features may appear. Analogs of the VRE may be predicted based on the wavelength for the peak photon-flux at the planetary surface if the incident stellar spectrum and the planetary atmospheric parameters are well known (Kiang et al. 2007a,b). However, if the most widespread or detectable surface organisms are not photosynthetic, then the strongest spectral breaks may not be at the predicted wavelengths. Even many anoxygenic photosynthesizers on Earth do not have spectral breaks near 0.7 μm due to bacteriochlorophylls that absorb at longer wavelengths (Hohmann-Marriott & Blankenship 2012). For this reason, and due to possible degeneracies with other planetary properties, a few pre-selected narrowband filters would not be able to distinguish between the vast diversity of possible features, and the best discrimination of the source of the surface reflectivity would likely require an evaluation of the whole visible spectrum with spectrally resolved data.

Examination of the planetary context could also rule out some of the false positive possibilities for biological surface reflectance features. For example, the minerals, such as sulfur compounds, that have been posited as a possible false positive for the VRE (Seager, E.L. Turner, et al. 2005) are much brighter at near-infrared wavelengths than water (Clark et al. 2007; Baldridge et al. 2009). Therefore, if a larger spectral range is accessible, it may be possible to discriminate minerals from pigments suspended in water, as the latter will show much lower albedos at near-infrared wavelengths because of absorption from the overlying water.

6.7.2 *Plausibility of widespread environments conducive to nonphotosynthetic life*

Pigmented non-photosynthetic organisms inhabit environments on Earth that could exist on other habitable terrestrial planets. An example of this type of environment is hypersaline ponds, whose spectral reflectances are often dominated by non-photosynthetic pigmented halophiles. The "halophile planet" modeled in this study is a best-case scenario for a planet that possesses significant coverage of non-photosynthetic pigments, although it is plausible that similar environments may exist on terrestrial planets with the right conditions. For example, high-salinity environments may be more extensive on a planet with shallower oceans, or different weathering rates (Pierrehumbert 2010). The high salinity environment is hostile to many potential grazers, and the resulting lack of predation allows the microbial inhabitants of high-salt ponds to exist at high densities even with low levels of primary productivity (Oren 2009). The same type of scenario is observed in high temperature hot springs, where thermophilic bacteria can grow into biofilms in part because they face little to no predation. Other "extreme" environmental conditions, such as an anoxic atmosphere, may also preclude macroscopic grazers, as was the case on Earth before the origin of animals ~575 Myr ago (Narbonne 2005). The suppression of predation due to lack of oxygen could potentially allow for a much larger - and therefore more detectable - steady state biomass, without requiring extremes in salinity or temperature. (And note that a lack of oxygen does not necessarily imply a lack of photosynthesis and therefore low primary productivity Anoxygenic photosynthesis is potentially very productive given an adequate source of appropriate reductants. Also, existence of oxygenic photosynthesis does not immediately lead to the buildup of oxygen in the atmosphere (Kump 2008; Lyons et al. 2014).)

6.7.3 *Remote detectability of non-photosynthetic life with spectrally resolved data*

In contrast to information from broadband filters, spectrally resolved data is sensitive to reflectance features, such as spectral breaks, that may be indicative of surface life, such as photosynthetic analogs to the VRE or the non-photosynthetic organisms included in this study. The reflective pigments of non-photosynthetic organisms suspended in water may be distinguished from abiotic features by examining the spectral shape of the feature and determining the environmental context from the full spectrum; for example, by detecting strong water vapor or searching for ocean glint (Williams & Gaidos 2008; Robinson et al. 2010, 2014). Glint that is spatially correlated with the observed pigment signature (using a mapping technique such as that described in Cowan et al. 2009) would argue for co-location on the planetary surface.

For an environment hosting wide-spread nonphotosynthetic pigmented halophilic organisms, the 3D spectral model spectra presented here predicts a characteristic spectral feature, and a time-varying signal in the disk-averaged spectrum that is potentially several times larger than that posited for the vegetation red edge. The VRE signal on Earth has been quantified from Earthshine data as the time-dependent fractional change in albedo at 0.7 μm due to the changing proportion of vegetation in the disk-view of the planet (Montanes-Rodriguez et al. 2006). The VRE signal defined in this way is a ~2% effect, though this quantification is dependent on the viewing geometry of the planet and would have varied through geological time (Arnold et al. 2009). In contrast, a shallow ocean populated by a significant density of pigmented halophiles could produce a maximum 13% time-variable signal at 0.68 μm, assuming the modern Earth's continental arrangement. The photometric variability due to changes in the proportional coverage of the visible planetary disk has been considered in other model scenarios as a method to

distinguish biological surfaces from abiotic ones (Sanromá et al. 2013, 2014). The increasing variability with wavelength of the amplitude of the infrared albedo modeled for the Archean Earth with different fractional coverage of anoxygenic photosynthetic purple bacteria (Sanromá et al. 2014) is due to the high reflectivity of purple bacteria at near infrared wavelengths (~1.1 μm). In contrast, the pigmented organisms found in the salt ponds are more reflective at visible wavelengths, and a planet populated with them would instead exhibit the greatest difference in spectral albedo between ocean and land in the visible portion of the spectrum.

6.7.4 *Future implications*

Near-future space-based direct-imaging telescopes are currently being designed that can probe the spectral surface reflectance of planets in the habitable zones of their stars. Because some of these telescopes designs, such as Exo-S and Exo-C, have relatively small apertures (≤ 1.4 m), they will not be able to observe wavelengths as long as those of the photosynthetic red-edge feature for planets in the habitable zones of all but the nearest stars (Stapelfeldt et al. 2014; Seager et al. 2014). This results from the relationship between telescope diameter, inner working angle, and spectral range. Even for instruments with spectral ranges that extend over the entire astronomical visible wavelength range (0.4-1.0 μm), a significant portion of range will be excluded for many targets depending on their distance from Earth and consequently whether their habitable zones are accessible given the inner working angle requirements for those wavelengths. In the case of long wavelength cutoffs shorter than 0.7 μm, which also excludes the strongest O_2 and CH_4 spectral features, surface reflectance biosignatures shortward of the traditional VRE (such as those shown in this paper) may be the only plausibly accessible class of biosignature. However, space based telescope concepts currently being developed have much larger telescope diameters, up to 10-16 meters. These include the AT-LAST, LUVOIR, HDST,

and HabEx concepts (Postman et al. 2010; Dalcanton et al. 2015; Rauscher et al. 2015; Swain et al. 2015). Such large space-based telescopes would have the capability to probe the spectra of many habitable zone planets throughout the visible wavelength range where surface pigments could produce detectable spectral features. As stated earlier, the determination of the biological origin of these spectral breaks will require a complete evaluation of the planetary context, including the presence or absence of gaseous habitability markers or biosignatures, to rule out potential false positives.

6.8 SUMMARY

In this chapter, I have examined the diversity of spectral features of organisms with nonphotosynthetic pigments using laboratory measurements. Using radiative transfer models of 1D and 3D, planet-wide, spatially resolved spectra, I have shown that a nonphotosynthetic pigment can create a significant effect in the disk-averaged spectrum of a terrestrial planet, given adequate surface coverage. I calculated broadband colors for a range of pigments and other biological and abiotic surface types in the visible wavelength range considering only their spectral reflectances, and for more realistic scenarios that included an overlying atmosphere and clouds. While the resultant broadband colors are dependent on the nature of spectral reflectance of the surface – including those of any biologically produced pigments – it would not be feasible to make a definitive determination of surface type based on the broadband color alone. Higher-resolution spectra would be far more informative, allowing observers to search for features such as line breaks or peaks that may indicate biological pigments. Highly reflective pigments suspended in water would possess a spectral reflectance that peaks in the visible spectrum, and would exhibit glint at small phase angles, possibly allowing an observer to distinguish between a nonphotosynthetic pigment biosignature and another reflective surface. This work has shown that

there is a diverse range of potential surface reflectance biosignatures beyond the commonly considered photosynthetic “red edge.” Nonphotosynthetic pigments with features in the UV-visible range may be the only potential surface biosignature accessible for future exoplanet observations with long-wavelength cutoffs shortward of the traditional VRE.

Chapter 7. CONCLUSIONS

In the coming years and decades humanity will have its first opportunity to survey the atmospheres of planets in nearby systems for signs of habitability and life. Within the lifetimes of the majority of those alive today, we will know whether life is common or extremely rare in the universe. To make these determinations will require the spectral investigation terrestrial planetary atmospheres and surfaces for signatures of liquid water and life. The ability to accurately interpret this information is paramount. The James Webb Space Telescope will provide the first opportunity to spectrally probe a small handful of worlds for signs of habitability. In depth characterization of habitable zone words will be made by future space telescopes, such as the LUVOIR and HabEx Surveyors, and extremely large ground based telescopes (~30 m) coming online in the 2020s. To inform the design of these instruments and the implementation of a coherent biosignatures strategy, the potential detectability of proposed biosignatures must be investigated, and approaches to mitigate against the potential for "false positives" must be formulated. This dissertation advances these areas in key ways by 1) creating a high fidelity, high cadence spectral Earth data base that includes spectral effects, useful as input to instrument and retrieval models, 2) demonstrating the detectability of N_2, a likely significant component of habitable exoplanet atmospheres, through its CIA absorption in transmission and direct-imaging spectroscopy, 3) determining spectral indicators for abiotic O_2 production, including CO from CO_2 photolysis and O_4 from large amounts of O_2 left behind by massive H-escape, and quantifying their detectability, and 4) investigating nonphotosynthetic pigments as additional surface reflectance signatures to be searched for as evidence of alien life

in addition to conventional signatures like the vegetation red edge. I include summaries of these findings below.

7.1 Summary of Findings

In chapter 3 I presented the VPL Spectral Earth Database. The database includes disk-averaged spectra (0.1 – 200 μm) of the Earth as seen from the Moon during an entire synodic month at one-hour cadence. The effects of Earth's surface inhomogeneity, cloud variability, spatial temperature gradients, obliquity, phase-dependent absorption and scattering effects, and rotation were included in the model. I described the main characteristics of the spectra including the effects of phase on the spectral features and overall spectral shape in the visible, NIR, and MIR spectral regions. I calculated UBVRIJHK absolute magnitudes and colors from this dataset and describe their time-dependent behavior. Future applications of this data set include use as input to space telescope instrument models, data model comparisons using data from interplanetary space craft, accurate modeling of Earthshine radiation in permanently shadowed lunar craters, and test cases for developing spectral retrieval models.

In chapter 4 I demonstrated the detectability of N_2 in Earth's disk-averaged spectrum and quantified its detectability in direct-imaging and transmission spectra for both N_2-H_2O-CO_2 and N_2-H_2 atmospheres. Using data model comparisons of spectra data form the EPOXI mission with synthetic spectra from the VPL spectral Earth model, I showed that $(N_2)_2$ is detectable in disk-integrated observations of the Earth from interplanetary spacecraft, creating a ~35% effect on the spectrum of the Earth at 4.15 μm. This significant because N_2 has often been presumed to be a spectrally inactive molecule with no potentially detectable absorption features, though detecting $(N_2)_2$ will still be difficult due to the low planetary flux at its spectrally active wavelengths. I calculated the strength of the $(N_2)_2$ collisional pair on the combined emission and reflection

spectra of self-consistent N_2-H_2O-CO_2 atmospheres and find a strong spectral response for N_2 abundances greater than 0.5 bar. A detectable amount of N_2 would imply surface pressures high enough to support liquid water. Additionally, recent studies indicate that significant abundances of both N_2 with O_2 together are a stronger and more unambiguous biosignature than O_2 alone. In transmission observations of planets orbiting in the habitable zones of late type stars, I find that $(N_2)_2$ absorption could produce transmission depths of 8-10 ppm at 4.1 μm. I find transit transmission depths several factors larger, up to 50 ppm, for N_2-H_2 atmospheres with larger scale heights. I demonstrated that for both direct imaging and transit transmission spectroscopy, $(N_2)_2$ could significantly widen the width of the 4.3 μm CO_2 band in thick N_2 atmospheres. The detection of N_2 would provide critical contextual information about planetary atmospheres and may be relevant to future exoplanet observing missions. This work also supports the conclusion that N_2 and O_2 together a strong, detectable biosignature pair.

In chapter 5 I showed that recently proposed mechanisms for developing abiotic O_2/O_3 in terrestrial exoplanet atmospheres would produce spectral discriminators that are potentially identifiable with future telescope observations. These discriminants are more detectable than O_2 or O_3 in transmission observations with JWST. CO seen at 2.35 μm or 4.6 μm with CO_2 at 2 or 4.3 μm would indicate robust CO_2 photolysis and suggest a high likelihood of abiotic O_2/O_3 generation. I find that CO in a realistic exoplanet atmosphere orbiting a late type star could be seen with a S/N > 3 at 2.35 μm in *JWST*-NIRISS with as few as 10 transits. O_4 bands seen in transmission or direct-imaging can be diagnostic of high-O_2 post-runaway atmospheres that have experienced a history of H-escape. The 1.06 and 1.27 μm O_4 bands in a massive, O_2-dominated atmosphere without high-altitude aerosols would be potentially detectable with a S/N $\gtrsim$ 3 with as few as 10 transits with *JWST*-NIRISS, assuming photon-limited noise. LUVOIR

would be able to detect visible and near-infrared O_4 bands (at 0.345, 0.36, 0.38, 0.445, 0.475, 0.53, 0.57, and 0.63 μm, 1.06, and 1.27 μm) in the spectra of high-O_2 planets orbiting in the HZ of the nearest late type stars with integration times of order ten hours or less. The detection of these strong O_4 bands would indicate an O_2 atmosphere too massive to have been biologically produced. Taken together these proposed spectral discriminants against "biosignature impostors" provide strategies that will assist us in identifying true evidence for photosynthetic life beyond the solar system.

In chapter 6, I examined the diversity of spectral features of organisms with nonphotosynthetic pigments using laboratory measurements. Using radiative transfer models of 1D and 3D, planet-wide, spatially resolved spectra, I showed that a nonphotosynthetic pigment can create a significant effect in the disk-averaged spectrum of a terrestrial planet, given adequate surface coverage. I calculated broadband colors for a range of pigments and other biological and abiotic surface types in the visible wavelength range considering only their spectral reflectances, and for more realistic scenarios that included an overlying atmosphere and clouds. Highly reflective pigments suspended in water would possess a spectral reflectance that peaks in the visible spectrum, and would exhibit glint at small phase angles, possibly allowing an observer to distinguish between a nonphotosynthetic pigment biosignature and another reflective surface. This work has shown that there is a diverse range of potential surface reflectance biosignatures beyond the commonly considered vegetation "red edge." Suggestive surface features, in conjunction with gaseous biosignatures, would provide stronger evidence that a planet is inhabited than gaseous biosignatures alone.

7.2 FUTURE WORK

As noted in Chapter 1, the "Earth-based" approach to biosignature investigation has several advantages over more exotic and hypothetical approaches, including the certainty that the candidate gases (or surface features) are produced by life and potentially detectable. While modern Earth is currently our only example of a habitable and inhabited planet, our world has maintained many stable (bio)geochemical states throughout its history and would have appeared quite differently to a remote observer at various points in its planetary evolution. For example, a planet in an intermediate redox state, such as Earth during portions of the Proterozoic eon (0.5 – 2.5 Ga), could have contained simultaneously large and detectable quantities of both oxidized and reduced gases (such as O_2/O_3 and CH_4), representing perhaps the most detectable type of biosphere in the universe due to the inferable presence of chemical disequilibrium (Meadows 2006; Kaltenegger et al. 2007). Conversely, recent work (e.g., Planavsky et al. 2014; Lyons et al. 2014) suggests the possibility of very low levels of O_2 and CH_4 during this period and thus a feasible 'false negative' scenario despite the presence of oceans beneath that atmosphere that were teeming with life (primary production of oxygenic photosynthesis was high despite the low O_2 concentrations). This potentially provides a strong contrast to the potential "false positive" scenarios outlined in Section 1.4 and Chapter 5. However, other known biosignature gases such as N_2O, CH_3Cl, and organosulfur gases DMS and DMDS would likely be linked to oxygenic photosynthesis through the total primary productivity of the biosphere and would potentially build up to detectable levels depending on the chemical state of the surface and atmosphere.

Knowledge of the Earth's characteristics in deep time is often difficult, but we are afforded far more knowledge about the young Earth than we will be able to obtain about the current state of most if not all exoplanets. There is therefore a need for a systemized study of the

suite of habitable and detectable environments informed by Earth's early chapters, which requires broadly interdisciplinary knowledge of geology, geochemistry, climatology, photochemistry, spectroscopy, and radiative transfer. By studying the Earth over time we can create a robust library of planetary templates to be searched for elsewhere and mitigate against "false positive" and "false negative" scenarios, increasing our confidence about our search for life outside of our solar system.

The tools used in this dissertation can be brought to bear on the problem by linking them to results from geochemical proxies for the atmospheric composition of the early Earth, and to models that can determine self-consistent fluxes from plausible biogeochemical systems. An example of the latter is the "Grid ENabled Integrated Earth system model" (GENIE) (Ridgwell et al. 2007). GENIE can be used to estimate the flux of biogenic gases from a photosynthetically active ocean, tracing the flux of gases such as O_2, CH_4, and N_2O. The results of GENIE can be linked to the photochemical-climate model (*Atmos*) to evaluate the impact of biogeochemical assumptions on the composition and climate of the early atmosphere. Inversely, the geologic record can provide constraints on those parameters that can then be translated to required fluxes and/or sinks using the photochemical model. Once these results are obtained, they can be iteratively applied to planets with varying types of stellar hosts or other planetary parameters -- which should change both the expected concentration of gases and their relative detectability -- and convolved with radiative transfer and instrument models. This would allow a comprehensive predictive analysis of biosignature detectability with planetary system models that self-consistent link geological, biology, photochemistry, and radiative transfer considerations. The planetary states need not exactly match the Earth's actual geological history, but be plausible planetary states based on physical, chemical, and biological constraints. Figure 7.1 provides an illustration

of this proposed scheme. The pursuit of this type of study would help prepare us to interpret the range of terrestrial habitable zone planets that will be characterized with ground and space-based telescopes in the coming years and decades.

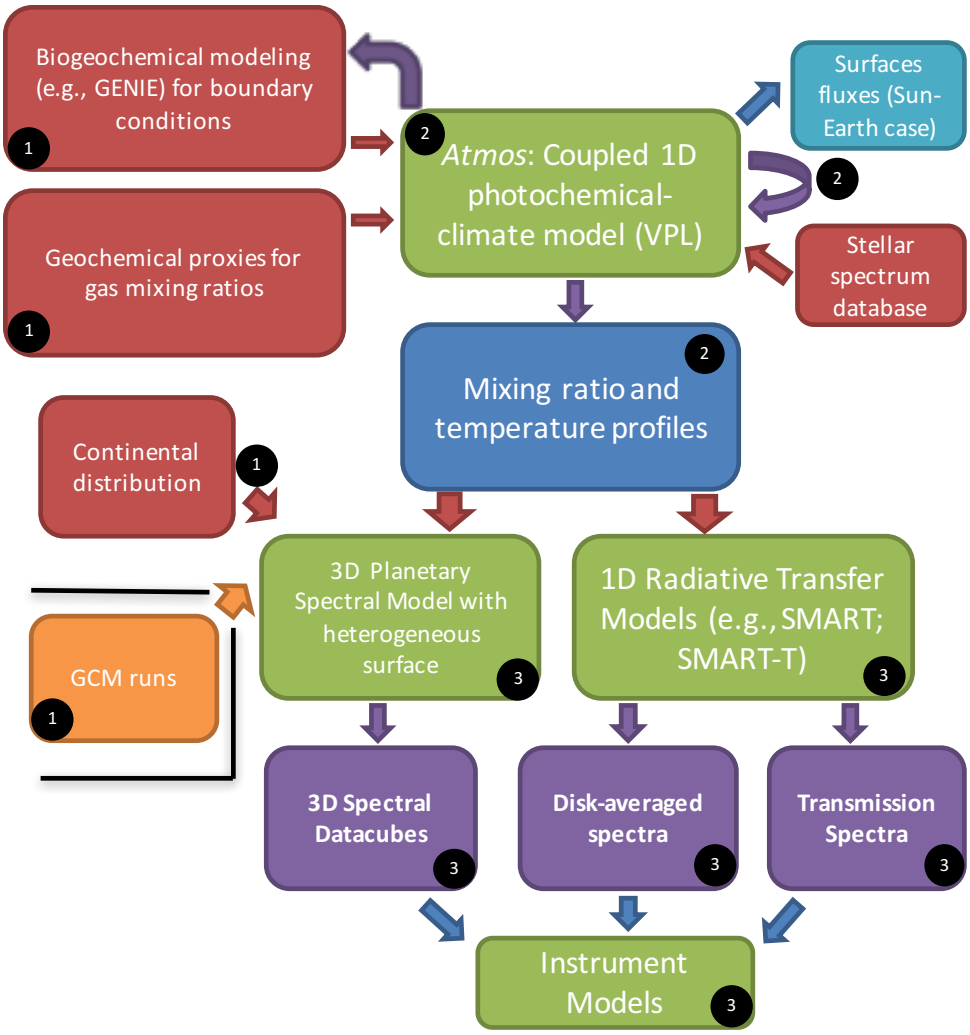

Figure 7.1. Schematic diagram of the inputs, models, and outputs described in Section 7.2 of the text. Inputs to models are in red/orange, models are in green, and model outputs are in purple. Intermediate model outputs are in blue.

BIBLIOGRAPHY

Abe, Y., Abe-Ouchi, A., Sleep, N.H. & Zahnle, K.J. (2011) Habitable zone limits for dry planets. *Astrobiology* 11:443–60.

Allard, F. & Hauschildt, P.H. (1995) Model atmospheres for M (sub)dwarf stars. 1: The base model grid. *The Astrophysical Journal* 445:433.

Allen, C.W. (1964) *Allen's Astrophysical Quantities*, Athlone Press.

Archetti, M., Döring, T.F., Hagen, S.B., Hughes, N.M., Leather, S.R., Lee, D.W., Lev-Yadun, S., Manetas, Y., Ougham, H.J., Schaberg, P.G. & Thomas, H. (2009) Unravelling the evolution of autumn colours: an interdisciplinary approach. *Trends in ecology & evolution* 24:166–73.

Arney, G., Domagal-Goldman, S.D., Meadows, V.S., Wolf, E., Schwieterman, E.W., Charnay, B. & Claire, M.W. (2016) The Pale Orange Dot: The Spectrum and Climate of Hazy Archean Earth. *Astrobiology* in press.

Arney, G., Meadows, V., Crisp, D., Schmidt, S.J., Bailey, J. & Robinson, T. (2014) Spatially-resolved measurements of H2O, HCl, CO, OCS, SO2 , cloud opacity, and acid concentration in the Venus near-infrared spectral windows. *Journal of Geophysical Research: Planets* 119:1860–1891.

Arnold, L., Bréon, F.-M. & Brewer, S. (2009) The Earth as an extrasolar planet: The vegetation spectral signature today and during the last Quaternary climatic extrema. *International Journal of Astrobiology* 8:81–94.

Aumann, H.H., Chahine, M.T., Gautier, C., Goldberg, M.D., Kalnay, E., McMillin, L.M., Revercomb, H., Rosenkranz, P.W., Smith, W.L., Staelin, D.H., Strow, L.L. & Susskind, J. (2003) AIRS/AMSU/HSB on the aqua mission: Design, science objectives, data products, and processing systems. *IEEE Transactions on Geoscience and Remote Sensing* 41:253–263.

Baldridge, A.M., Hook, S.J., Grove, C.I. & Rivera, G. (2009) The ASTER spectral library version 2.0. *Remote Sensing of Environment* 113:711–715.

Batalha, N.M., Rowe, J.F., Bryson, S.T., Barclay, T., Burke, C.J., Caldwell, D. a., Christiansen, J.L., Mullally, F., Thompson, S.E., Brown, T.M., Dupree, A.K., Fabrycky, D.C., Ford, E.B., Fortney, J.J., Gilliland, R.L., Isaacson, H., Latham, D.W., Marcy, G.W., Quinn, S.N., et al. (2013) Planetary Candidates Observed By Kepler . Iii. Analysis of the First 16 Months of Data. *The Astrophysical Journal Supplement Series* 204:24.

Beer, R., Glavich, T.A. & Rider, D.M. (2001) Tropospheric emission spectrometer for the Earth Observing System's Aura satellite. *Applied Optics* 40:2356.

Benneke, B. & Seager, S. (2012) Atmospheric Retrieval for Super-Earths: Uniquely Constraining the Atmospheric Composition With Transmission Spectroscopy. *The Astrophysical Journal* 753:100.

Bennett, J.W. & Bentley, R. (2000) Seeing red: the story of prodigiosin. *Advances in applied microbiology* 47:1–32.

Berta-Thompson, Z.K., Irwin, J., Charbonneau, D., Newton, E.R., Dittmann, J.A., Astudillo-Defru, N., Bonfils, X., Gillon, M., Jehin, E., Stark, A.A., Stalder, B., Bouchy, F., Delfosse, X., Forveille, T., Lovis, C., Mayor, M., Neves, V., Pepe, F., Santos, N.C., et al. (2015) A rocky planet transiting a nearby low-mass star. *Nature* 527:204–207.

Bessell, M.S. (1983) VRI photometry - an addendum. *Publications of the Astronomical Society of the Pacific* 95:480.

Bessell, M.S. & Brett, J.M. (1988) JHKLM photometry - Standard systems, passbands, and intrinsic colors. *Publications of the Astronomical Society of the Pacific* 100:1134.

Bétrémieux, Y. & Kaltenegger, L. (2014) Impact of Atmospheric Refraction: How Deeply can we Probe Exo-Earth's Atmospheres During Primary Eclipse Observations? *The Astrophysical Journal* 791:7.

Bétrémieux, Y. & Kaltenegger, L. (2013) Transmission Spetrum of Earth as a Transiting Exoplanet from the Ultraviolet to the Near-Infrared. *The Astrophysical Journal* 772:L31.

Boichenko, V. a, Wang, J.M., Antón, J., Lanyi, J.K. & Balashov, S.P. (2006) Functions of carotenoids in xanthorhodopsin and archaerhodopsin, from action spectra of photoinhibition of cell respiration. *Biochimica et biophysica acta* 1757:1649–56.

Borysow, A. & Frommhold, L. (1986) Collision-induced rototranslational absorption spectra of N2-N2 pairs for temperatures from 50 to 300 K. *The Astrophysical Journal* 311:1043.

Bosak, T., Greene, S.E. & Newman, D.K. (2007) A likely role for anoxygenic photosynthetic microbes in the formation of ancient stromatolites. *Geobiology* 5:119–126.

Brasier, M.D., Antcliffe, J., Saunders, M. & Wacey, D. (2015) Changing the picture of Earth's earliest fossils (3.5–1.9 Ga) with new approaches and new discoveries. *Proceedings of the National Academy of Sciences* 112:4859–4864.

Brock, T.D. & Freeze, H. (1969) Thermus aquaticus gen. n. and sp. n., a Non-sporulating Extreme Thermophile. *Journal of Bacteriology* 98:289–297.

Broschat, S.L., Loge, F.J., Peppin, J.D., White, D., Call, D.R. & Kuhn, E. (2014) Optical reflectance assay for the detection of biofilm formation. *Journal of biomedical optics* 10:44027.

Buick, R. (2007) Did the Proterozoic Canfield Ocean cause a laughing gas greenhouse? *Geobiology* 5:97–100.

Buick, R. (2008) When did oxygenic photosynthesis evolve? *Royal Society of London Philosophical Transactions Series B* 363:2731–2743.

Burke, C.J., Bryson, S.T., Mullally, F., Rowe, J.F., Christiansen, J.L., Thompson, S.E., Coughlin, J.L., Haas, M.R., Batalha, N.M., Caldwell, D. a., Jenkins, J.M., Still, M., Barclay, T., Borucki, W.J., Chaplin, W.J., Ciardi, D.R., Clarke, B.D., Cochran, W.D., Demory, B.-O., et al. (2014) Planetary Candidates Observed By Kepler Iv: Planet Sample From Q1-Q8 (22 Months). *The Astrophysical Journal Supplement Series* 210:19.

Burt, J. & Smith, B. (2012) Deep Space Climate Observatory: The DSCOVR mission. In *2012 IEEE Aerospace Conference*. IEEE, pp. 1–13.

Cao, C., Love, G.D., Hays, L.E., Wang, W., Shen, S. & Summons, R.E. (2009) Biogeochemical evidence for euxinic oceans and ecological disturbance presaging the end-Permian mass extinction event. *Earth and Planetary Science Letters* 281:188–201.

Cash, W. (2006) Detection of Earth-like planets around nearby stars using a petal-shaped occulter. *Nature* 442:51–3.

Catling, D.C. (2014) The Great Oxidation Event Transition. In *Treatise on Geochemistry*. Elsevier, pp. 177–195.

Cenarro, A.J., Peletier, R.F., Sanchez-Blazquez, P., Selam, S.O., Toloba, E., Cardiel, N., Falcon-Barroso, J., Gorgas, J., Jimenez-Vicente, J. & Vazdekis, A. (2007) Medium-resolution Isaac Newton Telescope library of empirical spectra - II. The stellar atmospheric parameters. *Monthly Notices of the Royal Astronomical Society* 374:664–690.

Chassefière, E. (1996a) Hydrodynamic escape of hydrogen from a hot water-rich atmosphere: The case of Venus. *Journal of Geophysical Research: Planets* 101:26039–26056.

Chassefière, E. (1996b) Hydrodynamic escape of oxygen from primitive atmospheres: applications to the cases of Venus and Mars. *Icarus* 552:537–552.

Chen, M.-Y., Wu, S.-H., Lin, G.-H., Lu, C.-P., Lin, Y.-T., Chang, W.-C. & Tsay, S.-S. (2004) Rubrobacter taiwanensis sp. nov., a novel thermophilic, radiation-resistant species isolated from hot springs. *International journal of systematic and evolutionary microbiology* 54:1849–55.

Chittka, L. & Raine, N.E. (2006) Recognition of flowers by pollinators. *Current opinion in plant biology* 9:428–35.

Claire, M.W., Kasting, J.F., Domagal-Goldman, S.D., Stüeken, E.E., Buick, R. & Meadows, V.S. (2014) Modeling the signature of sulfur mass-independent fractionation produced in the Archean atmosphere. *Geochimica et Cosmochimica Acta* 141:365–380.

Clark, R.N., Swayze, G.A., Wise, R., Livo, E., Hoefen, T., Kokaly, R. & Sutley, S.J. (2007) USGS digital spectral library splib06a: *U.S. Geological Survey, Digital Data Series 231, http://speclab.cr.usgs.gov/spectral.lib06*.

Clayton, R.K. (1966) Spectroscopic Analysis of Bacteriochlorophylls in vitro and in vivo. *Photochemistry and Photobiology* 5:669–677.

Clough, S.A., Kneizys, F.X. & Davies, R.W. (1989) Line shape and the water vapor continuum. *Atmospheric Research* 23:229–241.

Cockell, C.S., Léger, A., Fridlund, M., Herbst, T.M., Kaltenegger, L., Absil, O., Beichman, C., Benz, W., Blanc, M., Brack, A., Chelli, A., Colangeli, L., Cottin, H., Coudé du Foresto, F., Danchi, W.C., Defrère, D., den Herder, J.-W., Eiroa, C., Greaves, J., et al. (2009) Darwin--a mission to detect and search for life on extrasolar planets. *Astrobiology* 9:1–22.

Cogdell, R.J., Howard, T.D., Bittl, R., Schlodder, E., Geisenheimer, I. & Lubitz, W. (2000) How carotenoids protect bacterial photosynthesis. *Philosophical transactions of the Royal Society of London. Series B, Biological sciences* 355:1345–1349.

Cowan, N.B. (2009) *Exo-cartography: Time-resolved photometry of exoplanets*. Proquest Dissertations And Theses 2009. Section 0250, Part 0590 [Ph.D. dissertation].United States -- Washington: University of Washington; 2009. Publication Number: AAT 0822330. Source: DAI-B 71/02, Aug 2010

Cowan, N.B., Agol, E., Meadows, V.S., Robinson, T., Livengood, T. a., Deming, D., Lisse, C.M., A'Hearn, M.F., Wellnitz, D.D., Seager, S. & Charbonneau, D. (2009) Alien Maps of an Ocean-Bearing World. *The Astrophysical Journal* 700:915–923.

Cowan, N.B., Greene, T., Angerhausen, D., Batalha, N.E., Clampin, M., Colón, K., Crossfield, I.J.M., Fortney, J.J., Gaudi, B.S., Harrington, J., Iro, N., Lillie, C.F., Linsky, J.L., Lopez-Morales, M., Mandell, A.M. & Stevenson, K.B. (2015) Characterizing Transiting Planet Atmospheres through 2025. *Publications of the Astronomical Society of the Pacific* 127:311–327.

Cowan, N.B., Robinson, T., Livengood, T. a., Deming, D., Agol, E., A'Hearn, M.F., Charbonneau, D., Lisse, C.M., Meadows, V.S., Seager, S., Shields, A.L. & Wellnitz, D.D. (2011) Rotational Variability of Earth's Polar Regions: Implications for Detecting Snowball Planets. *The Astrophysical Journal* 731:19.

Cowan, N.B. & Strait, T.E. (2013) Determining Reflectance Spectra of Surfaces and Clouds on Exoplanets. *The Astrophysical Journal* 765:L17.

Cox, C. & Munk, W. (1954) Measurement of the Roughness of the Sea Surface from Photographs of the Sun's Glitter. *Journal of the Optical Society of America* 44:838.

Cox, M.M. & Battista, J.R. (2005) Deinococcus radiodurans - the consummate survivor. *Nature reviews. Microbiology* 3:882–92.

Crisp, D. (1997) Absorption of Sunlight by Water Vapor in Cloudy Conditions: A Partial Explanation for the Cloud Absorption Anomaly. *Geophysical Research Letters* 24:571–574.

Crisp, D. (1986) Radiative forcing of the Venus mesosphere. *Icarus* 514:484–514.

Crossfield, I.J.M., Knutson, H., Fortney, J., Showman, A.P., Cowan, N.B. & Deming, D. (2012) Spitzer /MIPS 24 μm Observations of HD 209458b: Three Eclipses, Two and a Half Transits, and a Phase Curve Corrupted by Instrumental Sensitivity Variations. *The Astrophysical Journal* 752:81.

Crow, C.A., McFadden, L.A., Robinson, T., Livengood, T.A., Hewagama, T., Barry, R.K., Deming, L.D., Meadows, V. & Lisse, C.M. (2010) Views from EPOXI. Colors in Our Solar System as an Analog for Extrasolar Planets. *The Astrophysical Journal* 729:130.

Dadachova, E., Bryan, R.A., Huang, X., Moadel, T., Schweitzer, A.D., Aisen, P., Nosanchuk, J.D. & Casadevall, A. (2007) Ionizing radiation changes the electronic properties of melanin and enhances the growth of melanized fungi. J. Rutherford, ed. *PloS one* 2:e457.

Dalcanton, J., Seager, S., Aigrain, S., Hirata, C., Battel, S., Mather, J., Brandt, N., Postman, M., Conroy, C., Redding, D., Feinberg, L., Schiminiovich, D., Gezari, S., Stahl, H., P., Guyon, O., Tumilinson, J. & Harris, W. (2015) From Cosmic Birth to Living Earths: The Future of UVOIR Space Astronomy. *From Cosmic Births to Living Earths Report. (Washington, DC: Association for Research in Astronomy), http://www.hdstvision.org/report/*.

Dalton, J.B., Mogul, R., Kagawa, H.K., Chan, S.L. & Jamieson, C.S. (2003) Near-infrared detection of potential evidence for microscopic organisms on Europa. *Astrobiology* 3:505–529.

Dalton, J.B., Palmer-Moloney, L.J., Rogoff, D., Hlavka, C. & Duncan, C. (2009) Remote monitoring of hypersaline environments in San Francisco Bay, CA, USA. *International Journal of Remote Sensing* 30:2933–2949.

Dartnell, L. (2011) Biological constraints on habitability. *Astronomy & Geophysics* 52:1.25–1.28.

DasSarma, S. (2006) Extreme halophiles are models for astrobiology. *Microbe-American Society for Microbiology* 1:120–126.

Decho, A.W., Kawaguchi, T., Allison, M.A., Louchard, E.M., Reid, R.P., Stephens, F.C., Voss, K.J., Wheatcroft, R.A. & Taylor, B.B. (2003) Sediment properties influencing upwelling spectral reflectance signatures: The "biofilm gel effect". *Limnology and Oceanography* 48:431–443.

Deming, D., Seager, S., Winn, J., Miller-Ricci, E., Clampin, M., Lindler, D., Greene, T., Charbonneau, D., Laughlin, G., Ricker, G., Latham, D. & Ennico, K. (2009) Discovery and Characterization of Transiting SuperEarths Using an All-Sky Transit Survey and Follow-up by the James Webb Space Telescope. *Publications of the Astronomical Society of the Pacific* 121:952–967.

Demore, W.B., Sander, S.P., Golden, D.M., Hampson, R.F., Kurylo, M.J., Howard, C.J., Ravishankara, A.R., Kolb, C.E. & Molina, M.J. (1997) Chemical Kinetics and Photochemical Data for Use in Stratospheric Modeling Evaluation Number 12 NASA Panel for Data Evaluation.

Demory, B.-O., Torres, G., Neves, V., Rogers, L., Gillon, M., Horch, E., Sullivan, P., Bonfils, X., Delfosse, X., Forveille, T., Lovis, C., Mayor, M., Santos, N., Seager, S., Smalley, B. & Udry, S. (2013) Spitzer Observations of GJ3470b: a Very Low-density Neptune-size Planet Orbiting a Metal-rich M dwarf. :9.

Des Marais, D. J. & Walter, M.. R.. (1999) Astrobiology: Exploring the Origins, Evolution, and Distribution of Life in the Universe. *Annual Review of Ecology and Systematics* 30:397–420.

Des Marais, D.J., Harwit, M.O., Jucks, K.W., Kasting, J.F., Lin, D.N.C., Lunine, J.I., Schneider, J., Seager, S., Traub, W.A. & Woolf, N.J. (2002) Remote sensing of planetary properties and biosignatures on extrasolar terrestrial planets. *Astrobiology* 2:153–181.

De sMarais, D.J., Nuth, J. a, Allamandola, L.J., Boss, A.P., Farmer, J.D., Hoehler, T.M., Jakosky, B.M., Meadows, V.S., Pohorille, A., Runnegar, B. & Spormann, A.M. (2008) The NASA Astrobiology Roadmap. *Astrobiology* 8:715–30.

Dogs, M., Voget, S., Teshima, H., Petersen, J., Davenport, K., Dalingault, H., Chen, A., Pati, A., Ivanova, N., Goodwin, L.A., Chain, P., Detter, J.C., Standfest, S., Rohde, M., Gronow, S., Kyrpides, N.C., Woyke, T., Simon, M., Klenk, H., et al. (2013) Genome sequence of Phaeobacter inhibens type strain (T5(T)), a secondary metabolite producing representative of the marine Roseobacter clade, and emendation of the species description of Phaeobacter inhibens. *Standards in genomic sciences* 9:334–50.

Domagal-Goldman, S.D., Meadows, V.S., Claire, M.W. & Kasting, J.F. (2011) Using Biogenic Sulfur Gases as Remotely Detectable Biosignatures on Anoxic Planets. *Astrobiology* 11:419–441.

Domagal-Goldman, S.D., Segura, A., Claire, M.W., Robinson, T.D. & Meadows, V.S. (2014) Abiotic Ozone and Oxygen in Atmospheres Similar to Prebiotic Earth. *The Astrophysical Journal* 792:43.

Doyon, R., Lafrenière, D., Albert, L., Artigau, E., Meyer, M. & Jayawardhana, R. (2014) Transit Spectroscopy with NIRISS on JWST. *Search for Life Beyond the Solar System. Exoplanets, Biosignatures, and Instruments*:id. 3.6.

Dressing, C.D. & Charbonneau, D. (2013) The Occurrence Rate of Small Planets around Small Stars. *The Astrophysical Journal* 767:20.

Driscoll, P. & Barnes, R. (2015) Tidal Heating of Earth-like Exoplanets around M Stars: Thermal, Magnetic, and Orbital Evolutions. *Astrobiology* 15:739–760.

Durán, N., Justo, G.Z., Ferreira, C. V, Melo, P.S., Cordi, L. & Martins, D. (2007) Violacein: properties and biological activities. *Biotechnology and applied biochemistry* 48:127–33.

Esteves, L.J., De Mooij, E.J.W. & Jayawardhana, R. (2013) Optical Phase Curves of Kepler Exoplanets. *The Astrophysical Journal* 772:51.

Farmer, C.B. & Houghton, J.T. (1966) Collision-induced Absorption in the Earth's Atmosphere. *Nature* 209:1341–1342.

Ferruit, P., Birkmann, S., Böker, T., Sirianni, M., Giardino, G., de Marchi, G., Alves de Oliveira, C. & Dorner, B. (2014) Observing transiting exoplanets with JWST/NIRSpec J. M. Oschmann et al., eds. *SPIE* 9143:91430A.

Flückiger, J., Monnin, E., Stauffer, B., Schwander, J., Stocker, T.F., Chappellaz, J., Raynaud, D. & Barnola, J.-M. (2002) High-resolution Holocene N2O ice core record and its relationship with CH4 and CO2. *Global Biogeochemical Cycles* 16:10–1–10–8.

Fortney, J.J. (2005) The effect of condensates on the characterization of transiting planet atmospheres with transmission spectroscopy. *Monthly Notices of the Royal Astronomical Society* 364:649–653.

Fortney, J.J., Robinson, T.D., Domagal-Goldman, S., Amundsen, D.S., Brogi, M., Claire, M., Crisp, D., Hebrard, E., Imanaka, H., de Kok, R., Marley, M.S., Teal, D., Barman, T., Bernath, P., Burrows, A., Charbonneau, D., Freedman, R.S., Gelino, D., Helling, C., et al. (2016) The Need for Laboratory Work to Aid in The Understanding of Exoplanetary Atmospheres. *arXiv preprint: 1602.06305*.

Fraine, J., Deming, D., Benneke, B., Knutson, H., Madhusudhan, N., Wilkins, A. & Todorov, K. (2014) Water vapour absorption in the clear atmosphere of a Neptune-sized exoplanet. *Nature* 513:556–529.

France, K., Froning, C.S., Linsky, J.L., Roberge, A., Stocke, J.T., Tian, F., Bushinsky, R., Désert, J.-M., Mauas, P., Vieytes, M. & Walkowicz, L.M. (2013) The Ultraviolet Radiation Environment Around M Dwarf Exoplanet Host Stars. *The Astrophysical Journal* 763:149.

Frommhold, L. (1993) *Collision-induced absorption in gases* 1st ed., Cambridge, UK: Cambridge University Press.

Fujii, Y., Kawahara, H., Suto, Y., Fukuda, S., Nakajima, T., Livengood, T. a. & Turner, E.L. (2011) Colors of a Second Earth. Ii. Effects of Clouds on Photometric Characterization of Earth-Like Exoplanets. *The Astrophysical Journal* 738:184.

Fujii, Y., Turner, E.L. & Suto, Y. (2013) Variability of Water and Oxygen Absorption Bands in the Disk-Integrated Spectra of Earth. *The Astrophysical Journal* 765:76.

Gao, P., Hu, R., Robinson, T.D., Li, C. & Yung, Y.L. (2015) Stability of CO2 Atmospheres on Dessicated M Dwarf Exoplanets. *The Astrophysical Journal* 806:249.

García Muñoz, A., Zapatero Osorio, M.R., Barrena, R., Montañés-Rodríguez, P., Martín, E.L. & Pallé, E. (2012) Glancing Views of the Earth: from a Lunar Eclipse to an Exoplanetary Transit. *The Astrophysical Journal* 755:103.

Gates, D.M., Keegan, H.J., Schleter, J.C. & Weidner, V.R. (1965) Spectral Properties of Plants. *Applied Optics* 4:11.

Gavrish, E.I., Krauzova, V.I., Potekhina, N. V, Karasev, S.G., Plotnikova, E.G., Altyntseva, O. V, Korosteleva, L.A. & Evtushenko, L.I. (2004) [Three new species of brevibacteria--Brevibacterium antiquum sp. nov., Brevibacterium aurantiacum sp. nov. and Brevibacterium permense sp. nov]. *Mikrobiologiia* 73:218–25.

Gilli, G., López-Valverde, M.A., Drossart, P., Piccioni, G., Erard, S. & Cardesín Moinelo, A. (2009) Limb observations of CO2 and CO non-LTE emissions in the Venus atmosphere by VIRTIS/Venus Express. *Journal of Geophysical Research* 114:E00B29.

Gillon, M., Jehin, E., Lederer, S.M., Delrez, L., de Wit, J., Burdanov, A., Van Grootel, V., Burgasser, A.J., Triaud, A.H.M.J., Opitom, C., Demory, B.-O., Sahu, D.K., Bardalez Gagliuffi, D., Magain, P. & Queloz, D. (2016) Temperate Earth-sized planets transiting a nearby ultracool dwarf star. *Nature* 533:221–224.

Giorgi, F. & Chameides, W.L. (1985) Rainout parameterization in a photochemical model. *Journal of Geophysical Research* 90:7872–7880.

Giorgini, J.D., Yeomans, D.K., Chamberlin, A.B., Chodas, P.W., Jacobson, R.A., Keesey, M.S., Lieske, J.H., Ostro, S.J., Standish, E.M. & Wimberly, R.N. (1996) JPL's On-Line Solar System Data Service. *American Astronomical Society, DPS meeting #28, id.25.04; Bulletin of the American Astronomical Society, Vol. 28, p.1158* 28:1158.

Glaeser, J. & Klug, G. (2005) Photo-oxidative stress in Rhodobacter sphaeroides: protective role of carotenoids and expression of selected genes. *Microbiology (Reading, England)* 151:1927–38.

Glenar, D., Stubbs, T., Schwieterman, E., Robinson, T. & Livengood, T. (2016) Earthshine as an Illumination Source in the Moon's Permanently Shadowed Regions. in prep.

Goldblatt, C., Claire, M.W., Lenton, T.M., Matthews, A.J., Watson, A.J. & Zahnle, K.J. (2009) Nitrogen-enhanced greenhouse warming on early Earth. *Nature Geoscience* 2:891–896.

Goldblatt, C. & Zahnle, K.J. (2011) Clouds and the Faint Young Sun Paradox. *Climate of the Past* 7:203–220.

González, J.E. & Keshavan, N.D. (2006) Messing with bacterial quorum sensing. *Microbiology and molecular biology reviews : MMBR* 70:859–75.

Goody, R.M. & Yung, Y.L. (1989) *Atmospheric Radiation, A Theoretical Basis*, New York, NY: Oxford University Press.

Gorski, K.M., Hivon, E., Banday, A.J., Wandelt, B.D., Hansen, F.K., Reinecke, M. & Bartelman, M. (2005) HEALPix -- a Framework for High Resolution Discretization, and Fast Analysis of Data Distributed on the Sphere. *The Astrophysical Journal* 622:759–771.

Greenblatt, C.L., Baum, J., Klein, B.Y., Nachshon, S., Koltunov, V. & Cano, R.J. (2004) Micrococcus luteus-survival in amber. *Microbial Ecology* 48:120–127.

Greenblatt, G.D., Orlando, J.J., Burkholder, J.B. & Ravishankara, a. R. (1990) Absorption measurements of oxygen between 330 and 1140 nm. *Journal of Geophysical Research* 95:18577.

Grote, M. & O'Malley, M.A. (2011) Enlightening the life sciences: the history of halobacterial and microbial rhodopsin research. *FEMS microbiology reviews* 35:1082–99.

Grundy, W.M. & Fink, U. (1991) The absorption coefficient of the liquid N2 2.15-micron band and application to Triton. *Icarus* 93:169–173.

Haddix, P.L., Jones, S., Patel, P., Burnham, S., Knights, K., Powell, J.N. & LaForm, A. (2008) Kinetic analysis of growth rate, ATP, and pigmentation suggests an energy-spilling function for the pigment prodigiosin of Serratia marcescens. *Journal of bacteriology* 190:7453–63.

Haddock, S.H.D., Moline, M.A. & Case, J.F. (2010) Bioluminescence in the Sea. *Annual Review of Marine Science* 2:443–493.

Halevy, I., Pierrehumbert, R.T. & Schrag, D.P. (2009) Radiative transfer in CO2 -rich paleoatmospheres. *Journal of Geophysical Research* 114:D18112.

Hall, D.K., Riggs, G. a & Salomonson, V. V (1995) Development of methods for mapping global snow cover using moderate resolution imaging spectroradiometer data. *Remote Sensing of Environment* 54:127–140.

Hampton, D.L., Baer, J.W., Huisjen, M.A., Varner, C.C., Delamere, A., Wellnitz, D.D., Hearn, M.F. a & Klaasen, K.P. (2005) An Overview of the Instrument Suite for the Deep Impact Mission. *Space Science Reviews* 117:43–93.

Han, E., Wang, S.X., Wright, J.T., Feng, Y.K., Zhao, M., Fakhouri, O., Brown, J.I. & Hancock, C. (2014) Exoplanet Orbit Database. II. Updates to Exoplanets.org. *Publications of the Astronomical Society of the Pacific* 126:827–837.

Haqq-Misra, J.D., Domagal-Goldman, S.D., Kasting, P.J. & Kasting, J.F. (2008) A revised, hazy methane greenhouse for the Archean Earth. *Astrobiology* 8:1127–1137.

Harman, C.E., Schwieterman, E.W., Schottelkotte, J.C. & Kasting, J.F. (2015) Abiotic O2 Levels on Planets Around F, G, K, and M Stars: Possible False Positives for Life? *The Astrophysical Journal* 812:137.

Hays, Lindsay E., Archenbach, L., Bailey, J., Barnes, R., Barros, J., Bertka, C., Boston, P., Boyd, E., Cable, M., Chen, I., Ciesa, F., Des Marai, D., Domagal-Goldman, S., Cook, J.E., Goldman, A., Hud, N., Laine, P., Lloyd, K., Lyons, T., Meadows, V., et al. (2015) 2015 NASA Astrobiology Strategy. :1–235.

Hegde, S. & Kaltenegger, L. (2013) Colors of extreme exo-Earth environments. *Astrobiology* 13:47–56.

Hejazi, A. & Falkiner, F.R. (1997) Serratia marcescens. *Journal of Medical Microbiology* 46:903–912.

Henyey, L.C. & Greenstein, J.L. (1941) Diffuse radiation in the Galaxy. *The Astrophysical Journal* 93:70.

Hermans, C., Vandaele, A.C., Carleer, M., Fally, S., Colin, R., Jenouvrier, A., Coquart, B. & Mérienne, M.-F. (1999) Absorption cross-sections of atmospheric constituents: NO2, O2, and H2O. *Environmental Science and Pollution Research* 6:151–158.

Hirono, M. & Nakazawa, T. (1982) The shape of spectral lines with combined impact and statistical broadenings. *Journal of the Physical Society of Japan* 51:265–268.

Hitchcock, D.R. & Lovelock, J.E. (1967) Life detection by atmospheric analysis. *Icarus* 7:149–159.

Hohmann-Marriott, M.F. & Blankenship, R.E. (2012) *Photosynthesis* J. J. Eaton-Rye, B. C. Tripathy, & T. D. Sharkey, eds., Dordrecht: Springer Netherlands.

Hurley, J., Irwin, P.G.J., Adriani, A., Moriconi, M., Oliva, F., Capaccioni, F., Smith, A., Filacchione, G., Tosi, F. & Thomas, G. (2014) Analysis of Rosetta/VIRTIS spectra of earth using observations from ENVISAT/AATSR, TERRA/MODIS and ENVISAT/SCIAMACHY, and radiative-transfer simulations. *Planetary and Space Science* 90:37–59.

Irwin, P.G., Barstow, J.K., Bowles, N.E., Fletcher, L.N., Aigrain, S. & Lee, J.M. (2014) The Transit Spectra of Earth and Jupiter. *Icarus* 242:1–53.

Johnson, B. & Goldblatt, C. (2015) The nitrogen budget of Earth. *Earth Science Reviews* 148:150–173.

Jorgensen, B.B. & Des Marais, D.J. (1988) Optical properties of benthic photosynthetic communities: fiber-optic studies of cyanobacterial mats. *Limnology and oceanography* 33:99–113.

Joshi, M. (2003) Climate Model Studies of Synchronously Rotating Planets. *Astrobiology* 3:415–427.

Joshi, M.M. & Haberle, R.M. (2012) Suppression of the Water Ice and Snow Albedo Feedback on Planets Orbiting Red Dwarf Stars and the Subsequent Widening of the Habitable Zone. *Astrobiology* 12:3–8.

Kaltenegger, L. & Selsis, F. (2007) Biomarkers set in context. In *Extrasolar planets: formation, detection and dynamics*. pp. 79–98 (ArXiv: 0710.0881).

Kaltenegger, L., Traub, W.A. & Jucks, K.W. (2007) Spectral Evolution of an Earth-like Planet. *The Astrophysical Journal* 658:598–616.

Kane, S.R., Hill, M.L., Kasting, J.F., Kopparapu, R.K., Quintana, E. V., Barclay, T., Batalha, N.M., Borucki, W.J., Ciardi, D.R., Haghighipour, N., Hinkel, N.R., Kaltenegger, L., Selsis, F. & Torres, G. (2016) A Catalog of Kepler Habitable Zone Exoplanet Candidates. *Astrophysical Journal* Accepted (ArXiv: 1608.00620).

Karakla, D., Beck., T., Blair, W., Keyes, C., Muzerolle, J., Pontoppidan, K., Soderblom, D., Tumlinson, J. & Valenti, J. (2010) Further Definition of the NIRSpec Science Templates. *Document JWST-STScI-002129, SM-12 (Baltimore, MD: Space Telescope Science Institute)*.

Karalidi, T., Stam, D.M., Snik, F., Bagnulo, S., Sparks, W.B. & Keller, C.U. (2012) Observing the Earth as an exoplanet with LOUPE, the lunar observatory for unresolved polarimetry of Earth. *Planetary and Space Science* 74:202–207.

Kasting, J.F. (2001) Earth History: The Rise of Atmospheric Oxygen. *Science* 293:819–820.

Kasting, J.F. (1988) Runaway and moist greenhouse atmospheres and the evolution of Earth and Venus. *Icarus* 74:472–494.

Kasting, J.F. & Ackerman, T.P. (1986) Climatic consequences of very high carbon dioxide levels in the earth's early atmosphere. *Science* 234:1383–1385.

Kasting, J.F. & Donahue, T.M. (1980) The evolution of atmospheric ozone. *Journal of Geophysical Research* 85:3255.

Kasting, J.F., Liu, S.C. & Donahue, T.M. (1979) Oxygen Levels in the Prebiological Atmosphere. *Journal of Geophysical Research* 84:3097–3207.

Kasting, J.F. & Pollack, J.B. (1983) Loss of water from Venus. I. Hydrodynamic escape of hydrogen. *Icarus* 53:479–508.

Kasting, J.F., Pollack, J.B. & Ackerman, T.P. (1984) Response of Earth's atmosphere to increases in solar flux and implications for loss of water from Venus. *Icarus* 57:335–55.

Kasting, J.F., Whitmire, D.P. & Reynolds, R.T. (1993) Habitable zones around main sequence stars. *Icarus* 101:108–128.

Kasting, J.F., Zahnle, K.J., Pinto, J.P. & Young, A.T. (1989) Sulfur, ultraviolet radiation, and the early evolution of life. *Origins of Life and Evolution of the Biosphere* 19:95–108.

Katsaros, K., Forde, E.B., Chang, P. & Liu, W.T. (2001) QuickSCAT's SeaWinds facilitates early identification of tropical depressions in 1999 hurricane season. *Geophysical Research Letters* 28:1043–1046.

Kawahara, H. (2016) Frequency Modulation Of Directly Imaged Exoplanets: Geometric Effect As A Probe Of Planetary Obliquity. *The Astrophysical Journal* 822:112.

Kawahara, H. & Fujii, Y. (2011) Mapping Clouds And Terrain Of Earth-like Planets From Photometric Variability: Demonstration With Planets In Face-on Orbits. *The Astrophysical Journal* 739:L62.

Kawahara, H., Matsuo, T., Takami, M., Fujii, Y., Kotani, T., Murakami, N., Tamura, M. & Guyon, O. (2012) Can Ground-based Telescopes Detect The Oxygen 1.27 μm Absorption Feature As A Biomarker In Exoplanets? *The Astrophysical Journal* 758:13.

Keeling, C.D. (1960) The Concentration and Isotopic Abundances of Carbon Dioxide in the Atmosphere. *Tellus* 12:200–203.

Keeling, C.D., Chin, J.F.S. & Whorf, T.P. (1996) Increased activity of northern vegetation inferred from atmospheric CO2 measurements. *Nature* 382:146–149.

Khalil, M.A.K. & Rasmussen, R.A. (1983) Sources, sinks, and seasonal cycles of atmospheric methane. *Journal of Geophysical Research* 88:5131.

Kiang, N.Y., Segura, A., Tinetti, G., Govindjee, Blankenship, R.E., Cohen, M., Siefert, J., Crisp, D. & Meadows, V.S. (2007b) Spectral signatures of photosynthesis. II. Coevolution with other stars and the atmosphere on extrasolar worlds. *Astrobiology* 7:252–74.

Kiang, N.Y., Siefert, J., Govindjee & Blankenship, R.E. (2007a) Spectral Signatures of Photosynthesis. I. Review of Earth Organisms. *Astrobiology* 7:222–251.

Kimmel, K.E. & Maier, S. (1969) Effect of cultural conditions on the synthesis of violacein in mesophilic and psychrophilic strains of Chromobacterium. *Canadian journal of microbiology* 15:111–6.

Kimura, H., Asada, R., Masta, A. & Naganuma, T. (2003) Distribution of microorganisms in the subsurface of the manus basin hydrothermal vent field in Papua New Guinea. *Applied and environmental microbiology* 69:644–8.

Klaasen, K.P., A'Hearn, M.F., Baca, M., Delamere, A., Desnoyer, M., Farnham, T., Groussin, O., Hampton, D., Ipatov, S., Li, J., Lisse, C., Mastrodemos, N., McLaughlin, S., Sunshine, J., Thomas, P. & Wellnitz, D. (2008) Invited Article: Deep Impact instrument calibration. *Review of Scientific Instruments* 79:091301–77.

Klassen, J.L. (2010) Phylogenetic and evolutionary patterns in microbial carotenoid biosynthesis are revealed by comparative genomics. F. Rodriguez-Valera, ed. *PloS one* 5:e11257.

Knutson, H.A., Benneke, B., Deming, D. & Homeier, D. (2014) A featureless transmission spectrum for the Neptune-mass exoplanet GJ 436b. *Nature* 505:66–8.

Knutson, H.A., Dragomir, D., Kreidberg, L., Kempton, E.M.-R., McCullough, P.R., Fortney, J.J., Bean, J.L., Gillon, M., Homeier, D. & Howard, A.W. (2014) Hubble Space Telescope Near-IR Transmission Spectroscopy Of The Super-Earth HD 97658b. *The Astrophysical Journal* 794:155.

Knutson, H.A., Lewis, N., Fortney, J.J., Burrows, A., Showman, A.P., Cowan, N.B., Agol, E., Aigrain, S., Charbonneau, D., Deming, D., Désert, J.-M., Henry, G.W., Langton, J. & Laughlin, G. (2012) 3.6 And 4.5 μm Phase Curves And Evidence For Non-equilibrium Chemistry In The Atmosphere Of Extrasolar Planet Hd 189733b. *The Astrophysical Journal* 754:22.

Kopparapu, R.K. (2013) A Revised Estimate of the Occurrence Rate of Terrestrial Planets in the Habitable Zones Around Kepler M-Dwarfs. *The Astrophysical Journal* 767:L8.

Kopparapu, R.K., Ramirez, R., Kasting, J.F., Eymet, V., Robinson, T.D., Mahadevan, S., Terrien, R.C., Domagal-Goldman, S., Meadows, V. & Deshpande, R. (2013) Habitable Zones Around Main-Sequence Stars: New Estimates. *The Astrophysical Journal* 765:16.

Kopparapu, R.K., Ramirez, R.M., SchottelKotte, J., Kasting, J.F., Domagal-Goldman, S. & Eymet, V. (2014) Habitable Zones Around Main-Sequence Stars: Dependence on Planetary Mass. *The Astrophysical Journal* 787:L29.

Kouveliotou, C., Agol, E., Batalha, N., Bean, J., Bentz, M., Cornish, N., Dressler, A., Figueroa-Feliciano, E., Gaudi, S., Guyon, O., Hartmann, D., Kalirai, J., Niemack, M., Ozel, F., Reynolds, C., Roberge, A., Straughn, K.S.A., Weinberg, D. & Zmuidzinas, J. (2014) Enduring Quests-Daring Visions (NASA Astrophysics in the Next Three Decades). *arXiv.org* 1401:3741.

Kreidberg, L., Bean, J.L., Désert, J.-M., Benneke, B., Deming, D., Stevenson, K.B., Seager, S., Berta-Thompson, Z., Seifahrt, A. & Homeier, D. (2014) Clouds in the atmosphere of the super-Earth exoplanet GJ 1214b. *Nature* 505:69–72.

Krissansen-Totton, J., Bergsman, D.S. & Catling, D.C. (2016a) On Detecting Biospheres from Chemical Thermodynamic Disequilibrium in Planetary Atmospheres. *Astrobiology* 16:39–67.

Krissansen-Totton, J., Schwieterman, E.W., Charnay, B., Arney, G., Robinson, T.D., Meadows, V. & Catling, D.C. (2016b) Is the Pale Blue Dot Unique? Optimized Photometric Bands for Identifying Earth-Like Exoplanets. *The Astrophysical Journal* 817:31.

Kühl, M., Lassen, C. & Revsbech, N.P. (1997) A simple light meter for measurements of PAR (400 to 700 nm) with fiber-optic microprobes: Application for P vs E0(PAR) measurements in a microbial mat. *Aquatic Microbial Ecology* 13:197–207.

Kump, L.R. (2008) The rise of atmospheric oxygen. *Nature* 451:277–278.

Kurucz, R.L. (1995) The Solar Spectrum: Atlases and Line Identifications. *Kurucz, R. L. 1995, in ASP Conf. Ser. 81, Laboratory and Astronomical High Resolution Spectra, ed. A.J. Sauval, R. Blomme, and N. Grevesse (Brussells, Belgium: ASP), 17*.

Lafferty, W.J., Solodov, A.M., Lugez, C.L. & Fraser, G.T. (1998) Rotational line strengths and self-pressure-broadening coefficients for the 127-μm, a^1Δ_g–X^3Σ_g^-, v = 0–0 band of O2. *Applied Optics* 37:2264.

Lafferty, W.J., Solodov, A.M., Weber, A., Olson, W.B. & Hartmann, J.M. (1996) Infrared collision-induced absorption by N(2) near 4.3 μm for atmospheric applications: measurements and empirical modeling. *Applied optics* 35:5911–5917.

Laidler, V., et al. (2008) *Synphot Data User's Guide*,

Larimer, F.W., Chain, P., Hauser, L., Lamerdin, J., Malfatti, S., Do, L., Land, M.L., Pelletier, D.A., Beatty, J.T., Lang, A.S., Tabita, F.R., Gibson, J.L., Hanson, T.E., Bobst, C., Torres, J.L.T. y, Peres, C., Harrison, F.H., Gibson, J. & Harwood, C.S. (2004) Complete genome sequence of the metabolically versatile photosynthetic bacterium Rhodopseudomonas palustris. *Nature biotechnology* 22:55–61.

Laughlin, G., Bodenheimer, P. & Adams, F.C. (1997) The End of the Main Sequence. *The Astrophysical Journal* 482:420–432.

Léger, a, Fontecave, M., Labeyrie, a, Samuel, B., Demangeon, O. & Valencia, D. (2011) Is the presence of oxygen on an exoplanet a reliable biosignature? *Astrobiology* 11:335–341.

Leger, A., Pirre, M. & Marceau, F.J. (1993) Search for primitive life on a distant planet: relevance of O2 and O3 detections. *Astronomy and Astrophysics* 277:309.

Lemee, L., Peuchant, E., Clerc, M., Brunner, M. & Pfander, H. (1997) Deinoxanthin: A new carotenoid isolated from Deinococcus radiodurans. *Tetrahedron* 53:919–926.

Leslie, M. (2009) On the origin of photosynthesis. *Science* 323:1286–1287.

Levine, M., Lisman, D., Shaklan, S., Kasting, J., Traub, W., Alexander, J., Angel, R., Blaurock, C., Brown, M., Brown, R., Burrows, C., Clampin, M., Cohen, E., Content, D., Dewell, L., Dumont, P., Egerman, R., Ferguson, H., Ford, V., et al. (2009) Terrestrial Planet Finder Coronagraph (TPF-C) Flight Baseline Concept. *ArXIv preprint 0911.3200L*.

Line, M.R., Liang, M.C. & Yung, Y.L. (2010) High-Temperature Photochemistry Iin the Atmosphere of HD 189733b. *The Astrophysical Journal* 717:496–502.

Line, M.R., Wolf, A.S., Zhang, X., Knutson, H., Kammer, J.A., Ellison, E., Deroo, P., Crisp, D. & Yung, Y.L. (2013) A Systematic Retrieval Analysis Of Secondary Eclipse Spectra. I. A Comparison Of Atmospheric Retrieval Techniques. *ApJ* 775:137.

Liu, G.Y. & Nizet, V. (2009) Color me bad: microbial pigments as virulence factors. *Trends in microbiology* 17:406–13.

Livengood, T.A., Deming, L.D., A'Hearn, M.F., Charbonneau, D., Hewagama, T., Lisse, C.M., McFadden, L.A., Meadows, V.S., Robinson, T.D., Seager, S. & Wellnitz, D.D. (2011) Properties of an Earth-like planet orbiting a Sun-like star: Earth observed by the EPOXI mission. *Astrobiology* 11:907–30.

Livesey, N.J., Read, W.G., Lambert, A., Cofield, R.E., Cuddy, D.T., Froidevaux, L., Fuller, R.A., Jarnot, R.F., Jiang, J.H., Jiang, Y.B., Knosp, B.W., Kovalenko, L.J., Picket, M.H., Pumphrey, H.C., Santee, M.L., Schwartz, M.J., Wang, S. & Co, R.E. (2007) *Earth Observing System (EOS) Aura Microwave Limb Sounder (MLS) description document*, Pasadena, California, 91109-8099.

Long, C.A., Henderson, G. & Ewing, G.E. (1973) The infrared spectrum of the (N2)2 van der waals molecule. *Chemical Physics* 2:485–489.

López-Puertas, M. & Taylor, F.W. (1989) Carbon dioxide 4.3-μm emission in the Earth's atmosphere: A comparison between Nimbus 7 SAMS measurements and non-local thermodynamic equilibrium radiative transfer calculations. *Journal of Geophysical Research* 94:13045.

López-Valverde, M.A., López-Puertas, M., Funke, B., Gilli, G., Garcia-Comas, M., Drossart, P., Piccioni, G. & Formisano, V. (2011) Modeling the atmospheric limb emission of CO2 at 4.3 μm in the terrestrial planets. *Planetary and Space Science* 59:988–998.

López-Valverde, M.A., López-Puertas, M., López-Moreno, J.J., Formisano, V., Grassi, D., Maturilli, A., Lellouch, E. & Drossart, P. (2005) Analysis of non-LTE emissions at in the Martian atmosphere as observed by PFS/Mars Express and SWS/ISO. *Planetary and Space Science* 53:1079–1087.

Lovelock, J.E. (1965) A Physical Basis for Life Detection Experiments. *Nature* 207:568–570.

Luger, R. & Barnes, R. (2015) Extreme Water Loss and Abiotic O2 Buildup on Planets Throughout the Habitable Zones of M Dwarfs. *Astrobiology* 15:119–143.

Lustig-Yaeger, J., Meadows, V., Line, M. & Crisp, D. (2015) A Novel Approach to Atmospheric Retrieval for Small Exoplanets. *American Astronomical Society, DPS meeting #47, id.416.10* 47.

Lyons, T.W., Reinhard, C.T. & Planavsky, N.J. (2014) The rise of oxygen in Earth's early ocean and atmosphere. *Nature* 506:307–315.

Mackenzie, C., Eraso, J.M., Choudhary, M., Roh, J.H., Zeng, X., Bruscella, P., Puskás, A. & Kaplan, S. (2007) Postgenomic adventures with Rhodobacter sphaeroides. *Annual review of microbiology* 61:283–307.

Maíz Apellániz, J. (2006) A Recalibration of Optical Photometry: Tycho-2, Strömgren, and Johnson Systems. *The Astronomical Journal* 131:1184–1199.

Mallama, A. (2009) Characterization of terrestrial exoplanets based on the phase curves and albedos of Mercury, Venus and Mars. *Icarus* 204:11–14.

Manabe, S. & Wetherald, R.T. (1967) Thermal Equilibrium of the Atmosphere with a Given Distribution of Relative Humidity. *Journal of the Atmospheric Sciences* 24:241–259.

Martens, T., Heidorn, T., Pukall, R., Simon, M., Tindall, B.J. & Brinkhoff, T. (2006) Reclassification of Roseobacter gallaeciensis Ruiz-Ponte et al. 1998 as Phaeobacter gallaeciensis gen. nov., comb. nov., description of Phaeobacter inhibens sp. nov., reclassification of Ruegeria algicola (Lafay et al. 1995) Uchino et al. 1999 as Marinovu. *International journal of systematic and evolutionary microbiology* 56:1293–304.

Marty, B., Zimmermann, L., Pujol, M., Burgess, R. & Philippot, P. (2013) Nitrogen isotopic composition and density of the Archean atmosphere. *Science* 342:101–104.

Maté, B., Lugez, C., Fraser, G.T. & Lafferty, W.J. (1999) Absolute intensities for the Oe 1.27 continuum absorption. *Journal of Geophysical Research* 104:585–590.

Maurin, A.S., Selsis, F., Hersant, F. & Belu, A. (2012) Thermal phase curves of nontransiting terrestrial exoplanets. *Astronomy & Astrophysics* 538:A95.

McClean, K.H., Winson, M.K., Fish, L., Taylor, A., Chhabra, S.R., Camara, M., Daykin, M., Lamb, J.H., Swift, S., Bycroft, B.W., Stewart, G.S.A.B. & Williams, P. (1997) Quorum sensing and Chromobacterium violaceum: exploitation of violacein production and inhibition for the detection of N-acylhomoserine lactones. *Microbiology* 143:3703–3711.

McLinden, C.A., McConnell, J.C., Griffoen, E., McElroy, C.T. & Pfister, L. (1997) Estimating the wavelength-dependent ocean albedo under clear-sky conditions using NASA ER 2 spectroradiometer measurements. *Journal of Geophysical Research* 102:18801–18811.

Meadows, V. & Seager, S. (2010) Terrestrial Planet Atmospheres and Biosignatures. *Exoplanets, edited by S. Seager. Tucson, AZ: University of Arizona Press, 2010, 526 pp. ISBN 978-0-8165-2945-2., p.441-470*:441–470.

Meadows, V.S. (2006) Modelling the Diversity of Extrasolar Terrestrial Planets. *Proceedings of the International Astronomical Union* 1:25.

Meadows, V.S. & Crisp, D. (1996) Ground-based near-infrared observations of the Venus nightside: The thermal structure and water abundance near the surface. *Journal of Geophysical Research* 101:4595–4622.

Meeks, J.C. & Castenholz, R.W. (1971) Growth and photosynthesis in an extreme thermophile, Synechococcus lividus (Cyanophyta). *Archiv für Mikrobiologie* 78:25–41.

Meyer, J.-M. (2000) Pyoverdines: pigments, siderophores and potential taxonomic markers of fluorescent Pseudomonas species. *Archives of Microbiology* 174:135–142.

Miller-Ricci, E., Seager, S. & Sasselov, D. (2009) The Atmospheric Signatures Of Super-earths: How To Distinguish Between Hydrogen-rich And Hydrogen-poor Atmospheres. *The Astrophysical Journal* 690:1056–1067.

Misra, A. (2014) The Effects of Refraction and Forward Scattering on Exoplanet Transit Transmission Spectroscopy.

Misra, A., Meadows, V., Claire, M. & Crisp, D. (2014a) Using dimers to measure biosignatures and atmospheric pressure for terrestrial exoplanets. *Astrobiology* 14:67–86.

Misra, A., Meadows, V. & Crisp, D. (2014b) The Effects Of Refraction On Transit Transmission Spectroscopy: Application To Earth-like Exoplanets. *The Astrophysical Journal* 792:61.

Misra, A.K. & Meadows, V.S. (2014) Discriminating Between Cloudy, Hazy, And Clear Sky Exoplanets Using Refraction. *The Astrophysical Journal* 795:L14.

Montanes-Rodriguez, P., Palle, E., Goode, P.R. & Martin-Torres, F.J. (2006) Vegetation Signature in the Observed Globally Integrated Spectrum of Earth Considering Simultaneous Cloud Data: Applications for Extrasolar Planets. *The Astrophysical Journal* 651:544–552.

Muinonen, K., Lumme, K., Peltoniemi, J. & Irvine, W.M. (1989) Light scattering by randomly oriented crystals. *Applied optics* 28:3051–60.

Narbonne, G.M. (2005) The Ediacara Biota: Neoproterozoic Origin of Animals and Their Ecosystems. *Annual Review of Earth and Planetary Sciences* 33:421–442.

Oren, A. (2013) Salinibacter: an extremely halophilic bacterium with archaeal properties. *FEMS microbiology letters* 342:1–9.

Oren, A. (2009) Saltern evaporation ponds as model systems for the study of primary production processes under hypersaline conditions. *Aquatic Microbial Ecology* 56:193–204.

Oren, A. & Dubinsky, Z. (1994) On the red coloration of saltern crystallizer ponds. II. Additional evidence for the contribution of halobacterial pigments. *International Journal of Salt Lake Research* 3:9–13.

Oren, A., Stambler, N. & Dubinsky, Z. (1992) On the red coloration of saltern crystallizer ponds. *International Journal of Salt Lake Research* 1:77–89.

Painter, T.H., Duval, B., Thomas, W.H., Mendez, M., Heintzelman, S. & Dozier, J. (2001) Detection and Quantification of Snow Algae with an Airborne Imaging Spectrometer. *Applied and Environmental Microbiology* 67:5267–5272.

Palle, E., Ford, E.B., Seager, S., Montanes-Rodriguez, P. & Vazquez, M. (2008) Identifying the rotation rate and the presence of dynamic weather on extrasolar Earth-like planets from photometric observations. *The Astrophysical Journal* 676:1319–1329.

Pantanella, F., Berlutti, F., Passariello, C., Sarli, S., Morea, C. & Schippa, S. (2007) Violacein and biofilm production in Janthinobacterium lividum. *Journal of applied microbiology* 102:992–9.

von Paris, P., Grenfell, J.L., Hedelt, P., Rauer, H., Selsis, F. & Stracke, B. (2013a) Atmospheric constraints for the CO2 partial pressure on terrestrial planets near the outer edge of the habitable zone. *Astronomy & Astrophysics* 549:A94.

von Paris, P., Hedelt, P., Selsis, F., Schreier, F. & Trautmann, T. (2013b) Characterization of potentially habitable planets: Retrieval of atmospheric and planetary properties from emission spectra. *Astronomy & Astrophysics* 551:A120.

Patel, M.R., Brces, A., Kolb, C., Lammer, H., Rettberg, P., Zarnecki, J.C. & Selsis, F. (2003) Seasonal and diurnal variations in Martian surface ultraviolet irradiation: biological and chemical implications for the Martian regolith. *International Journal of Astrobiology* 2:S1473550402001180.

Pavlov, A.A. & Kasting, J.F. (2002) Mass-independent fractionation of sulfur isotopes in Archean sediments: strong evidence for an anoxic Archean atmosphere. *Astrobiology* 2:27–41.

Payne, V.H., Clough, S.A., Shephard, M.W., Nassar, R. & Logan, J.A. (2009) Information-centered representation of retrievals with limited degrees of freedom for signal: Application to methane from the Tropospheric Emission Spectrometer. *Journal of Geophysical Research* 114:D10307.

Perrin, M.Y. & Hartmann, J.M. (1989) Temperature-dependent measurements and modeling of absorption by CO2-N2 mixtures in the far line-wings of the 4.3μm CO2 band. *Journal of Quantitative Spectroscopy and Radiative Transfer* 42:311–317.

Pfennig, N. & Truper, H.G. (1971) Type and Neotype Strains of the Species of Phototrophic Bacteria Maintained in Pure Culture. *International Journal of Systematic Bacteriology* 21:19–24.

Pierrehumbert, R. & Gaidos, E. (2011) Hydrogen Greenhouse Planets Beyond the Habitable Zone. *The Astrophysical Journal Letters* 734:L13.

Pierrehumbert, R.T. (2010) *Principles of Planetary Climate*, Cambridge University Press.

Pilcher, C.B. (2003) Biosignatures of Early Earths. *Astrobiology* 3:471–486.

Planavsky, N.J., Reinhard, C.T., Wang, X., Thomson, D., McGoldrick, P., Rainbird, R.H., Johnson, T., Fischer, W.W. & Lyons, T.W. (2014) Low Mid-Proterozoic atmospheric oxygen levels and the delayed rise of animals. *Science* 346:635–638.

Porsby, C.H., Nielsen, K.F. & Gram, L. (2008) Phaeobacter and Ruegeria species of the Roseobacter clade colonize separate niches in a Danish Turbot (Scophthalmus maximus)-rearing farm and antagonize Vibrio anguillarum under different growth conditions. *Applied and environmental microbiology* 74:7356–64.

Postman, M., Traub, W.A., Krist, J., Stapelfeldt, K., Brown, R., Oegerle, W., Lo, A., Clampin, M., Soummer, R., Wiseman, J. & Mountain, M. (2010) Advanced Technology Large-Aperture Space Telescope (ATLAST): Characterizing Habitable Worlds. *Pathways Towards Habitable Planets*.

Pravdo, S.H., Shaklan, S.B. & Lisman, P.D. (2010) Occulting Ozone Observatory ability to discover and locate single and multiple Earth-like planets in habitable zones. In *Proceedings of the SPIE*. p. 77314Z–77314Z–7.

Prescott, L., Harley, J. & Klein, D. (2005) *Microbiology*, New York, NY: McGraw Hill.

Proteau, P.J., Gerwick, W.H., Garcia-Pichel, F. & Castenholz, R. (1993) The structure of scytonemin, an ultraviolet sunscreen pigment from the sheaths of cyanobacteria. *Experientia* 49:825–829.

Rasmussen, R.A. & Khalil, M.A.K. (1981) Atmospheric methane (CH 4): Trends and seasonal cycles. *Journal of Geophysical Research* 86:9826.

Rauscher, B.J., Bolcar, M.R., Clampin, M., Domagal-Goldman, S.D., McElwain, M.W., Moseley, S.H., Stahle, C., Stark, C.C. & Thronson, H. a. (2015) ATLAST detector needs for direct spectroscopic biosignature characterization in the visible and near-IR. *SPIE*:9602–12 (ArXiv: 1508.06661).

Richard, C., Gordon, I.E., Rothman, L.S., Abel, M., Frommhold, L., Gustafsson, M., Hartmann, J.M., Hermans, C., Lafferty, W.J., Orton, G.S., Smith, K.M. & Tran, H. (2012) New section of the HITRAN database: Collision-induced absorption (CIA). *Journal of Quantitative Spectroscopy and Radiative Transfer* 113:1276–1285.

Ricker, G.R., Winn, J.N., Vanderspek, R., Latham, D.W., Bakos, G.Á., Bean, J.L., Berta-Thompson, Z.K., Brown, T.M., Buchhave, L., Butler, N.R., Butler, R.P., Chaplin, W.J., Charbonneau, D., Christensen-Dalsgaard, J., Clampin, M., Deming, D., Doty, J., De Lee, N., Dressing, C., et al. (2014) Transiting Exoplanet Survey Satellite (TESS). In J. M. Oschmann et al., eds. *Journal of Astronomical Telescopes, Instruments, and Systems*. p. 914320.

Ridgwell, a., Hargreaves, J.C., Edwards, N.R., Annan, J.D., Lenton, T.M., Marsh, R., Yool, a. & Watson, a. (2007) Marine geochemical data assimilation in an efficient Earth System Model of global biogeochemical cycling. *Biogeosciences* 4:87–104.

Riggs, G.A., Hall, D.K. & Ackerman, S.A. (1999) Sea Ice Extent and Classification Mapping with the Moderate Resolution Imaging Spectroradiometer Airborne Simulator. *Remote Sensing of Environment* 68:152–163.

Rinsland, C.P. (2004) Lower stratospheric densities from solar occultation measurements of continuum absorption near 2400 cm −1. *Journal of Geophysical Research* 109:D01301.

Rinsland, C.P., Chiou, L.S., Boone, C. & Bernath, P. (2010) Carbon dioxide retrievals from Atmospheric Chemistry Experiment solar occultation measurements. *Journal of Geophysical Research: Atmospheres* 115:1–12.

Robinson, T.D. (2011) Modeling the Infrared Spectrum of the Earth-Moon System: Implications for the Detection and Characterization of Earthlike Extrasolar Planets and Their Moonlike Companions. *The Astrophysical Journal* 741:51.

Robinson, T.D. (2012) Simulating and Characterizing the Pale Blue Dot. *ProQuest Dissertations And Theses; Thesis (Ph.D.)--University of Washington*.

Robinson, T.D., Ennico, K., Meadows, V.S., Sparks, W., Bussey, D.B.J., Schwieterman, E.W. & Breiner, J. (2014) Detection of Ocean Glint and Ozone Absorption Using LCROSS Earth Observations. *The Astrophysical Journal* 787:171.

Robinson, T.D., Meadows, V.S. & Crisp, D. (2010) Detecting Oceans on Extrasolar Planets Using the Glint Effect. *The Astrophysical Journal* 721:L67–L71.

Robinson, T.D., Meadows, V.S., Crisp, D., Deming, D., A'Hearn, M.F., Charbonneau, D., Livengood, T.A., Seager, S., Barry, R.K., Hearty, T., Hewagama, T., Lisse, C.M., McFadden, L.A. & Wellnitz, D.D. (2011) Earth as an Extrasolar Planet: Earth Model Validation Using EPOXI Earth Observations. *Astrobiology* 11:393–408.

Robinson, T.D., Stapelfeldt, K.R. & Marley, M.S. (2016) Characterizing Rocky and Gaseous Exoplanets with 2 m Class Space-based Coronagraphs. *Publications of the Astronomical Society of the Pacific* 128:025003.

Rogers, L.A. (2015) Most 1.6 Earth-Radius Planets are not Rocky. *The Astrophysical Journal* 801:41.

Rojas-Ayala, B., Covey, K.R., Muirhead, P.S. & Lloyd, J.P. (2012) Metallicity And Temperature Indicators In M Dwarf K -band Spectra: Testing New And Updated Calibrations With Observations Of 133 Solar Neighborhood M Dwarfs. *The Astrophysical Journal* 748:93.

Rothman, L.S., Gordon, I.E., Barbe, a., Benner, D.C., Bernath, P.F., Birk, M., Boudon, V., Brown, L.R., Campargue, a., Champion, J.-P., Chance, K., Coudert, L.H., Dana, V., Devi, V.M., Fally, S., Flaud, J.-M., Gamache, R.R., Goldman, a., Jacquemart, D., et al. (2009) The HITRAN 2008 molecular spectroscopic database. *Journal of Quantitative Spectroscopy and Radiative Transfer* 110:533–572.

Rugheimer, S., Kaltenegger, L., Segura, A., Linsky, J. & Mohanty, S. (2015) Effect Of UV Radiation On The Spectral Fingerprints Of Earth-like Planets Orbiting M Stars. *The Astrophysical Journal* 809:57.

Rugheimer, S., Kaltenegger, L., Zsom, A., Segura, A. & Sasselov, D. (2013) Spectral fingerprints of Earth-like planets around FGK stars. *Astrobiology* 13:251–69.

Rugheimer, S., Segura, A., Kaltenegger, L. & Sasselov, D. (2015) UV Surface Environment Of Earth-like Planets Orbiting FGKM Stars Through Geological Evolution. *The Astrophysical Journal* 806:137.

Sagan, C., Thompson, W.R., Carlson, R., Gurnett, D. & Hord, C. (1993) A search for life on Earth from the Galileo spacecraft. *Nature* 365:715–21.

Saito, T., Miyabe, Y., Ide, H. & Yamamoto, O. (1997) Hydroxyl Radical Scavenging Ability. *Radiation Physics and Chemistry* 50:267–269.

Saito, T., Terato, H. & Yamamoto, O. (1994) Pigments of Rubrobacter radiotolerans. *Archives of Microbiology* 162:414–421.

Salomonson, V.V., Barnes, W.L., Maymon, P.W., Montgomery, H.E. & Ostrow, H. (1989) MODIS: advanced facility instrument for studies of the Earth as a system. *IEEE Transactions on Geoscience and Remote Sensing* 27:145–153.

Samson, J.A.R., Masuoka, T., Pareek, P.N. & Angel, G.C. (1987) Total and dissociative photoionization cross sections of N2 from threshold to 107 eV. *The Journal of Chemical Physics* 86:6128.

Sanromá, E., Pallé, E. & García Munõz, A. (2013) On The Effects Of The Evolution Of Microbial Mats And Land Plants On The Earth As A Planet. Photometric And Spectroscopic Light Curves Of Paleo-Earths. *The Astrophysical Journal* 766:133.

Sanromá, E., Pallé, E., Parenteau, M.N., Kiang, N.Y., Gutiérrez-Navarro, A. M., López, R. & Montañés-Rodríguez, P. (2014) Characterizing the Purple Earth: Modeling the Globally Integrated Spectral Variability of the Archean Earth. *The Astrophysical Journal* 780:52.

Savransky, D., Spergel, D.N., Kasdin, N.J.D., Cady, E.J., Lisman, P.D., Pravdo, S.H., Shaklan, S.B. & Fujii, Y. (2010) Occulting ozone observatory science overview. In *Proceedings of the SPIE*. p. 77312H.

Scalo, J., Kaltenegger, L., Segura, A., Fridlund, M., Ribas, I., Kulikov, Y.N., Grenfell, J.L., Rauer, H., Odert, P., Leitzinger, M., Selsis, F., Khodachenko, M.L., Eiroa, C., Kasting, J. & Lammer, H. (2007) M Stars as Targets for Terrestrial Exoplanet Searches And Biosignature Detection. *http://dx.doi.org/10.1089/ast.2006.0125*.

Schabereiter-Gurtner, C., Piñar, G., Vybiral, D., Lubitz, W. & Rölleke, S. (2001) Rubrobacter-related bacteria associated with rosy discolouration of masonry and lime wall paintings. *Archives of microbiology* 176:347–54.

Schindler, T.L. & Kasting, J.F. (2000) Synthetic spectra of simulated terrestrial atmospheres containing possible biomarker gases. *Icarus* 145:262–271.

Schloss, P.D., Allen, H.K., Klimowicz, A.K., Mlot, C., Gross, J.A., Savengsuksa, S., McEllin, J., Clardy, J., Ruess, R.W. & Handelsman, J. (2010) Psychrotrophic strain of Janthinobacterium lividum from a cold Alaskan soil produces prodigiosin. *DNA and cell biology* 29:533–41.

Schopf, J.W. (1993) Microfossils of the Early Archean Apex Chert: New Evidence of the Antiquity of Life. *Science* 260:640–646.

Schuerger, A.C., Ulrich, R., Berry, B.J. & Nicholson, W.L. (2013) Growth of Serratia liquefaciens under 7 mbar, 0°C, and CO2-enriched anoxic atmospheres. *Astrobiology* 13:115–31.

Schwartz, J.C., Sekowski, C., Haggard, H.M., Pallé, E. & Cowan, N.B. (2016) Inferring planetary obliquity using rotational and orbital photometry. *Monthly Notices of the Royal Astronomical Society* 457:926–938.

Schwieterman, E.W., Cockell, C.S. & Meadows, V.S. (2015a) Nonphotosynthetic Pigments as Potential Biosignatures. *Astrobiology* 15:341–361.

Schwieterman, E.W., Meadows, V.S., Domagal-Goldman, S.D., Deming, D., Arney, G.N., Luger, R., Harman, C.E., Misra, A. & Barnes, R. (2016) Identifying Planetary Biosignature Impostors: Spectral Features of CO And O4 Resulting From Abiotic O2/O3 Production. *The Astrophysical Journal* 819:L13.

Schwieterman, E.W., Robinson, T.D., Meadows, V.S., Misra, A. & Domagal-Goldman, S. (2015b) Detecting and Constraining N2 Abundances in Planetary Atmospheres Using Collisional Pairs. *The Astrophysical Journal* 810:57.

Seager, S. (2013) Exoplanet habitability. *Science* 340:577–81.

Seager, S., Bains, W. & Hu, R. (2013a) A Biomass-based Model to Estimate The Plausibility of Exoplanet Biosignature Gases. *The Astrophysical Journal* 775:104.

Seager, S., Bains, W. & Hu, R. (2013b) Biosignature Gases in H2-Dominated Atmosphers on Rocky Exoplanets. *The Astrophysical Journal* 777:95.

Seager, S., Bains, W. & Petkowski, J.J. (2016) Toward a List of Molecules as Potential Biosignature Gases for the Search for Life on Exoplanets and Applications to Terrestrial Biochemistry. *Astrobiology* 16:465–485.

Seager, S., Cash, W.C., Kasdin, N.J., Sparks, W.B., Turnbull, M.C., Kuchner, M.J., Roberge, A., Domagal-Goldman, S., Shaklan, S., Thomson, M., Lisman, D., Martin, S., Cady, E. & Webb, D. (2014) Exo-S: A Probe-scale Space Mission to Directly Image and Spectroscopically Characterize Exoplanetary Systems Using a Starshade and Telescope System. *American Astronomical Society* #224:#311.06.

Seager, S., Dalcanton, J.J., Postman, M., Tumlinson, J. & Mather, J.C. (2015) A Response to Elvis' 2015 Critique of the AURA Report "From Cosmic Birth to Living Earths."

Seager, S., Turner, E.L., Schafer, J. & Ford, E.B. (2005) Vegetation's Red Edge : A Possible Spectroscopic. 5:372–393.

Seager, S., Turner, E.L., Schafer, J. & Ford, E.B. (2005) Vegetation's Red Edge: A Possible Spectroscopic Biosignature of Extraterrestrial Plants. *Astrobiology* 5:372–390.

Segura, A., Kasting, J.F., Meadows, V., Cohen, M., Scalo, J., Crisp, D., Butler, R.A.H. & Tinetti, G. (2005) Biosignatures from Earth-like planets around M dwarfs. *Astrobiology* 5:706–725.

Segura, A., Krelove, K., Kasting, J.F., Sommerlatt, D., Meadows, V., Crisp, D., Cohen, M. & Mlawer, E. (2003) Ozone concentrations and ultraviolet fluxes on Earth-like planets around other stars. *Astrobiology* 3:689–708.

Segura, A., Meadows, V.S., Kasting, J.F., Crisp, D. & Cohen, M. (2007) Abiotic formation of O2 and O3 in high-CO2 terrestrial atmospheres. *Astronomy and Astrophysics* 472:665–679.

Segura, A., Walkowicz, L.M., Meadows, V., Kasting, J. & Hawley, S. (2010) The effect of a strong stellar flare on the atmospheric chemistry of an earth-like planet orbiting an M dwarf. *Astrobiology* 10:751–71.

Selsis, F. (2002) Occurrence and Detectability of O2-Rich Atmospheres in Circumstellar "Habitable Zones." *The Evolving Sun and its Influence on Planetary Environments. ASP Conference Proceedings* 269.

Selsis, F., Despois, D. & Parisot, J.-P. (2002) Signature of life on exoplanets: Can Darwin produce falsepositive detections? *Astronomy and Astrophysics* 388:985–1003.

Selsis, F., Wordsworth, R.D. & Forget, F. (2011) Thermal phase curves of nontransiting terrestrial exoplanets. *Astronomy & Astrophysics* 532:A1.

Shahmohammadi, H.R., Asgarani, E., Terato, H., Saito, T., Ohyama, Y., Gekko, K., Yamamoto, O. & Ide, H. (1998) Protective Roles of Bacterioruberin and Intracellular KCl in the Resistance of Halobacterium salinarium against DNA-damaging Agents. *Journal of Radiation Research* 39:251–262.

Shapiro, M.M. & Gush, H.P. (1966) The Collision-Induced Fundamental And First Overtone Bands Of Oxygen And Nitrogen. *Canadian Journal of Physics* 44:949–963.

Shields, A.L., Meadows, V.S., Bitz, C.M., Pierrehumbert, R.T., Joshi, M.M. & Robinson, T.D. (2013) The Effect of Host Star Spectral Energy Distribution and Ice-Albedo Feedback on the Climate of Extrasolar Planets. *Astrobiology* 13:715–739.

Sidis, O. & Sari, R. (2010) Transits of Transparent Planets—Atmospheric Lensing Effects. *The Astrophysical Journal* 720:904–911.

Sioris, C.E., Boone, C.D., Nassar, R., Sutton, K.J., Gordon, I.E., Walker, K. a. & Bernath, P.F. (2014) Retrieval of carbon dioxide vertical profiles from solar occultation observations and associated error budgets for ACE-FTS and CASS-FTS. *Atmospheric Measurement Techniques* 7:2243–2262.

Smith, M.L., Claire, M.W., Catling, D.C. & Zahnle, K.J. (2014) The formation of sulfate, nitrate and perchlorate salts in the martian atmosphere. *Icarus* 231:51–64.

Snellen, I., de Kok, R., Poole, R. Le, Brogi, M. & Birkby, J. (2013) Finding extraterrestrial life using ground-based high-resolution spectroscopy. :22.

Snellen, I.A.G., de Kok, R.J., le Poole, R., Brogi, M. & Birkby, J. (2013) Finding Extraterrestrial Life Using Ground-based High-Dispersion Spectroscopy. *The Astrophysical Journal* 764:182.

Solovchenko, A.E. & Merzlyak, M.N. (2008) Screening of visible and UV radiation as a photoprotective mechanism in plants. *Russian Journal of Plant Physiology* 55:719–737.

Som, S.M., Catling, D.C., Harnmeijer, J.P., Polivka, P.M. & Buick, R. (2012) Air density 2.7 billion years ago limited to less than twice modern levels by fossil raindrop imprints. *Nature* 484:359–362.

Sparks, W.B., Meadows, V., McCullough, P., Postman, M., Bussey, B. & Christian, C. (2010) Lunar Based Observations of the Earth as a Planet. *Astrobiology Science Conference 2010: Evolution and Life: Surviving Catastrophes and Extremes on Earth and Beyond*.

Spergel, D., Gehrels, N., Baltay, C., Bennett, D., Breckinridge, J., Donahue, M., Dressler, A., Gaudi, B.S., Greene, T., Guyon, O., Hirata, C., Kalirai, J., Kasdin, N.J., Macintosh, B., Moos, W., Perlmutter, S., Postman, M., Rauscher, B., Rhodes, J., et al. (2015) Wide-Field InfrarRed Survey Telescope-Astrophysics Focused Telescope Assets WFIRST-AFTA 2015 Report. *(arXiv:1503.03757)*.

Stamnes, K., Tsay, S.C., Wiscombe, W. & Jayaweera, K. (1988) Numerically stable algorithm for discrete-ordinate-method radiative transfer in multiple scattering and emitting layered media. *Applied optics* 27:2502–2509.

Stapelfeldt, K.R., Brenner, M.P., Warfield, K.R., Dekens, F.G., Belikov, R., Brugarolas, P.B., Bryden, G., Cahoy, K.L., Chakrabarti, S., Dubovitsky, S., Effinger, R.T., Hirsch, B., Kissil, A., Krist, J.E., Lang, J.J., Marley, M.S., McElwain, M.W., Meadows, V.S., Nissen, J., et al. (2014) Exo-C: a probe-scale space mission to directly image and spectroscopically characterize exoplanetary systems using an internal coronagraph. In J. M. Oschmann et al., eds. *American Astronomical Society*. p. 91432K.

Stark, C.C., Roberge, A., Mandell, A. & Robinson, T.D. (2014) Maximizing The Exoearth Candidate Yield From A Future Direct Imaging Mission. *The Astrophysical Journal* 795:122.

Stark, G., Smith, P.L., Huber, K.P., Yoshino, K., Stevens, M.H. & Ito, K. (1992) Absorption band oscillator strengths of N2 transitions between 95.8 and 99.4 nm. *The Journal of Chemical Physics* 97:4809.

Stevenson, D. (1999) Life-sustaining planets in interstellar space? *Nature* 400:32.

Stone, R.P.S. (1996) Spectrophotometry of Flux Calibration Stars for Hubble Space Telescope. *The Astrophysical Journal Supplement Series* 107:423.

Sullivan, P.W., Winn, J.N., Berta-Thompson, Z.K., Charbonneau, D., Deming, D., Dressing, C.D., Latham, D.W., Levine, A.M., McCullough, P.R., Morton, T., Ricker, G.R., Vanderspek, R. & Woods, D. (2015) The Transiting Exoplanet Survey Satellite: Simulations Of Planet Detections And Astrophysical False Positives. *The Astrophysical Journal* 809:77.

Swain, M.R., Redfield, S., Fischer, D. a, Marley, M., Greene, T., Cowan, N.B., Griffith, C., Yung, Y.L., Mandell, A.M., Lawrence, C., Rhodes, J., Kiessling, A., Martin, C., Vasisht, G., Beichman, C. & Dore, O. (2015) HabX2: a 2020 mission concept for flagship science at modest cost. *CoPag Report (white paper), http://cor.gsfc.nasa.gov/copag/rfi/HabEx_2020_30apr2015_submitted.pdf*.

Tabataba-Vakili, F., Grenfell, J.L., Grießmeier, J.-M. & Rauer, H. (2015) Atmospheric effects of stellar cosmic rays on Earth-like exoplanets orbiting M-dwarfs. :14.

Takano, H., Asker, D., Beppu, T. & Ueda, K. (2006) Genetic control for light-induced carotenoid production in non-phototrophic bacteria. *Journal of industrial microbiology & biotechnology* 33:88–93.

Tanaka, Y., Sasaki, N. & Ohmiya, A. (2008) Biosynthesis of plant pigments: anthocyanins, betalains and carotenoids. *The Plant journal : for cell and molecular biology* 54:733–49.

Tarter, J.C., Backus, P.R., Mancinelli, R.L., Aurnou, J.M., Backman, D.E., Basri, G.S., Boss, A.P., Clarke, A., Deming, D., Doyle, L.R., Feigelson, E.D., Freund, F., Grinspoon, D.H., Haberle, R.M., Hauck, S. a, Heath, M.J., Henry, T.J., Hollingsworth, J.L., Joshi, M.M., et al. (2007) A reappraisal of the habitability of planets around M dwarf stars. *Astrobiology* 7:30–65.

Thalman, R. & Volkamer, R. (2013) Temperature dependent absorption cross-sections of O2-O2 collision pairs between 340 and 630 nm and at atmospherically relevant pressure. *Physical chemistry chemical physics* 15:15371–81.

Tian, B., Sun, Z., Xu, Z., Shen, S., Wang, H. & Hua, Y. (2008) Carotenoid 3',4'-desaturase is involved in carotenoid biosynthesis in the radioresistant bacterium Deinococcus radiodurans. *Microbiology (Reading, England)* 154:3697–706.

Tian, F. (2015) History of water loss and atmospheric O2 buildup on rocky exoplanets near M dwarfs. *Earth and Planetary Science Letters* 432:126–132.

Tian, F., France, K., Linsky, J.L., Mauas, P.J.D. & Vieytes, M.C. (2014) High stellar FUV/NUV ratio and oxygen contents in the atmospheres of potentially habitable planets. *Earth and Planetary Science Letters* 385:22–27.

Tinetti, G., Meadows, V.S., Crisp, D., Fong, W., Fishbein, E., Turnbull, M. & Bibring, J.-P. (2006a) Detectability of planetary characteristics in disk-averaged spectra. I: The Earth model. *Astrobiology* 6:34–47.

Tinetti, G., Meadows, V.S., Crisp, D., Kiang, N.Y., Kahn, B.H., Bosc, E., Fishbein, E., Velusamy, T. & Turnbull, M. (2006b) Detectability of planetary characteristics in disk-averaged spectra II: synthetic spectra and light-curves of earth. *Astrobiology* 6:881–900.

Tinetti, G., Rashby, S. & Yung, Y.L. (2006c) Detectability of Red-Edge-shifted Vegetation on Terrestrial Planets Orbiting M Stars. *The Astrophysical Journal* 644:L129–L132.

Toon, O.B., Mckay, C.P., Ackerman, T.P. & Santhanam, K. (1989) Rapid calculation of radiative heating rates and photodissociation rates in inhomogeneous multiple scattering atmospheres. *Journal of Geophysical Research* 94:287–301.

Trauger, J.T. & Traub, W. a (2007) A laboratory demonstration of the capability to image an Earth-like extrasolar planet. *Nature* 446:771–3.

Tucker, C., Pinzon, J., Brown, M., Slayback, D., Pak, E., Mahoney, R., Vermote, E. & El Saleous, N. (2005) An extended AVHRR 8-km NDVI dataset compatible with MODIS and SPOT vegetation NDVI data. *International Journal of Remote Sensing* 26:4485–4498.

Tucker, C.J. (1979) Red and photographic infrared linear combinations for monitoring vegetation. *Remote Sensing of Environment* 8:127–150.

Tumlinson, J. (2010) NIRSpec in the Dense Field Limit: An Observing Scenario. *Document JWST-STScI-002129, SM-12 (Baltimore, MD: Space Telescope Science Institute)*.

Turnbull, M.C., Traub, W.A., Jucks, K.W., Woolf, N.J., Meyer, M.R., Gorlova, N., Skrutskie, M.F. & Wilson, J.C. (2006) Spectrum of a Habitable World: Earthshine in the Near-Infrared. *The Astrophysical Journal* 644:551–559.

Ungers, G.E. & Cooney, J.J. (1968) Isolation and characterization of carotenoid pigments of Micrococcus roseus. *Journal of bacteriology* 96:234–41.

Valadon, L.R. & Mummery, R.S. (1968) Carotenoids in floral parts of a narcissus, a daffodil and a tulip. *The Biochemical journal* 106:479–84.

Venil, C. & Lakshmanaperumalsamy, P. (2009) An insightful overview on microbial pigment, prodigiosin. *Electronic Journal of Biology* 5:49–61.

Wacey, D., Kilburn, M.R., Saunders, M., Cliff, J. & Brasier, M.D. (2011) Microfossils of sulphur-metabolizing cells in 3.4-billion-year-old rocks of Western Australia. *Nature Geoscience* 4:698–702.

Wagner, T., von Friedbeburg, C., Wenig, M., Otten, C. & Platt, U. (2002) UV-visible observations of atmospheric O4 absorptions using direct moonlight and zenith-scattered sunlight for clear-sky and cloudy sky conditions. *Journal of Geophysical Research* 107:4424.

Wahlund, T.M., Woese, C.R., Castenholz, R.W. & Madigan, M.T. (1991) A thermophilic green sulfur bacterium from New Zealand hot springs, Chlorobium tepidum sp. nov. *Archives of Microbiology* 156:81–90.

Walker, J.C.G., Hays, P.B. & Kasting, J.F. (1981) A negative feedback mechanism for the long-term stabilization of Earth's surface temperature. *Journal of Geophysical Research* 86:9776.

Waters, J.W., Froidevaux, L., Harwood, R.S., Jarnot, R.F., Pickett, H.M., Read, W.G., Siegel, P.H., Cofield, R.E., Filipiak, M.J., Flower, D.A., Holden, J.R., Lau, G.K., Livesey, N.J., Manney, G.L., Pumphrey, H.C., Santee, M.L., Wu, D.L., Cuddy, D.T., Lay, R.R., et al. (2006) The Earth observing system microwave limb sounder (EOS MLS) on the aura Satellite. *IEEE Transactions on Geoscience and Remote Sensing* 44:1075–1092.

Werf, S.Y. Van Der (2008) Comment on " Improved ray tracing air mass numbers model ." 47:153–156.

Werner, M., Swain, M., Vasisht, G., Wang, X., Macenka, S., Mandell, A., Domagal-Goldman, S., Green, J. & Stark, C. (2016) Extension of ATLAST/LUVOIR's Capabilities to 5 Microns, or Beyond. *SPIE Journal of Astronomical Telescopes and Instrumentation Systems*.

West, R., Crisp, D. & Chen, L. (1990) Mapping transformations for broadband atmospheric radiation calculations. *Journal of Quantitative Spectroscopy and Radiative Transfer* 43:191–199.

Wiggli, M., Smallcombe, A. & Bachofen, R. (1999) Reflectance spectroscopy and laser confocal microscopy as tools in an ecophysiological study of microbial mats in an alpine bog pond. *Journal of Microbiological Methods* 34:173–182.

Williams, D.M. & Gaidos, E. (2008) Detecting the glint of starlight on the oceans of distant planets. *Icarus* 195:927–937.

Williams, P., Winzer, K., Chan, W.C. & Cámara, M. (2007) Look who's talking: communication and quorum sensing in the bacterial world. *Philosophical transactions of the Royal Society of London. Series B, Biological sciences* 362:1119–34.

Williams, W.E., Gorton, H.L. & Vogelmann, T.C. (2003) Surface gas-exchange processes of snow algae. *Proceedings of the National Academy of Sciences of the United States of America* 100:562–6.

Wiscombe, W.J. (1980) Improved Mie scattering algorithms. *Applied Optics* 19:1505.

de Wit, J., Wakeford, H.R., Gillon, M., Lewis, N.K., Valenti, J.A., Demory, B.-O., Burgasser, A.J., Delrez, L., Jehin, E., Lederer, S.M., Triaud, A.H.M.J. & Van Grootel, V. (2016) A combined transmission spectrum of the Earth-sized exoplanets TRAPPIST-1 b and c. :1–27.

Woolf, N.J., Smith, P.S., Traub, W.A. & Jucks, K.W. (2002) The Spectrum of Earthshine: A Pale Blue Dot Observed from the Ground. *The Astrophysical Journal* 574:430–433.

Wordsworth, R. & Pierrehumbert, R. (2014) Abiotic Oxygen-dominated Atmospheres On Terrestrial Habitable Zone Planets. *The Astrophysical Journal* 785:L20.

Wright, D.J., Wittenmyer, R.A., Tinney, C.G., Bentley, J.S. & Zhao, J. (2016) Three Planets Orbiting Wolf 1061. *The Astrophysical Journal* 817:L20.

Zahnle, K., Claire, M. & Catling, D. (2006) The loss of mass-independent fractionation in sulfur due to a Palaeoproterozoic collapse of atmospheric methane. *Geobiology* 4:271–283.

Zerkle, A.L., Claire, M.W., Domagal-Goldman, S.D., Farquhar, J. & Poulton, S.W. (2012) A bistable organic-rich atmosphere on the Neoarchaean Earth. *Nature Geoscience* 5:359–363.

Ziegelhoffer, E.C. & Donohue, T.J. (2009) Bacterial responses to photo-oxidative stress. *Nature reviews. Microbiology* 7:856–863.

APPENDIX A

Table A.1 Full Earth-Lunar Observing Table

ObsID	JD(+2454544)	α(°)	Illum(%)	$\lambda_{\leftmoon}$(°)	$\beta_{\leftmoon}$(°)	$\lambda_{\odot}$(°)	$\beta_{\odot}$(°)	Δr ($\times 10^{-3}$ km)
0	0.5	147.12	8	331.3	13.1	182	-0.5	383.7
1	0.54	147.62	7.8	316.8	12.9	167	-0.5	383.8
2	0.58	148.13	7.5	302.2	12.6	152	-0.5	384
3	0.62	148.63	7.3	287.7	12.4	136.9	-0.4	384.1
4	0.67	149.13	7.1	273.2	12.2	122	-0.4	384.3
5	0.71	149.63	6.9	258.6	11.9	107	-0.4	384.4
6	0.75	150.13	6.6	244.1	11.7	91.9	-0.4	384.5
7	0.79	150.63	6.4	229.5	11.5	76.9	-0.4	384.7
8	0.83	151.14	6.2	215	11.2	61.9	-0.4	384.8
9	0.88	151.64	6	200.5	11	46.9	-0.3	384.9
10	0.92	152.13	5.8	185.9	10.7	31.9	-0.3	385.1
11	0.96	152.63	5.6	171.4	10.5	16.9	-0.3	385.2
12	1	153.13	5.4	156.8	10.3	1.9	-0.3	385.4
13	1.04	153.63	5.2	142.3	10	346.9	-0.3	385.5
14	1.08	154.13	5	127.7	9.8	331.9	-0.3	385.6
15	1.12	154.63	4.8	113.2	9.5	316.9	-0.2	385.8
16	1.17	155.12	4.6	98.6	9.3	301.9	-0.2	385.9
17	1.21	155.62	4.5	84.1	9.1	286.9	-0.2	386.1
18	1.25	156.11	4.3	69.5	8.8	271.9	-0.2	386.2
19	1.29	156.61	4.1	55	8.6	256.9	-0.2	386.4
20	1.33	157.1	3.9	40.4	8.3	241.9	-0.2	386.5
21	1.38	157.6	3.8	25.9	8.1	226.9	-0.1	386.6
22	1.42	158.09	3.6	11.3	7.8	211.9	-0.1	386.8
23	1.46	158.58	3.5	356.7	7.6	196.9	-0.1	386.9
24	1.5	159.08	3.3	342.2	7.3	181.9	-0.1	387.1
25	1.54	159.57	3.1	327.6	7.1	166.9	-0.1	387.2
26	1.58	160.06	3	313.1	6.8	151.9	-0.1	387.3
27	1.62	160.55	2.9	298.5	6.6	136.9	-0.1	387.5
28	1.67	161.04	2.7	284	6.3	121.9	0	387.6
29	1.71	161.53	2.6	269.4	6.1	106.9	0	387.8
30	1.75	162.02	2.4	254.8	5.8	91.9	0	387.9
31	1.79	162.51	2.3	240.3	5.6	76.9	0	388
32	1.83	162.99	2.2	225.7	5.3	61.9	0	388.2

ObsID is the simulated observation number (the first observation is 2008-03-19 00:00 UT), **JD** is the Julian Date of the observation minus 2454544, **α** is the Sun-Earth-Moon phase angle in degrees, **illum** is the Earth's illumination percentage, $\lambda_{\leftmoon}$ is the sub-Lunar longitude, $\beta_{\leftmoon}$ is the sub-Lunar latitude, $\lambda_{\odot}$ is the sub-solar longitude, $\beta_{\odot}$ is the sub-solar latitude, and **Δr** is the Earth-Moon distance ($\times 10^{-3}$ km).

ObsID	JD(+2454544)	α(°)	Illum(%)	$\lambda_{\leftmoon}$(°)	$\beta_{\leftmoon}$(°)	$\lambda_{\odot}$(°)	$\beta_{\odot}$(°)	Δr ($\times 10^{-3}$ km)
33	1.88	163.48	2.1	211.1	5.1	46.9	0.1	388.3
34	1.92	163.97	1.9	196.6	4.9	31.9	0.1	388.5
35	1.96	164.45	1.8	182	4.6	16.9	0.1	388.6
36	2	164.93	1.7	167.4	4.4	1.9	0.1	388.7
37	2.04	165.42	1.6	152.9	4.1	346.9	0.1	388.9
38	2.08	165.9	1.5	138.3	3.9	331.8	0.1	389
39	2.12	166.38	1.4	123.7	3.6	316.8	0.1	389.2
40	2.17	166.86	1.3	109.2	3.4	301.8	0.2	389.3
41	2.21	167.34	1.2	94.6	3.1	286.8	0.2	389.5
42	2.25	167.81	1.1	80	2.9	271.8	0.2	389.6
43	2.29	168.29	1	65.5	2.6	256.8	0.2	389.7
44	2.33	168.76	1	50.9	2.4	241.8	0.2	389.9
45	2.38	169.23	0.9	36.3	2.1	226.8	0.2	390
46	2.42	169.7	0.8	21.7	1.9	211.8	0.3	390.2
47	2.46	170.17	0.7	7.2	1.6	196.8	0.3	390.3
48	2.5	170.64	0.7	352.6	1.4	181.8	0.3	390.4
49	2.54	171.1	0.6	338	1.1	166.8	0.3	390.6
50	2.58	171.56	0.5	323.5	0.9	151.8	0.3	390.7
51	2.62	172.01	0.5	308.9	0.6	136.8	0.3	390.9
52	2.67	172.47	0.4	294.3	0.4	121.8	0.4	391
53	2.71	172.91	0.4	279.7	0.1	106.8	0.4	391.1
54	2.75	173.35	0.3	265.2	-0.1	91.8	0.4	391.3
55	2.79	173.78	0.3	250.6	-0.4	76.8	0.4	391.4
56	2.83	174.21	0.3	236	-0.6	61.8	0.4	391.6
57	2.88	174.62	0.2	221.4	-0.9	46.8	0.5	391.7
58	2.92	175.02	0.2	206.9	-1.1	31.8	0.5	391.8
59	2.96	175.4	0.2	192.3	-1.4	16.8	0.5	392
60	3	175.77	0.1	177.7	-1.6	1.8	0.5	392.1
61	3.04	176.1	0.1	163.1	-1.9	346.8	0.5	392.3
62	3.08	176.4	0.1	148.5	-2.1	331.8	0.5	392.4
63	3.12	176.66	0.1	134	-2.4	316.8	0.6	392.5
64	3.17	176.87	0.1	119.4	-2.6	301.8	0.6	392.7
65	3.21	177.01	0.1	104.8	-2.9	286.8	0.6	392.8
66	3.25	177.07	0.1	90.2	-3.1	271.8	0.6	392.9
67	3.29	177.06	0.1	75.7	-3.4	256.8	0.6	393.1
68	3.33	176.97	0.1	61.1	-3.6	241.8	0.6	393.2
69	3.38	176.81	0.1	46.5	-3.9	226.8	0.7	393.4
70	3.42	176.59	0.1	31.9	-4.1	211.8	0.7	393.5

ObsID is the simulated observation number (the first observation is 2008-03-19 00:00 UT), **JD** is the Julian Date of the observation minus 2454544, **α** is the Sun-Earth-Moon phase angle in degrees, **illum** is the Earth's illumination percentage, $\boldsymbol{\lambda}_{\leftmoon}$ is the sub-Lunar longitude, $\boldsymbol{\beta}_{\leftmoon}$ is the sub-Lunar latitude, $\boldsymbol{\lambda}_{\odot}$ is the sub-solar longitude, $\boldsymbol{\beta}_{\odot}$ is the sub-solar latitude, and **Δr** is the Earth-Moon distance ($\times 10^{-3}$ km).

ObsID	JD(+2454544)	α(°)	Illum(%)	$\lambda_{\leftmoon}$(°)	$\beta_{\leftmoon}$(°)	$\lambda_{\odot}$(°)	$\beta_{\odot}$(°)	Δr ($\times 10^{-3}$ km)
71	3.46	176.32	0.1	17.3	-4.3	196.7	0.7	393.6
72	3.5	176.01	0.1	2.8	-4.6	181.7	0.7	393.8
73	3.54	175.67	0.1	348.2	-4.8	166.7	0.7	393.9
74	3.58	175.3	0.2	333.6	-5.1	151.7	0.7	394
75	3.62	174.92	0.2	319	-5.3	136.7	0.8	394.2
76	3.67	174.52	0.2	304.5	-5.6	121.7	0.8	394.3
77	3.71	174.11	0.3	289.9	-5.8	106.7	0.8	394.4
78	3.75	173.69	0.3	275.3	-6	91.7	0.8	394.6
79	3.79	173.27	0.3	260.7	-6.3	76.7	0.8	394.7
80	3.83	172.84	0.4	246.1	-6.5	61.7	0.8	394.8
81	3.88	172.4	0.4	231.6	-6.8	46.7	0.8	395
82	3.92	171.96	0.5	217	-7	31.7	0.9	395.1
83	3.96	171.51	0.5	202.4	-7.2	16.7	0.9	395.2
84	4	171.06	0.6	187.8	-7.5	1.7	0.9	395.4
85	4.04	170.61	0.7	173.3	-7.7	346.7	0.9	395.5
86	4.08	170.16	0.7	158.7	-7.9	331.7	0.9	395.6
87	4.12	169.71	0.8	144.1	-8.2	316.7	0.9	395.7
88	4.17	169.25	0.9	129.5	-8.4	301.7	1	395.9
89	4.21	168.79	1	115	-8.6	286.7	1	396
90	4.25	168.34	1	100.4	-8.9	271.7	1	396.1
91	4.29	167.88	1.1	85.8	-9.1	256.7	1	396.3
92	4.33	167.42	1.2	71.2	-9.3	241.7	1	396.4
93	4.38	166.96	1.3	56.7	-9.6	226.7	1.1	396.5
94	4.42	166.5	1.4	42.1	-9.8	211.7	1.1	396.6
95	4.46	166.04	1.5	27.5	-10	196.7	1.1	396.8
96	4.5	165.58	1.6	12.9	-10.2	181.7	1.1	396.9
97	4.54	165.12	1.7	358.4	-10.5	166.7	1.1	397
98	4.58	164.65	1.8	343.8	-10.7	151.7	1.1	397.1
99	4.62	164.19	1.9	329.2	-10.9	136.7	1.1	397.3
100	4.67	163.73	2	314.6	-11.2	121.7	1.2	397.4
101	4.71	163.27	2.1	300.1	-11.4	106.7	1.2	397.5
102	4.75	162.81	2.2	285.5	-11.6	91.6	1.2	397.6
103	4.79	162.34	2.4	270.9	-11.8	76.6	1.2	397.7
104	4.83	161.88	2.5	256.4	-12	61.6	1.2	397.9
105	4.88	161.42	2.6	241.8	-12.3	46.6	1.2	398
106	4.92	160.96	2.7	227.2	-12.5	31.6	1.3	398.1
107	4.96	160.5	2.9	212.6	-12.7	16.6	1.3	398.2
108	5	160.03	3	198.1	-12.9	1.6	1.3	398.3

ObsID is the simulated observation number (the first observation is 2008-03-19 00:00 UT), **JD** is the Julian Date of the observation minus 2454544, **α** is the Sun-Earth-Moon phase angle in degrees, **illum** is the Earth's illumination percentage, $\lambda_{\leftmoon}$ is the sub-Lunar longitude, $\beta_{\leftmoon}$ is the sub-Lunar latitude, $\lambda_{\odot}$ is the sub-solar longitude, $\beta_{\odot}$ is the sub-solar latitude, and **Δr** is the Earth-Moon distance ($\times 10^{-3}$ km).

ObsID	JD(+2454544)	α(°)	Illum(%)	$\lambda_{\leftmoon}$(°)	$\beta_{\leftmoon}$(°)	$\lambda_{\odot}$(°)	$\beta_{\odot}$(°)	Δr ($\times 10^{-3}$ km)
109	5.04	159.57	3.1	183.5	-13.1	346.6	1.3	398.4
110	5.08	159.11	3.3	168.9	-13.3	331.6	1.3	398.5
111	5.12	158.65	3.4	154.4	-13.6	316.6	1.3	398.7
112	5.17	158.19	3.6	139.8	-13.8	301.6	1.4	398.8
113	5.21	157.72	3.7	125.2	-14	286.6	1.4	398.9
114	5.25	157.26	3.9	110.7	-14.2	271.6	1.4	399
115	5.29	156.8	4	96.1	-14.4	256.6	1.4	399.1
116	5.33	156.34	4.2	81.5	-14.6	241.6	1.4	399.2
117	5.38	155.88	4.4	67	-14.8	226.6	1.4	399.3
118	5.42	155.42	4.5	52.4	-15	211.6	1.5	399.4
119	5.46	154.96	4.7	37.9	-15.2	196.6	1.5	399.5
120	5.5	154.5	4.9	23.3	-15.4	181.6	1.5	399.6
121	5.54	154.04	5	8.7	-15.6	166.6	1.5	399.7
122	5.58	153.58	5.2	354.2	-15.8	151.6	1.5	399.8
123	5.62	153.12	5.4	339.6	-16	136.6	1.5	399.9
124	5.67	152.66	5.6	325.1	-16.2	121.6	1.6	400
125	5.71	152.2	5.8	310.5	-16.4	106.6	1.6	400.1
126	5.75	151.74	6	295.9	-16.6	91.6	1.6	400.2
127	5.79	151.28	6.2	281.4	-16.8	76.6	1.6	400.3
128	5.83	150.82	6.3	266.8	-17	61.6	1.6	400.4
129	5.88	150.36	6.5	252.3	-17.2	46.6	1.6	400.5
130	5.92	149.9	6.7	237.7	-17.4	31.6	1.7	400.6
131	5.96	149.45	6.9	223.2	-17.6	16.6	1.7	400.7
132	6	148.99	7.2	208.6	-17.8	1.6	1.7	400.8
133	6.04	148.53	7.4	194.1	-18	346.6	1.7	400.9
134	6.08	148.07	7.6	179.5	-18.2	331.5	1.7	401
135	6.12	147.61	7.8	165	-18.4	316.5	1.7	401.1
136	6.17	147.16	8	150.4	-18.5	301.5	1.8	401.2
137	6.21	146.7	8.2	135.9	-18.7	286.5	1.8	401.2
138	6.25	146.24	8.4	121.3	-18.9	271.5	1.8	401.3
139	6.29	145.79	8.7	106.8	-19.1	256.5	1.8	401.4
140	6.33	145.33	8.9	92.2	-19.3	241.5	1.8	401.5
141	6.38	144.87	9.1	77.7	-19.4	226.5	1.8	401.6
142	6.42	144.42	9.3	63.1	-19.6	211.5	1.9	401.6
143	6.46	143.96	9.6	48.6	-19.8	196.5	1.9	401.7
144	6.5	143.51	9.8	34	-20	181.5	1.9	401.8
145	6.54	143.05	10	19.5	-20.1	166.5	1.9	401.9
146	6.58	142.6	10.3	4.9	-20.3	151.5	1.9	401.9

ObsID is the simulated observation number (the first observation is 2008-03-19 00:00 UT), **JD** is the Julian Date of the observation minus 2454544, **α** is the Sun-Earth-Moon phase angle in degrees, **illum** is the Earth's illumination percentage, $\boldsymbol{\lambda}_{\leftmoon}$ is the sub-Lunar longitude, $\boldsymbol{\beta}_{\leftmoon}$ is the sub-Lunar latitude, $\boldsymbol{\lambda}_{\odot}$ is the sub-solar longitude, $\boldsymbol{\beta}_{\odot}$ is the sub-solar latitude, and **Δr** is the Earth-Moon distance ($\times 10^{-3}$ km).

ObsID	JD(+2454544)	α(°)	Illum(%)	$\lambda_{☾}$(°)	$\beta_{☾}$(°)	$\lambda_{☉}$(°)	$\beta_{☉}$(°)	Δr ($\times 10^{-3}$ km)
147	6.62	142.14	10.5	350.4	-20.5	136.5	1.9	402
148	6.67	141.69	10.8	335.9	-20.6	121.5	1.9	402.1
149	6.71	141.23	11	321.3	-20.8	106.5	2	402.2
150	6.75	140.78	11.3	306.8	-21	91.5	2	402.2
151	6.79	140.32	11.5	292.2	-21.1	76.5	2	402.3
152	6.83	139.87	11.8	277.7	-21.3	61.5	2	402.3
153	6.88	139.41	12	263.2	-21.4	46.5	2	402.4
154	6.92	138.96	12.3	248.6	-21.6	31.5	2	402.5
155	6.96	138.51	12.6	234.1	-21.8	16.5	2.1	402.5
156	7	138.05	12.8	219.6	-21.9	1.5	2.1	402.6
157	7.04	137.6	13.1	205	-22.1	346.5	2.1	402.6
158	7.08	137.15	13.3	190.5	-22.2	331.5	2.1	402.7
159	7.12	136.69	13.6	176	-22.4	316.5	2.1	402.8
160	7.17	136.24	13.9	161.5	-22.5	301.5	2.1	402.8
161	7.21	135.79	14.2	146.9	-22.7	286.5	2.2	402.9
162	7.25	135.33	14.4	132.4	-22.8	271.5	2.2	402.9
163	7.29	134.88	14.7	117.9	-22.9	256.4	2.2	403
164	7.33	134.43	15	103.3	-23.1	241.4	2.2	403
165	7.38	133.98	15.3	88.8	-23.2	226.4	2.2	403
166	7.42	133.52	15.6	74.3	-23.4	211.4	2.2	403.1
167	7.46	133.07	15.9	59.8	-23.5	196.4	2.3	403.1
168	7.5	132.62	16.1	45.2	-23.6	181.4	2.3	403.2
169	7.54	132.17	16.4	30.7	-23.8	166.4	2.3	403.2
170	7.58	131.72	16.7	16.2	-23.9	151.4	2.3	403.2
171	7.62	131.27	17	1.7	-24	136.4	2.3	403.3
172	7.67	130.81	17.3	347.2	-24.1	121.4	2.4	403.3
173	7.71	130.36	17.6	332.6	-24.3	106.4	2.4	403.3
174	7.75	129.91	17.9	318.1	-24.4	91.4	2.4	403.4
175	7.79	129.46	18.2	303.6	-24.5	76.4	2.4	403.4
176	7.83	129.01	18.5	289.1	-24.6	61.4	2.4	403.4
177	7.88	128.56	18.8	274.6	-24.8	46.4	2.4	403.4
178	7.92	128.11	19.1	260.1	-24.9	31.4	2.5	403.5
179	7.96	127.66	19.5	245.6	-25	16.4	2.5	403.5
180	8	127.21	19.8	231	-25.1	1.4	2.5	403.5
181	8.04	126.76	20.1	216.5	-25.2	346.4	2.5	403.5
182	8.08	126.31	20.4	202	-25.3	331.4	2.5	403.5
183	8.12	125.86	20.7	187.5	-25.4	316.4	2.5	403.5
184	8.17	125.4	21	173	-25.5	301.4	2.5	403.5

ObsID is the simulated observation number (the first observation is 2008-03-19 00:00 UT), **JD** is the Julian Date of the observation minus 2454544, **α** is the Sun-Earth-Moon phase angle in degrees, **illum** is the Earth's illumination percentage, $\lambda_{☾}$ is the sub-Lunar longitude, $\beta_{☾}$ is the sub-Lunar latitude, $\lambda_{☉}$ is the sub-solar longitude, $\beta_{☉}$ is the sub-solar latitude, and **Δr** is the Earth-Moon distance ($\times 10^{-3}$ km).

ObsID	JD(+2454544)	α(°)	Illum(%)	$\lambda_{\leftmoon}$(°)	$\beta_{\leftmoon}$(°)	$\lambda_{\odot}$(°)	$\beta_{\odot}$(°)	Δr ($\times 10^{-3}$ km)
185	8.21	124.95	21.4	158.5	-25.6	286.4	2.6	403.6
186	8.25	124.5	21.7	144	-25.7	271.4	2.6	403.6
187	8.29	124.05	22	129.5	-25.8	256.4	2.6	403.6
188	8.33	123.6	22.3	115	-25.9	241.4	2.6	403.6
189	8.38	123.15	22.7	100.5	-26	226.4	2.6	403.6
190	8.42	122.7	23	86	-26.1	211.4	2.6	403.6
191	8.46	122.25	23.3	71.5	-26.2	196.4	2.7	403.6
192	8.5	121.8	23.7	57	-26.3	181.4	2.7	403.6
193	8.54	121.35	24	42.5	-26.4	166.4	2.7	403.5
194	8.58	120.9	24.3	28	-26.5	151.3	2.7	403.5
195	8.62	120.45	24.7	13.5	-26.5	136.3	2.7	403.5
196	8.67	120	25	359	-26.6	121.3	2.7	403.5
197	8.71	119.55	25.3	344.5	-26.7	106.3	2.8	403.5
198	8.75	119.1	25.7	330	-26.8	91.3	2.8	403.5
199	8.79	118.65	26	315.5	-26.8	76.3	2.8	403.5
200	8.83	118.2	26.4	301	-26.9	61.3	2.8	403.4
201	8.88	117.75	26.7	286.5	-27	46.3	2.8	403.4
202	8.92	117.3	27.1	272	-27.1	31.3	2.8	403.4
203	8.96	116.85	27.4	257.5	-27.1	16.3	2.9	403.4
204	9	116.4	27.8	243	-27.2	1.3	2.9	403.3
205	9.04	115.95	28.1	228.5	-27.2	346.3	2.9	403.3
206	9.08	115.5	28.5	214	-27.3	331.3	2.9	403.3
207	9.12	115.05	28.8	199.5	-27.4	316.3	2.9	403.2
208	9.17	114.6	29.2	185	-27.4	301.3	2.9	403.2
209	9.21	114.15	29.5	170.6	-27.5	286.3	3	403.1
210	9.25	113.7	29.9	156.1	-27.5	271.3	3	403.1
211	9.29	113.25	30.3	141.6	-27.6	256.3	3	403.1
212	9.33	112.8	30.6	127.1	-27.6	241.3	3	403
213	9.38	112.35	31	112.6	-27.7	226.3	3	403
214	9.42	111.89	31.4	98.1	-27.7	211.3	3	402.9
215	9.46	111.44	31.7	83.6	-27.7	196.3	3	402.9
216	9.5	110.99	32.1	69.1	-27.8	181.3	3.1	402.8
217	9.54	110.54	32.5	54.7	-27.8	166.3	3.1	402.8
218	9.58	110.09	32.8	40.2	-27.8	151.3	3.1	402.7
219	9.62	109.64	33.2	25.7	-27.9	136.3	3.1	402.6
220	9.67	109.19	33.6	11.2	-27.9	121.3	3.1	402.6
221	9.71	108.73	33.9	356.7	-27.9	106.3	3.1	402.5
222	9.75	108.28	34.3	342.2	-28	91.3	3.2	402.4

ObsID is the simulated observation number (the first observation is 2008-03-19 00:00 UT), **JD** is the Julian Date of the observation minus 2454544, **α** is the Sun-Earth-Moon phase angle in degrees, **illum** is the Earth's illumination percentage, $\boldsymbol{\lambda}_{\leftmoon}$ is the sub-Lunar longitude, $\boldsymbol{\beta}_{\leftmoon}$ is the sub-Lunar latitude, $\boldsymbol{\lambda}_{\odot}$ is the sub-solar longitude, $\boldsymbol{\beta}_{\odot}$ is the sub-solar latitude, and **Δr** is the Earth-Moon distance ($\times 10^{-3}$ km).

ObsID	JD(+2454544)	α(°)	Illum(%)	$\lambda_{\leftmoon}$(°)	$\beta_{\leftmoon}$(°)	$\lambda_{\odot}$(°)	$\beta_{\odot}$(°)	Δr ($\times 10^{-3}$ km)
223	9.79	107.83	34.7	327.7	-28	76.3	3.2	402.4
224	9.83	107.38	35.1	313.3	-28	61.3	3.2	402.3
225	9.88	106.93	35.4	298.8	-28	46.3	3.2	402.2
226	9.92	106.47	35.8	284.3	-28	31.2	3.2	402.1
227	9.96	106.02	36.2	269.8	-28	16.2	3.2	402.1
228	10	105.57	36.6	255.3	-28.1	1.2	3.3	402
229	10.04	105.11	37	240.9	-28.1	346.2	3.3	401.9
230	10.08	104.66	37.3	226.4	-28.1	331.2	3.3	401.8
231	10.12	104.21	37.7	211.9	-28.1	316.2	3.3	401.7
232	10.17	103.75	38.1	197.4	-28.1	301.2	3.3	401.6
233	10.21	103.3	38.5	182.9	-28.1	286.2	3.4	401.5
234	10.25	102.85	38.9	168.5	-28.1	271.2	3.4	401.5
235	10.29	102.39	39.3	154	-28.1	256.2	3.4	401.4
236	10.33	101.94	39.7	139.5	-28.1	241.2	3.4	401.3
237	10.38	101.48	40	125	-28	226.2	3.4	401.2
238	10.42	101.03	40.4	110.5	-28	211.2	3.4	401.1
239	10.46	100.57	40.8	96.1	-28	196.2	3.5	401
240	10.5	100.12	41.2	81.6	-28	181.2	3.5	400.8
241	10.54	99.66	41.6	67.1	-28	166.2	3.5	400.7
242	10.58	99.2	42	52.6	-28	151.2	3.5	400.6
243	10.62	98.75	42.4	38.1	-27.9	136.2	3.5	400.5
244	10.67	98.29	42.8	23.7	-27.9	121.2	3.5	400.4
245	10.71	97.84	43.2	9.2	-27.9	106.2	3.5	400.3
246	10.75	97.38	43.6	354.7	-27.8	91.2	3.6	400.2
247	10.79	96.92	44	340.2	-27.8	76.2	3.6	400
248	10.83	96.46	44.4	325.8	-27.8	61.2	3.6	399.9
249	10.88	96.01	44.8	311.3	-27.7	46.2	3.6	399.8
250	10.92	95.55	45.2	296.8	-27.7	31.2	3.6	399.7
251	10.96	95.09	45.6	282.3	-27.7	16.2	3.6	399.5
252	11	94.63	46	267.8	-27.6	1.2	3.7	399.4
253	11.04	94.17	46.4	253.4	-27.6	346.2	3.7	399.3
254	11.08	93.71	46.8	238.9	-27.5	331.2	3.7	399.1
255	11.12	93.25	47.2	224.4	-27.5	316.2	3.7	399
256	11.17	92.79	47.6	209.9	-27.4	301.2	3.7	398.9
257	11.21	92.33	48	195.4	-27.4	286.2	3.7	398.7
258	11.25	91.87	48.4	181	-27.3	271.1	3.8	398.6
259	11.29	91.41	48.8	166.5	-27.2	256.1	3.8	398.4
260	11.33	90.95	49.2	152	-27.2	241.2	3.8	398.3

ObsID is the simulated observation number (the first observation is 2008-03-19 00:00 UT), **JD** is the Julian Date of the observation minus 2454544, **α** is the Sun-Earth-Moon phase angle in degrees, **illum** is the Earth's illumination percentage, $\lambda_{\leftmoon}$ is the sub-Lunar longitude, $\beta_{\leftmoon}$ is the sub-Lunar latitude, $\lambda_{\odot}$ is the sub-solar longitude, $\beta_{\odot}$ is the sub-solar latitude, and **Δr** is the Earth-Moon distance ($\times 10^{-3}$ km).

ObsID	JD(+2454544)	α(°)	Illum(%)	$\lambda_{\leftmoon}$(°)	$\beta_{\leftmoon}$(°)	$\lambda_{\odot}$(°)	$\beta_{\odot}$(°)	Δr ($\times 10^{-3}$ km)
261	11.38	90.48	49.6	137.5	-27.1	226.1	3.8	398.1
262	11.42	90.02	50	123	-27	211.1	3.8	398
263	11.46	89.56	50.4	108.6	-27	196.1	3.8	397.8
264	11.5	89.1	50.8	94.1	-26.9	181.1	3.9	397.7
265	11.54	88.63	51.2	79.6	-26.8	166.1	3.9	397.5
266	11.58	88.17	51.6	65.1	-26.8	151.1	3.9	397.4
267	11.62	87.7	52	50.6	-26.7	136.1	3.9	397.2
268	11.67	87.24	52.4	36.2	-26.6	121.1	3.9	397
269	11.71	86.77	52.8	21.7	-26.5	106.1	3.9	396.9
270	11.75	86.31	53.2	7.2	-26.4	91.1	4	396.7
271	11.79	85.84	53.6	352.7	-26.3	76.1	4	396.5
272	11.83	85.37	54	338.2	-26.2	61.1	4	396.4
273	11.88	84.91	54.4	323.7	-26.2	46.1	4	396.2
274	11.92	84.44	54.8	309.3	-26.1	31.1	4	396
275	11.96	83.97	55.2	294.8	-26	16.1	4	395.8
276	12	83.5	55.7	280.3	-25.9	1.1	4	395.7
277	12.04	83.04	56.1	265.8	-25.8	346.1	4.1	395.5
278	12.08	82.57	56.5	251.3	-25.7	331.1	4.1	395.3
279	12.12	82.1	56.9	236.8	-25.6	316.1	4.1	395.1
280	12.17	81.63	57.3	222.3	-25.4	301.1	4.1	394.9
281	12.21	81.16	57.7	207.9	-25.3	286.1	4.1	394.7
282	12.25	80.68	58.1	193.4	-25.2	271.1	4.2	394.5
283	12.29	80.21	58.5	178.9	-25.1	256.1	4.2	394.4
284	12.33	79.74	58.9	164.4	-25	241.1	4.2	394.2
285	12.38	79.27	59.3	149.9	-24.9	226.1	4.2	394
286	12.42	78.79	59.7	135.4	-24.8	211.1	4.2	393.8
287	12.46	78.32	60.1	120.9	-24.6	196.1	4.2	393.6
288	12.5	77.85	60.5	106.4	-24.5	181.1	4.2	393.4
289	12.54	77.37	60.9	91.9	-24.4	166.1	4.3	393.2
290	12.58	76.9	61.3	77.4	-24.2	151.1	4.3	393
291	12.62	76.42	61.7	63	-24.1	136.1	4.3	392.8
292	12.67	75.94	62.1	48.5	-24	121	4.3	392.6
293	12.71	75.47	62.5	34	-23.8	106	4.3	392.4
294	12.75	74.99	63	19.5	-23.7	91	4.3	392.2
295	12.79	74.51	63.4	5	-23.6	76	4.4	391.9
296	12.83	74.03	63.8	350.5	-23.4	61	4.4	391.7
297	12.88	73.55	64.2	336	-23.3	46	4.4	391.5
298	12.92	73.07	64.6	321.5	-23.1	31	4.4	391.3

ObsID is the simulated observation number (the first observation is 2008-03-19 00:00 UT), **JD** is the Julian Date of the observation minus 2454544, **α** is the Sun-Earth-Moon phase angle in degrees, **illum** is the Earth's illumination percentage, $\boldsymbol{\lambda}_{\leftmoon}$ is the sub-Lunar longitude, $\boldsymbol{\beta}_{\leftmoon}$ is the sub-Lunar latitude, $\boldsymbol{\lambda}_{\odot}$ is the sub-solar longitude, $\boldsymbol{\beta}_{\odot}$ is the sub-solar latitude, and **Δr** is the Earth-Moon distance ($\times 10^{-3}$ km).

ObsID	JD(+2454544)	α(°)	Illum(%)	$\lambda_{☾}$(°)	$\beta_{☾}$(°)	$\lambda_{☉}$(°)	$\beta_{☉}$(°)	Δr ($\times 10^{-3}$ km)
299	12.96	72.59	65	307	-23	16	4.4	391.1
300	13	72.11	65.4	292.5	-22.8	1	4.4	390.9
301	13.04	71.63	65.8	278	-22.7	346	4.5	390.7
302	13.08	71.15	66.2	263.5	-22.5	331	4.5	390.4
303	13.12	70.66	66.6	249	-22.4	316	4.5	390.2
304	13.17	70.18	67	234.5	-22.2	301	4.5	390
305	13.21	69.69	67.3	220	-22.1	286	4.5	389.8
306	13.25	69.21	67.7	205.5	-21.9	271	4.5	389.6
307	13.29	68.72	68.1	191	-21.7	256	4.5	389.3
308	13.33	68.24	68.5	176.5	-21.6	241	4.6	389.1
309	13.38	67.75	68.9	162	-21.4	226	4.6	388.9
310	13.42	67.26	69.3	147.5	-21.2	211	4.6	388.7
311	13.46	66.78	69.7	133	-21.1	196	4.6	388.4
312	13.5	66.29	70.1	118.5	-20.9	181	4.6	388.2
313	13.54	65.8	70.5	104	-20.7	166	4.7	388
314	13.58	65.31	70.9	89.5	-20.5	151	4.7	387.7
315	13.62	64.82	71.3	75	-20.4	136	4.7	387.5
316	13.67	64.33	71.7	60.5	-20.2	121	4.7	387.3
317	13.71	63.83	72	46	-20	106	4.7	387
318	13.75	63.34	72.4	31.5	-19.8	91	4.7	386.8
319	13.79	62.85	72.8	17	-19.6	76	4.8	386.6
320	13.83	62.36	73.2	2.4	-19.4	61	4.8	386.3
321	13.88	61.86	73.6	347.9	-19.2	46	4.8	386.1
322	13.92	61.37	74	333.4	-19	30.9	4.8	385.8
323	13.96	60.87	74.3	318.9	-18.9	15.9	4.8	385.6
324	14	60.37	74.7	304.4	-18.7	0.9	4.8	385.4
325	14.04	59.88	75.1	289.9	-18.5	345.9	4.8	385.1
326	14.08	59.38	75.5	275.4	-18.3	330.9	4.9	384.9
327	14.12	58.88	75.8	260.9	-18.1	315.9	4.9	384.6
328	14.17	58.38	76.2	246.4	-17.9	300.9	4.9	384.4
329	14.21	57.88	76.6	231.8	-17.7	285.9	4.9	384.1
330	14.25	57.38	77	217.3	-17.4	270.9	4.9	383.9
331	14.29	56.88	77.3	202.8	-17.2	255.9	4.9	383.6
332	14.33	56.37	77.7	188.3	-17	240.9	5	383.4
333	14.38	55.87	78.1	173.8	-16.8	225.9	5	383.2
334	14.42	55.37	78.4	159.3	-16.6	210.9	5	382.9
335	14.46	54.86	78.8	144.8	-16.4	195.9	5	382.7
336	14.5	54.36	79.1	130.2	-16.2	180.9	5	382.4

ObsID is the simulated observation number (the first observation is 2008-03-19 00:00 UT), **JD** is the Julian Date of the observation minus 2454544, **α** is the Sun-Earth-Moon phase angle in degrees, **illum** is the Earth's illumination percentage, $\lambda_{☾}$ is the sub-Lunar longitude, $\beta_{☾}$ is the sub-Lunar latitude, $\lambda_{☉}$ is the sub-solar longitude, $\beta_{☉}$ is the sub-solar latitude, and **Δr** is the Earth-Moon distance ($\times 10^{-3}$ km).

ObsID	JD(+2454544)	α(°)	Illum(%)	$\lambda_{\leftmoon}$(°)	$\beta_{\leftmoon}$(°)	$\lambda_{\odot}$(°)	$\beta_{\odot}$(°)	Δr ($\times 10^{-3}$ km)
337	14.54	53.85	79.5	115.7	-16	165.9	5	382.2
338	14.58	53.34	79.8	101.2	-15.7	150.9	5	381.9
339	14.62	52.84	80.2	86.7	-15.5	135.9	5.1	381.7
340	14.67	52.33	80.6	72.2	-15.3	120.9	5.1	381.4
341	14.71	51.82	80.9	57.7	-15.1	105.9	5.1	381.2
342	14.75	51.31	81.3	43.1	-14.8	90.9	5.1	380.9
343	14.79	50.8	81.6	28.6	-14.6	75.9	5.1	380.7
344	14.83	50.29	81.9	14.1	-14.4	60.9	5.2	380.4
345	14.88	49.78	82.3	359.6	-14.2	45.9	5.2	380.2
346	14.92	49.26	82.6	345.1	-13.9	30.9	5.2	379.9
347	14.96	48.75	83	330.5	-13.7	15.9	5.2	379.7
348	15	48.24	83.3	316	-13.5	0.9	5.2	379.4
349	15.04	47.72	83.6	301.5	-13.2	345.9	5.2	379.2
350	15.08	47.21	84	287	-13	330.9	5.2	378.9
351	15.12	46.69	84.3	272.5	-12.8	315.9	5.3	378.7
352	15.17	46.17	84.6	257.9	-12.5	300.9	5.3	378.4
353	15.21	45.66	84.9	243.4	-12.3	285.9	5.3	378.2
354	15.25	45.14	85.3	228.9	-12	270.9	5.3	377.9
355	15.29	44.62	85.6	214.4	-11.8	255.8	5.3	377.7
356	15.33	44.1	85.9	199.9	-11.5	240.8	5.3	377.4
357	15.38	43.58	86.2	185.3	-11.3	225.8	5.4	377.2
358	15.42	43.06	86.5	170.8	-11.1	210.8	5.4	377
359	15.46	42.53	86.8	156.3	-10.8	195.8	5.4	376.7
360	15.5	42.01	87.1	141.8	-10.6	180.8	5.4	376.5
361	15.54	41.49	87.5	127.2	-10.3	165.8	5.4	376.2
362	15.58	40.96	87.8	112.7	-10.1	150.8	5.4	376
363	15.62	40.44	88.1	98.2	-9.8	135.8	5.5	375.7
364	15.67	39.91	88.3	83.7	-9.5	120.8	5.5	375.5
365	15.71	39.39	88.6	69.1	-9.3	105.8	5.5	375.2
366	15.75	38.86	88.9	54.6	-9	90.8	5.5	375
367	15.79	38.33	89.2	40.1	-8.8	75.8	5.5	374.8
368	15.83	37.8	89.5	25.6	-8.5	60.8	5.5	374.5
369	15.88	37.28	89.8	11.1	-8.3	45.8	5.5	374.3
370	15.92	36.75	90.1	356.5	-8	30.8	5.6	374
371	15.96	36.22	90.3	342	-7.7	15.8	5.6	373.8
372	16	35.68	90.6	327.5	-7.5	0.8	5.6	373.6
373	16.04	35.15	90.9	313	-7.2	345.8	5.6	373.3
374	16.08	34.62	91.1	298.4	-6.9	330.8	5.6	373.1

ObsID is the simulated observation number (the first observation is 2008-03-19 00:00 UT), **JD** is the Julian Date of the observation minus 2454544, **α** is the Sun-Earth-Moon phase angle in degrees, **illum** is the Earth's illumination percentage, $\lambda_{\leftmoon}$ is the sub-Lunar longitude, $\beta_{\leftmoon}$ is the sub-Lunar latitude, $\lambda_{\odot}$ is the sub-solar longitude, $\beta_{\odot}$ is the sub-solar latitude, and **Δr** is the Earth-Moon distance ($\times 10^{-3}$ km).

ObsID	JD(+2454544)	α(°)	Illum(%)	$\lambda_{\leftmoon}$(°)	$\beta_{\leftmoon}$(°)	$\lambda_{\odot}$(°)	$\beta_{\odot}$(°)	Δr ($\times 10^{-3}$ km)
375	16.12	34.09	91.4	283.9	-6.7	315.8	5.7	372.9
376	16.17	33.55	91.7	269.4	-6.4	300.8	5.7	372.6
377	16.21	33.02	91.9	254.9	-6.1	285.8	5.7	372.4
378	16.25	32.48	92.2	240.3	-5.9	270.8	5.7	372.2
379	16.29	31.95	92.4	225.8	-5.6	255.8	5.7	371.9
380	16.33	31.41	92.7	211.3	-5.3	240.8	5.7	371.7
381	16.38	30.87	92.9	196.8	-5.1	225.8	5.8	371.5
382	16.42	30.34	93.2	182.3	-4.8	210.8	5.8	371.3
383	16.46	29.8	93.4	167.7	-4.5	195.8	5.8	371
384	16.5	29.26	93.6	153.2	-4.3	180.8	5.8	370.8
385	16.54	28.72	93.8	138.7	-4	165.8	5.8	370.6
386	16.58	28.18	94.1	124.2	-3.7	150.8	5.8	370.4
387	16.62	27.64	94.3	109.7	-3.4	135.8	5.8	370.1
388	16.67	27.1	94.5	95.1	-3.2	120.8	5.9	369.9
389	16.71	26.56	94.7	80.6	-2.9	105.8	5.9	369.7
390	16.75	26.02	94.9	66.1	-2.6	90.8	5.9	369.5
391	16.79	25.48	95.1	51.6	-2.3	75.7	5.9	369.3
392	16.83	24.93	95.3	37.1	-2.1	60.7	5.9	369.1
393	16.88	24.39	95.5	22.5	-1.8	45.7	5.9	368.9
394	16.92	23.85	95.7	8	-1.5	30.7	6	368.7
395	16.96	23.3	95.9	353.5	-1.2	15.7	6	368.4
396	17	22.76	96.1	339	-0.9	0.7	6	368.2
397	17.04	22.22	96.3	324.5	-0.7	345.7	6	368
398	17.08	21.67	96.5	310	-0.4	330.7	6	367.8
399	17.12	21.13	96.6	295.4	-0.1	315.7	6	367.6
400	17.17	20.58	96.8	280.9	0.2	300.7	6	367.4
401	17.21	20.04	97	266.4	0.5	285.7	6.1	367.2
402	17.25	19.49	97.1	251.9	0.7	270.7	6.1	367
403	17.29	18.95	97.3	237.4	1	255.7	6.1	366.9
404	17.33	18.4	97.4	222.9	1.3	240.7	6.1	366.7
405	17.38	17.86	97.6	208.4	1.6	225.7	6.1	366.5
406	17.42	17.31	97.7	193.9	1.9	210.7	6.1	366.3
407	17.46	16.77	97.9	179.4	2.2	195.7	6.2	366.1
408	17.5	16.23	98	164.8	2.4	180.7	6.2	365.9
409	17.54	15.68	98.1	150.3	2.7	165.7	6.2	365.7
410	17.58	15.14	98.3	135.8	3	150.7	6.2	365.6
411	17.62	14.6	98.4	121.3	3.3	135.7	6.2	365.4
412	17.67	14.06	98.5	106.8	3.6	120.7	6.2	365.2

ObsID is the simulated observation number (the first observation is 2008-03-19 00:00 UT), **JD** is the Julian Date of the observation minus 2454544, **α** is the Sun-Earth-Moon phase angle in degrees, **illum** is the Earth's illumination percentage, $\boldsymbol{\lambda}_{\leftmoon}$ is the sub-Lunar longitude, $\boldsymbol{\beta}_{\leftmoon}$ is the sub-Lunar latitude, $\boldsymbol{\lambda}_{\odot}$ is the sub-solar longitude, $\boldsymbol{\beta}_{\odot}$ is the sub-solar latitude, and **Δr** is the Earth-Moon distance ($\times 10^{-3}$ km).

ObsID	JD(+2454544)	α(°)	Illum(%)	$\lambda_{\leftmoon}$(°)	$\beta_{\leftmoon}$(°)	$\lambda_{\odot}$(°)	$\beta_{\odot}$(°)	Δr ($\times 10^{-3}$ km)
413	17.71	13.52	98.6	92.3	3.8	105.7	6.3	365
414	17.75	12.98	98.7	77.8	4.1	90.7	6.3	364.9
415	17.79	12.44	98.8	63.3	4.4	75.7	6.3	364.7
416	17.83	11.91	98.9	48.8	4.7	60.7	6.3	364.5
417	17.88	11.38	99	34.3	5	45.7	6.3	364.4
418	17.92	10.85	99.1	19.8	5.3	30.7	6.3	364.2
419	17.96	10.32	99.2	5.3	5.5	15.7	6.3	364.1
420	18	9.8	99.3	350.8	5.8	0.7	6.4	363.9
421	18.04	9.29	99.3	336.3	6.1	345.6	6.4	363.8
422	18.08	8.78	99.4	321.8	6.4	330.6	6.4	363.6
423	18.12	8.27	99.5	307.3	6.7	315.6	6.4	363.5
424	18.17	7.78	99.5	292.8	6.9	300.6	6.4	363.3
425	18.21	7.29	99.6	278.3	7.2	285.6	6.5	363.2
426	18.25	6.82	99.6	263.8	7.5	270.6	6.5	363
427	18.29	6.36	99.7	249.4	7.8	255.6	6.5	362.9
428	18.33	5.93	99.7	234.9	8.1	240.6	6.5	362.8
429	18.38	5.51	99.8	220.4	8.3	225.6	6.5	362.6
430	18.42	5.13	99.8	205.9	8.6	210.6	6.5	362.5
431	18.46	4.79	99.8	191.4	8.9	195.6	6.5	362.4
432	18.5	4.49	99.8	176.9	9.2	180.6	6.6	362.2
433	18.54	4.25	99.9	162.4	9.4	165.6	6.6	362.1
434	18.58	4.07	99.9	148	9.7	150.6	6.6	362
435	18.62	3.97	99.9	133.5	10	135.6	6.6	361.9
436	18.67	3.95	99.9	119	10.3	120.6	6.6	361.8
437	18.71	4.02	99.9	104.5	10.5	105.6	6.6	361.7
438	18.75	4.16	99.9	90	10.8	90.6	6.7	361.5
439	18.79	4.38	99.9	75.6	11.1	75.6	6.7	361.4
440	18.83	4.66	99.8	61.1	11.3	60.6	6.7	361.3
441	18.88	4.98	99.8	46.6	11.6	45.6	6.7	361.2
442	18.92	5.36	99.8	32.1	11.9	30.6	6.7	361.1
443	18.96	5.76	99.7	17.7	12.1	15.6	6.7	361
444	19	6.19	99.7	3.2	12.4	0.6	6.8	361
445	19.04	6.65	99.7	348.7	12.7	345.6	6.8	360.9
446	19.08	7.12	99.6	334.3	12.9	330.6	6.8	360.8
447	19.12	7.61	99.6	319.8	13.2	315.6	6.8	360.7
448	19.17	8.11	99.5	305.3	13.5	300.6	6.8	360.6
449	19.21	8.62	99.4	290.9	13.7	285.6	6.8	360.5
450	19.25	9.14	99.4	276.4	14	270.6	6.8	360.5

ObsID is the simulated observation number (the first observation is 2008-03-19 00:00 UT), **JD** is the Julian Date of the observation minus 2454544, **α** is the Sun-Earth-Moon phase angle in degrees, **illum** is the Earth's illumination percentage, $\boldsymbol{\lambda}_{\leftmoon}$ is the sub-Lunar longitude, $\boldsymbol{\beta}_{\leftmoon}$ is the sub-Lunar latitude, $\boldsymbol{\lambda}_{\odot}$ is the sub-solar longitude, $\boldsymbol{\beta}_{\odot}$ is the sub-solar latitude, and **Δr** is the Earth-Moon distance ($\times 10^{-3}$ km).

ObsID	JD(+2454544)	α(°)	Illum(%)	$\lambda_{\leftmoon}$(°)	$\beta_{\leftmoon}$(°)	$\lambda_{\odot}$(°)	$\beta_{\odot}$(°)	Δr ($\times 10^{-3}$ km)
451	19.29	9.66	99.3	262	14.2	255.6	6.9	360.4
452	19.33	10.19	99.2	247.5	14.5	240.6	6.9	360.3
453	19.38	10.73	99.1	233	14.7	225.6	6.9	360.2
454	19.42	11.27	99	218.6	15	210.6	6.9	360.2
455	19.46	11.81	98.9	204.1	15.2	195.6	6.9	360.1
456	19.5	12.36	98.8	189.7	15.5	180.6	6.9	360.1
457	19.54	12.91	98.7	175.2	15.7	165.6	7	360
458	19.58	13.47	98.6	160.8	16	150.5	7	360
459	19.62	14.02	98.5	146.4	16.2	135.5	7	359.9
460	19.67	14.58	98.4	131.9	16.5	120.5	7	359.9
461	19.71	15.14	98.3	117.5	16.7	105.5	7	359.8
462	19.75	15.7	98.1	103	17	90.5	7	359.8
463	19.79	16.26	98	88.6	17.2	75.5	7	359.7
464	19.83	16.83	97.9	74.1	17.4	60.5	7.1	359.7
465	19.88	17.39	97.7	59.7	17.7	45.5	7.1	359.7
466	19.92	17.96	97.6	45.3	17.9	30.5	7.1	359.6
467	19.96	18.53	97.4	30.8	18.1	15.5	7.1	359.6
468	20	19.1	97.2	16.4	18.4	0.5	7.1	359.6
469	20.04	19.67	97.1	2	18.6	345.5	7.1	359.6
470	20.08	20.24	96.9	347.6	18.8	330.5	7.2	359.5
471	20.12	20.81	96.7	333.1	19	315.5	7.2	359.5
472	20.17	21.38	96.6	318.7	19.3	300.5	7.2	359.5
473	20.21	21.95	96.4	304.3	19.5	285.5	7.2	359.5
474	20.25	22.52	96.2	289.9	19.7	270.5	7.2	359.5
475	20.29	23.09	96	275.4	19.9	255.5	7.2	359.5
476	20.33	23.67	95.8	261	20.1	240.5	7.2	359.5
477	20.38	24.24	95.6	246.6	20.3	225.5	7.3	359.5
478	20.42	24.81	95.4	232.2	20.6	210.5	7.3	359.5
479	20.46	25.39	95.2	217.8	20.8	195.5	7.3	359.5
480	20.5	25.96	95	203.4	21	180.5	7.3	359.5
481	20.54	26.54	94.7	189	21.2	165.5	7.3	359.5
482	20.58	27.11	94.5	174.5	21.4	150.5	7.3	359.6
483	20.62	27.69	94.3	160.1	21.6	135.5	7.4	359.6
484	20.67	28.26	94	145.7	21.8	120.5	7.4	359.6
485	20.71	28.84	93.8	131.3	21.9	105.5	7.4	359.6
486	20.75	29.41	93.6	116.9	22.1	90.5	7.4	359.6
487	20.79	29.99	93.3	102.5	22.3	75.5	7.4	359.7
488	20.83	30.56	93.1	88.1	22.5	60.5	7.4	359.7

ObsID is the simulated observation number (the first observation is 2008-03-19 00:00 UT), **JD** is the Julian Date of the observation minus 2454544, **α** is the Sun-Earth-Moon phase angle in degrees, **illum** is the Earth's illumination percentage, $\boldsymbol{\lambda}_{\leftmoon}$ is the sub-Lunar longitude, $\boldsymbol{\beta}_{\leftmoon}$ is the sub-Lunar latitude, $\boldsymbol{\lambda}_{\odot}$ is the sub-solar longitude, $\boldsymbol{\beta}_{\odot}$ is the sub-solar latitude, and **Δr** is the Earth-Moon distance ($\times 10^{-3}$ km).

ObsID	JD(+2454544)	α(°)	Illum(%)	$\lambda_{\leftmoon}$(°)	$\beta_{\leftmoon}$(°)	$\lambda_{\odot}$(°)	$\beta_{\odot}$(°)	Δr ($\times 10^{-3}$ km)
489	20.88	31.14	92.8	73.7	22.7	45.5	7.5	359.7
490	20.92	31.71	92.5	59.3	22.9	30.4	7.5	359.8
491	20.96	32.29	92.3	44.9	23	15.4	7.5	359.8
492	21	32.86	92	30.5	23.2	0.5	7.5	359.9
493	21.04	33.44	91.7	16.2	23.4	345.4	7.5	359.9
494	21.08	34.01	91.4	1.8	23.6	330.4	7.5	359.9
495	21.12	34.59	91.2	347.4	23.7	315.4	7.5	360
496	21.17	35.16	90.9	333	23.9	300.4	7.6	360.1
497	21.21	35.74	90.6	318.6	24	285.4	7.6	360.1
498	21.25	36.31	90.3	304.2	24.2	270.4	7.6	360.2
499	21.29	36.89	90	289.8	24.4	255.4	7.6	360.2
500	21.33	37.46	89.7	275.5	24.5	240.4	7.6	360.3
501	21.38	38.04	89.4	261.1	24.7	225.4	7.6	360.4
502	21.42	38.61	89.1	246.7	24.8	210.4	7.7	360.4
503	21.46	39.18	88.8	232.3	24.9	195.4	7.7	360.5
504	21.5	39.76	88.4	217.9	25.1	180.4	7.7	360.6
505	21.54	40.33	88.1	203.6	25.2	165.4	7.7	360.6
506	21.58	40.9	87.8	189.2	25.3	150.4	7.7	360.7
507	21.62	41.48	87.5	174.8	25.5	135.4	7.7	360.8
508	21.67	42.05	87.1	160.4	25.6	120.4	7.8	360.9
509	21.71	42.62	86.8	146.1	25.7	105.4	7.8	361
510	21.75	43.2	86.5	131.7	25.8	90.4	7.8	361
511	21.79	43.77	86.1	117.3	26	75.4	7.8	361.1
512	21.83	44.34	85.8	103	26.1	60.4	7.8	361.2
513	21.88	44.91	85.4	88.6	26.2	45.4	7.8	361.3
514	21.92	45.48	85.1	74.2	26.3	30.4	7.8	361.4
515	21.96	46.05	84.7	59.9	26.4	15.4	7.9	361.5
516	22	46.62	84.3	45.5	26.5	0.4	7.9	361.6
517	22.04	47.19	84	31.1	26.6	345.4	7.9	361.7
518	22.08	47.76	83.6	16.8	26.7	330.4	7.9	361.8
519	22.12	48.33	83.2	2.4	26.8	315.4	7.9	361.9
520	22.17	48.9	82.9	348	26.9	300.4	7.9	362
521	22.21	49.47	82.5	333.7	27	285.4	8	362.1
522	22.25	50.04	82.1	319.3	27	270.4	8	362.3
523	22.29	50.61	81.7	305	27.1	255.4	8	362.4
524	22.33	51.17	81.4	290.6	27.2	240.4	8	362.5
525	22.38	51.74	81	276.2	27.3	225.3	8	362.6
526	22.42	52.31	80.6	261.9	27.3	210.3	8	362.7

ObsID is the simulated observation number (the first observation is 2008-03-19 00:00 UT), **JD** is the Julian Date of the observation minus 2454544, **α** is the Sun-Earth-Moon phase angle in degrees, **illum** is the Earth's illumination percentage, $\boldsymbol{\lambda}_{\leftmoon}$ is the sub-Lunar longitude, $\boldsymbol{\beta}_{\leftmoon}$ is the sub-Lunar latitude, $\boldsymbol{\lambda}_{\odot}$ is the sub-solar longitude, $\boldsymbol{\beta}_{\odot}$ is the sub-solar latitude, and **Δr** is the Earth-Moon distance ($\times 10^{-3}$ km).

ObsID	JD(+2454544)	α(°)	Illum(%)	$\lambda_{\leftmoon}$(°)	$\beta_{\leftmoon}$(°)	$\lambda_{\odot}$(°)	$\beta_{\odot}$(°)	Δr ($\times 10^{-3}$ km)
527	22.46	52.87	80.2	247.5	27.4	195.3	8.1	362.8
528	22.5	53.44	79.8	233.2	27.5	180.3	8.1	363
529	22.54	54	79.4	218.8	27.5	165.3	8.1	363.1
530	22.58	54.57	79	204.4	27.6	150.3	8.1	363.2
531	22.62	55.13	78.6	190.1	27.6	135.3	8.1	363.3
532	22.67	55.7	78.2	175.7	27.7	120.3	8.1	363.5
533	22.71	56.26	77.8	161.4	27.7	105.3	8.1	363.6
534	22.75	56.82	77.4	147	27.8	90.3	8.2	363.7
535	22.79	57.39	77	132.6	27.8	75.3	8.2	363.9
536	22.83	57.95	76.5	118.3	27.8	60.3	8.2	364
537	22.88	58.51	76.1	103.9	27.9	45.3	8.2	364.2
538	22.92	59.07	75.7	89.6	27.9	30.3	8.2	364.3
539	22.96	59.63	75.3	75.2	27.9	15.3	8.2	364.4
540	23	60.19	74.9	60.9	27.9	0.3	8.2	364.6
541	23.04	60.75	74.4	46.5	28	345.3	8.3	364.7
542	23.08	61.31	74	32.1	28	330.3	8.3	364.9
543	23.12	61.87	73.6	17.8	28	315.3	8.3	365
544	23.17	62.43	73.1	3.4	28	300.3	8.3	365.2
545	23.21	62.99	72.7	349	28	285.3	8.3	365.3
546	23.25	63.55	72.3	334.7	28	270.3	8.3	365.5
547	23.29	64.1	71.8	320.3	28	255.3	8.4	365.6
548	23.33	64.66	71.4	306	28	240.3	8.4	365.8
549	23.38	65.21	71	291.6	28	225.3	8.4	365.9
550	23.42	65.77	70.5	277.2	28	210.3	8.4	366.1
551	23.46	66.32	70.1	262.9	28	195.3	8.4	366.2
552	23.5	66.88	69.6	248.5	27.9	180.3	8.4	366.4
553	23.54	67.43	69.2	234.1	27.9	165.3	8.4	366.6
554	23.58	67.98	68.7	219.8	27.9	150.3	8.5	366.7
555	23.62	68.54	68.3	205.4	27.9	135.3	8.5	366.9
556	23.67	69.09	67.8	191	27.8	120.3	8.5	367.1
557	23.71	69.64	67.4	176.6	27.8	105.3	8.5	367.2
558	23.75	70.19	66.9	162.3	27.8	90.3	8.5	367.4
559	23.79	70.74	66.5	147.9	27.7	75.3	8.5	367.6
560	23.83	71.29	66	133.5	27.7	60.3	8.6	367.7
561	23.88	71.84	65.6	119.2	27.6	45.2	8.6	367.9
562	23.92	72.39	65.1	104.8	27.6	30.2	8.6	368.1
563	23.96	72.94	64.7	90.4	27.5	15.2	8.6	368.2
564	24	73.48	64.2	76	27.5	0.2	8.6	368.4

ObsID is the simulated observation number (the first observation is 2008-03-19 00:00 UT), **JD** is the Julian Date of the observation minus 2454544, **α** is the Sun-Earth-Moon phase angle in degrees, **illum** is the Earth's illumination percentage, $\boldsymbol{\lambda}_{\leftmoon}$ is the sub-Lunar longitude, $\boldsymbol{\beta}_{\leftmoon}$ is the sub-Lunar latitude, $\boldsymbol{\lambda}_{\odot}$ is the sub-solar longitude, $\boldsymbol{\beta}_{\odot}$ is the sub-solar latitude, and **Δr** is the Earth-Moon distance ($\times 10^{-3}$ km).

ObsID	JD(+2454544)	α(°)	Illum(%)	$\lambda_{\leftmoon}$(°)	$\beta_{\leftmoon}$(°)	$\lambda_{\odot}$(°)	$\beta_{\odot}$(°)	Δr ($\times 10^{-3}$ km)
565	24.04	74.03	63.8	61.6	27.4	345.2	8.6	368.6
566	24.08	74.58	63.3	47.2	27.3	330.2	8.7	368.7
567	24.12	75.12	62.8	32.9	27.3	315.2	8.7	368.9
568	24.17	75.67	62.4	18.5	27.2	300.2	8.7	369.1
569	24.21	76.21	61.9	4.1	27.1	285.2	8.7	369.3
570	24.25	76.76	61.5	349.7	27	270.2	8.7	369.5
571	24.29	77.3	61	335.3	27	255.2	8.7	369.6
572	24.33	77.84	60.5	320.9	26.9	240.2	8.7	369.8
573	24.38	78.39	60.1	306.5	26.8	225.2	8.8	370
574	24.42	78.93	59.6	292.1	26.7	210.2	8.8	370.2
575	24.46	79.47	59.1	277.7	26.6	195.2	8.8	370.3
576	24.5	80.01	58.7	263.3	26.5	180.2	8.8	370.5
577	24.54	80.55	58.2	248.9	26.4	165.2	8.8	370.7
578	24.58	81.09	57.7	234.5	26.3	150.2	8.8	370.9
579	24.62	81.63	57.3	220.1	26.2	135.2	8.8	371.1
580	24.67	82.16	56.8	205.7	26.1	120.2	8.9	371.2
581	24.71	82.7	56.4	191.3	26	105.2	8.9	371.4
582	24.75	83.24	55.9	176.9	25.9	90.2	8.9	371.6
583	24.79	83.78	55.4	162.5	25.8	75.2	8.9	371.8
584	24.83	84.31	55	148.1	25.7	60.2	8.9	372
585	24.88	84.85	54.5	133.7	25.6	45.2	8.9	372.2
586	24.92	85.38	54	119.3	25.5	30.2	8.9	372.4
587	24.96	85.92	53.6	104.8	25.3	15.2	9	372.5
588	25	86.45	53.1	90.4	25.2	0.2	9	372.7
589	25.04	86.98	52.6	76	25.1	345.2	9	372.9
590	25.08	87.52	52.2	61.6	25	330.2	9	373.1
591	25.12	88.05	51.7	47.2	24.8	315.2	9	373.3
592	25.17	88.58	51.2	32.7	24.7	300.2	9.1	373.5
593	25.21	89.11	50.8	18.3	24.6	285.2	9.1	373.7
594	25.25	89.64	50.3	3.9	24.4	270.2	9.1	373.8
595	25.29	90.17	49.9	349.4	24.3	255.2	9.1	374
596	25.33	90.7	49.4	335	24.1	240.2	9.1	374.2
597	25.38	91.23	48.9	320.6	24	225.2	9.1	374.4
598	25.42	91.75	48.5	306.1	23.8	210.2	9.1	374.6
599	25.46	92.28	48	291.7	23.7	195.2	9.2	374.8
600	25.5	92.81	47.5	277.2	23.5	180.2	9.2	375
601	25.54	93.33	47.1	262.8	23.4	165.2	9.2	375.2
602	25.58	93.86	46.6	248.4	23.2	150.1	9.2	375.3

ObsID is the simulated observation number (the first observation is 2008-03-19 00:00 UT), **JD** is the Julian Date of the observation minus 2454544, **α** is the Sun-Earth-Moon phase angle in degrees, **illum** is the Earth's illumination percentage, $\boldsymbol{\lambda}_{\leftmoon}$ is the sub-Lunar longitude, $\boldsymbol{\beta}_{\leftmoon}$ is the sub-Lunar latitude, $\boldsymbol{\lambda}_{\odot}$ is the sub-solar longitude, $\boldsymbol{\beta}_{\odot}$ is the sub-solar latitude, and **Δr** is the Earth-Moon distance ($\times 10^{-3}$ km).

ObsID	JD(+2454544)	α(°)	Illum(%)	$\lambda_{\leftmoon}$(°)	$\beta_{\leftmoon}$(°)	$\lambda_{\odot}$(°)	$\beta_{\odot}$(°)	Δr ($\times 10^{-3}$ km)
603	25.62	94.38	46.2	233.9	23.1	135.1	9.2	375.5
604	25.67	94.91	45.7	219.5	22.9	120.1	9.2	375.7
605	25.71	95.43	45.3	205	22.8	105.1	9.2	375.9
606	25.75	95.96	44.8	190.5	22.6	90.1	9.3	376.1
607	25.79	96.48	44.4	176.1	22.4	75.1	9.3	376.3
608	25.83	97	43.9	161.6	22.3	60.1	9.3	376.5
609	25.88	97.52	43.5	147.2	22.1	45.1	9.3	376.7
610	25.92	98.04	43	132.7	21.9	30.1	9.3	376.8
611	25.96	98.56	42.6	118.2	21.7	15.1	9.3	377
612	26	99.08	42.1	103.8	21.6	0.1	9.3	377.2
613	26.04	99.6	41.7	89.3	21.4	345.1	9.4	377.4
614	26.08	100.12	41.2	74.8	21.2	330.1	9.4	377.6
615	26.12	100.64	40.8	60.4	21	315.1	9.4	377.8
616	26.17	101.16	40.3	45.9	20.8	300.1	9.4	378
617	26.21	101.68	39.9	31.4	20.7	285.1	9.4	378.2
618	26.25	102.19	39.4	16.9	20.5	270.1	9.4	378.3
619	26.29	102.71	39	2.5	20.3	255.1	9.4	378.5
620	26.33	103.23	38.6	348	20.1	240.1	9.5	378.7
621	26.38	103.74	38.1	333.5	19.9	225.1	9.5	378.9
622	26.42	104.25	37.7	319	19.7	210.1	9.5	379.1
623	26.46	104.77	37.3	304.5	19.5	195.1	9.5	379.3
624	26.5	105.28	36.8	290	19.3	180.1	9.5	379.5
625	26.54	105.8	36.4	275.5	19.1	165.1	9.6	379.6
626	26.58	106.31	36	261	18.9	150.1	9.6	379.8
627	26.62	106.82	35.5	246.6	18.7	135.1	9.6	380
628	26.67	107.33	35.1	232.1	18.5	120.1	9.6	380.2
629	26.71	107.84	34.7	217.6	18.3	105.1	9.6	380.4
630	26.75	108.35	34.3	203.1	18.1	90.1	9.6	380.6
631	26.79	108.86	33.8	188.6	17.9	75.1	9.6	380.7
632	26.83	109.37	33.4	174.1	17.7	60.1	9.7	380.9
633	26.88	109.88	33	159.6	17.5	45.1	9.7	381.1
634	26.92	110.39	32.6	145	17.3	30.1	9.7	381.3
635	26.96	110.9	32.2	130.5	17.1	15.1	9.7	381.5
636	27	111.4	31.8	116	16.9	0.1	9.7	381.7
637	27.04	111.91	31.3	101.5	16.7	345.1	9.7	381.8
638	27.08	112.42	30.9	87	16.4	330.1	9.7	382
639	27.12	112.92	30.5	72.5	16.2	315.1	9.8	382.2
640	27.17	113.43	30.1	58	16	300.1	9.8	382.4

ObsID is the simulated observation number (the first observation is 2008-03-19 00:00 UT), **JD** is the Julian Date of the observation minus 2454544, **α** is the Sun-Earth-Moon phase angle in degrees, **illum** is the Earth's illumination percentage, $\boldsymbol{\lambda}_{\leftmoon}$ is the sub-Lunar longitude, $\boldsymbol{\beta}_{\leftmoon}$ is the sub-Lunar latitude, $\boldsymbol{\lambda}_{\odot}$ is the sub-solar longitude, $\boldsymbol{\beta}_{\odot}$ is the sub-solar latitude, and **Δr** is the Earth-Moon distance ($\times 10^{-3}$ km).

ObsID	JD(+2454544)	α(°)	Illum(%)	$\lambda_{☾}$(°)	$\beta_{☾}$(°)	$\lambda_{☉}$(°)	$\beta_{☉}$(°)	Δr ($\times 10^{-3}$ km)
641	27.21	113.93	29.7	43.5	15.8	285	9.8	382.5
642	27.25	114.44	29.3	28.9	15.6	270	9.8	382.7
643	27.29	114.94	28.9	14.4	15.4	255	9.8	382.9
644	27.33	115.45	28.5	359.9	15.1	240	9.8	383.1
645	27.38	115.95	28.1	345.4	14.9	225	9.8	383.3
646	27.42	116.45	27.7	330.8	14.7	210	9.9	383.4
647	27.46	116.95	27.3	316.3	14.5	195	9.9	383.6
648	27.5	117.45	26.9	301.8	14.3	180	9.9	383.8
649	27.54	117.95	26.6	287.3	14	165	9.9	384
650	27.58	118.46	26.2	272.7	13.8	150	9.9	384.1
651	27.62	118.96	25.8	258.2	13.6	135	9.9	384.3
652	27.67	119.45	25.4	243.7	13.3	120	9.9	384.5
653	27.71	119.95	25	229.1	13.1	105	10	384.7
654	27.75	120.45	24.7	214.6	12.9	90	10	384.8
655	27.79	120.95	24.3	200	12.7	75	10	385
656	27.83	121.45	23.9	185.5	12.4	60	10	385.2
657	27.88	121.95	23.5	171	12.2	45	10	385.3
658	27.92	122.44	23.2	156.4	12	30	10	385.5
659	27.96	122.94	22.8	141.9	11.7	15	10.1	385.7
660	28	123.43	22.4	127.3	11.5	360	10.1	385.8
661	28.04	123.93	22.1	112.8	11.3	345	10.1	386
662	28.08	124.42	21.7	98.2	11	330	10.1	386.2
663	28.12	124.92	21.4	83.7	10.8	315	10.1	386.4
664	28.17	125.41	21	69.1	10.6	300	10.1	386.5
665	28.21	125.91	20.7	54.6	10.3	285	10.1	386.7
666	28.25	126.4	20.3	40	10.1	270	10.2	386.9
667	28.29	126.89	20	25.5	9.9	255	10.2	387
668	28.33	127.38	19.6	10.9	9.6	240	10.2	387.2
669	28.38	127.88	19.3	356.4	9.4	225	10.2	387.3
670	28.42	128.37	19	341.8	9.1	210	10.2	387.5
671	28.46	128.86	18.6	327.3	8.9	195	10.2	387.7
672	28.5	129.35	18.3	312.7	8.7	180	10.2	387.8
673	28.54	129.84	18	298.2	8.4	165	10.3	388
674	28.58	130.33	17.6	283.6	8.2	150	10.3	388.2
675	28.62	130.82	17.3	269	7.9	135	10.3	388.3
676	28.67	131.31	17	254.5	7.7	120	10.3	388.5
677	28.71	131.8	16.7	239.9	7.5	105	10.3	388.6
678	28.75	132.28	16.4	225.3	7.2	90	10.3	388.8

ObsID is the simulated observation number (the first observation is 2008-03-19 00:00 UT), **JD** is the Julian Date of the observation minus 2454544, **α** is the Sun-Earth-Moon phase angle in degrees, **illum** is the Earth's illumination percentage, $\lambda_{☾}$ is the sub-Lunar longitude, $\beta_{☾}$ is the sub-Lunar latitude, $\lambda_{☉}$ is the sub-solar longitude, $\beta_{☉}$ is the sub-solar latitude, and **Δr** is the Earth-Moon distance ($\times 10^{-3}$ km).

ObsID	JD(+2454544)	α(°)	Illum(%)	$\lambda_{\leftmoon}$(°)	$\beta_{\leftmoon}$(°)	$\lambda_{\odot}$(°)	$\beta_{\odot}$(°)	Δr ($\times 10^{-3}$ km)
679	28.79	132.77	16	210.8	7	75	10.3	388.9
680	28.83	133.26	15.7	196.2	6.7	60	10.4	389.1
681	28.88	133.74	15.4	181.6	6.5	44.9	10.4	389.3
682	28.92	134.23	15.1	167.1	6.2	29.9	10.4	389.4
683	28.96	134.72	14.8	152.5	6	14.9	10.4	389.6
684	29	135.2	14.5	137.9	5.7	359.9	10.4	389.7
685	29.04	135.69	14.2	123.4	5.5	344.9	10.4	389.9
686	29.08	136.17	13.9	108.8	5.3	329.9	10.5	390
687	29.12	136.65	13.6	94.2	5	314.9	10.5	390.2
688	29.17	137.14	13.3	79.7	4.8	299.9	10.5	390.3
689	29.21	137.62	13.1	65.1	4.5	284.9	10.5	390.5
690	29.25	138.1	12.8	50.5	4.3	269.9	10.5	390.6
691	29.29	138.59	12.5	36	4	254.9	10.5	390.8
692	29.33	139.07	12.2	21.4	3.8	239.9	10.5	390.9
693	29.38	139.55	11.9	6.8	3.5	224.9	10.6	391.1
694	29.42	140.03	11.7	352.2	3.3	209.9	10.6	391.2
695	29.46	140.51	11.4	337.7	3.1	194.9	10.6	391.4
696	29.5	140.99	11.1	323.1	2.8	179.9	10.6	391.5
697	29.54	141.47	10.9	308.5	2.6	164.9	10.6	391.7
698	29.58	141.95	10.6	293.9	2.3	149.9	10.6	391.8
699	29.62	142.43	10.4	279.4	2.1	134.9	10.7	392
700	29.67	142.91	10.1	264.8	1.8	119.9	10.7	392.1
701	29.71	143.39	9.9	250.2	1.6	104.9	10.7	392.2
702	29.75	143.86	9.6	235.6	1.3	89.9	10.7	392.4
703	29.79	144.34	9.4	221	1.1	74.9	10.7	392.5
704	29.83	144.82	9.1	206.5	0.8	59.9	10.7	392.7
705	29.88	145.29	8.9	191.9	0.6	44.9	10.7	392.8
706	29.92	145.77	8.7	177.3	0.4	29.9	10.8	392.9
707	29.96	146.25	8.4	162.7	0.1	14.9	10.8	393.1
708	30	146.72	8.2	148.1	-0.1	359.9	10.8	393.2
709	30.04	147.2	8	133.6	-0.4	344.9	10.8	393.4
710	30.08	147.67	7.7	119	-0.6	329.9	10.8	393.5
711	30.12	148.14	7.5	104.4	-0.9	314.9	10.8	393.6
712	30.17	148.62	7.3	89.8	-1.1	299.9	10.8	393.8
713	30.21	149.09	7.1	75.2	-1.4	284.9	10.8	393.9
714	30.25	149.56	6.9	60.7	-1.6	269.9	10.9	394
715	30.29	150.03	6.7	46.1	-1.8	254.9	10.9	394.2
716	30.33	150.5	6.5	31.5	-2.1	239.9	10.9	394.3

ObsID is the simulated observation number (the first observation is 2008-03-19 00:00 UT), **JD** is the Julian Date of the observation minus 2454544, **α** is the Sun-Earth-Moon phase angle in degrees, **illum** is the Earth's illumination percentage, $\lambda_{\leftmoon}$ is the sub-Lunar longitude, $\beta_{\leftmoon}$ is the sub-Lunar latitude, $\lambda_{\odot}$ is the sub-solar longitude, $\beta_{\odot}$ is the sub-solar latitude, and **Δr** is the Earth-Moon distance ($\times 10^{-3}$ km).

ObsID	JD(+2454544)	α(°)	Illum(%)	$\lambda_{\leftmoon}$(°)	$\beta_{\leftmoon}$(°)	$\lambda_{\odot}$(°)	$\beta_{\odot}$(°)	Δr ($\times 10^{-3}$ km)
717	30.38	150.98	6.3	16.9	-2.3	224.9	10.9	394.4
718	30.42	151.45	6.1	2.3	-2.6	209.9	10.9	394.6
719	30.46	151.92	5.9	347.7	-2.8	194.8	10.9	394.7
720	30.5	152.38	5.7	333.2	-3	179.8	11	394.8
721	30.54	152.85	5.5	318.6	-3.3	164.8	11	395
722	30.58	153.32	5.3	304	-3.5	149.8	11	395.1
723	30.62	153.79	5.1	289.4	-3.8	134.8	11	395.2
724	30.67	154.26	5	274.8	-4	119.8	11	395.3
725	30.71	154.72	4.8	260.2	-4.3	104.8	11	395.5
726	30.75	155.19	4.6	245.7	-4.5	89.8	11	395.6
727	30.79	155.65	4.4	231.1	-4.7	74.8	11.1	395.7
728	30.83	156.12	4.3	216.5	-5	59.8	11.1	395.8
729	30.88	156.58	4.1	201.9	-5.2	44.8	11.1	396
730	30.92	157.05	4	187.3	-5.4	29.8	11.1	396.1
731	30.96	157.51	3.8	172.8	-5.7	14.8	11.1	396.2
732	31	157.97	3.6	158.2	-5.9	359.8	11.1	396.3
733	31.04	158.43	3.5	143.6	-6.2	344.8	11.1	396.5
734	31.08	158.89	3.4	129	-6.4	329.8	11.2	396.6
735	31.12	159.35	3.2	114.4	-6.6	314.8	11.2	396.7
736	31.17	159.81	3.1	99.8	-6.9	299.8	11.2	396.8
737	31.21	160.27	2.9	85.3	-7.1	284.8	11.2	396.9
738	31.25	160.73	2.8	70.7	-7.3	269.8	11.2	397
739	31.29	161.18	2.7	56.1	-7.6	254.8	11.2	397.2
740	31.33	161.64	2.5	41.5	-7.8	239.8	11.2	397.3
741	31.38	162.09	2.4	26.9	-8	224.8	11.3	397.4
742	31.42	162.55	2.3	12.4	-8.3	209.8	11.3	397.5
743	31.46	163	2.2	357.8	-8.5	194.8	11.3	397.6
744	31.5	163.45	2.1	343.2	-8.7	179.8	11.3	397.7
745	31.54	163.9	2	328.6	-8.9	164.8	11.3	397.8
746	31.58	164.35	1.9	314	-9.2	149.8	11.3	398
747	31.62	164.8	1.7	299.5	-9.4	134.8	11.3	398.1
748	31.67	165.24	1.6	284.9	-9.6	119.8	11.4	398.2
749	31.71	165.69	1.6	270.3	-9.8	104.8	11.4	398.3
750	31.75	166.13	1.5	255.7	-10.1	89.8	11.4	398.4
751	31.79	166.57	1.4	241.2	-10.3	74.8	11.4	398.5
752	31.83	167.01	1.3	226.6	-10.5	59.8	11.4	398.6
753	31.88	167.44	1.2	212	-10.7	44.8	11.4	398.7
754	31.92	167.87	1.1	197.4	-11	29.8	11.4	398.8

ObsID is the simulated observation number (the first observation is 2008-03-19 00:00 UT), **JD** is the Julian Date of the observation minus 2454544, **α** is the Sun-Earth-Moon phase angle in degrees, **illum** is the Earth's illumination percentage, $\boldsymbol{\lambda}_{\leftmoon}$ is the sub-Lunar longitude, $\boldsymbol{\beta}_{\leftmoon}$ is the sub-Lunar latitude, $\boldsymbol{\lambda}_{\odot}$ is the sub-solar longitude, $\boldsymbol{\beta}_{\odot}$ is the sub-solar latitude, and **Δr** is the Earth-Moon distance ($\times 10^{-3}$ km).

ObsID	JD(+2454544)	α(°)	Illum(%)	$\lambda_{☾}$(°)	$\beta_{☾}$(°)	$\lambda_{\odot}$(°)	$\beta_{\odot}$(°)	Δr ($\times 10^{-3}$ km)
755	31.96	168.3	1	182.9	-11.2	14.8	11.5	398.9
756	32	168.73	1	168.3	-11.4	359.8	11.5	399
757	32.04	169.15	0.9	153.7	-11.6	344.8	11.5	399.1
758	32.08	169.57	0.8	139.1	-11.8	329.8	11.5	399.2
759	32.12	169.99	0.8	124.6	-12.1	314.8	11.5	399.3
760	32.17	170.4	0.7	110	-12.3	299.8	11.5	399.4
761	32.21	170.81	0.6	95.4	-12.5	284.8	11.6	399.5
762	32.25	171.21	0.6	80.8	-12.7	269.8	11.6	399.6
763	32.29	171.6	0.5	66.3	-12.9	254.8	11.6	399.7
764	32.33	171.98	0.5	51.7	-13.1	239.8	11.6	399.8
765	32.38	172.36	0.4	37.1	-13.3	224.8	11.6	399.9
766	32.42	172.72	0.4	22.6	-13.6	209.8	11.6	400
767	32.46	173.08	0.4	8	-13.8	194.7	11.6	400.1
768	32.5	173.42	0.3	353.4	-14	179.7	11.7	400.2
769	32.54	173.74	0.3	338.9	-14.2	164.7	11.7	400.3
770	32.58	174.04	0.3	324.3	-14.4	149.7	11.7	400.4
771	32.62	174.33	0.2	309.7	-14.6	134.7	11.7	400.5
772	32.67	174.58	0.2	295.2	-14.8	119.7	11.7	400.6
773	32.71	174.81	0.2	280.6	-15	104.7	11.7	400.7
774	32.75	175.01	0.2	266	-15.2	89.7	11.7	400.7
775	32.79	175.17	0.2	251.5	-15.4	74.7	11.8	400.8
776	32.83	175.29	0.2	236.9	-15.6	59.7	11.8	400.9
777	32.88	175.37	0.2	222.3	-15.8	44.7	11.8	401
778	32.92	175.41	0.2	207.8	-16	29.7	11.8	401.1
779	32.96	175.39	0.2	193.2	-16.2	14.7	11.8	401.2
780	33	175.33	0.2	178.7	-16.4	359.7	11.8	401.3
781	33.04	175.23	0.2	164.1	-16.6	344.7	11.8	401.3
782	33.08	175.09	0.2	149.5	-16.8	329.7	11.8	401.4
783	33.12	174.91	0.2	135	-17	314.7	11.9	401.5
784	33.17	174.69	0.2	120.4	-17.2	299.7	11.9	401.6
785	33.21	174.45	0.2	105.9	-17.4	284.7	11.9	401.7
786	33.25	174.18	0.3	91.3	-17.6	269.7	11.9	401.7
787	33.29	173.88	0.3	76.8	-17.7	254.7	11.9	401.8
788	33.33	173.57	0.3	62.2	-17.9	239.7	11.9	401.9
789	33.38	173.24	0.3	47.7	-18.1	224.7	11.9	402
790	33.42	172.9	0.4	33.1	-18.3	209.7	12	402
791	33.46	172.54	0.4	18.6	-18.5	194.7	12	402.1
792	33.5	172.18	0.5	4	-18.7	179.7	12	402.2

ObsID is the simulated observation number (the first observation is 2008-03-19 00:00 UT), **JD** is the Julian Date of the observation minus 2454544, **α** is the Sun-Earth-Moon phase angle in degrees, **illum** is the Earth's illumination percentage, $\lambda_{☾}$ is the sub-Lunar longitude, $\beta_{☾}$ is the sub-Lunar latitude, $\lambda_{\odot}$ is the sub-solar longitude, $\beta_{\odot}$ is the sub-solar latitude, and **Δr** is the Earth-Moon distance ($\times 10^{-3}$ km).

ObsID	JD(+2454544)	α(°)	Illum(%)	$\lambda_{☾}$(°)	$\beta_{☾}$(°)	$\lambda_{☉}$(°)	$\beta_{☉}$(°)	Δr ($\times 10^{-3}$ km)
793	33.54	171.8	0.5	349.5	-18.8	164.7	12	402.3
794	33.58	171.42	0.6	334.9	-19	149.7	12	402.3
795	33.62	171.03	0.6	320.4	-19.2	134.7	12	402.4
796	33.67	170.63	0.7	305.8	-19.4	119.7	12.1	402.5
797	33.71	170.23	0.7	291.3	-19.5	104.7	12.1	402.5
798	33.75	169.83	0.8	276.7	-19.7	89.7	12.1	402.6
799	33.79	169.42	0.9	262.2	-19.9	74.7	12.1	402.7
800	33.83	169	0.9	247.6	-20.1	59.7	12.1	402.7
801	33.88	168.59	1	233.1	-20.2	44.7	12.1	402.8
802	33.92	168.17	1.1	218.6	-20.4	29.7	12.1	402.8
803	33.96	167.75	1.1	204	-20.6	14.7	12.2	402.9
804	34	167.32	1.2	189.5	-20.7	359.7	12.2	403
805	34.04	166.9	1.3	174.9	-20.9	344.7	12.2	403
806	34.08	166.47	1.4	160.4	-21	329.7	12.2	403.1
807	34.12	166.04	1.5	145.9	-21.2	314.7	12.2	403.1
808	34.17	165.61	1.6	131.3	-21.4	299.7	12.2	403.2
809	34.21	165.18	1.7	116.8	-21.5	284.7	12.2	403.2
810	34.25	164.74	1.8	102.3	-21.7	269.6	12.2	403.3
811	34.29	164.31	1.9	87.7	-21.8	254.7	12.3	403.4
812	34.33	163.87	2	73.2	-22	239.7	12.3	403.4
813	34.38	163.44	2.1	58.7	-22.1	224.7	12.3	403.5
814	34.42	163	2.2	44.1	-22.3	209.6	12.3	403.5
815	34.46	162.56	2.3	29.6	-22.4	194.6	12.3	403.5
816	34.5	162.12	2.4	15.1	-22.6	179.6	12.3	403.6
817	34.54	161.68	2.5	0.6	-22.7	164.6	12.3	403.6
818	34.58	161.24	2.7	346	-22.8	149.6	12.4	403.7
819	34.62	160.8	2.8	331.5	-23	134.6	12.4	403.7
820	34.67	160.36	2.9	317	-23.1	119.6	12.4	403.8
821	34.71	159.92	3	302.5	-23.3	104.6	12.4	403.8
822	34.75	159.48	3.2	287.9	-23.4	89.6	12.4	403.8
823	34.79	159.04	3.3	273.4	-23.5	74.6	12.4	403.9
824	34.83	158.59	3.5	258.9	-23.6	59.6	12.4	403.9
825	34.88	158.15	3.6	244.4	-23.8	44.6	12.5	404
826	34.92	157.71	3.7	229.9	-23.9	29.6	12.5	404
827	34.96	157.26	3.9	215.3	-24	14.6	12.5	404
828	35	156.82	4	200.8	-24.2	359.6	12.5	404.1
829	35.04	156.38	4.2	186.3	-24.3	344.6	12.5	404.1
830	35.08	155.93	4.3	171.8	-24.4	329.6	12.5	404.1

ObsID is the simulated observation number (the first observation is 2008-03-19 00:00 UT), **JD** is the Julian Date of the observation minus 2454544, **α** is the Sun-Earth-Moon phase angle in degrees, **illum** is the Earth's illumination percentage, $\lambda_{☾}$ is the sub-Lunar longitude, $\beta_{☾}$ is the sub-Lunar latitude, $\lambda_{☉}$ is the sub-solar longitude, $\beta_{☉}$ is the sub-solar latitude, and **Δr** is the Earth-Moon distance ($\times 10^{-3}$ km).

ObsID	JD(+2454544)	α(°)	Illum(%)	$\lambda_{\leftmoon}$(°)	$\beta_{\leftmoon}$(°)	$\lambda_{\odot}$(°)	$\beta_{\odot}$(°)	Δr ($\times 10^{-3}$ km)
831	35.12	155.49	4.5	157.3	-24.5	314.6	12.5	404.1
832	35.17	155.04	4.7	142.8	-24.6	299.6	12.6	404.2
833	35.21	154.6	4.8	128.2	-24.7	284.6	12.6	404.2
834	35.25	154.15	5	113.7	-24.9	269.6	12.6	404.2
835	35.29	153.71	5.2	99.2	-25	254.6	12.6	404.2
836	35.33	153.26	5.3	84.7	-25.1	239.6	12.6	404.3
837	35.38	152.82	5.5	70.2	-25.2	224.6	12.6	404.3
838	35.42	152.37	5.7	55.7	-25.3	209.6	12.6	404.3
839	35.46	151.93	5.9	41.2	-25.4	194.6	12.7	404.3

ObsID is the simulated observation number (the first observation is 2008-03-19 00:00 UT), **JD** is the Julian Date of the observation minus 2454544, **α** is the Sun-Earth-Moon phase angle in degrees, **illum** is the Earth's illumination percentage, $\lambda_{\leftmoon}$ is the sub-Lunar longitude, $\beta_{\leftmoon}$ is the sub-Lunar latitude, $\lambda_{\odot}$ is the sub-solar longitude, $\beta_{\odot}$ is the sub-solar latitude, and **Δr** is the Earth-Moon distance ($\times 10^{-3}$ km).

Table A.2 Absolute Earth HST Standard Magnitudes

ObsID	U	B	V	R	I	J	H	K
0	31.71	30.98	31.01	31.05	31.09	32.33	32.92	34.42
1	31.75	30.99	31.00	31.01	31.03	32.26	32.86	34.32
2	31.76	30.98	30.95	30.95	30.98	32.18	32.75	34.21
3	31.79	30.98	30.93	30.92	30.93	32.13	32.66	34.15
4	31.78	30.96	30.90	30.89	30.92	32.14	32.66	34.14
5	31.78	30.97	30.91	30.87	30.86	32.06	32.69	34.17
6	31.81	30.96	30.87	30.84	30.84	32.04	32.58	34.08
7	31.88	31.05	30.95	30.91	30.91	32.14	32.66	34.17
8	31.92	31.09	31.01	30.97	30.94	32.16	32.77	34.26
9	31.97	31.16	31.09	31.06	31.04	32.25	32.87	34.36
10	31.94	31.11	31.12	31.13	31.13	32.28	33.04	34.48
11	31.99	31.17	31.17	31.17	31.15	32.33	33.00	34.50
12	32.05	31.29	31.32	31.26	31.20	32.41	33.00	34.51
13	32.13	31.34	31.31	31.22	31.14	32.36	32.86	34.39
14	32.22	31.48	31.53	31.47	31.39	32.65	33.14	34.68
15	32.25	31.52	31.65	31.63	31.52	32.73	33.31	34.81
16	32.25	31.50	31.63	31.64	31.54	32.71	33.36	34.85
17	32.28	31.50	31.59	31.54	31.44	32.59	33.21	34.69
18	32.28	31.49	31.51	31.37	31.19	32.40	32.86	34.39
19	32.36	31.51	31.34	31.09	30.88	32.14	32.46	34.00
20	32.35	31.44	31.28	31.07	30.87	32.07	32.51	34.02
21	32.40	31.51	31.37	31.18	30.99	32.17	32.63	34.14
22	32.42	31.53	31.42	31.26	31.08	32.26	32.75	34.24
23	32.47	31.56	31.40	31.20	31.01	32.20	32.65	34.14
24	32.51	31.66	31.55	31.34	31.14	32.38	32.75	34.29
25	32.57	31.69	31.55	31.30	31.07	32.28	32.65	34.18
26	32.58	31.62	31.44	31.18	30.93	32.07	32.52	34.01
27	32.66	31.70	31.48	31.18	30.91	32.09	32.46	33.97
28	32.65	31.65	31.44	31.16	30.89	32.04	32.44	33.96
29	32.70	31.66	31.41	31.13	30.86	32.01	32.42	33.93
30	32.71	31.64	31.36	31.08	30.81	31.95	32.37	33.87
31	32.81	31.78	31.50	31.17	30.88	32.05	32.39	33.92
32	32.88	31.86	31.61	31.29	31.00	32.17	32.52	34.05
33	32.94	31.90	31.69	31.41	31.14	32.26	32.68	34.18
34	32.90	31.78	31.60	31.38	31.13	32.15	32.73	34.17
35	33.00	31.90	31.73	31.51	31.26	32.30	32.86	34.30
36	33.10	32.04	31.81	31.53	31.26	32.37	32.80	34.30
37	33.20	32.17	31.97	31.67	31.38	32.52	32.91	34.42
38	33.29	32.28	32.03	31.64	31.30	32.48	32.79	34.34
39	33.42	32.53	32.47	32.18	31.85	32.98	33.36	34.87

ObsID = observation number (same as Table A.1). UBVRIJHK absolute STMAG magnitudes are given in the remaining columns.

ObsID	U	B	V	R	I	J	H	K
40	33.47	32.53	32.54	32.34	32.03	33.05	33.57	35.02
41	33.48	32.43	32.33	32.12	31.82	32.84	33.41	34.83
42	33.60	32.57	32.38	32.05	31.72	32.81	33.21	34.68
43	33.72	32.69	32.39	31.95	31.55	32.70	32.97	34.49
44	33.75	32.64	32.33	31.90	31.50	32.62	32.94	34.44
45	33.83	32.65	32.38	32.02	31.64	32.67	33.10	34.55
46	33.98	32.91	32.72	32.38	31.99	33.00	33.41	34.84
47	34.13	33.14	32.88	32.45	32.05	33.17	33.45	34.92
48	34.28	33.32	33.02	32.55	32.14	33.32	33.50	35.02
49	34.37	33.38	33.09	32.61	32.18	33.36	33.56	35.10
50	34.44	33.32	32.99	32.53	32.11	33.21	33.49	34.99
51	34.54	33.33	32.98	32.53	32.12	33.15	33.48	34.96
52	34.70	33.52	33.18	32.71	32.27	33.34	33.62	35.13
53	34.83	33.61	33.26	32.80	32.37	33.42	33.71	35.21
54	34.95	33.65	33.27	32.83	32.43	33.45	33.78	35.25
55	35.08	33.72	33.35	32.93	32.51	33.50	33.88	35.34
56	35.30	34.02	33.69	33.26	32.84	33.82	34.18	35.64
57	35.52	34.29	33.98	33.56	33.13	34.10	34.43	35.89
58	35.64	34.30	33.99	33.59	33.17	34.08	34.49	35.91
59	35.86	34.54	34.20	33.78	33.36	34.28	34.65	36.07
60	36.07	34.73	34.36	33.92	33.49	34.42	34.76	36.20
61	36.34	35.09	34.73	34.26	33.80	34.75	35.02	36.49
62	36.57	35.32	34.97	34.47	34.00	34.97	35.25	36.73
63	36.84	35.75	35.46	34.95	34.45	35.42	35.64	37.14
64	36.97	35.86	35.64	35.18	34.70	35.57	35.85	37.28
65	37.03	35.75	35.45	35.01	34.54	35.36	35.72	37.12
66	37.18	35.83	35.47	35.00	34.52	35.34	35.67	37.08
67	37.17	35.83	35.50	35.05	34.57	35.38	35.75	37.16
68	37.14	35.84	35.55	35.12	34.65	35.45	35.85	37.25
69	37.10	35.89	35.65	35.21	34.73	35.52	35.88	37.29
70	36.90	35.71	35.47	35.04	34.57	35.38	35.75	37.16
71	36.69	35.50	35.24	34.81	34.34	35.16	35.50	36.92
72	36.46	35.25	34.98	34.54	34.08	34.91	35.24	36.66
73	36.19	34.87	34.57	34.17	33.73	34.57	34.99	36.39
74	36.00	34.78	34.51	34.12	33.68	34.56	34.97	36.39
75	35.78	34.57	34.32	33.92	33.49	34.37	34.78	36.20
76	35.56	34.28	34.01	33.64	33.22	34.08	34.54	35.94
77	35.41	34.22	33.97	33.58	33.16	34.02	34.42	35.82
78	35.23	34.09	33.80	33.37	32.94	33.89	34.21	35.64
79	35.05	33.83	33.51	33.09	32.68	33.62	34.00	35.42
80	34.88	33.66	33.35	32.95	32.54	33.51	33.91	35.35

ObsID = observation number (same as Table 1). UBVRIJHK absolute STMAG magnitudes (Stone 1996; Laidler 2008) are given in the remaining columns.

ObsID	U	B	V	R	I	J	H	K
81	34.70	33.47	33.16	32.78	32.40	33.35	33.77	35.20
82	34.59	33.43	33.16	32.80	32.43	33.40	33.83	35.25
83	34.43	33.22	32.94	32.61	32.25	33.19	33.65	35.05
84	34.30	33.15	32.83	32.43	32.06	33.11	33.49	34.93
85	34.24	33.07	32.73	32.31	31.92	32.94	33.29	34.75
86	34.05	32.83	32.50	32.12	31.76	32.78	33.20	34.65
87	34.00	32.84	32.53	32.13	31.74	32.76	33.14	34.59
88	33.82	32.58	32.29	31.95	31.60	32.57	33.05	34.46
89	33.71	32.46	32.17	31.83	31.49	32.49	32.96	34.40
90	33.58	32.38	32.06	31.73	31.40	32.45	32.92	34.34
91	33.60	32.43	32.12	31.77	31.44	32.47	32.88	34.32
92	33.48	32.32	32.03	31.70	31.38	32.41	32.89	34.33
93	33.48	32.45	32.22	31.89	31.56	32.62	33.03	34.50
94	33.42	32.41	32.20	31.88	31.55	32.59	33.01	34.45
95	33.32	32.27	32.03	31.72	31.41	32.46	32.88	34.33
96	33.17	32.10	31.82	31.51	31.21	32.29	32.73	34.17
97	33.18	32.12	31.85	31.52	31.23	32.32	32.71	34.19
98	33.11	32.08	31.80	31.46	31.15	32.28	32.65	34.14
99	33.03	31.98	31.73	31.44	31.16	32.25	32.68	34.17
100	33.03	32.06	31.81	31.50	31.22	32.36	32.74	34.22
101	33.00	32.10	31.94	31.67	31.40	32.53	32.93	34.41
102	32.84	31.86	31.63	31.35	31.09	32.22	32.63	34.10
103	32.86	31.91	31.62	31.29	31.02	32.21	32.52	34.04
104	32.77	31.78	31.50	31.19	30.92	32.08	32.46	33.96
105	32.68	31.63	31.37	31.11	30.87	31.98	32.44	33.93
106	32.62	31.58	31.38	31.19	31.00	32.07	32.64	34.10
107	32.64	31.70	31.56	31.38	31.19	32.30	32.83	34.28
108	32.58	31.66	31.47	31.24	31.04	32.21	32.62	34.10
109	32.57	31.67	31.41	31.14	30.92	32.16	32.47	34.00
110	32.51	31.58	31.32	31.05	30.83	32.05	32.40	33.92
111	32.49	31.58	31.35	31.10	30.90	32.11	32.48	33.99
112	32.40	31.44	31.24	31.03	30.85	32.01	32.47	33.97
113	32.35	31.40	31.22	31.03	30.87	32.02	32.52	34.02
114	32.31	31.38	31.20	31.01	30.86	32.04	32.50	33.99
115	32.26	31.35	31.15	30.97	30.84	32.04	32.50	34.01
116	32.27	31.37	31.18	30.99	30.85	32.05	32.51	34.01
117	32.26	31.41	31.29	31.14	31.01	32.21	32.70	34.19
118	32.21	31.37	31.30	31.21	31.11	32.28	32.87	34.34
119	32.18	31.33	31.24	31.16	31.08	32.24	32.83	34.30
120	32.11	31.24	31.12	31.03	30.97	32.15	32.72	34.19
121	32.08	31.22	31.10	30.99	30.91	32.13	32.65	34.15

ObsID = observation number (same as Table 1). UBVRIJHK absolute STMAG magnitudes (Stone 1996; Laidler 2008) are given in the remaining columns.

ObsID	U	B	V	R	I	J	H	K
122	32.08	31.22	31.07	30.96	30.90	32.13	32.61	34.10
123	32.05	31.20	31.09	30.99	30.93	32.14	32.66	34.15
124	32.06	31.23	31.10	31.02	30.98	32.24	32.70	34.20
125	32.04	31.26	31.20	31.18	31.15	32.39	32.93	34.42
126	32.03	31.25	31.20	31.21	31.23	32.47	33.02	34.49
127	31.96	31.14	30.99	30.93	30.93	32.21	32.64	34.13
128	31.90	31.09	30.97	30.91	30.91	32.17	32.68	34.16
129	31.83	31.00	30.90	30.87	30.86	32.04	32.62	34.11
130	31.81	30.98	30.90	30.90	30.93	32.12	32.76	34.23
131	31.86	31.09	31.07	31.09	31.12	32.36	32.94	34.40
132	31.85	31.10	31.07	31.10	31.17	32.45	33.01	34.47
133	31.78	30.98	30.89	30.89	30.96	32.21	32.67	34.16
134	31.77	30.97	30.85	30.84	30.92	32.19	32.62	34.11
135	31.73	30.94	30.86	30.84	30.89	32.13	32.67	34.14
136	31.68	30.88	30.81	30.83	30.88	32.11	32.69	34.17
137	31.64	30.84	30.76	30.79	30.88	32.07	32.68	34.15
138	31.63	30.86	30.83	30.88	30.97	32.15	32.76	34.22
139	31.57	30.78	30.72	30.77	30.85	32.07	32.70	34.15
140	31.57	30.80	30.76	30.81	30.90	32.12	32.73	34.20
141	31.56	30.82	30.80	30.83	30.90	32.11	32.72	34.20
142	31.56	30.84	30.87	30.96	31.05	32.26	32.96	34.42
143	31.52	30.79	30.81	30.91	31.02	32.22	32.97	34.41
144	31.47	30.73	30.73	30.82	30.93	32.11	32.82	34.27
145	31.40	30.64	30.62	30.73	30.90	32.10	32.76	34.23
146	31.48	30.73	30.69	30.78	30.94	32.18	32.77	34.23
147	31.45	30.73	30.71	30.78	30.92	32.14	32.68	34.16
148	31.44	30.73	30.73	30.86	31.03	32.23	32.80	34.30
149	31.43	30.73	30.75	30.87	31.00	32.29	32.87	34.36
150	31.43	30.74	30.78	30.92	31.06	32.33	32.98	34.45
151	31.34	30.61	30.60	30.75	30.94	32.18	32.83	34.28
152	31.31	30.58	30.55	30.67	30.85	32.12	32.70	34.15
153	31.25	30.53	30.53	30.65	30.83	32.06	32.76	34.21
154	31.24	30.50	30.49	30.63	30.83	32.03	32.74	34.20
155	31.26	30.57	30.60	30.74	30.91	32.14	32.84	34.30
156	31.27	30.60	30.66	30.82	30.97	32.24	32.98	34.43
157	31.23	30.54	30.56	30.73	30.93	32.20	32.84	34.29
158	31.23	30.53	30.54	30.69	30.93	32.19	32.84	34.27
159	31.20	30.50	30.51	30.65	30.86	32.12	32.77	34.20
160	31.15	30.46	30.47	30.62	30.83	32.05	32.70	34.15
161	31.12	30.43	30.45	30.60	30.83	32.05	32.81	34.24
162	31.10	30.44	30.51	30.66	30.88	32.09	32.88	34.34

ObsID = observation number (same as Table 1). UBVRIJHK absolute STMAG magnitudes (Stone 1996; Laidler 2008) are given in the remaining columns.

ObsID	U	B	V	R	I	J	H	K
163	31.06	30.39	30.45	30.62	30.87	32.04	32.79	34.25
164	31.05	30.40	30.46	30.62	30.86	32.07	32.85	34.30
165	31.01	30.35	30.41	30.59	30.83	32.02	32.93	34.36
166	31.01	30.36	30.43	30.60	30.81	32.02	32.90	34.35
167	30.97	30.32	30.40	30.57	30.78	31.98	32.92	34.36
168	30.97	30.31	30.38	30.57	30.83	32.04	32.88	34.34
169	30.92	30.26	30.32	30.50	30.76	31.98	32.82	34.26
170	30.96	30.31	30.37	30.56	30.81	32.04	32.83	34.30
171	30.97	30.34	30.39	30.57	30.86	32.13	32.91	34.34
172	30.95	30.34	30.43	30.63	30.90	32.15	32.96	34.42
173	30.95	30.32	30.39	30.58	30.81	32.08	32.89	34.35
174	30.95	30.33	30.42	30.60	30.80	32.09	32.90	34.38
175	30.89	30.26	30.34	30.53	30.76	32.01	32.86	34.31
176	30.86	30.21	30.27	30.45	30.71	31.95	32.76	34.20
177	30.83	30.18	30.24	30.41	30.68	31.93	32.75	34.18
178	30.78	30.14	30.20	30.38	30.64	31.86	32.73	34.15
179	30.77	30.13	30.20	30.38	30.60	31.83	32.70	34.13
180	30.81	30.20	30.29	30.47	30.66	31.92	32.75	34.20
181	30.79	30.19	30.29	30.49	30.71	31.97	32.78	34.22
182	30.80	30.20	30.29	30.49	30.76	32.01	32.82	34.23
183	30.80	30.20	30.29	30.48	30.76	32.01	32.80	34.20
184	30.77	30.17	30.26	30.46	30.74	31.97	32.79	34.19
185	30.74	30.13	30.22	30.41	30.69	31.91	32.76	34.17
186	30.71	30.12	30.22	30.41	30.68	31.89	32.79	34.21
187	30.67	30.09	30.20	30.40	30.67	31.86	32.83	34.27
188	30.65	30.07	30.18	30.38	30.66	31.85	32.83	34.25
189	30.64	30.07	30.20	30.39	30.67	31.87	32.84	34.28
190	30.64	30.07	30.18	30.39	30.62	31.83	32.81	34.25
191	30.62	30.05	30.18	30.37	30.58	31.80	32.79	34.25
192	30.60	30.03	30.16	30.35	30.57	31.80	32.80	34.27
193	30.58	30.01	30.13	30.34	30.58	31.83	32.78	34.25
194	30.61	30.06	30.19	30.40	30.66	31.94	32.83	34.30
195	30.63	30.09	30.23	30.45	30.72	32.02	32.85	34.32
196	30.62	30.09	30.23	30.45	30.73	32.01	32.88	34.35
197	30.59	30.04	30.17	30.38	30.62	31.89	32.80	34.26
198	30.57	30.02	30.14	30.33	30.54	31.81	32.71	34.19
199	30.55	30.00	30.13	30.33	30.53	31.80	32.68	34.15
200	30.54	29.99	30.12	30.32	30.55	31.81	32.65	34.10
201	30.50	29.94	30.07	30.27	30.53	31.78	32.61	34.04
202	30.47	29.91	30.04	30.25	30.51	31.75	32.64	34.07
203	30.43	29.86	29.98	30.19	30.44	31.68	32.62	34.06

ObsID = observation number (same as Table 1). UBVRIJHK absolute STMAG magnitudes (Stone 1996; Laidler 2008) are given in the remaining columns.

ObsID	U	B	V	R	I	J	H	K
204	30.45	29.90	30.03	30.23	30.43	31.68	32.60	34.06
205	30.46	29.93	30.08	30.29	30.48	31.74	32.64	34.10
206	30.47	29.94	30.10	30.32	30.55	31.81	32.70	34.14
207	30.47	29.95	30.12	30.34	30.61	31.86	32.72	34.16
208	30.46	29.95	30.12	30.35	30.64	31.87	32.76	34.19
209	30.42	29.90	30.06	30.29	30.59	31.81	32.72	34.14
210	30.38	29.85	30.00	30.22	30.52	31.72	32.69	34.12
211	30.34	29.81	29.97	30.20	30.50	31.69	32.74	34.18
212	30.34	29.82	29.99	30.22	30.52	31.71	32.79	34.23
213	30.33	29.82	29.97	30.20	30.48	31.69	32.73	34.18
214	30.32	29.80	29.96	30.19	30.46	31.67	32.74	34.19
215	30.30	29.78	29.94	30.16	30.39	31.61	32.69	34.16
216	30.29	29.78	29.93	30.15	30.37	31.60	32.68	34.16
217	30.28	29.78	29.94	30.15	30.38	31.63	32.67	34.17
218	30.29	29.79	29.96	30.19	30.44	31.74	32.69	34.22
219	30.32	29.84	30.01	30.25	30.52	31.85	32.72	34.25
220	30.32	29.85	30.04	30.27	30.54	31.85	32.72	34.23
221	30.32	29.84	30.02	30.24	30.49	31.77	32.69	34.19
222	30.31	29.83	29.99	30.20	30.40	31.69	32.60	34.11
223	30.32	29.85	30.03	30.24	30.40	31.70	32.59	34.11
224	30.30	29.84	30.02	30.24	30.43	31.71	32.58	34.07
225	30.26	29.78	29.96	30.19	30.43	31.70	32.57	34.03
226	30.21	29.72	29.90	30.14	30.41	31.66	32.60	34.04
227	30.18	29.68	29.86	30.09	30.35	31.60	32.60	34.06
228	30.16	29.67	29.83	30.05	30.27	31.53	32.56	34.03
229	30.17	29.69	29.86	30.08	30.27	31.53	32.55	34.03
230	30.18	29.71	29.90	30.13	30.33	31.59	32.57	34.04
231	30.19	29.73	29.93	30.17	30.41	31.67	32.62	34.07
232	30.18	29.73	29.95	30.21	30.50	31.74	32.68	34.12
233	30.16	29.71	29.93	30.19	30.51	31.73	32.67	34.09
234	30.13	29.67	29.88	30.13	30.45	31.66	32.66	34.08
235	30.08	29.62	29.82	30.07	30.39	31.59	32.68	34.11
236	30.07	29.61	29.82	30.07	30.40	31.59	32.75	34.20
237	30.07	29.61	29.81	30.05	30.36	31.56	32.70	34.15
238	30.06	29.60	29.79	30.04	30.32	31.53	32.66	34.13
239	30.04	29.58	29.76	30.00	30.25	31.47	32.62	34.10
240	30.02	29.54	29.72	29.95	30.17	31.41	32.54	34.03
241	30.01	29.54	29.72	29.95	30.16	31.42	32.49	34.00
242	30.03	29.57	29.76	29.99	30.22	31.51	32.49	34.03
243	30.05	29.62	29.82	30.06	30.31	31.65	32.55	34.13
244	30.08	29.66	29.88	30.13	30.40	31.74	32.63	34.20

ObsID = observation number (same as Table 1). UBVRIJHK absolute STMAG magnitudes (Stone 1996; Laidler 2008) are given in the remaining columns.

ObsID	U	B	V	R	I	J	H	K
245	30.09	29.67	29.88	30.12	30.36	31.67	32.58	34.12
246	30.08	29.66	29.86	30.08	30.26	31.57	32.49	34.03
247	30.07	29.66	29.85	30.06	30.20	31.51	32.43	33.98
248	30.06	29.65	29.85	30.06	30.21	31.50	32.42	33.95
249	30.03	29.61	29.82	30.04	30.24	31.52	32.44	33.94
250	29.99	29.56	29.77	30.02	30.26	31.54	32.51	33.99
251	29.94	29.51	29.72	29.96	30.21	31.48	32.52	33.99
252	29.92	29.47	29.67	29.91	30.13	31.40	32.49	33.97
253	29.91	29.47	29.66	29.90	30.09	31.36	32.44	33.93
254	29.92	29.49	29.69	29.93	30.11	31.39	32.44	33.92
255	29.94	29.52	29.74	29.99	30.21	31.47	32.48	33.95
256	29.95	29.55	29.80	30.06	30.33	31.58	32.56	34.01
257	29.93	29.54	29.80	30.07	30.38	31.62	32.60	34.03
258	29.89	29.48	29.73	30.00	30.33	31.55	32.59	34.01
259	29.85	29.43	29.66	29.93	30.27	31.48	32.60	34.03
260	29.84	29.42	29.66	29.92	30.26	31.47	32.65	34.10
261	29.84	29.43	29.66	29.93	30.25	31.46	32.66	34.11
262	29.83	29.42	29.65	29.91	30.20	31.43	32.62	34.09
263	29.82	29.39	29.61	29.86	30.12	31.35	32.55	34.04
264	29.79	29.36	29.56	29.80	30.03	31.27	32.47	33.98
265	29.76	29.32	29.50	29.74	29.95	31.21	32.39	33.92
266	29.76	29.32	29.51	29.75	29.96	31.25	32.37	33.93
267	29.79	29.37	29.58	29.82	30.06	31.39	32.42	34.02
268	29.84	29.45	29.69	29.94	30.18	31.54	32.49	34.10
269	29.86	29.49	29.73	29.97	30.19	31.53	32.43	34.01
270	29.87	29.50	29.72	29.95	30.12	31.45	32.37	33.95
271	29.85	29.47	29.67	29.89	30.03	31.33	32.28	33.85
272	29.84	29.45	29.66	29.87	30.00	31.29	32.26	33.83
273	29.81	29.43	29.63	29.86	30.01	31.30	32.28	33.82
274	29.77	29.38	29.60	29.84	30.04	31.32	32.33	33.84
275	29.73	29.33	29.56	29.81	30.04	31.32	32.36	33.85
276	29.69	29.29	29.51	29.75	29.97	31.24	32.35	33.84
277	29.67	29.26	29.46	29.71	29.90	31.17	32.29	33.78
278	29.67	29.27	29.47	29.71	29.89	31.16	32.26	33.76
279	29.68	29.30	29.52	29.77	29.95	31.22	32.29	33.79
280	29.69	29.32	29.56	29.82	30.05	31.31	32.37	33.85
281	29.69	29.32	29.59	29.86	30.15	31.39	32.45	33.90
282	29.66	29.29	29.56	29.85	30.18	31.40	32.50	33.93
283	29.63	29.25	29.52	29.80	30.15	31.36	32.51	33.94
284	29.62	29.24	29.50	29.79	30.14	31.35	32.54	33.97
285	29.61	29.23	29.50	29.78	30.11	31.33	32.54	33.99

ObsID = observation number (same as Table 1). UBVRIJHK absolute STMAG magnitudes (Stone 1996; Laidler 2008) are given in the remaining columns.

ObsID	U	B	V	R	I	J	H	K
286	29.60	29.22	29.47	29.74	30.05	31.28	32.49	33.95
287	29.58	29.20	29.44	29.70	29.97	31.21	32.40	33.88
288	29.56	29.16	29.38	29.63	29.86	31.11	32.29	33.80
289	29.53	29.12	29.32	29.56	29.78	31.04	32.21	33.74
290	29.53	29.12	29.32	29.56	29.77	31.06	32.20	33.76
291	29.55	29.16	29.37	29.61	29.82	31.15	32.24	33.83
292	29.58	29.21	29.45	29.70	29.92	31.27	32.28	33.90
293	29.62	29.26	29.51	29.75	29.96	31.30	32.25	33.85
294	29.64	29.29	29.52	29.75	29.91	31.24	32.16	33.75
295	29.62	29.26	29.47	29.69	29.82	31.13	32.07	33.66
296	29.60	29.23	29.42	29.64	29.75	31.05	32.01	33.59
297	29.56	29.18	29.38	29.59	29.73	31.01	31.99	33.55
298	29.51	29.13	29.33	29.55	29.72	31.00	32.01	33.54
299	29.46	29.08	29.29	29.52	29.73	31.00	32.05	33.56
300	29.42	29.03	29.24	29.49	29.70	30.97	32.06	33.55
301	29.40	29.00	29.21	29.45	29.64	30.91	32.03	33.51
302	29.40	29.00	29.21	29.45	29.63	30.90	32.01	33.50
303	29.42	29.04	29.25	29.50	29.67	30.94	32.03	33.52
304	29.44	29.07	29.31	29.57	29.76	31.03	32.10	33.58
305	29.44	29.09	29.36	29.63	29.87	31.13	32.19	33.65
306	29.44	29.09	29.38	29.67	29.97	31.21	32.27	33.72
307	29.42	29.08	29.37	29.67	30.01	31.24	32.33	33.75
308	29.41	29.07	29.36	29.66	30.02	31.24	32.35	33.77
309	29.40	29.06	29.36	29.65	30.00	31.23	32.37	33.80
310	29.39	29.05	29.33	29.62	29.95	31.18	32.34	33.79
311	29.38	29.02	29.29	29.56	29.85	31.10	32.28	33.75
312	29.35	28.98	29.22	29.48	29.72	30.98	32.18	33.68
313	29.32	28.94	29.16	29.41	29.63	30.91	32.09	33.62
314	29.31	28.93	29.15	29.40	29.60	30.90	32.05	33.61
315	29.33	28.96	29.18	29.43	29.62	30.95	32.05	33.65
316	29.37	29.02	29.25	29.50	29.70	31.06	32.09	33.71
317	29.40	29.06	29.31	29.55	29.74	31.10	32.06	33.69
318	29.42	29.08	29.32	29.55	29.71	31.05	31.99	33.61
319	29.40	29.06	29.28	29.49	29.63	30.94	31.90	33.51
320	29.37	29.02	29.22	29.43	29.54	30.84	31.82	33.41
321	29.33	28.96	29.15	29.36	29.49	30.77	31.77	33.35
322	29.28	28.90	29.09	29.30	29.46	30.74	31.75	33.30
323	29.23	28.84	29.04	29.26	29.46	30.72	31.77	33.29
324	29.18	28.79	28.99	29.23	29.44	30.70	31.77	33.27
325	29.15	28.76	28.96	29.20	29.42	30.68	31.77	33.26
326	29.15	28.76	28.96	29.21	29.41	30.68	31.77	33.26

ObsID = observation number (same as Table 1). UBVRIJHK absolute STMAG magnitudes (Stone 1996; Laidler 2008) are given in the remaining columns.

ObsID	U	B	V	R	I	J	H	K
327	29.17	28.78	28.99	29.23	29.43	30.70	31.78	33.27
328	29.19	28.82	29.05	29.30	29.50	30.77	31.82	33.31
329	29.21	28.86	29.11	29.37	29.60	30.87	31.90	33.37
330	29.22	28.88	29.16	29.44	29.72	30.98	31.99	33.45
331	29.21	28.88	29.18	29.47	29.79	31.04	32.08	33.52
332	29.20	28.87	29.17	29.47	29.82	31.06	32.13	33.57
333	29.19	28.86	29.16	29.45	29.81	31.05	32.17	33.61
334	29.17	28.83	29.12	29.41	29.75	31.00	32.15	33.60
335	29.14	28.80	29.06	29.34	29.65	30.90	32.08	33.55
336	29.11	28.75	28.99	29.26	29.53	30.79	31.99	33.49
337	29.09	28.72	28.95	29.21	29.44	30.73	31.91	33.44
338	29.09	28.72	28.95	29.20	29.41	30.71	31.85	33.42
339	29.11	28.75	28.97	29.22	29.42	30.75	31.84	33.43
340	29.14	28.80	29.03	29.27	29.46	30.81	31.83	33.47
341	29.17	28.83	29.06	29.30	29.48	30.84	31.79	33.43
342	29.18	28.84	29.06	29.30	29.45	30.80	31.73	33.35
343	29.17	28.82	29.03	29.24	29.38	30.71	31.63	33.25
344	29.15	28.79	28.98	29.19	29.32	30.62	31.56	33.17
345	29.12	28.75	28.93	29.14	29.27	30.55	31.52	33.10
346	29.07	28.69	28.87	29.08	29.23	30.50	31.49	33.05
347	29.03	28.64	28.83	29.05	29.23	30.49	31.50	33.05
348	28.99	28.61	28.80	29.03	29.24	30.51	31.55	33.07
349	28.97	28.58	28.79	29.03	29.24	30.51	31.58	33.10
350	28.96	28.58	28.79	29.03	29.23	30.52	31.61	33.13
351	28.97	28.60	28.81	29.06	29.25	30.54	31.64	33.15
352	28.99	28.62	28.85	29.10	29.29	30.59	31.67	33.18
353	29.00	28.65	28.89	29.15	29.36	30.66	31.71	33.21
354	29.01	28.68	28.94	29.22	29.47	30.76	31.79	33.28
355	29.01	28.69	28.97	29.26	29.56	30.82	31.86	33.33
356	29.00	28.67	28.96	29.26	29.59	30.85	31.92	33.38
357	28.98	28.65	28.94	29.24	29.59	30.84	31.97	33.42
358	28.96	28.62	28.90	29.19	29.53	30.78	31.96	33.42
359	28.93	28.58	28.84	29.12	29.44	30.70	31.91	33.39
360	28.90	28.54	28.78	29.05	29.34	30.61	31.81	33.33
361	28.89	28.52	28.75	29.01	29.26	30.54	31.73	33.27
362	28.89	28.52	28.75	29.00	29.23	30.53	31.66	33.23
363	28.90	28.54	28.76	29.01	29.21	30.53	31.62	33.21
364	28.92	28.56	28.79	29.03	29.22	30.56	31.59	33.21
365	28.94	28.59	28.81	29.05	29.23	30.57	31.56	33.18
366	28.95	28.60	28.80	29.03	29.20	30.54	31.49	33.11
367	28.95	28.58	28.78	28.99	29.14	30.47	31.41	33.03

ObsID = observation number (same as Table 1). UBVRIJHK absolute STMAG magnitudes (Stone 1996; Laidler 2008) are given in the remaining columns.

ObsID	U	B	V	R	I	J	H	K
368	28.93	28.56	28.75	28.96	29.10	30.40	31.35	32.96
369	28.90	28.53	28.71	28.91	29.05	30.33	31.31	32.91
370	28.87	28.49	28.66	28.87	29.03	30.30	31.29	32.86
371	28.83	28.44	28.62	28.84	29.02	30.28	31.29	32.85
372	28.80	28.41	28.60	28.83	29.03	30.29	31.32	32.86
373	28.78	28.39	28.59	28.83	29.04	30.31	31.35	32.88
374	28.77	28.39	28.60	28.84	29.06	30.34	31.39	32.91
375	28.77	28.40	28.61	28.87	29.07	30.36	31.42	32.95
376	28.78	28.42	28.64	28.89	29.10	30.39	31.45	32.97
377	28.80	28.44	28.67	28.93	29.15	30.44	31.48	32.99
378	28.81	28.46	28.71	28.98	29.23	30.52	31.53	33.03
379	28.81	28.47	28.74	29.03	29.31	30.58	31.59	33.08
380	28.81	28.48	28.76	29.06	29.38	30.63	31.66	33.13
381	28.78	28.46	28.75	29.05	29.39	30.64	31.69	33.16
382	28.76	28.43	28.71	29.01	29.36	30.61	31.69	33.16
383	28.75	28.41	28.68	28.97	29.31	30.56	31.68	33.16
384	28.74	28.39	28.65	28.93	29.24	30.50	31.64	33.14
385	28.74	28.38	28.63	28.91	29.18	30.46	31.60	33.13
386	28.74	28.39	28.63	28.90	29.14	30.44	31.57	33.12
387	28.75	28.40	28.64	28.90	29.11	30.43	31.54	33.11
388	28.76	28.41	28.65	28.91	29.10	30.43	31.51	33.11
389	28.77	28.43	28.66	28.91	29.09	30.43	31.48	33.09
390	28.78	28.43	28.64	28.88	29.05	30.38	31.41	33.02
391	28.77	28.41	28.61	28.84	28.99	30.31	31.32	32.94
392	28.76	28.40	28.58	28.80	28.95	30.25	31.26	32.87
393	28.74	28.37	28.55	28.76	28.91	30.19	31.20	32.80
394	28.71	28.34	28.51	28.73	28.88	30.15	31.16	32.75
395	28.69	28.31	28.49	28.71	28.89	30.14	31.15	32.72
396	28.66	28.28	28.48	28.71	28.90	30.15	31.17	32.72
397	28.64	28.27	28.47	28.71	28.91	30.17	31.19	32.73
398	28.63	28.27	28.48	28.73	28.94	30.21	31.22	32.75
399	28.64	28.27	28.49	28.74	28.96	30.23	31.25	32.78
400	28.64	28.28	28.51	28.77	28.98	30.26	31.29	32.81
401	28.65	28.30	28.53	28.80	29.01	30.30	31.31	32.83
402	28.66	28.31	28.55	28.82	29.06	30.34	31.34	32.85
403	28.66	28.32	28.58	28.86	29.13	30.41	31.40	32.90
404	28.66	28.32	28.60	28.89	29.20	30.46	31.45	32.94
405	28.65	28.32	28.61	28.90	29.24	30.49	31.50	32.97
406	28.63	28.31	28.60	28.90	29.25	30.49	31.53	33.00
407	28.62	28.29	28.58	28.88	29.22	30.47	31.53	33.01
408	28.61	28.28	28.55	28.84	29.16	30.42	31.51	33.01

ObsID = observation number (same as Table 1). UBVRIJHK absolute STMAG magnitudes (Stone 1996; Laidler 2008) are given in the remaining columns.

ObsID	U	B	V	R	I	J	H	K
409	28.61	28.27	28.54	28.82	29.10	30.38	31.50	33.03
410	28.62	28.28	28.55	28.82	29.07	30.37	31.50	33.05
411	28.64	28.30	28.56	28.83	29.04	30.36	31.48	33.06
412	28.66	28.33	28.59	28.85	29.04	30.37	31.47	33.07
413	28.68	28.35	28.60	28.86	29.03	30.37	31.44	33.06
414	28.68	28.36	28.60	28.85	29.00	30.33	31.38	33.01
415	28.68	28.34	28.56	28.80	28.95	30.27	31.30	32.93
416	28.67	28.32	28.52	28.75	28.88	30.19	31.21	32.83
417	28.65	28.29	28.48	28.70	28.84	30.12	31.14	32.76
418	28.62	28.26	28.45	28.66	28.81	30.08	31.10	32.70
419	28.60	28.23	28.42	28.64	28.80	30.06	31.08	32.67
420	28.57	28.20	28.40	28.63	28.81	30.06	31.09	32.67
421	28.56	28.19	28.39	28.63	28.83	30.08	31.12	32.68
422	28.55	28.18	28.40	28.65	28.85	30.11	31.15	32.70
423	28.55	28.19	28.42	28.67	28.87	30.14	31.18	32.72
424	28.56	28.20	28.43	28.69	28.89	30.17	31.20	32.74
425	28.56	28.20	28.44	28.70	28.91	30.19	31.21	32.75
426	28.56	28.20	28.45	28.72	28.94	30.22	31.22	32.75
427	28.56	28.21	28.46	28.74	28.99	30.26	31.25	32.77
428	28.56	28.22	28.48	28.76	29.05	30.31	31.29	32.80
429	28.56	28.22	28.49	28.78	29.10	30.35	31.35	32.84
430	28.55	28.21	28.49	28.79	29.12	30.36	31.39	32.89
431	28.58	28.25	28.53	28.84	29.17	30.40	31.45	32.94
432	28.54	28.19	28.46	28.76	29.08	30.33	31.43	32.94
433	28.58	28.24	28.51	28.80	29.09	30.34	31.45	32.98
434	28.56	28.21	28.48	28.76	29.01	30.30	31.44	33.00
435	28.58	28.23	28.49	28.77	28.98	30.30	31.43	33.02
436	28.60	28.26	28.52	28.79	28.98	30.30	31.43	33.03
437	28.62	28.29	28.54	28.81	28.97	30.31	31.41	33.03
438	28.63	28.30	28.54	28.80	28.95	30.28	31.36	32.99
439	28.64	28.30	28.53	28.77	28.91	30.24	31.29	32.93
440	28.63	28.28	28.49	28.73	28.86	30.17	31.20	32.82
441	28.62	28.26	28.46	28.68	28.80	30.09	31.11	32.73
442	28.61	28.24	28.42	28.64	28.77	30.05	31.05	32.66
443	28.58	28.21	28.39	28.61	28.76	30.02	31.02	32.62
444	28.56	28.18	28.37	28.60	28.77	30.02	31.03	32.61
445	28.55	28.17	28.37	28.61	28.79	30.05	31.06	32.63
446	28.54	28.17	28.38	28.62	28.82	30.08	31.09	32.65
447	28.55	28.18	28.40	28.65	28.84	30.11	31.13	32.69
448	28.56	28.19	28.42	28.68	28.87	30.16	31.17	32.72
449	28.56	28.21	28.44	28.70	28.90	30.19	31.20	32.76

ObsID = observation number (same as Table 1). UBVRIJHK absolute STMAG magnitudes (Stone 1996; Laidler 2008) are given in the remaining columns.

ObsID	U	B	V	R	I	J	H	K
450	28.57	28.21	28.45	28.72	28.93	30.23	31.23	32.77
451	28.58	28.23	28.48	28.75	28.98	30.28	31.28	32.81
452	28.58	28.24	28.50	28.78	29.05	30.34	31.35	32.86
453	28.58	28.24	28.52	28.80	29.11	30.39	31.42	32.92
454	28.58	28.25	28.52	28.82	29.15	30.42	31.48	32.97
455	28.58	28.24	28.52	28.82	29.16	30.43	31.52	33.01
456	28.57	28.23	28.51	28.80	29.13	30.41	31.54	33.04
457	28.58	28.24	28.51	28.80	29.10	30.39	31.54	33.06
458	28.60	28.26	28.52	28.80	29.07	30.37	31.54	33.08
459	28.62	28.28	28.54	28.81	29.04	30.35	31.53	33.10
460	28.64	28.30	28.56	28.82	29.01	30.35	31.52	33.12
461	28.66	28.32	28.57	28.83	29.00	30.34	31.50	33.12
462	28.68	28.35	28.58	28.83	28.98	30.33	31.47	33.10
463	28.70	28.36	28.58	28.82	28.96	30.30	31.41	33.05
464	28.70	28.36	28.56	28.79	28.92	30.25	31.32	32.96
465	28.71	28.35	28.54	28.75	28.88	30.19	31.25	32.88
466	28.70	28.34	28.52	28.73	28.85	30.14	31.19	32.81
467	28.68	28.32	28.50	28.71	28.84	30.12	31.16	32.77
468	28.67	28.30	28.48	28.70	28.86	30.13	31.16	32.76
469	28.66	28.29	28.49	28.71	28.89	30.16	31.19	32.77
470	28.66	28.29	28.50	28.74	28.93	30.21	31.24	32.80
471	28.66	28.30	28.53	28.77	28.96	30.26	31.29	32.85
472	28.67	28.32	28.55	28.81	28.99	30.30	31.34	32.90
473	28.68	28.32	28.56	28.82	29.00	30.32	31.37	32.92
474	28.68	28.32	28.55	28.82	29.01	30.34	31.39	32.94
475	28.68	28.32	28.55	28.82	29.04	30.37	31.42	32.96
476	28.67	28.31	28.55	28.82	29.08	30.41	31.47	32.99
477	28.67	28.32	28.58	28.86	29.15	30.47	31.57	33.07
478	28.67	28.32	28.59	28.88	29.20	30.50	31.62	33.11
479	28.68	28.33	28.59	28.88	29.23	30.52	31.66	33.15
480	28.68	28.33	28.60	28.88	29.23	30.52	31.70	33.18
481	28.70	28.34	28.61	28.89	29.22	30.52	31.72	33.22
482	28.72	28.37	28.62	28.90	29.19	30.51	31.72	33.24
483	28.73	28.38	28.63	28.90	29.15	30.48	31.70	33.26
484	28.75	28.40	28.64	28.90	29.10	30.46	31.68	33.26
485	28.77	28.42	28.64	28.89	29.07	30.43	31.64	33.25
486	28.80	28.44	28.67	28.91	29.06	30.43	31.62	33.24
487	28.82	28.47	28.68	28.91	29.05	30.41	31.56	33.19
488	28.83	28.47	28.67	28.89	29.02	30.36	31.47	33.10
489	28.83	28.46	28.64	28.85	28.97	30.30	31.38	33.02
490	28.83	28.45	28.61	28.82	28.94	30.25	31.31	32.94

ObsID = observation number (same as Table 1). UBVRIJHK absolute STMAG magnitudes (Stone 1996; Laidler 2008) are given in the remaining columns.

ObsID	U	B	V	R	I	J	H	K
491	28.82	28.44	28.60	28.80	28.93	30.22	31.28	32.90
492	28.81	28.43	28.59	28.80	28.95	30.23	31.28	32.88
493	28.81	28.43	28.61	28.83	29.00	30.27	31.31	32.89
494	28.81	28.43	28.63	28.86	29.05	30.33	31.35	32.92
495	28.81	28.44	28.65	28.88	29.08	30.38	31.40	32.96
496	28.82	28.45	28.66	28.91	29.10	30.42	31.45	32.99
497	28.82	28.45	28.67	28.92	29.11	30.45	31.49	33.03
498	28.81	28.44	28.65	28.91	29.11	30.45	31.49	33.03
499	28.81	28.42	28.64	28.89	29.11	30.46	31.49	33.01
500	28.81	28.43	28.65	28.91	29.15	30.49	31.54	33.05
501	28.82	28.44	28.67	28.94	29.22	30.55	31.62	33.11
502	28.83	28.46	28.70	28.98	29.29	30.61	31.70	33.18
503	28.83	28.47	28.72	29.00	29.33	30.64	31.76	33.23
504	28.84	28.47	28.72	29.00	29.34	30.65	31.79	33.26
505	28.85	28.48	28.73	29.01	29.35	30.66	31.82	33.29
506	28.87	28.51	28.76	29.03	29.34	30.66	31.84	33.34
507	28.89	28.52	28.76	29.03	29.29	30.63	31.81	33.35
508	28.92	28.54	28.77	29.02	29.23	30.60	31.78	33.34
509	28.94	28.56	28.77	29.02	29.19	30.57	31.76	33.35
510	28.96	28.59	28.79	29.03	29.18	30.55	31.74	33.35
511	28.99	28.61	28.81	29.04	29.17	30.55	31.72	33.34
512	29.00	28.62	28.81	29.03	29.16	30.52	31.66	33.28
513	29.01	28.62	28.79	29.00	29.12	30.46	31.57	33.19
514	29.02	28.62	28.78	28.97	29.09	30.41	31.48	33.10
515	29.02	28.62	28.77	28.96	29.08	30.38	31.43	33.04
516	29.02	28.62	28.78	28.97	29.09	30.38	31.41	33.00
517	29.03	28.64	28.80	29.00	29.15	30.44	31.44	33.02
518	29.03	28.65	28.84	29.05	29.23	30.51	31.51	33.06
519	29.04	28.66	28.86	29.09	29.29	30.59	31.57	33.11
520	29.04	28.66	28.87	29.11	29.31	30.63	31.64	33.16
521	29.03	28.65	28.86	29.11	29.31	30.65	31.68	33.20
522	29.01	28.62	28.83	29.08	29.28	30.63	31.68	33.19
523	29.01	28.61	28.81	29.05	29.26	30.62	31.66	33.16
524	29.00	28.61	28.81	29.06	29.29	30.64	31.67	33.16
525	29.01	28.61	28.83	29.08	29.34	30.68	31.72	33.19
526	29.02	28.64	28.86	29.12	29.42	30.74	31.79	33.25
527	29.04	28.65	28.90	29.16	29.48	30.79	31.85	33.30
528	29.04	28.66	28.90	29.17	29.50	30.80	31.89	33.33
529	29.04	28.66	28.89	29.16	29.50	30.80	31.93	33.38
530	29.06	28.67	28.91	29.17	29.49	30.81	31.97	33.44
531	29.08	28.69	28.92	29.18	29.46	30.79	31.99	33.49

ObsID = observation number (same as Table 1). UBVRIJHK absolute STMAG magnitudes (Stone 1996; Laidler 2008) are given in the remaining columns.

ObsID	U	B	V	R	I	J	H	K
532	29.10	28.71	28.92	29.17	29.40	30.76	31.98	33.51
533	29.13	28.73	28.93	29.17	29.35	30.72	31.95	33.52
534	29.15	28.76	28.95	29.18	29.33	30.70	31.93	33.53
535	29.19	28.79	28.99	29.21	29.34	30.72	31.93	33.54
536	29.22	28.83	29.01	29.23	29.35	30.72	31.89	33.51
537	29.24	28.85	29.02	29.23	29.35	30.70	31.83	33.44
538	29.26	28.86	29.02	29.22	29.33	30.67	31.74	33.35
539	29.27	28.87	29.02	29.20	29.31	30.62	31.65	33.26
540	29.27	28.87	29.01	29.19	29.30	30.60	31.59	33.19
541	29.28	28.88	29.04	29.22	29.35	30.63	31.61	33.20
542	29.29	28.90	29.08	29.28	29.44	30.72	31.69	33.25
543	29.29	28.91	29.12	29.35	29.54	30.83	31.80	33.34
544	29.30	28.92	29.15	29.39	29.59	30.91	31.90	33.42
545	29.29	28.91	29.14	29.38	29.58	30.93	31.98	33.49
546	29.27	28.88	29.10	29.35	29.54	30.91	32.01	33.52
547	29.26	28.86	29.07	29.31	29.50	30.88	32.00	33.51
548	29.26	28.86	29.06	29.30	29.51	30.88	32.00	33.50
549	29.26	28.86	29.07	29.31	29.55	30.91	32.02	33.50
550	29.27	28.87	29.09	29.34	29.61	30.95	32.05	33.52
551	29.28	28.88	29.11	29.37	29.66	30.99	32.08	33.53
552	29.28	28.89	29.13	29.39	29.71	31.02	32.12	33.55
553	29.30	28.90	29.14	29.41	29.74	31.04	32.17	33.60
554	29.31	28.91	29.16	29.43	29.75	31.06	32.24	33.68
555	29.33	28.92	29.16	29.42	29.72	31.04	32.28	33.75
556	29.34	28.93	29.15	29.40	29.66	31.00	32.27	33.78
557	29.36	28.95	29.15	29.39	29.60	30.96	32.24	33.79
558	29.38	28.96	29.15	29.37	29.54	30.91	32.19	33.77
559	29.41	29.00	29.18	29.39	29.54	30.91	32.16	33.76
560	29.45	29.04	29.22	29.43	29.56	30.94	32.15	33.76
561	29.49	29.08	29.26	29.47	29.59	30.95	32.12	33.74
562	29.52	29.12	29.29	29.49	29.60	30.95	32.06	33.69
563	29.55	29.14	29.30	29.49	29.59	30.92	31.97	33.60
564	29.56	29.14	29.29	29.47	29.56	30.87	31.88	33.51
565	29.57	29.15	29.30	29.48	29.58	30.88	31.86	33.47
566	29.58	29.17	29.35	29.54	29.67	30.95	31.93	33.51
567	29.58	29.20	29.41	29.62	29.79	31.09	32.06	33.62
568	29.58	29.20	29.43	29.67	29.88	31.19	32.21	33.73
569	29.56	29.18	29.41	29.66	29.88	31.22	32.31	33.82
570	29.54	29.14	29.35	29.60	29.81	31.17	32.33	33.85
571	29.53	29.11	29.31	29.55	29.74	31.12	32.32	33.83
572	29.53	29.11	29.30	29.54	29.74	31.12	32.31	33.83

ObsID = observation number (same as Table 1). UBVRIJHK absolute STMAG magnitudes (Stone 1996; Laidler 2008) are given in the remaining columns.

ObsID	U	B	V	R	I	J	H	K
573	29.55	29.13	29.34	29.58	29.79	31.18	32.35	33.86
574	29.56	29.15	29.37	29.62	29.86	31.23	32.40	33.89
575	29.57	29.16	29.39	29.65	29.92	31.27	32.43	33.89
576	29.57	29.16	29.40	29.66	29.96	31.29	32.45	33.89
577	29.58	29.17	29.41	29.67	29.99	31.30	32.48	33.91
578	29.59	29.17	29.41	29.67	30.00	31.30	32.52	33.95
579	29.59	29.17	29.40	29.66	29.97	31.28	32.54	33.99
580	29.60	29.17	29.38	29.63	29.92	31.24	32.54	34.03
581	29.61	29.17	29.36	29.60	29.84	31.18	32.49	34.02
582	29.63	29.19	29.37	29.59	29.79	31.14	32.45	34.01
583	29.67	29.22	29.40	29.62	29.77	31.14	32.42	34.02
584	29.71	29.28	29.46	29.67	29.80	31.17	32.42	34.04
585	29.76	29.33	29.52	29.73	29.85	31.22	32.43	34.05
586	29.79	29.38	29.56	29.76	29.89	31.24	32.39	34.02
587	29.82	29.39	29.56	29.75	29.87	31.21	32.29	33.91
588	29.84	29.41	29.57	29.75	29.86	31.18	32.21	33.84
589	29.86	29.43	29.58	29.76	29.85	31.15	32.14	33.76
590	29.87	29.45	29.62	29.80	29.90	31.19	32.15	33.75
591	29.88	29.47	29.67	29.87	30.02	31.30	32.26	33.83
592	29.87	29.46	29.68	29.91	30.12	31.40	32.39	33.91
593	29.84	29.42	29.65	29.89	30.13	31.43	32.48	33.97
594	29.81	29.37	29.58	29.82	30.06	31.38	32.49	33.98
595	29.80	29.35	29.54	29.77	29.98	31.33	32.46	33.95
596	29.81	29.35	29.53	29.75	29.95	31.32	32.43	33.94
597	29.83	29.38	29.58	29.81	30.01	31.40	32.51	34.02
598	29.86	29.42	29.63	29.87	30.09	31.47	32.57	34.06
599	29.87	29.43	29.65	29.90	30.15	31.51	32.58	34.06
600	29.87	29.43	29.65	29.90	30.18	31.50	32.57	34.01
601	29.86	29.42	29.64	29.89	30.19	31.49	32.58	34.01
602	29.87	29.42	29.64	29.89	30.20	31.48	32.62	34.05
603	29.88	29.42	29.64	29.89	30.20	31.48	32.66	34.09
604	29.89	29.43	29.64	29.88	30.18	31.48	32.71	34.16
605	29.90	29.43	29.64	29.87	30.14	31.45	32.72	34.21
606	29.90	29.43	29.61	29.84	30.06	31.39	32.66	34.18
607	29.94	29.46	29.64	29.85	30.04	31.38	32.63	34.18
608	29.98	29.52	29.70	29.91	30.06	31.42	32.65	34.23
609	30.03	29.58	29.76	29.98	30.11	31.47	32.68	34.28
610	30.08	29.64	29.83	30.03	30.17	31.52	32.69	34.29
611	30.12	29.68	29.86	30.07	30.20	31.54	32.63	34.25
612	30.14	29.70	29.88	30.07	30.19	31.51	32.55	34.17
613	30.16	29.72	29.89	30.08	30.18	31.49	32.48	34.10

ObsID = observation number (same as Table 1). UBVRIJHK absolute STMAG magnitudes (Stone 1996; Laidler 2008) are given in the remaining columns.

ObsID	U	B	V	R	I	J	H	K
614	30.18	29.74	29.91	30.09	30.18	31.48	32.43	34.05
615	30.19	29.75	29.95	30.14	30.26	31.54	32.49	34.08
616	30.17	29.74	29.95	30.17	30.36	31.62	32.59	34.13
617	30.14	29.69	29.90	30.14	30.38	31.64	32.66	34.16
618	30.10	29.62	29.82	30.05	30.30	31.57	32.63	34.10
619	30.08	29.58	29.75	29.98	30.21	31.51	32.58	34.04
620	30.09	29.59	29.75	29.97	30.17	31.51	32.55	34.02
621	30.11	29.62	29.78	30.00	30.20	31.56	32.59	34.08
622	30.16	29.68	29.87	30.10	30.31	31.67	32.72	34.23
623	30.19	29.71	29.92	30.16	30.38	31.73	32.77	34.26
624	30.18	29.69	29.89	30.12	30.39	31.70	32.71	34.15
625	30.16	29.66	29.86	30.09	30.38	31.65	32.64	34.07
626	30.16	29.66	29.86	30.10	30.39	31.65	32.67	34.09
627	30.19	29.69	29.89	30.12	30.42	31.68	32.74	34.16
628	30.21	29.71	29.90	30.14	30.43	31.71	32.80	34.24
629	30.23	29.73	29.92	30.15	30.43	31.72	32.89	34.35
630	30.23	29.73	29.91	30.13	30.37	31.68	32.85	34.34
631	30.25	29.74	29.90	30.12	30.33	31.64	32.81	34.34
632	30.27	29.76	29.93	30.14	30.32	31.64	32.82	34.36
633	30.30	29.80	29.97	30.18	30.34	31.67	32.85	34.40
634	30.34	29.85	30.02	30.23	30.38	31.71	32.86	34.42
635	30.39	29.91	30.09	30.29	30.46	31.77	32.90	34.48
636	30.43	29.95	30.12	30.32	30.48	31.78	32.83	34.41
637	30.47	30.01	30.20	30.39	30.51	31.82	32.81	34.42
638	30.49	30.01	30.18	30.37	30.48	31.77	32.73	34.34
639	30.50	30.02	30.20	30.39	30.51	31.78	32.74	34.33
640	30.49	30.01	30.21	30.41	30.57	31.82	32.77	34.31
641	30.47	29.98	30.17	30.39	30.62	31.85	32.82	34.30
642	30.44	29.92	30.08	30.31	30.57	31.81	32.78	34.22
643	30.43	29.88	30.03	30.24	30.48	31.75	32.68	34.13
644	30.43	29.87	30.01	30.22	30.44	31.74	32.67	34.13
645	30.45	29.90	30.04	30.25	30.46	31.79	32.71	34.17
646	30.49	29.97	30.13	30.34	30.53	31.88	32.81	34.29
647	30.53	30.02	30.20	30.42	30.63	31.96	32.92	34.41
648	30.51	29.98	30.15	30.36	30.59	31.89	32.84	34.29
649	30.50	29.94	30.10	30.30	30.56	31.82	32.72	34.14
650	30.50	29.93	30.07	30.29	30.56	31.79	32.70	34.11
651	30.52	29.96	30.11	30.32	30.59	31.83	32.78	34.19
652	30.55	29.99	30.14	30.34	30.61	31.84	32.81	34.24
653	30.55	29.98	30.12	30.33	30.59	31.82	32.86	34.30
654	30.57	30.00	30.13	30.34	30.59	31.85	32.90	34.35

ObsID = observation number (same as Table 1). UBVRIJHK absolute STMAG magnitudes (Stone 1996; Laidler 2008) are given in the remaining columns.

ObsID	U	B	V	R	I	J	H	K
655	30.61	30.04	30.18	30.38	30.59	31.87	32.89	34.36
656	30.62	30.05	30.20	30.40	30.58	31.87	32.91	34.41
657	30.64	30.09	30.24	30.44	30.61	31.89	32.98	34.49
658	30.66	30.11	30.25	30.44	30.60	31.88	32.94	34.46
659	30.70	30.15	30.30	30.50	30.66	31.95	33.03	34.56
660	30.76	30.22	30.37	30.56	30.73	32.02	33.01	34.54
661	30.83	30.32	30.49	30.67	30.82	32.12	33.02	34.58
662	30.85	30.34	30.52	30.69	30.80	32.09	32.97	34.55
663	30.84	30.32	30.49	30.68	30.80	32.08	32.99	34.55
664	30.84	30.31	30.47	30.66	30.81	32.04	32.93	34.47
665	30.82	30.27	30.42	30.61	30.80	32.02	32.92	34.41
666	30.80	30.21	30.31	30.50	30.74	31.95	32.83	34.26
667	30.81	30.18	30.28	30.46	30.71	31.95	32.79	34.20
668	30.81	30.17	30.24	30.43	30.66	31.92	32.75	34.19
669	30.82	30.19	30.29	30.48	30.71	32.00	32.86	34.30
670	30.87	30.25	30.35	30.55	30.77	32.08	32.94	34.38
671	30.91	30.33	30.46	30.66	30.86	32.17	33.05	34.52
672	30.91	30.32	30.44	30.63	30.84	32.12	32.97	34.43
673	30.90	30.28	30.38	30.56	30.79	32.02	32.86	34.27
674	30.90	30.25	30.33	30.51	30.76	31.98	32.79	34.20
675	30.92	30.26	30.32	30.50	30.76	31.97	32.78	34.21
676	30.94	30.29	30.38	30.55	30.79	32.01	32.83	34.25
677	30.96	30.29	30.36	30.53	30.78	31.99	32.90	34.32
678	30.95	30.27	30.33	30.51	30.77	32.00	32.84	34.31
679	31.01	30.34	30.40	30.59	30.83	32.08	32.89	34.35
680	31.04	30.39	30.47	30.66	30.87	32.12	33.04	34.49
681	31.06	30.44	30.56	30.76	30.97	32.20	33.10	34.61
682	31.08	30.47	30.60	30.78	30.92	32.15	33.10	34.59
683	31.10	30.47	30.58	30.75	30.92	32.19	33.16	34.65
684	31.18	30.57	30.70	30.88	31.06	32.33	33.15	34.68
685	31.26	30.66	30.76	30.93	31.06	32.38	33.07	34.59
686	31.29	30.70	30.86	31.01	31.10	32.39	33.14	34.67
687	31.28	30.67	30.83	30.99	31.11	32.36	33.19	34.70
688	31.26	30.64	30.78	30.94	31.07	32.27	33.10	34.61
689	31.26	30.63	30.76	30.91	31.05	32.24	33.07	34.56
690	31.28	30.65	30.72	30.84	30.99	32.19	32.89	34.35
691	31.30	30.60	30.62	30.74	30.90	32.14	32.74	34.21
692	31.31	30.56	30.54	30.66	30.82	32.08	32.73	34.16
693	31.31	30.57	30.57	30.71	30.88	32.15	32.84	34.27
694	31.33	30.63	30.66	30.80	30.96	32.26	32.86	34.32
695	31.41	30.72	30.76	30.88	31.02	32.33	32.95	34.41

ObsID = observation number (same as Table 1). UBVRIJHK absolute STMAG magnitudes (Stone 1996; Laidler 2008) are given in the remaining columns.

ObsID	U	B	V	R	I	J	H	K
696	31.42	30.72	30.78	30.91	31.06	32.34	33.01	34.47
697	31.43	30.75	30.80	30.89	30.98	32.24	32.89	34.35
698	31.43	30.72	30.75	30.82	30.93	32.16	32.77	34.21
699	31.44	30.67	30.66	30.75	30.89	32.09	32.75	34.18
700	31.43	30.68	30.67	30.76	30.88	32.10	32.71	34.18
701	31.48	30.72	30.69	30.75	30.85	32.10	32.67	34.15
702	31.48	30.67	30.61	30.69	30.79	32.01	32.64	34.11
703	31.52	30.73	30.70	30.77	30.87	32.12	32.72	34.24
704	31.56	30.78	30.74	30.83	30.94	32.18	32.77	34.29
705	31.59	30.85	30.85	30.95	31.03	32.28	32.95	34.44
706	31.61	30.89	30.98	31.10	31.18	32.35	33.13	34.60
707	31.61	30.86	30.89	30.97	31.06	32.27	33.02	34.52
708	31.69	30.97	31.01	31.10	31.15	32.40	33.07	34.59
709	31.79	31.08	31.11	31.17	31.23	32.56	33.06	34.57
710	31.83	31.14	31.23	31.35	31.45	32.70	33.17	34.75
711	31.85	31.19	31.36	31.46	31.47	32.73	33.41	34.93
712	31.83	31.14	31.30	31.40	31.42	32.62	33.36	34.85
713	31.79	31.08	31.19	31.22	31.24	32.40	33.13	34.60
714	31.89	31.17	31.22	31.21	31.18	32.40	32.95	34.46
715	31.91	31.13	31.08	31.03	31.02	32.25	32.74	34.22
716	31.93	31.14	31.06	31.00	30.97	32.23	32.69	34.19
717	31.93	31.10	31.00	30.96	30.95	32.21	32.70	34.19
718	31.96	31.16	31.11	31.07	31.05	32.30	32.77	34.28
719	32.00	31.22	31.14	31.08	31.05	32.36	32.75	34.26
720	32.07	31.28	31.20	31.11	31.06	32.38	32.82	34.34
721	32.07	31.27	31.20	31.12	31.06	32.34	32.79	34.31
722	32.08	31.26	31.17	31.08	31.02	32.28	32.73	34.21
723	32.12	31.28	31.15	31.01	30.90	32.15	32.60	34.10
724	32.12	31.23	31.08	30.94	30.83	32.03	32.51	34.01
725	32.11	31.23	31.08	30.93	30.82	32.06	32.49	34.01
726	32.18	31.27	31.07	30.89	30.77	32.03	32.44	33.97
727	32.18	31.26	31.10	30.94	30.81	32.02	32.49	34.01
728	32.25	31.34	31.16	31.00	30.87	32.12	32.52	34.06
729	32.28	31.39	31.25	31.09	30.96	32.19	32.65	34.18
730	32.29	31.37	31.28	31.17	31.04	32.20	32.76	34.25
731	32.26	31.33	31.25	31.16	31.04	32.16	32.79	34.25
732	32.38	31.45	31.35	31.22	31.08	32.22	32.79	34.29
733	32.45	31.56	31.41	31.21	31.04	32.28	32.66	34.21
734	32.55	31.72	31.59	31.36	31.16	32.46	32.73	34.31
735	32.60	31.85	31.93	31.85	31.68	32.90	33.38	34.91
736	32.58	31.73	31.78	31.71	31.55	32.66	33.28	34.75

ObsID = observation number (same as Table 1). UBVRIJHK absolute STMAG magnitudes (Stone 1996; Laidler 2008) are given in the remaining columns.

ObsID	U	B	V	R	I	J	H	K
737	32.59	31.70	31.67	31.54	31.36	32.47	33.02	34.49
738	32.67	31.79	31.69	31.48	31.27	32.46	32.87	34.39
739	32.75	31.87	31.63	31.31	31.03	32.30	32.55	34.11
740	32.79	31.88	31.66	31.35	31.08	32.29	32.59	34.11
741	32.80	31.85	31.65	31.38	31.13	32.30	32.69	34.19
742	32.83	31.86	31.68	31.43	31.17	32.31	32.74	34.22
743	32.90	31.94	31.69	31.38	31.10	32.29	32.62	34.12
744	32.97	32.01	31.74	31.41	31.12	32.34	32.63	34.16
745	33.03	32.08	31.79	31.43	31.14	32.39	32.63	34.19
746	33.06	32.05	31.74	31.38	31.07	32.27	32.56	34.10
747	33.13	32.12	31.81	31.44	31.12	32.30	32.60	34.10
748	33.16	32.10	31.79	31.41	31.08	32.26	32.56	34.09
749	33.16	32.00	31.69	31.35	31.04	32.15	32.54	34.05
750	33.23	32.07	31.74	31.38	31.06	32.18	32.56	34.06
751	33.29	32.14	31.83	31.48	31.17	32.29	32.66	34.17
752	33.39	32.24	31.95	31.61	31.29	32.40	32.79	34.30
753	33.53	32.48	32.21	31.84	31.50	32.67	32.97	34.50
754	33.56	32.43	32.15	31.80	31.47	32.58	32.95	34.44
755	33.54	32.28	32.01	31.72	31.42	32.43	32.94	34.37
756	33.62	32.32	32.01	31.70	31.40	32.41	32.91	34.37
757	33.84	32.72	32.38	31.97	31.62	32.77	33.07	34.60
758	34.02	33.03	32.68	32.18	31.78	33.05	33.18	34.78
759	34.08	33.07	32.90	32.56	32.20	33.31	33.65	35.16
760	34.12	33.03	32.88	32.63	32.31	33.30	33.82	35.23
761	34.20	33.02	32.77	32.45	32.12	33.14	33.58	35.02
762	34.37	33.28	32.99	32.58	32.20	33.28	33.60	35.09
763	34.50	33.43	33.09	32.60	32.17	33.32	33.54	35.07
764	34.59	33.44	33.10	32.65	32.25	33.34	33.60	35.11
765	34.68	33.53	33.27	32.90	32.52	33.52	33.90	35.34
766	34.81	33.66	33.43	33.08	32.70	33.67	34.07	35.49
767	34.92	33.72	33.38	32.95	32.54	33.52	33.85	35.28
768	35.11	34.02	33.64	33.13	32.69	33.74	33.96	35.45
769	35.22	34.07	33.69	33.20	32.77	33.82	34.06	35.55
770	35.27	33.94	33.54	33.11	32.70	33.68	34.04	35.50
771	35.36	34.01	33.62	33.19	32.78	33.73	34.11	35.56
772	35.49	34.14	33.77	33.35	32.93	33.87	34.27	35.71
773	35.61	34.25	33.88	33.46	33.04	33.97	34.36	35.79
774	35.72	34.38	34.03	33.61	33.18	34.08	34.48	35.90
775	35.94	34.76	34.46	33.99	33.52	34.46	34.78	36.24
776	36.01	34.80	34.55	34.14	33.70	34.56	34.97	36.39
777	35.98	34.73	34.47	34.07	33.63	34.49	34.92	36.32

ObsID = observation number (same as Table 1). UBVRIJHK absolute STMAG magnitudes (Stone 1996; Laidler 2008) are given in the remaining columns.

ObsID	U	B	V	R	I	J	H	K
778	36.01	34.73	34.45	34.05	33.60	34.44	34.87	36.27
779	35.99	34.68	34.39	33.98	33.53	34.39	34.82	36.23
780	35.90	34.56	34.28	33.90	33.46	34.31	34.81	36.20
781	35.84	34.42	34.12	33.74	33.31	34.13	34.64	36.03
782	35.75	34.31	34.00	33.63	33.22	34.04	34.57	35.95
783	35.62	34.19	33.87	33.51	33.11	33.93	34.46	35.83
784	35.52	34.06	33.74	33.39	33.01	33.83	34.39	35.76
785	35.38	33.92	33.59	33.25	32.86	33.69	34.25	35.62
786	35.28	33.87	33.54	33.19	32.81	33.65	34.18	35.56
787	35.14	33.73	33.40	33.04	32.67	33.53	34.04	35.43
788	35.01	33.58	33.24	32.88	32.51	33.37	33.91	35.30
789	34.91	33.52	33.20	32.86	32.48	33.36	33.90	35.29
790	34.82	33.50	33.21	32.88	32.51	33.38	33.90	35.30
791	34.71	33.43	33.12	32.75	32.36	33.28	33.77	35.16
792	34.61	33.35	33.05	32.69	32.31	33.22	33.70	35.11
793	34.51	33.34	33.04	32.65	32.26	33.27	33.68	35.12
794	34.41	33.24	32.94	32.54	32.14	33.15	33.55	35.01
795	34.28	33.03	32.74	32.39	32.02	32.98	33.46	34.88
796	34.14	32.88	32.62	32.29	31.93	32.86	33.38	34.79
797	34.00	32.75	32.52	32.21	31.87	32.82	33.40	34.78
798	34.01	32.79	32.54	32.19	31.81	32.75	33.23	34.64
799	33.82	32.59	32.30	31.96	31.62	32.62	33.12	34.53
800	33.74	32.49	32.20	31.85	31.49	32.48	32.96	34.40
801	33.71	32.54	32.27	31.93	31.58	32.58	33.04	34.47
802	33.53	32.23	31.98	31.73	31.44	32.35	32.99	34.37
803	33.40	32.14	31.90	31.65	31.38	32.34	32.97	34.37
804	33.49	32.31	32.04	31.72	31.39	32.38	32.87	34.31
805	33.36	32.24	31.91	31.54	31.21	32.32	32.70	34.20
806	33.36	32.27	31.95	31.57	31.23	32.31	32.69	34.16
807	33.22	32.02	31.70	31.37	31.07	32.11	32.57	34.04
808	33.18	32.06	31.75	31.42	31.13	32.21	32.62	34.11
809	33.15	32.11	31.80	31.43	31.11	32.23	32.60	34.09
810	33.11	32.00	31.69	31.35	31.05	32.12	32.54	34.02
811	32.95	31.85	31.54	31.22	30.95	32.07	32.47	33.98
812	32.99	31.96	31.68	31.34	31.05	32.17	32.55	34.05
813	32.97	32.00	31.77	31.47	31.19	32.30	32.71	34.20
814	32.92	31.98	31.80	31.54	31.28	32.37	32.81	34.29
815	32.78	31.73	31.52	31.28	31.02	32.07	32.61	34.05
816	32.76	31.70	31.45	31.19	30.93	32.01	32.50	33.98
817	32.65	31.60	31.33	31.05	30.81	31.95	32.39	33.90
818	32.69	31.71	31.45	31.15	30.90	32.07	32.44	33.95

ObsID = observation number (same as Table 1). UBVRIJHK absolute STMAG magnitudes (Stone 1996; Laidler 2008) are given in the remaining columns.

ObsID	U	B	V	R	I	J	H	K
819	32.69	31.76	31.52	31.22	30.97	32.16	32.50	34.03
820	32.57	31.57	31.38	31.18	30.99	32.09	32.61	34.09
821	32.58	31.68	31.58	31.41	31.22	32.33	32.87	34.32
822	32.59	31.73	31.60	31.39	31.17	32.35	32.76	34.27
823	32.44	31.47	31.26	31.04	30.84	31.99	32.46	33.95
824	32.41	31.45	31.23	30.99	30.79	31.96	32.39	33.90
825	32.39	31.46	31.26	31.04	30.85	32.01	32.48	33.98
826	32.33	31.38	31.26	31.13	31.00	32.09	32.71	34.16
827	32.34	31.46	31.41	31.33	31.21	32.33	32.96	34.41
828	32.34	31.50	31.40	31.27	31.13	32.33	32.82	34.32
829	32.29	31.40	31.19	31.00	30.85	32.07	32.48	33.99
830	32.27	31.41	31.19	30.97	30.82	32.09	32.45	33.97
831	32.19	31.30	31.07	30.88	30.75	31.97	32.40	33.91
832	32.21	31.33	31.11	30.92	30.81	32.07	32.45	33.97
833	32.18	31.31	31.09	30.92	30.81	32.08	32.47	33.99
834	32.14	31.28	31.10	30.93	30.83	32.08	32.47	34.00
835	32.10	31.23	31.03	30.88	30.80	32.06	32.47	33.99
836	32.05	31.20	31.04	30.90	30.83	32.09	32.52	34.04
837	32.02	31.19	31.08	30.98	30.91	32.11	32.62	34.12
838	32.05	31.28	31.22	31.16	31.11	32.34	32.85	34.35
839	31.98	31.19	31.16	31.16	31.17	32.36	32.96	34.42

ObsID = observation number (same as Table 1). UBVRIJHK absolute STMAG magnitudes (Stone 1996; Laidler 2008) are given in the remaining columns.

Table A.3 Earth HST Standard UBVRIJHK Colors

ObsID	U-B	B-V	V-R	R-I	I-J	J-H	H-K
0	0.73	-0.03	-0.05	-0.03	-1.25	-0.58	-1.5
1	0.76	-0.01	-0.02	-0.02	-1.23	-0.6	-1.46
2	0.78	0.02	0	-0.03	-1.19	-0.57	-1.46
3	0.81	0.05	0.01	-0.01	-1.19	-0.54	-1.49
4	0.82	0.06	0.01	-0.03	-1.22	-0.53	-1.47
5	0.82	0.06	0.04	0.01	-1.19	-0.63	-1.48
6	0.84	0.09	0.03	0	-1.2	-0.54	-1.5
7	0.84	0.1	0.04	0	-1.23	-0.52	-1.51
8	0.83	0.08	0.04	0.02	-1.22	-0.61	-1.49
9	0.81	0.07	0.03	0.02	-1.21	-0.62	-1.48
10	0.83	-0.01	-0.01	0	-1.15	-0.76	-1.45
11	0.82	0	0	0.02	-1.18	-0.67	-1.5
12	0.76	-0.03	0.06	0.06	-1.21	-0.59	-1.51
13	0.79	0.03	0.08	0.08	-1.22	-0.5	-1.53
14	0.74	-0.04	0.06	0.08	-1.26	-0.49	-1.53
15	0.72	-0.13	0.02	0.1	-1.21	-0.58	-1.51
16	0.74	-0.13	-0.01	0.09	-1.17	-0.65	-1.49
17	0.77	-0.08	0.04	0.11	-1.16	-0.61	-1.49
18	0.79	-0.01	0.14	0.18	-1.2	-0.46	-1.53
19	0.85	0.17	0.25	0.21	-1.26	-0.32	-1.54
20	0.91	0.16	0.21	0.19	-1.2	-0.44	-1.51
21	0.89	0.14	0.19	0.19	-1.18	-0.46	-1.5
22	0.89	0.11	0.16	0.18	-1.18	-0.49	-1.5
23	0.92	0.16	0.2	0.19	-1.19	-0.45	-1.49
24	0.85	0.11	0.21	0.2	-1.24	-0.37	-1.54
25	0.88	0.14	0.25	0.23	-1.21	-0.37	-1.53
26	0.96	0.18	0.26	0.25	-1.14	-0.44	-1.5
27	0.95	0.22	0.3	0.27	-1.17	-0.37	-1.52
28	1	0.21	0.29	0.27	-1.16	-0.4	-1.52
29	1.04	0.24	0.29	0.27	-1.15	-0.41	-1.5
30	1.07	0.27	0.29	0.26	-1.13	-0.42	-1.5
31	1.03	0.28	0.33	0.29	-1.17	-0.34	-1.52
32	1.02	0.25	0.32	0.29	-1.18	-0.35	-1.53
33	1.03	0.22	0.28	0.27	-1.12	-0.42	-1.5
34	1.12	0.18	0.22	0.26	-1.03	-0.58	-1.44
35	1.1	0.17	0.22	0.25	-1.04	-0.57	-1.44
36	1.07	0.23	0.28	0.27	-1.11	-0.43	-1.5
37	1.03	0.21	0.3	0.29	-1.15	-0.38	-1.52
38	1.01	0.26	0.38	0.34	-1.18	-0.31	-1.55
39	0.89	0.05	0.29	0.34	-1.13	-0.37	-1.51

ObsID = observation number (same as Table 1). UBVRIJHK absolute STMAG colors (Stone 1996; Laidler 2008) are given in the remaining columns.

ObsID	U-B	B-V	V-R	R-I	I-J	J-H	H-K
40	0.94	-0.01	0.2	0.32	-1.03	-0.52	-1.44
41	1.05	0.09	0.22	0.29	-1.02	-0.57	-1.42
42	1.03	0.19	0.33	0.34	-1.09	-0.4	-1.48
43	1.03	0.29	0.44	0.4	-1.15	-0.27	-1.52
44	1.12	0.31	0.43	0.4	-1.12	-0.32	-1.5
45	1.18	0.27	0.36	0.37	-1.02	-0.43	-1.45
46	1.08	0.19	0.34	0.38	-1.01	-0.41	-1.43
47	1	0.26	0.43	0.4	-1.13	-0.28	-1.47
48	0.96	0.29	0.47	0.41	-1.18	-0.18	-1.53
49	0.99	0.29	0.48	0.42	-1.18	-0.2	-1.54
50	1.13	0.33	0.46	0.42	-1.1	-0.28	-1.5
51	1.21	0.35	0.45	0.42	-1.03	-0.33	-1.48
52	1.18	0.34	0.48	0.44	-1.08	-0.27	-1.51
53	1.22	0.35	0.46	0.43	-1.05	-0.29	-1.49
54	1.3	0.38	0.43	0.41	-1.02	-0.33	-1.48
55	1.35	0.37	0.43	0.41	-0.99	-0.38	-1.46
56	1.28	0.33	0.43	0.42	-0.98	-0.36	-1.46
57	1.23	0.31	0.42	0.42	-0.96	-0.34	-1.45
58	1.34	0.31	0.4	0.42	-0.91	-0.41	-1.42
59	1.32	0.34	0.42	0.42	-0.92	-0.37	-1.43
60	1.34	0.37	0.44	0.43	-0.93	-0.34	-1.44
61	1.25	0.36	0.48	0.46	-0.95	-0.27	-1.46
62	1.25	0.35	0.49	0.47	-0.97	-0.29	-1.48
63	1.1	0.29	0.51	0.5	-0.97	-0.22	-1.49
64	1.11	0.23	0.45	0.48	-0.87	-0.27	-1.44
65	1.29	0.3	0.44	0.47	-0.82	-0.36	-1.4
66	1.35	0.35	0.48	0.48	-0.82	-0.33	-1.42
67	1.34	0.32	0.45	0.48	-0.81	-0.37	-1.4
68	1.3	0.28	0.43	0.47	-0.81	-0.4	-1.4
69	1.21	0.25	0.43	0.48	-0.79	-0.36	-1.41
70	1.19	0.24	0.43	0.47	-0.81	-0.37	-1.41
71	1.19	0.26	0.44	0.47	-0.82	-0.34	-1.41
72	1.21	0.28	0.44	0.46	-0.84	-0.32	-1.42
73	1.32	0.3	0.4	0.44	-0.83	-0.43	-1.4
74	1.23	0.26	0.4	0.43	-0.88	-0.41	-1.42
75	1.22	0.25	0.39	0.43	-0.88	-0.42	-1.42
76	1.28	0.27	0.37	0.42	-0.86	-0.46	-1.4
77	1.19	0.25	0.39	0.42	-0.87	-0.4	-1.4
78	1.14	0.29	0.43	0.43	-0.94	-0.33	-1.43
79	1.23	0.32	0.42	0.41	-0.94	-0.38	-1.43
80	1.22	0.31	0.4	0.4	-0.97	-0.4	-1.44

ObsID = observation number (same as Table 1). UBVRIJHK absolute STMAG colors (Stone 1996; Laidler 2008) are given in the remaining columns.

ObsID	U-B	B-V	V-R	R-I	I-J	J-H	H-K
81	1.23	0.31	0.38	0.38	-0.95	-0.42	-1.42
82	1.16	0.27	0.36	0.37	-0.97	-0.43	-1.42
83	1.21	0.27	0.34	0.36	-0.94	-0.47	-1.4
84	1.15	0.32	0.4	0.37	-1.05	-0.37	-1.44
85	1.17	0.34	0.42	0.39	-1.02	-0.35	-1.46
86	1.22	0.32	0.38	0.37	-1.02	-0.42	-1.45
87	1.16	0.31	0.4	0.38	-1.02	-0.38	-1.45
88	1.24	0.3	0.34	0.35	-0.97	-0.48	-1.41
89	1.25	0.3	0.34	0.34	-1	-0.47	-1.44
90	1.21	0.31	0.34	0.32	-1.05	-0.46	-1.43
91	1.17	0.31	0.35	0.34	-1.03	-0.42	-1.44
92	1.16	0.29	0.33	0.32	-1.04	-0.47	-1.44
93	1.03	0.23	0.33	0.33	-1.06	-0.41	-1.47
94	1.01	0.21	0.32	0.33	-1.04	-0.42	-1.44
95	1.04	0.24	0.32	0.31	-1.06	-0.42	-1.45
96	1.07	0.28	0.32	0.3	-1.08	-0.44	-1.44
97	1.06	0.28	0.32	0.3	-1.1	-0.39	-1.48
98	1.03	0.28	0.35	0.31	-1.13	-0.37	-1.5
99	1.05	0.24	0.3	0.28	-1.09	-0.43	-1.48
100	0.97	0.25	0.31	0.28	-1.14	-0.38	-1.49
101	0.9	0.16	0.26	0.27	-1.12	-0.4	-1.48
102	0.97	0.23	0.28	0.26	-1.13	-0.41	-1.47
103	0.95	0.29	0.33	0.27	-1.19	-0.31	-1.52
104	1	0.28	0.31	0.27	-1.16	-0.38	-1.51
105	1.05	0.26	0.26	0.24	-1.11	-0.45	-1.49
106	1.04	0.19	0.19	0.19	-1.07	-0.57	-1.45
107	0.93	0.14	0.18	0.19	-1.11	-0.53	-1.45
108	0.91	0.2	0.23	0.21	-1.17	-0.42	-1.47
109	0.9	0.26	0.28	0.22	-1.23	-0.32	-1.53
110	0.93	0.26	0.27	0.22	-1.21	-0.36	-1.52
111	0.91	0.23	0.25	0.2	-1.22	-0.37	-1.51
112	0.96	0.21	0.21	0.18	-1.16	-0.47	-1.5
113	0.95	0.18	0.19	0.16	-1.15	-0.5	-1.5
114	0.93	0.19	0.19	0.15	-1.19	-0.46	-1.49
115	0.92	0.19	0.18	0.13	-1.21	-0.45	-1.51
116	0.91	0.19	0.18	0.14	-1.2	-0.45	-1.5
117	0.85	0.12	0.15	0.13	-1.2	-0.49	-1.49
118	0.85	0.06	0.09	0.1	-1.17	-0.59	-1.47
119	0.85	0.09	0.08	0.08	-1.16	-0.58	-1.47
120	0.87	0.12	0.08	0.06	-1.18	-0.57	-1.47
121	0.86	0.13	0.11	0.08	-1.22	-0.52	-1.5

ObsID = observation number (same as Table 1). UBVRIJHK absolute STMAG colors (Stone 1996; Laidler 2008) are given in the remaining columns.

ObsID	U-B	B-V	V-R	R-I	I-J	J-H	H-K
122	0.86	0.15	0.11	0.06	-1.23	-0.48	-1.49
123	0.84	0.12	0.1	0.05	-1.21	-0.52	-1.49
124	0.83	0.14	0.08	0.03	-1.26	-0.46	-1.5
125	0.78	0.05	0.03	0.02	-1.24	-0.54	-1.49
126	0.78	0.05	-0.01	-0.02	-1.25	-0.54	-1.48
127	0.81	0.15	0.06	0	-1.28	-0.43	-1.49
128	0.81	0.12	0.07	-0.01	-1.26	-0.51	-1.48
129	0.83	0.1	0.04	0.01	-1.18	-0.59	-1.49
130	0.84	0.08	0	-0.03	-1.19	-0.63	-1.47
131	0.77	0.03	-0.02	-0.04	-1.24	-0.58	-1.46
132	0.76	0.03	-0.03	-0.07	-1.28	-0.56	-1.46
133	0.8	0.09	0	-0.07	-1.25	-0.46	-1.49
134	0.8	0.12	0.01	-0.07	-1.27	-0.43	-1.5
135	0.79	0.08	0.02	-0.04	-1.24	-0.54	-1.46
136	0.8	0.07	-0.02	-0.05	-1.23	-0.58	-1.48
137	0.8	0.07	-0.03	-0.08	-1.19	-0.61	-1.47
138	0.77	0.02	-0.04	-0.09	-1.18	-0.61	-1.46
139	0.8	0.06	-0.05	-0.08	-1.22	-0.62	-1.45
140	0.77	0.04	-0.05	-0.09	-1.22	-0.61	-1.47
141	0.74	0.02	-0.04	-0.07	-1.21	-0.61	-1.48
142	0.72	-0.03	-0.09	-0.09	-1.21	-0.7	-1.46
143	0.73	-0.03	-0.1	-0.1	-1.2	-0.75	-1.44
144	0.75	0	-0.09	-0.11	-1.18	-0.71	-1.45
145	0.76	0.02	-0.12	-0.17	-1.2	-0.65	-1.47
146	0.75	0.04	-0.09	-0.16	-1.24	-0.59	-1.46
147	0.72	0.03	-0.07	-0.14	-1.22	-0.54	-1.48
148	0.71	0	-0.13	-0.17	-1.2	-0.57	-1.5
149	0.7	-0.02	-0.12	-0.13	-1.29	-0.57	-1.49
150	0.69	-0.04	-0.14	-0.13	-1.28	-0.64	-1.47
151	0.73	0.01	-0.15	-0.19	-1.24	-0.64	-1.46
152	0.73	0.03	-0.12	-0.18	-1.27	-0.59	-1.45
153	0.72	0	-0.12	-0.17	-1.24	-0.69	-1.45
154	0.74	0.01	-0.14	-0.2	-1.21	-0.71	-1.46
155	0.69	-0.03	-0.14	-0.17	-1.23	-0.7	-1.46
156	0.67	-0.06	-0.16	-0.15	-1.27	-0.74	-1.45
157	0.69	-0.02	-0.17	-0.2	-1.27	-0.64	-1.45
158	0.7	-0.01	-0.15	-0.24	-1.26	-0.65	-1.42
159	0.7	-0.01	-0.14	-0.21	-1.26	-0.64	-1.43
160	0.69	-0.01	-0.15	-0.21	-1.22	-0.65	-1.45
161	0.69	-0.02	-0.15	-0.23	-1.22	-0.76	-1.43
162	0.66	-0.06	-0.16	-0.21	-1.21	-0.78	-1.47

ObsID = observation number (same as Table 1). UBVRIJHK absolute STMAG colors (Stone 1996; Laidler 2008) are given in the remaining columns.

ObsID	U-B	B-V	V-R	R-I	I-J	J-H	H-K
163	0.66	-0.06	-0.17	-0.24	-1.18	-0.75	-1.46
164	0.65	-0.06	-0.16	-0.24	-1.21	-0.78	-1.45
165	0.66	-0.06	-0.17	-0.24	-1.19	-0.91	-1.43
166	0.65	-0.07	-0.17	-0.21	-1.21	-0.88	-1.45
167	0.65	-0.08	-0.17	-0.21	-1.21	-0.94	-1.44
168	0.66	-0.07	-0.19	-0.26	-1.21	-0.85	-1.46
169	0.66	-0.06	-0.18	-0.26	-1.22	-0.84	-1.43
170	0.65	-0.06	-0.19	-0.26	-1.23	-0.79	-1.46
171	0.63	-0.05	-0.18	-0.29	-1.27	-0.77	-1.43
172	0.61	-0.09	-0.19	-0.27	-1.25	-0.81	-1.46
173	0.63	-0.08	-0.19	-0.23	-1.26	-0.81	-1.46
174	0.61	-0.09	-0.18	-0.2	-1.29	-0.81	-1.48
175	0.62	-0.08	-0.19	-0.23	-1.25	-0.85	-1.45
176	0.65	-0.06	-0.19	-0.26	-1.24	-0.8	-1.44
177	0.65	-0.05	-0.18	-0.27	-1.24	-0.82	-1.43
178	0.64	-0.06	-0.18	-0.26	-1.22	-0.87	-1.42
179	0.64	-0.07	-0.18	-0.22	-1.23	-0.87	-1.43
180	0.61	-0.09	-0.18	-0.19	-1.26	-0.83	-1.45
181	0.6	-0.1	-0.19	-0.22	-1.26	-0.81	-1.44
182	0.6	-0.09	-0.2	-0.27	-1.25	-0.81	-1.41
183	0.6	-0.09	-0.19	-0.28	-1.25	-0.79	-1.4
184	0.6	-0.09	-0.2	-0.28	-1.23	-0.81	-1.41
185	0.6	-0.09	-0.19	-0.28	-1.22	-0.86	-1.4
186	0.6	-0.1	-0.19	-0.28	-1.21	-0.9	-1.42
187	0.58	-0.12	-0.2	-0.27	-1.19	-0.97	-1.43
188	0.58	-0.11	-0.2	-0.28	-1.19	-0.97	-1.43
189	0.57	-0.13	-0.19	-0.28	-1.2	-0.97	-1.44
190	0.57	-0.12	-0.2	-0.23	-1.21	-0.98	-1.45
191	0.57	-0.12	-0.19	-0.22	-1.21	-0.99	-1.46
192	0.57	-0.13	-0.2	-0.22	-1.22	-1.01	-1.46
193	0.57	-0.12	-0.21	-0.24	-1.25	-0.96	-1.47
194	0.55	-0.13	-0.21	-0.26	-1.28	-0.89	-1.47
195	0.54	-0.15	-0.21	-0.27	-1.3	-0.83	-1.48
196	0.53	-0.14	-0.22	-0.27	-1.28	-0.87	-1.47
197	0.55	-0.13	-0.2	-0.24	-1.27	-0.91	-1.46
198	0.55	-0.12	-0.19	-0.2	-1.28	-0.9	-1.48
199	0.54	-0.13	-0.2	-0.19	-1.27	-0.88	-1.48
200	0.55	-0.13	-0.2	-0.23	-1.26	-0.85	-1.45
201	0.56	-0.12	-0.21	-0.26	-1.24	-0.83	-1.43
202	0.56	-0.13	-0.21	-0.27	-1.24	-0.89	-1.43
203	0.57	-0.12	-0.21	-0.25	-1.24	-0.95	-1.43

ObsID = observation number (same as Table 1). UBVRIJHK absolute STMAG colors (Stone 1996; Laidler 2008) are given in the remaining columns.

ObsID	U-B	B-V	V-R	R-I	I-J	J-H	H-K
204	0.55	-0.13	-0.2	-0.2	-1.25	-0.92	-1.46
205	0.52	-0.15	-0.21	-0.19	-1.26	-0.9	-1.47
206	0.52	-0.16	-0.22	-0.23	-1.26	-0.89	-1.45
207	0.51	-0.16	-0.23	-0.27	-1.25	-0.87	-1.44
208	0.51	-0.17	-0.23	-0.29	-1.23	-0.89	-1.42
209	0.52	-0.17	-0.23	-0.29	-1.22	-0.92	-1.42
210	0.53	-0.15	-0.22	-0.29	-1.2	-0.97	-1.43
211	0.52	-0.16	-0.23	-0.3	-1.19	-1.05	-1.44
212	0.52	-0.17	-0.23	-0.3	-1.19	-1.09	-1.44
213	0.52	-0.16	-0.23	-0.29	-1.2	-1.04	-1.44
214	0.52	-0.16	-0.22	-0.27	-1.21	-1.07	-1.45
215	0.52	-0.16	-0.22	-0.24	-1.22	-1.08	-1.47
216	0.51	-0.15	-0.22	-0.22	-1.23	-1.08	-1.48
217	0.51	-0.16	-0.22	-0.22	-1.26	-1.04	-1.5
218	0.5	-0.17	-0.23	-0.25	-1.3	-0.95	-1.53
219	0.48	-0.18	-0.23	-0.28	-1.32	-0.88	-1.53
220	0.47	-0.19	-0.23	-0.27	-1.3	-0.88	-1.51
221	0.48	-0.18	-0.22	-0.24	-1.29	-0.92	-1.5
222	0.48	-0.16	-0.21	-0.19	-1.29	-0.92	-1.51
223	0.46	-0.18	-0.21	-0.16	-1.3	-0.9	-1.52
224	0.46	-0.19	-0.22	-0.18	-1.28	-0.87	-1.5
225	0.47	-0.18	-0.23	-0.24	-1.26	-0.87	-1.46
226	0.49	-0.18	-0.23	-0.27	-1.25	-0.94	-1.44
227	0.49	-0.17	-0.23	-0.26	-1.25	-1.01	-1.46
228	0.49	-0.16	-0.23	-0.22	-1.25	-1.04	-1.47
229	0.48	-0.17	-0.22	-0.19	-1.26	-1.02	-1.48
230	0.47	-0.19	-0.23	-0.2	-1.26	-0.97	-1.47
231	0.46	-0.2	-0.24	-0.25	-1.26	-0.95	-1.45
232	0.45	-0.22	-0.25	-0.29	-1.24	-0.94	-1.43
233	0.45	-0.22	-0.26	-0.32	-1.22	-0.95	-1.42
234	0.46	-0.21	-0.25	-0.32	-1.21	-1	-1.42
235	0.47	-0.2	-0.25	-0.32	-1.2	-1.09	-1.44
236	0.46	-0.21	-0.25	-0.33	-1.19	-1.16	-1.45
237	0.46	-0.2	-0.24	-0.31	-1.2	-1.14	-1.45
238	0.46	-0.2	-0.24	-0.28	-1.21	-1.13	-1.46
239	0.47	-0.19	-0.24	-0.25	-1.22	-1.14	-1.48
240	0.47	-0.18	-0.23	-0.23	-1.23	-1.13	-1.49
241	0.47	-0.18	-0.23	-0.22	-1.25	-1.08	-1.51
242	0.46	-0.19	-0.23	-0.23	-1.3	-0.98	-1.54
243	0.44	-0.2	-0.24	-0.25	-1.34	-0.9	-1.57
244	0.42	-0.22	-0.25	-0.27	-1.34	-0.89	-1.57

ObsID = observation number (same as Table 1). UBVRIJHK absolute STMAG colors (Stone 1996; Laidler 2008) are given in the remaining columns.

ObsID	U-B	B-V	V-R	R-I	I-J	J-H	H-K
245	0.41	-0.21	-0.24	-0.24	-1.32	-0.9	-1.54
246	0.42	-0.2	-0.22	-0.18	-1.31	-0.92	-1.54
247	0.42	-0.19	-0.22	-0.14	-1.3	-0.92	-1.55
248	0.42	-0.2	-0.22	-0.14	-1.29	-0.92	-1.54
249	0.42	-0.21	-0.23	-0.19	-1.28	-0.92	-1.5
250	0.43	-0.21	-0.24	-0.25	-1.27	-0.98	-1.47
251	0.43	-0.21	-0.25	-0.25	-1.27	-1.04	-1.47
252	0.44	-0.19	-0.24	-0.22	-1.27	-1.09	-1.48
253	0.44	-0.19	-0.24	-0.19	-1.27	-1.09	-1.49
254	0.43	-0.2	-0.24	-0.18	-1.27	-1.05	-1.49
255	0.41	-0.22	-0.25	-0.21	-1.27	-1.01	-1.47
256	0.4	-0.25	-0.26	-0.27	-1.25	-0.98	-1.45
257	0.39	-0.26	-0.27	-0.31	-1.23	-0.99	-1.43
258	0.41	-0.24	-0.27	-0.34	-1.21	-1.05	-1.42
259	0.42	-0.23	-0.27	-0.34	-1.2	-1.12	-1.43
260	0.42	-0.24	-0.27	-0.34	-1.2	-1.19	-1.44
261	0.41	-0.24	-0.27	-0.33	-1.21	-1.2	-1.45
262	0.41	-0.23	-0.26	-0.3	-1.22	-1.2	-1.47
263	0.42	-0.21	-0.25	-0.26	-1.23	-1.2	-1.49
264	0.43	-0.2	-0.24	-0.23	-1.24	-1.2	-1.51
265	0.44	-0.19	-0.23	-0.22	-1.26	-1.18	-1.53
266	0.43	-0.19	-0.23	-0.22	-1.29	-1.12	-1.56
267	0.41	-0.21	-0.24	-0.23	-1.33	-1.03	-1.6
268	0.38	-0.24	-0.25	-0.24	-1.36	-0.94	-1.61
269	0.37	-0.24	-0.24	-0.22	-1.35	-0.9	-1.58
270	0.37	-0.22	-0.23	-0.17	-1.33	-0.92	-1.58
271	0.38	-0.2	-0.22	-0.13	-1.31	-0.95	-1.57
272	0.38	-0.2	-0.22	-0.12	-1.3	-0.97	-1.57
273	0.39	-0.21	-0.22	-0.15	-1.29	-0.98	-1.54
274	0.39	-0.22	-0.24	-0.2	-1.28	-1	-1.51
275	0.39	-0.23	-0.25	-0.23	-1.28	-1.05	-1.49
276	0.4	-0.22	-0.25	-0.21	-1.28	-1.1	-1.49
277	0.41	-0.21	-0.24	-0.19	-1.27	-1.12	-1.5
278	0.4	-0.21	-0.24	-0.17	-1.28	-1.1	-1.5
279	0.39	-0.22	-0.25	-0.18	-1.27	-1.07	-1.5
280	0.38	-0.25	-0.26	-0.23	-1.26	-1.05	-1.48
281	0.37	-0.27	-0.28	-0.29	-1.24	-1.06	-1.45
282	0.37	-0.27	-0.28	-0.33	-1.22	-1.1	-1.43
283	0.38	-0.26	-0.28	-0.35	-1.21	-1.15	-1.43
284	0.38	-0.26	-0.28	-0.35	-1.21	-1.19	-1.44
285	0.38	-0.26	-0.28	-0.34	-1.21	-1.22	-1.45

ObsID = observation number (same as Table 1). UBVRIJHK absolute STMAG colors (Stone 1996; Laidler 2008) are given in the remaining columns.

ObsID	U-B	B-V	V-R	R-I	I-J	J-H	H-K
286	0.38	-0.25	-0.27	-0.31	-1.23	-1.21	-1.46
287	0.39	-0.24	-0.26	-0.27	-1.24	-1.19	-1.48
288	0.4	-0.22	-0.25	-0.23	-1.25	-1.18	-1.51
289	0.41	-0.2	-0.24	-0.21	-1.27	-1.17	-1.53
290	0.4	-0.2	-0.24	-0.21	-1.29	-1.14	-1.56
291	0.39	-0.21	-0.24	-0.21	-1.32	-1.09	-1.59
292	0.37	-0.23	-0.25	-0.22	-1.35	-1.02	-1.62
293	0.35	-0.24	-0.25	-0.21	-1.34	-0.95	-1.6
294	0.35	-0.23	-0.23	-0.17	-1.33	-0.92	-1.59
295	0.36	-0.21	-0.22	-0.13	-1.31	-0.93	-1.59
296	0.37	-0.2	-0.21	-0.12	-1.29	-0.96	-1.58
297	0.38	-0.19	-0.21	-0.13	-1.28	-0.98	-1.56
298	0.39	-0.2	-0.22	-0.17	-1.28	-1.01	-1.53
299	0.39	-0.21	-0.24	-0.21	-1.27	-1.05	-1.5
300	0.39	-0.21	-0.24	-0.21	-1.27	-1.09	-1.49
301	0.4	-0.21	-0.24	-0.2	-1.27	-1.11	-1.49
302	0.4	-0.21	-0.24	-0.18	-1.27	-1.11	-1.49
303	0.38	-0.22	-0.24	-0.17	-1.27	-1.08	-1.49
304	0.37	-0.24	-0.25	-0.2	-1.27	-1.07	-1.49
305	0.35	-0.26	-0.27	-0.25	-1.26	-1.06	-1.47
306	0.34	-0.29	-0.28	-0.3	-1.24	-1.06	-1.45
307	0.34	-0.29	-0.29	-0.34	-1.23	-1.09	-1.43
308	0.34	-0.29	-0.3	-0.36	-1.22	-1.11	-1.42
309	0.34	-0.29	-0.3	-0.35	-1.23	-1.14	-1.43
310	0.35	-0.28	-0.29	-0.33	-1.24	-1.16	-1.45
311	0.35	-0.26	-0.27	-0.29	-1.25	-1.18	-1.48
312	0.37	-0.24	-0.26	-0.24	-1.26	-1.19	-1.5
313	0.38	-0.23	-0.25	-0.22	-1.28	-1.19	-1.53
314	0.38	-0.22	-0.24	-0.2	-1.3	-1.15	-1.56
315	0.37	-0.22	-0.24	-0.2	-1.33	-1.1	-1.6
316	0.35	-0.24	-0.25	-0.2	-1.36	-1.03	-1.63
317	0.34	-0.24	-0.24	-0.19	-1.36	-0.97	-1.63
318	0.33	-0.24	-0.23	-0.16	-1.34	-0.94	-1.62
319	0.34	-0.22	-0.22	-0.13	-1.32	-0.95	-1.61
320	0.35	-0.2	-0.21	-0.12	-1.3	-0.98	-1.6
321	0.37	-0.19	-0.21	-0.13	-1.28	-1	-1.58
322	0.38	-0.19	-0.21	-0.16	-1.27	-1.02	-1.55
323	0.39	-0.19	-0.22	-0.19	-1.27	-1.04	-1.52
324	0.39	-0.2	-0.23	-0.22	-1.26	-1.07	-1.5
325	0.39	-0.2	-0.24	-0.21	-1.27	-1.09	-1.49
326	0.39	-0.21	-0.24	-0.2	-1.27	-1.09	-1.49

ObsID = observation number (same as Table 1). UBVRIJHK absolute STMAG colors (Stone 1996; Laidler 2008) are given in the remaining columns.

ObsID	U-B	B-V	V-R	R-I	I-J	J-H	H-K
327	0.38	-0.21	-0.24	-0.19	-1.27	-1.08	-1.49
328	0.37	-0.23	-0.25	-0.2	-1.28	-1.05	-1.49
329	0.35	-0.25	-0.26	-0.23	-1.27	-1.02	-1.48
330	0.33	-0.28	-0.28	-0.27	-1.26	-1.02	-1.46
331	0.33	-0.29	-0.29	-0.32	-1.25	-1.04	-1.44
332	0.33	-0.3	-0.3	-0.35	-1.24	-1.08	-1.43
333	0.33	-0.3	-0.3	-0.36	-1.24	-1.12	-1.43
334	0.34	-0.28	-0.29	-0.34	-1.25	-1.16	-1.45
335	0.35	-0.26	-0.28	-0.31	-1.26	-1.18	-1.47
336	0.36	-0.24	-0.26	-0.27	-1.27	-1.2	-1.5
337	0.37	-0.23	-0.25	-0.24	-1.28	-1.19	-1.53
338	0.37	-0.23	-0.25	-0.21	-1.3	-1.14	-1.56
339	0.36	-0.23	-0.25	-0.2	-1.33	-1.09	-1.59
340	0.35	-0.23	-0.25	-0.19	-1.36	-1.02	-1.63
341	0.34	-0.23	-0.24	-0.17	-1.36	-0.95	-1.64
342	0.34	-0.22	-0.23	-0.16	-1.35	-0.93	-1.63
343	0.35	-0.2	-0.22	-0.14	-1.33	-0.92	-1.62
344	0.36	-0.19	-0.21	-0.12	-1.3	-0.95	-1.6
345	0.37	-0.18	-0.21	-0.13	-1.28	-0.97	-1.59
346	0.38	-0.18	-0.21	-0.15	-1.27	-0.99	-1.56
347	0.39	-0.18	-0.22	-0.18	-1.26	-1.01	-1.55
348	0.39	-0.2	-0.23	-0.2	-1.27	-1.04	-1.53
349	0.38	-0.2	-0.24	-0.21	-1.27	-1.07	-1.52
350	0.38	-0.21	-0.24	-0.2	-1.28	-1.09	-1.51
351	0.37	-0.22	-0.25	-0.19	-1.29	-1.1	-1.51
352	0.36	-0.22	-0.25	-0.19	-1.3	-1.08	-1.51
353	0.35	-0.24	-0.26	-0.21	-1.3	-1.05	-1.5
354	0.34	-0.27	-0.28	-0.25	-1.29	-1.03	-1.49
355	0.33	-0.28	-0.29	-0.3	-1.27	-1.04	-1.47
356	0.33	-0.29	-0.3	-0.34	-1.25	-1.07	-1.46
357	0.33	-0.29	-0.3	-0.35	-1.25	-1.13	-1.45
358	0.34	-0.28	-0.29	-0.35	-1.25	-1.17	-1.47
359	0.35	-0.26	-0.28	-0.32	-1.26	-1.21	-1.49
360	0.36	-0.24	-0.27	-0.29	-1.27	-1.21	-1.51
361	0.37	-0.23	-0.26	-0.26	-1.28	-1.18	-1.54
362	0.37	-0.22	-0.25	-0.23	-1.3	-1.14	-1.57
363	0.36	-0.22	-0.25	-0.2	-1.32	-1.09	-1.59
364	0.36	-0.22	-0.25	-0.19	-1.34	-1.03	-1.62
365	0.35	-0.22	-0.24	-0.18	-1.35	-0.98	-1.63
366	0.35	-0.21	-0.23	-0.16	-1.34	-0.96	-1.62
367	0.36	-0.19	-0.22	-0.15	-1.32	-0.95	-1.62

ObsID = observation number (same as Table 1). UBVRIJHK absolute STMAG colors (Stone 1996; Laidler 2008) are given in the remaining columns.

ObsID	U-B	B-V	V-R	R-I	I-J	J-H	H-K
368	0.37	-0.18	-0.21	-0.14	-1.3	-0.96	-1.61
369	0.37	-0.18	-0.21	-0.14	-1.28	-0.98	-1.6
370	0.38	-0.18	-0.21	-0.15	-1.27	-0.99	-1.58
371	0.39	-0.18	-0.22	-0.18	-1.26	-1	-1.56
372	0.39	-0.19	-0.23	-0.2	-1.26	-1.02	-1.54
373	0.39	-0.2	-0.24	-0.22	-1.27	-1.04	-1.53
374	0.38	-0.21	-0.25	-0.22	-1.27	-1.05	-1.52
375	0.37	-0.21	-0.25	-0.21	-1.29	-1.06	-1.52
376	0.37	-0.22	-0.26	-0.21	-1.29	-1.06	-1.52
377	0.36	-0.23	-0.26	-0.22	-1.29	-1.03	-1.51
378	0.35	-0.25	-0.27	-0.25	-1.29	-1.01	-1.5
379	0.34	-0.27	-0.28	-0.29	-1.27	-1	-1.49
380	0.33	-0.28	-0.29	-0.32	-1.25	-1.02	-1.47
381	0.33	-0.29	-0.3	-0.35	-1.25	-1.05	-1.47
382	0.34	-0.28	-0.3	-0.35	-1.25	-1.09	-1.47
383	0.34	-0.27	-0.29	-0.34	-1.25	-1.12	-1.48
384	0.35	-0.26	-0.28	-0.31	-1.27	-1.14	-1.5
385	0.35	-0.25	-0.27	-0.27	-1.28	-1.14	-1.53
386	0.35	-0.24	-0.27	-0.24	-1.3	-1.13	-1.56
387	0.35	-0.24	-0.26	-0.21	-1.32	-1.11	-1.58
388	0.34	-0.24	-0.26	-0.19	-1.33	-1.08	-1.59
389	0.34	-0.23	-0.25	-0.18	-1.34	-1.05	-1.61
390	0.35	-0.22	-0.24	-0.17	-1.33	-1.03	-1.62
391	0.36	-0.2	-0.23	-0.16	-1.32	-1.01	-1.62
392	0.36	-0.19	-0.22	-0.15	-1.3	-1.01	-1.61
393	0.37	-0.18	-0.21	-0.15	-1.28	-1.01	-1.6
394	0.38	-0.18	-0.21	-0.16	-1.26	-1.01	-1.59
395	0.38	-0.18	-0.22	-0.17	-1.25	-1.01	-1.57
396	0.38	-0.19	-0.23	-0.19	-1.25	-1.01	-1.55
397	0.38	-0.2	-0.24	-0.21	-1.26	-1.01	-1.54
398	0.37	-0.21	-0.25	-0.21	-1.27	-1.02	-1.53
399	0.36	-0.22	-0.25	-0.21	-1.28	-1.02	-1.53
400	0.36	-0.23	-0.26	-0.21	-1.28	-1.03	-1.53
401	0.35	-0.23	-0.26	-0.22	-1.29	-1.01	-1.52
402	0.35	-0.24	-0.27	-0.24	-1.28	-0.99	-1.51
403	0.34	-0.26	-0.28	-0.27	-1.27	-0.99	-1.5
404	0.33	-0.28	-0.29	-0.31	-1.26	-0.99	-1.49
405	0.33	-0.29	-0.3	-0.33	-1.25	-1.01	-1.48
406	0.33	-0.29	-0.3	-0.35	-1.24	-1.04	-1.47
407	0.33	-0.29	-0.3	-0.34	-1.25	-1.06	-1.48
408	0.34	-0.27	-0.29	-0.32	-1.26	-1.09	-1.5

ObsID = observation number (same as Table 1). UBVRIJHK absolute STMAG colors (Stone 1996; Laidler 2008) are given in the remaining columns.

ObsID	U-B	B-V	V-R	R-I	I-J	J-H	H-K
409	0.34	-0.27	-0.28	-0.28	-1.28	-1.12	-1.53
410	0.34	-0.26	-0.28	-0.24	-1.3	-1.13	-1.55
411	0.33	-0.26	-0.27	-0.21	-1.32	-1.12	-1.58
412	0.33	-0.26	-0.27	-0.19	-1.33	-1.1	-1.6
413	0.33	-0.25	-0.26	-0.17	-1.34	-1.08	-1.62
414	0.33	-0.24	-0.25	-0.15	-1.33	-1.05	-1.63
415	0.34	-0.22	-0.24	-0.14	-1.32	-1.03	-1.63
416	0.35	-0.2	-0.23	-0.14	-1.3	-1.02	-1.62
417	0.36	-0.19	-0.22	-0.14	-1.28	-1.02	-1.61
418	0.37	-0.19	-0.22	-0.15	-1.27	-1.02	-1.6
419	0.37	-0.19	-0.22	-0.16	-1.25	-1.03	-1.59
420	0.37	-0.2	-0.23	-0.18	-1.25	-1.03	-1.57
421	0.37	-0.21	-0.24	-0.2	-1.25	-1.03	-1.56
422	0.37	-0.22	-0.25	-0.2	-1.26	-1.04	-1.55
423	0.36	-0.23	-0.25	-0.2	-1.27	-1.04	-1.55
424	0.36	-0.23	-0.26	-0.2	-1.28	-1.03	-1.54
425	0.36	-0.24	-0.26	-0.2	-1.28	-1.02	-1.54
426	0.36	-0.24	-0.27	-0.22	-1.28	-1	-1.53
427	0.35	-0.25	-0.28	-0.25	-1.27	-0.98	-1.52
428	0.35	-0.26	-0.28	-0.28	-1.26	-0.98	-1.51
429	0.34	-0.27	-0.29	-0.31	-1.25	-1	-1.5
430	0.34	-0.28	-0.3	-0.33	-1.24	-1.03	-1.49
431	0.33	-0.29	-0.3	-0.33	-1.23	-1.05	-1.5
432	0.35	-0.27	-0.29	-0.32	-1.26	-1.1	-1.51
433	0.34	-0.27	-0.29	-0.29	-1.25	-1.11	-1.53
434	0.34	-0.26	-0.28	-0.25	-1.29	-1.14	-1.56
435	0.34	-0.26	-0.28	-0.21	-1.31	-1.14	-1.58
436	0.34	-0.26	-0.27	-0.18	-1.33	-1.12	-1.61
437	0.33	-0.25	-0.26	-0.16	-1.34	-1.1	-1.62
438	0.33	-0.24	-0.25	-0.15	-1.34	-1.07	-1.63
439	0.34	-0.23	-0.24	-0.14	-1.33	-1.05	-1.64
440	0.35	-0.21	-0.23	-0.13	-1.31	-1.03	-1.63
441	0.36	-0.19	-0.22	-0.13	-1.29	-1.01	-1.62
442	0.37	-0.19	-0.22	-0.13	-1.27	-1.01	-1.61
443	0.38	-0.18	-0.22	-0.15	-1.26	-1.01	-1.6
444	0.38	-0.19	-0.22	-0.17	-1.25	-1.01	-1.58
445	0.38	-0.2	-0.23	-0.19	-1.25	-1.01	-1.57
446	0.37	-0.21	-0.24	-0.2	-1.26	-1.02	-1.56
447	0.37	-0.22	-0.25	-0.2	-1.27	-1.02	-1.56
448	0.36	-0.23	-0.26	-0.19	-1.28	-1.02	-1.55
449	0.36	-0.23	-0.26	-0.19	-1.3	-1.01	-1.55

ObsID = observation number (same as Table 1). UBVRIJHK absolute STMAG colors (Stone 1996; Laidler 2008) are given in the remaining columns.

ObsID	U-B	B-V	V-R	R-I	I-J	J-H	H-K
450	0.36	-0.24	-0.27	-0.21	-1.3	-1	-1.54
451	0.35	-0.25	-0.28	-0.23	-1.3	-1	-1.53
452	0.34	-0.26	-0.28	-0.27	-1.3	-1.01	-1.52
453	0.34	-0.27	-0.29	-0.3	-1.28	-1.03	-1.5
454	0.34	-0.28	-0.29	-0.33	-1.27	-1.06	-1.49
455	0.34	-0.28	-0.3	-0.34	-1.27	-1.09	-1.49
456	0.34	-0.28	-0.29	-0.33	-1.27	-1.13	-1.5
457	0.34	-0.27	-0.29	-0.3	-1.28	-1.16	-1.52
458	0.34	-0.26	-0.28	-0.27	-1.3	-1.17	-1.54
459	0.34	-0.26	-0.27	-0.22	-1.32	-1.18	-1.57
460	0.34	-0.25	-0.27	-0.19	-1.33	-1.17	-1.6
461	0.34	-0.25	-0.26	-0.16	-1.35	-1.16	-1.62
462	0.33	-0.24	-0.25	-0.15	-1.35	-1.14	-1.63
463	0.34	-0.22	-0.24	-0.14	-1.34	-1.11	-1.64
464	0.35	-0.21	-0.23	-0.13	-1.33	-1.08	-1.63
465	0.36	-0.19	-0.22	-0.12	-1.31	-1.06	-1.63
466	0.36	-0.18	-0.21	-0.13	-1.29	-1.05	-1.62
467	0.37	-0.18	-0.21	-0.14	-1.28	-1.04	-1.61
468	0.37	-0.19	-0.22	-0.16	-1.27	-1.03	-1.59
469	0.37	-0.2	-0.23	-0.18	-1.27	-1.03	-1.58
470	0.36	-0.21	-0.24	-0.19	-1.28	-1.03	-1.57
471	0.36	-0.22	-0.25	-0.19	-1.29	-1.03	-1.56
472	0.35	-0.23	-0.25	-0.19	-1.31	-1.04	-1.55
473	0.35	-0.23	-0.26	-0.19	-1.32	-1.04	-1.55
474	0.36	-0.23	-0.26	-0.19	-1.33	-1.05	-1.54
475	0.36	-0.24	-0.27	-0.22	-1.33	-1.05	-1.53
476	0.36	-0.24	-0.27	-0.25	-1.33	-1.07	-1.52
477	0.35	-0.26	-0.28	-0.29	-1.32	-1.1	-1.51
478	0.35	-0.27	-0.29	-0.32	-1.3	-1.12	-1.49
479	0.35	-0.27	-0.29	-0.34	-1.3	-1.14	-1.48
480	0.35	-0.27	-0.29	-0.34	-1.3	-1.17	-1.49
481	0.35	-0.26	-0.28	-0.32	-1.3	-1.2	-1.5
482	0.35	-0.26	-0.28	-0.29	-1.32	-1.21	-1.53
483	0.35	-0.25	-0.27	-0.24	-1.34	-1.22	-1.56
484	0.35	-0.24	-0.26	-0.2	-1.35	-1.22	-1.59
485	0.36	-0.23	-0.25	-0.17	-1.37	-1.21	-1.61
486	0.35	-0.22	-0.24	-0.15	-1.37	-1.19	-1.63
487	0.35	-0.21	-0.23	-0.14	-1.36	-1.15	-1.63
488	0.36	-0.2	-0.22	-0.13	-1.35	-1.11	-1.63
489	0.37	-0.18	-0.21	-0.12	-1.33	-1.09	-1.63
490	0.38	-0.16	-0.2	-0.12	-1.31	-1.07	-1.62

ObsID = observation number (same as Table 1). UBVRIJHK absolute STMAG colors (Stone 1996; Laidler 2008) are given in the remaining columns.

ObsID	U-B	B-V	V-R	R-I	I-J	J-H	H-K
491	0.39	-0.16	-0.2	-0.13	-1.29	-1.06	-1.62
492	0.39	-0.17	-0.21	-0.15	-1.28	-1.05	-1.6
493	0.38	-0.18	-0.22	-0.17	-1.28	-1.03	-1.58
494	0.38	-0.2	-0.23	-0.19	-1.28	-1.02	-1.57
495	0.37	-0.21	-0.24	-0.2	-1.3	-1.02	-1.55
496	0.37	-0.21	-0.25	-0.2	-1.32	-1.03	-1.54
497	0.37	-0.22	-0.25	-0.19	-1.34	-1.04	-1.54
498	0.38	-0.22	-0.25	-0.2	-1.35	-1.04	-1.54
499	0.38	-0.21	-0.25	-0.22	-1.35	-1.03	-1.52
500	0.38	-0.22	-0.26	-0.24	-1.34	-1.05	-1.51
501	0.38	-0.23	-0.27	-0.28	-1.34	-1.07	-1.5
502	0.37	-0.25	-0.27	-0.31	-1.32	-1.09	-1.48
503	0.37	-0.25	-0.28	-0.33	-1.31	-1.12	-1.47
504	0.37	-0.25	-0.28	-0.34	-1.31	-1.14	-1.47
505	0.37	-0.25	-0.28	-0.34	-1.31	-1.16	-1.48
506	0.37	-0.25	-0.27	-0.31	-1.33	-1.18	-1.5
507	0.37	-0.24	-0.26	-0.26	-1.35	-1.18	-1.53
508	0.37	-0.22	-0.25	-0.21	-1.36	-1.18	-1.56
509	0.38	-0.21	-0.24	-0.18	-1.37	-1.19	-1.59
510	0.37	-0.21	-0.23	-0.15	-1.38	-1.19	-1.61
511	0.37	-0.2	-0.23	-0.13	-1.37	-1.18	-1.62
512	0.38	-0.19	-0.22	-0.13	-1.36	-1.14	-1.62
513	0.39	-0.17	-0.2	-0.12	-1.34	-1.1	-1.62
514	0.4	-0.15	-0.19	-0.12	-1.33	-1.07	-1.62
515	0.4	-0.15	-0.19	-0.12	-1.31	-1.04	-1.61
516	0.4	-0.15	-0.19	-0.13	-1.29	-1.02	-1.6
517	0.39	-0.17	-0.2	-0.15	-1.28	-1	-1.58
518	0.38	-0.19	-0.21	-0.18	-1.29	-0.99	-1.56
519	0.38	-0.2	-0.23	-0.2	-1.3	-0.99	-1.54
520	0.38	-0.21	-0.24	-0.2	-1.32	-1	-1.52
521	0.38	-0.21	-0.24	-0.2	-1.34	-1.03	-1.52
522	0.39	-0.21	-0.25	-0.2	-1.36	-1.04	-1.51
523	0.4	-0.2	-0.24	-0.21	-1.36	-1.04	-1.5
524	0.4	-0.2	-0.25	-0.23	-1.35	-1.03	-1.49
525	0.4	-0.21	-0.25	-0.26	-1.34	-1.03	-1.48
526	0.39	-0.23	-0.26	-0.29	-1.33	-1.05	-1.46
527	0.38	-0.24	-0.27	-0.31	-1.32	-1.06	-1.45
528	0.38	-0.24	-0.27	-0.33	-1.3	-1.09	-1.44
529	0.39	-0.24	-0.27	-0.34	-1.3	-1.13	-1.45
530	0.39	-0.24	-0.27	-0.32	-1.31	-1.16	-1.47
531	0.39	-0.23	-0.26	-0.28	-1.33	-1.2	-1.5

ObsID = observation number (same as Table 1). UBVRIJHK absolute STMAG colors (Stone 1996; Laidler 2008) are given in the remaining columns.

ObsID	U-B	B-V	V-R	R-I	I-J	J-H	H-K
532	0.39	-0.21	-0.25	-0.23	-1.35	-1.22	-1.54
533	0.4	-0.2	-0.24	-0.19	-1.37	-1.23	-1.57
534	0.4	-0.19	-0.23	-0.15	-1.37	-1.23	-1.6
535	0.39	-0.19	-0.22	-0.13	-1.38	-1.21	-1.61
536	0.39	-0.19	-0.21	-0.12	-1.37	-1.17	-1.61
537	0.39	-0.18	-0.2	-0.12	-1.36	-1.12	-1.62
538	0.4	-0.16	-0.19	-0.11	-1.34	-1.07	-1.61
539	0.4	-0.15	-0.18	-0.11	-1.32	-1.02	-1.61
540	0.41	-0.14	-0.18	-0.11	-1.29	-1	-1.6
541	0.4	-0.16	-0.19	-0.13	-1.28	-0.98	-1.58
542	0.39	-0.18	-0.2	-0.16	-1.28	-0.97	-1.56
543	0.38	-0.21	-0.22	-0.19	-1.29	-0.97	-1.54
544	0.37	-0.23	-0.24	-0.21	-1.32	-0.99	-1.52
545	0.38	-0.23	-0.25	-0.2	-1.35	-1.05	-1.51
546	0.39	-0.22	-0.25	-0.19	-1.37	-1.1	-1.51
547	0.4	-0.21	-0.24	-0.19	-1.38	-1.12	-1.51
548	0.41	-0.2	-0.24	-0.2	-1.38	-1.11	-1.51
549	0.41	-0.21	-0.25	-0.23	-1.37	-1.1	-1.49
550	0.4	-0.22	-0.25	-0.27	-1.35	-1.1	-1.47
551	0.4	-0.23	-0.26	-0.29	-1.33	-1.09	-1.45
552	0.39	-0.24	-0.26	-0.31	-1.31	-1.1	-1.43
553	0.4	-0.24	-0.27	-0.33	-1.3	-1.13	-1.43
554	0.4	-0.24	-0.27	-0.33	-1.31	-1.18	-1.44
555	0.4	-0.23	-0.26	-0.3	-1.32	-1.24	-1.47
556	0.41	-0.22	-0.25	-0.26	-1.34	-1.27	-1.51
557	0.41	-0.2	-0.24	-0.21	-1.36	-1.28	-1.55
558	0.42	-0.19	-0.23	-0.17	-1.37	-1.27	-1.58
559	0.42	-0.18	-0.22	-0.14	-1.38	-1.25	-1.6
560	0.41	-0.18	-0.21	-0.13	-1.38	-1.21	-1.61
561	0.41	-0.18	-0.21	-0.12	-1.37	-1.17	-1.62
562	0.4	-0.17	-0.2	-0.11	-1.35	-1.11	-1.63
563	0.41	-0.16	-0.19	-0.1	-1.33	-1.05	-1.63
564	0.41	-0.15	-0.18	-0.09	-1.31	-1.01	-1.62
565	0.41	-0.15	-0.18	-0.1	-1.29	-0.99	-1.61
566	0.4	-0.17	-0.19	-0.13	-1.29	-0.97	-1.58
567	0.39	-0.21	-0.21	-0.17	-1.29	-0.98	-1.55
568	0.38	-0.23	-0.24	-0.22	-1.31	-1.02	-1.52
569	0.39	-0.23	-0.25	-0.23	-1.34	-1.09	-1.51
570	0.4	-0.22	-0.24	-0.21	-1.37	-1.16	-1.51
571	0.42	-0.2	-0.24	-0.19	-1.38	-1.19	-1.52
572	0.43	-0.2	-0.24	-0.19	-1.39	-1.18	-1.52

ObsID = observation number (same as Table 1). UBVRIJHK absolute STMAG colors (Stone 1996; Laidler 2008) are given in the remaining columns.

ObsID	U-B	B-V	V-R	R-I	I-J	J-H	H-K
573	0.42	-0.21	-0.24	-0.21	-1.39	-1.17	-1.51
574	0.41	-0.22	-0.25	-0.24	-1.37	-1.16	-1.49
575	0.41	-0.23	-0.26	-0.27	-1.35	-1.16	-1.46
576	0.41	-0.24	-0.26	-0.3	-1.33	-1.16	-1.44
577	0.41	-0.24	-0.26	-0.32	-1.31	-1.18	-1.43
578	0.42	-0.24	-0.26	-0.32	-1.3	-1.22	-1.43
579	0.42	-0.23	-0.26	-0.31	-1.3	-1.27	-1.45
580	0.43	-0.22	-0.25	-0.28	-1.32	-1.31	-1.49
581	0.44	-0.2	-0.24	-0.24	-1.34	-1.32	-1.53
582	0.44	-0.18	-0.22	-0.19	-1.35	-1.31	-1.56
583	0.44	-0.18	-0.22	-0.16	-1.37	-1.28	-1.59
584	0.43	-0.18	-0.21	-0.13	-1.38	-1.25	-1.61
585	0.42	-0.18	-0.21	-0.12	-1.37	-1.21	-1.62
586	0.42	-0.18	-0.2	-0.12	-1.35	-1.16	-1.63
587	0.43	-0.17	-0.19	-0.12	-1.33	-1.08	-1.62
588	0.42	-0.16	-0.18	-0.1	-1.32	-1.03	-1.63
589	0.43	-0.15	-0.17	-0.09	-1.3	-0.98	-1.62
590	0.42	-0.17	-0.18	-0.1	-1.29	-0.96	-1.6
591	0.41	-0.2	-0.2	-0.14	-1.28	-0.96	-1.57
592	0.41	-0.22	-0.23	-0.21	-1.28	-0.99	-1.53
593	0.42	-0.23	-0.24	-0.24	-1.3	-1.05	-1.5
594	0.43	-0.21	-0.24	-0.23	-1.33	-1.1	-1.49
595	0.45	-0.19	-0.23	-0.21	-1.35	-1.13	-1.49
596	0.46	-0.18	-0.23	-0.19	-1.37	-1.11	-1.5
597	0.45	-0.19	-0.23	-0.2	-1.39	-1.11	-1.51
598	0.44	-0.21	-0.24	-0.22	-1.38	-1.09	-1.5
599	0.44	-0.22	-0.25	-0.25	-1.36	-1.07	-1.47
600	0.44	-0.22	-0.25	-0.28	-1.32	-1.07	-1.45
601	0.45	-0.23	-0.25	-0.3	-1.3	-1.09	-1.43
602	0.45	-0.22	-0.25	-0.31	-1.28	-1.14	-1.43
603	0.46	-0.22	-0.25	-0.31	-1.28	-1.18	-1.44
604	0.46	-0.21	-0.24	-0.29	-1.3	-1.23	-1.46
605	0.47	-0.2	-0.24	-0.27	-1.31	-1.27	-1.49
606	0.47	-0.18	-0.23	-0.23	-1.33	-1.27	-1.53
607	0.47	-0.17	-0.22	-0.18	-1.34	-1.25	-1.55
608	0.46	-0.18	-0.21	-0.15	-1.36	-1.23	-1.57
609	0.45	-0.19	-0.21	-0.13	-1.36	-1.21	-1.59
610	0.44	-0.19	-0.21	-0.13	-1.36	-1.17	-1.6
611	0.44	-0.19	-0.2	-0.13	-1.34	-1.1	-1.61
612	0.44	-0.18	-0.19	-0.12	-1.32	-1.04	-1.62
613	0.44	-0.17	-0.18	-0.1	-1.31	-0.99	-1.62

ObsID = observation number (same as Table 1). UBVRIJHK absolute STMAG colors (Stone 1996; Laidler 2008) are given in the remaining columns.

ObsID	U-B	B-V	V-R	R-I	I-J	J-H	H-K
614	0.44	-0.17	-0.18	-0.09	-1.3	-0.95	-1.61
615	0.43	-0.19	-0.19	-0.12	-1.28	-0.95	-1.59
616	0.44	-0.21	-0.22	-0.19	-1.26	-0.97	-1.54
617	0.45	-0.22	-0.24	-0.25	-1.26	-1.02	-1.49
618	0.48	-0.2	-0.23	-0.25	-1.27	-1.06	-1.46
619	0.5	-0.17	-0.23	-0.23	-1.3	-1.06	-1.47
620	0.5	-0.16	-0.22	-0.2	-1.33	-1.04	-1.48
621	0.5	-0.16	-0.22	-0.2	-1.36	-1.03	-1.49
622	0.48	-0.19	-0.23	-0.21	-1.36	-1.05	-1.5
623	0.47	-0.21	-0.24	-0.23	-1.35	-1.04	-1.48
624	0.48	-0.2	-0.24	-0.26	-1.31	-1.01	-1.45
625	0.5	-0.19	-0.24	-0.29	-1.27	-0.99	-1.43
626	0.5	-0.2	-0.24	-0.29	-1.26	-1.02	-1.42
627	0.5	-0.2	-0.24	-0.3	-1.26	-1.06	-1.42
628	0.5	-0.2	-0.24	-0.29	-1.27	-1.09	-1.44
629	0.5	-0.19	-0.23	-0.28	-1.29	-1.16	-1.46
630	0.51	-0.18	-0.22	-0.24	-1.31	-1.16	-1.49
631	0.51	-0.17	-0.22	-0.2	-1.32	-1.17	-1.52
632	0.51	-0.17	-0.21	-0.18	-1.32	-1.18	-1.54
633	0.5	-0.17	-0.21	-0.16	-1.33	-1.18	-1.55
634	0.49	-0.17	-0.21	-0.15	-1.33	-1.15	-1.56
635	0.48	-0.18	-0.21	-0.16	-1.32	-1.13	-1.58
636	0.48	-0.17	-0.2	-0.16	-1.3	-1.05	-1.58
637	0.47	-0.19	-0.2	-0.12	-1.3	-0.99	-1.61
638	0.48	-0.17	-0.19	-0.11	-1.3	-0.96	-1.61
639	0.47	-0.18	-0.19	-0.12	-1.28	-0.96	-1.59
640	0.48	-0.2	-0.2	-0.16	-1.25	-0.95	-1.54
641	0.5	-0.19	-0.22	-0.24	-1.23	-0.97	-1.48
642	0.52	-0.17	-0.23	-0.26	-1.24	-0.97	-1.44
643	0.55	-0.15	-0.22	-0.24	-1.27	-0.94	-1.45
644	0.55	-0.14	-0.21	-0.22	-1.3	-0.93	-1.45
645	0.55	-0.14	-0.21	-0.21	-1.33	-0.92	-1.46
646	0.53	-0.17	-0.21	-0.19	-1.34	-0.93	-1.48
647	0.51	-0.18	-0.22	-0.2	-1.33	-0.97	-1.49
648	0.53	-0.17	-0.21	-0.23	-1.3	-0.95	-1.45
649	0.56	-0.15	-0.21	-0.26	-1.26	-0.9	-1.42
650	0.57	-0.14	-0.21	-0.27	-1.23	-0.9	-1.41
651	0.56	-0.15	-0.21	-0.27	-1.24	-0.95	-1.42
652	0.56	-0.15	-0.2	-0.27	-1.23	-0.97	-1.43
653	0.57	-0.14	-0.21	-0.26	-1.23	-1.04	-1.44
654	0.57	-0.14	-0.2	-0.25	-1.26	-1.05	-1.45

ObsID = observation number (same as Table 1). UBVRIJHK absolute STMAG colors (Stone 1996; Laidler 2008) are given in the remaining columns.

ObsID	U-B	B-V	V-R	R-I	I-J	J-H	H-K
655	0.57	-0.14	-0.2	-0.21	-1.28	-1.02	-1.47
656	0.56	-0.15	-0.2	-0.18	-1.28	-1.05	-1.5
657	0.55	-0.15	-0.2	-0.17	-1.29	-1.09	-1.51
658	0.56	-0.14	-0.19	-0.16	-1.28	-1.06	-1.53
659	0.55	-0.15	-0.19	-0.17	-1.28	-1.08	-1.53
660	0.54	-0.15	-0.19	-0.17	-1.29	-0.99	-1.53
661	0.51	-0.17	-0.18	-0.15	-1.31	-0.9	-1.56
662	0.51	-0.18	-0.18	-0.11	-1.29	-0.88	-1.58
663	0.53	-0.17	-0.19	-0.13	-1.27	-0.91	-1.56
664	0.53	-0.17	-0.18	-0.15	-1.23	-0.9	-1.53
665	0.55	-0.15	-0.19	-0.2	-1.22	-0.9	-1.49
666	0.6	-0.1	-0.19	-0.24	-1.22	-0.88	-1.43
667	0.63	-0.09	-0.19	-0.24	-1.24	-0.84	-1.42
668	0.65	-0.07	-0.19	-0.23	-1.26	-0.83	-1.43
669	0.63	-0.09	-0.19	-0.23	-1.29	-0.86	-1.44
670	0.62	-0.1	-0.19	-0.22	-1.31	-0.87	-1.43
671	0.59	-0.13	-0.2	-0.21	-1.3	-0.89	-1.46
672	0.59	-0.12	-0.19	-0.21	-1.28	-0.86	-1.46
673	0.62	-0.11	-0.18	-0.23	-1.23	-0.83	-1.41
674	0.65	-0.08	-0.18	-0.25	-1.22	-0.82	-1.4
675	0.66	-0.07	-0.18	-0.25	-1.22	-0.81	-1.43
676	0.65	-0.09	-0.17	-0.24	-1.22	-0.82	-1.42
677	0.67	-0.07	-0.18	-0.25	-1.21	-0.91	-1.42
678	0.68	-0.06	-0.18	-0.26	-1.23	-0.84	-1.47
679	0.68	-0.07	-0.18	-0.24	-1.26	-0.81	-1.46
680	0.65	-0.09	-0.19	-0.21	-1.25	-0.92	-1.45
681	0.62	-0.12	-0.2	-0.2	-1.23	-0.9	-1.51
682	0.61	-0.13	-0.17	-0.14	-1.23	-0.95	-1.49
683	0.63	-0.11	-0.17	-0.17	-1.27	-0.97	-1.5
684	0.6	-0.13	-0.18	-0.17	-1.27	-0.82	-1.53
685	0.6	-0.11	-0.16	-0.14	-1.31	-0.69	-1.52
686	0.58	-0.15	-0.16	-0.09	-1.29	-0.75	-1.53
687	0.6	-0.15	-0.17	-0.12	-1.25	-0.82	-1.51
688	0.61	-0.14	-0.16	-0.12	-1.2	-0.82	-1.52
689	0.62	-0.13	-0.14	-0.14	-1.2	-0.82	-1.49
690	0.64	-0.08	-0.12	-0.15	-1.2	-0.7	-1.46
691	0.7	-0.02	-0.12	-0.16	-1.25	-0.6	-1.47
692	0.75	0.01	-0.12	-0.15	-1.26	-0.65	-1.43
693	0.74	-0.01	-0.14	-0.16	-1.27	-0.69	-1.43
694	0.71	-0.04	-0.14	-0.16	-1.3	-0.59	-1.47
695	0.69	-0.04	-0.13	-0.14	-1.31	-0.62	-1.46

ObsID = observation number (same as Table 1). UBVRIJHK absolute STMAG colors (Stone 1996; Laidler 2008) are given in the remaining columns.

ObsID	U-B	B-V	V-R	R-I	I-J	J-H	H-K
696	0.69	-0.05	-0.14	-0.14	-1.28	-0.67	-1.47
697	0.69	-0.05	-0.1	-0.09	-1.26	-0.65	-1.46
698	0.72	-0.03	-0.07	-0.11	-1.24	-0.6	-1.45
699	0.77	0.01	-0.1	-0.14	-1.2	-0.65	-1.43
700	0.76	0.01	-0.09	-0.12	-1.22	-0.61	-1.48
701	0.77	0.03	-0.06	-0.1	-1.25	-0.57	-1.48
702	0.81	0.05	-0.07	-0.1	-1.22	-0.64	-1.47
703	0.78	0.04	-0.08	-0.1	-1.25	-0.61	-1.51
704	0.79	0.03	-0.09	-0.11	-1.24	-0.59	-1.52
705	0.75	0	-0.1	-0.08	-1.25	-0.67	-1.49
706	0.72	-0.08	-0.12	-0.08	-1.17	-0.77	-1.48
707	0.75	-0.03	-0.08	-0.09	-1.21	-0.75	-1.5
708	0.72	-0.04	-0.08	-0.05	-1.25	-0.68	-1.51
709	0.71	-0.03	-0.06	-0.07	-1.33	-0.5	-1.51
710	0.69	-0.09	-0.12	-0.09	-1.25	-0.47	-1.58
711	0.66	-0.17	-0.1	0	-1.26	-0.68	-1.52
712	0.69	-0.16	-0.09	-0.02	-1.2	-0.74	-1.49
713	0.71	-0.11	-0.04	-0.01	-1.16	-0.74	-1.47
714	0.72	-0.05	0.01	0.03	-1.22	-0.55	-1.51
715	0.78	0.05	0.05	0.02	-1.23	-0.49	-1.48
716	0.8	0.08	0.06	0.02	-1.25	-0.47	-1.49
717	0.83	0.1	0.04	0.01	-1.26	-0.49	-1.5
718	0.8	0.05	0.03	0.03	-1.26	-0.47	-1.51
719	0.78	0.08	0.06	0.03	-1.31	-0.4	-1.51
720	0.79	0.08	0.09	0.05	-1.31	-0.44	-1.52
721	0.8	0.07	0.08	0.06	-1.28	-0.45	-1.52
722	0.82	0.09	0.09	0.06	-1.26	-0.45	-1.49
723	0.84	0.13	0.14	0.11	-1.25	-0.45	-1.51
724	0.89	0.15	0.14	0.11	-1.2	-0.48	-1.5
725	0.88	0.15	0.15	0.11	-1.24	-0.43	-1.52
726	0.9	0.2	0.18	0.12	-1.26	-0.41	-1.53
727	0.93	0.16	0.15	0.13	-1.21	-0.47	-1.51
728	0.9	0.18	0.17	0.13	-1.26	-0.4	-1.54
729	0.89	0.14	0.16	0.13	-1.23	-0.46	-1.53
730	0.92	0.09	0.11	0.13	-1.16	-0.56	-1.5
731	0.94	0.08	0.09	0.12	-1.11	-0.63	-1.47
732	0.93	0.1	0.13	0.14	-1.14	-0.57	-1.5
733	0.89	0.15	0.2	0.17	-1.23	-0.38	-1.55
734	0.83	0.13	0.23	0.2	-1.3	-0.27	-1.58
735	0.76	-0.09	0.09	0.17	-1.22	-0.48	-1.53
736	0.85	-0.05	0.07	0.16	-1.11	-0.63	-1.47

ObsID = observation number (same as Table 1). UBVRIJHK absolute STMAG colors (Stone 1996; Laidler 2008) are given in the remaining columns.

ObsID	U-B	B-V	V-R	R-I	I-J	J-H	H-K
737	0.89	0.03	0.13	0.18	-1.11	-0.55	-1.47
738	0.88	0.1	0.21	0.21	-1.19	-0.41	-1.52
739	0.88	0.23	0.33	0.27	-1.27	-0.24	-1.56
740	0.91	0.22	0.31	0.28	-1.21	-0.3	-1.52
741	0.95	0.2	0.27	0.25	-1.18	-0.38	-1.5
742	0.97	0.18	0.25	0.26	-1.14	-0.43	-1.48
743	0.96	0.24	0.31	0.28	-1.18	-0.34	-1.5
744	0.96	0.27	0.33	0.29	-1.22	-0.29	-1.54
745	0.95	0.29	0.36	0.29	-1.25	-0.24	-1.56
746	1.01	0.31	0.37	0.31	-1.2	-0.29	-1.54
747	1.01	0.31	0.37	0.32	-1.18	-0.3	-1.5
748	1.06	0.31	0.38	0.33	-1.17	-0.31	-1.53
749	1.16	0.31	0.34	0.31	-1.12	-0.39	-1.51
750	1.16	0.33	0.36	0.32	-1.12	-0.38	-1.5
751	1.16	0.31	0.35	0.32	-1.12	-0.38	-1.51
752	1.16	0.29	0.34	0.32	-1.11	-0.4	-1.5
753	1.05	0.27	0.37	0.34	-1.17	-0.3	-1.53
754	1.13	0.28	0.35	0.33	-1.12	-0.36	-1.49
755	1.26	0.27	0.28	0.3	-1	-0.52	-1.43
756	1.29	0.31	0.31	0.3	-1.02	-0.5	-1.46
757	1.13	0.34	0.41	0.36	-1.15	-0.3	-1.53
758	0.99	0.36	0.5	0.39	-1.26	-0.14	-1.59
759	1	0.18	0.34	0.36	-1.11	-0.34	-1.51
760	1.1	0.14	0.25	0.32	-0.99	-0.52	-1.41
761	1.17	0.25	0.32	0.33	-1.02	-0.44	-1.44
762	1.08	0.29	0.41	0.38	-1.09	-0.31	-1.49
763	1.07	0.35	0.49	0.42	-1.15	-0.22	-1.53
764	1.15	0.34	0.44	0.4	-1.09	-0.27	-1.5
765	1.16	0.26	0.37	0.38	-1	-0.38	-1.44
766	1.15	0.24	0.35	0.38	-0.97	-0.4	-1.42
767	1.2	0.34	0.43	0.41	-0.98	-0.33	-1.44
768	1.1	0.37	0.51	0.44	-1.05	-0.21	-1.49
769	1.15	0.38	0.49	0.43	-1.05	-0.24	-1.5
770	1.34	0.4	0.43	0.41	-0.98	-0.36	-1.46
771	1.35	0.39	0.43	0.41	-0.96	-0.38	-1.45
772	1.35	0.37	0.42	0.42	-0.94	-0.39	-1.45
773	1.36	0.37	0.42	0.42	-0.93	-0.39	-1.44
774	1.34	0.35	0.42	0.43	-0.9	-0.4	-1.43
775	1.17	0.31	0.47	0.47	-0.94	-0.32	-1.46
776	1.21	0.26	0.41	0.44	-0.87	-0.41	-1.42
777	1.25	0.26	0.4	0.44	-0.85	-0.43	-1.4

ObsID = observation number (same as Table 1). UBVRIJHK absolute STMAG colors (Stone 1996; Laidler 2008) are given in the remaining columns.

ObsID	U-B	B-V	V-R	R-I	I-J	J-H	H-K
778	1.29	0.28	0.4	0.44	-0.84	-0.43	-1.4
779	1.31	0.29	0.41	0.45	-0.85	-0.43	-1.41
780	1.35	0.28	0.38	0.43	-0.85	-0.5	-1.4
781	1.42	0.3	0.38	0.43	-0.82	-0.51	-1.39
782	1.44	0.31	0.37	0.41	-0.82	-0.53	-1.38
783	1.43	0.31	0.36	0.41	-0.82	-0.53	-1.37
784	1.46	0.32	0.34	0.39	-0.83	-0.56	-1.37
785	1.46	0.33	0.35	0.39	-0.83	-0.55	-1.37
786	1.41	0.33	0.35	0.38	-0.85	-0.53	-1.38
787	1.41	0.34	0.35	0.38	-0.86	-0.51	-1.39
788	1.43	0.34	0.35	0.38	-0.87	-0.54	-1.38
789	1.39	0.32	0.34	0.37	-0.87	-0.54	-1.39
790	1.32	0.29	0.34	0.37	-0.87	-0.52	-1.4
791	1.27	0.31	0.37	0.39	-0.92	-0.49	-1.4
792	1.27	0.29	0.36	0.38	-0.92	-0.48	-1.4
793	1.18	0.3	0.39	0.39	-1.01	-0.41	-1.44
794	1.18	0.3	0.4	0.4	-1.01	-0.4	-1.45
795	1.24	0.29	0.35	0.37	-0.96	-0.48	-1.43
796	1.26	0.26	0.33	0.36	-0.93	-0.52	-1.42
797	1.24	0.24	0.3	0.35	-0.95	-0.58	-1.38
798	1.21	0.26	0.35	0.38	-0.95	-0.48	-1.41
799	1.23	0.29	0.34	0.35	-1	-0.49	-1.42
800	1.24	0.29	0.35	0.36	-1	-0.47	-1.44
801	1.17	0.27	0.34	0.35	-0.99	-0.46	-1.43
802	1.3	0.26	0.25	0.29	-0.91	-0.64	-1.38
803	1.26	0.24	0.24	0.27	-0.96	-0.63	-1.41
804	1.18	0.27	0.32	0.33	-0.99	-0.49	-1.44
805	1.13	0.33	0.37	0.33	-1.1	-0.38	-1.5
806	1.09	0.33	0.38	0.34	-1.09	-0.37	-1.48
807	1.2	0.32	0.33	0.3	-1.04	-0.46	-1.47
808	1.13	0.31	0.33	0.3	-1.08	-0.42	-1.48
809	1.04	0.31	0.37	0.32	-1.12	-0.37	-1.49
810	1.11	0.31	0.33	0.3	-1.07	-0.41	-1.48
811	1.1	0.31	0.32	0.27	-1.12	-0.4	-1.51
812	1.03	0.29	0.34	0.3	-1.13	-0.37	-1.5
813	0.97	0.22	0.3	0.28	-1.11	-0.41	-1.49
814	0.95	0.18	0.26	0.26	-1.09	-0.44	-1.48
815	1.05	0.21	0.24	0.26	-1.05	-0.54	-1.44
816	1.06	0.24	0.26	0.25	-1.07	-0.49	-1.48
817	1.05	0.27	0.28	0.24	-1.14	-0.44	-1.51
818	0.98	0.26	0.3	0.25	-1.17	-0.37	-1.52

ObsID = observation number (same as Table 1). UBVRIJHK absolute STMAG colors (Stone 1996; Laidler 2008) are given in the remaining columns.

ObsID	U-B	B-V	V-R	R-I	I-J	J-H	H-K
819	0.93	0.24	0.3	0.25	-1.19	-0.34	-1.53
820	1	0.19	0.2	0.19	-1.1	-0.52	-1.48
821	0.91	0.1	0.16	0.2	-1.11	-0.54	-1.45
822	0.86	0.13	0.21	0.22	-1.18	-0.42	-1.51
823	0.97	0.21	0.22	0.19	-1.15	-0.47	-1.49
824	0.97	0.22	0.23	0.2	-1.16	-0.43	-1.51
825	0.94	0.19	0.22	0.19	-1.16	-0.47	-1.5
826	0.95	0.12	0.13	0.14	-1.09	-0.62	-1.45
827	0.88	0.05	0.08	0.12	-1.11	-0.64	-1.45
828	0.84	0.1	0.14	0.14	-1.2	-0.49	-1.5
829	0.89	0.21	0.19	0.14	-1.22	-0.41	-1.51
830	0.86	0.22	0.22	0.15	-1.27	-0.35	-1.52
831	0.9	0.22	0.19	0.13	-1.22	-0.43	-1.51
832	0.88	0.22	0.18	0.11	-1.26	-0.39	-1.52
833	0.87	0.22	0.18	0.1	-1.27	-0.39	-1.52
834	0.86	0.19	0.17	0.1	-1.25	-0.39	-1.53
835	0.87	0.2	0.15	0.08	-1.26	-0.41	-1.52
836	0.85	0.16	0.14	0.07	-1.26	-0.43	-1.53
837	0.83	0.11	0.1	0.07	-1.2	-0.51	-1.5
838	0.77	0.05	0.07	0.05	-1.23	-0.51	-1.5
839	0.79	0.03	0	-0.01	-1.19	-0.6	-1.47

ObsID = observation number (same as Table 1). UBVRIJHK absolute STMAG colors (Stone 1996; Laidler 2008) are given in the remaining columns.

VITA

EDWARD W. SCHWIETERMAN

Education

- Ph.D. in Astronomy and Astrobiology, University of Washington (UW) (2016)
- Master of Science in Astronomy, UW (2011)
- Bachelor of Science in Astronomy and Astrophysics, *Magna Cum Laude*, Florida Institute of Technology (FIT) (2010)
- Bachelor of Science in Physics, *Magna Cum Laude*, FIT (2010)

Honors and Awards

- NASA Postdoctoral Program Fellowship, NASA Astrobiology Institute (NAI) (2016-)
- Wildcard Award, NASA Famelab Contest, Chicago/AbSciCon Regional Heat (2015)
- NAI Scholar, International Summer School in Astrobiology, 2013
- NAI Scholar, Nordic-NASA Summer School, 2012
- Outstanding Senior in Astrophysics (FIT, 2009)
- Outstanding Junior campus-wide, and in Astrophysics (FIT, 2008)
- Distinguished Student Scholar (FIT, 2008, 2009, 2010)
- Florida Tech Trustee Scholarship (FIT, 2006-2010)
- Robert C. Byrd Scholarship (2006-2010)
- Florida Bright Futures Scholarship (FIT, 2006-2010)
- Paul Hermansen Scholarship (FIT, 2008-2010)
- Frederick W. And Grace P. Brecht Scholarship (2008-2010)
- Universities Space Research Association (USRA) undergraduate scholarship (2008)

Teaching Experience

- Facilitator, "Being an RA in the Physical Sciences" workshop, TA/RA Conf. (UW, 2015)
- Instructor, ASTR 192 "Pre-Major in Astronomy (Pre-MAP) seminar" (UW, 2014)
- Teaching Assistant, ASTBIO 115 "Intro to Astrobiology" (UW, 2013)
- Teaching Assistant, ASTR 101 "Introduction to Astronomy" (UW, 2011)
- Teaching Assistant, ASTR 150 "The Planets" (UW, 2010, 2011)
- Astronomy Tutor, CLUE program (UW, 2011, 2014)
- Physics/Astronomy Tutor, Student Athlete Academic Services (UW, 2012-2013)

Academic Service

- Referee for the journal *Astrobiology*
- Member, Student Technology Fee Committee ($5 million/yr fund) (UW, 2015-2016)
- Executive Secretary, NASA Solar System Workings Panel (2015)
- Senator, Graduate and Professional Student Senate (GPSS) (UW, 2010-2015) *GPSS Committees:* Executive (2014-2015), Finance & Budget (2012-2014; Chair: 2012-2013), Elections (2014, 2015), STF Oversight (2015), Judiciary (2010-2011)
- Student member, Academic Grievance Hearing Panel (UW, 2015)

Workshops/Schools

- NASA/Famelab Science Communication Workshop, Chicago Field Museum (Spring 2015)
- Northwest Astronomy Teaching Exchange (NATE), Center for Astronomy Education (CAE) (Fall 2013; Fall 2015)
- International Summer School in Astrobiology, Santander, Spain (Summer 2013)
- Nordic-NASA Summer School "Water, Ice, and the Origin of Life in the Universe", Reykjavik, Iceland (Summer 2012)
- NASA/Space Florida Space Academy (Winter 2008)

Grants

- NASA Astrobiology Institute Director's Discretionary Fund (PI; 2016) ($46 K)
- Kenilworth Foundation Grant for the Pre-Major in Astronomy Program 2015 ($16.5 K)
- UW Student Technology Fee (STF) Grant, Planetarium Upgrade (Co-I; 2015) ($47 K)
- UW STF Grant, Manastash Ridge Observatory Imaging Camera (Co-I; 2015) ($37 K)
- American Philosophical Society Lewis and Clark Fund for Research, 2013 (PI; $4 K)
- UW GPSS grants for graduate student life improvements: 2015 ($700), 2013 ($460), 2011 ($360)

Outreach/Community Service

- UW Planetarium and Mobile Planetarium Show Presenter (UW, 2010-2016)
- Staff Member & Events Organizer, Pre-Major in Astronomy Program (UW 2010-2016)
- NASA International Year of Astronomy Student Ambassador, Florida (2009)
- Coach, Brevard County, FL Collaborative High School Science Bowl Team (2006-2008)

Press Releases & Media

- Life or an illusion? Avoiding 'false positives' in the search for living worlds. Peter Kelley – UW Today. (2016).
- Nitrogen may be a sign of habitability. Elizabeth Howell – Astrobiology Magazine. (2016).
- Earth observations show how nitrogen may be detected on exoplanets, aiding search for life. Peter Kelley – UW Today. (2015).
- Spectrum of life: Nonphotosynthetic pigments could be biosignatures of life on other worlds. Peter Kelley - UW Today. (2015).

Refereed Journal Publications

- **Schwieterman, E.W.** Meadows, V.S., Domagal-Goldman, S.D., Deming, D., Arney, A.N., Luger, R., Harman, C., Misra, M., Barnes, R. 2016. Identifying Planetary Biosignature Impostors: Spectral Features of CO and O_4 Resulting from Abiotic O_2/O_3 Production. *The Astrophysical Journal Letters*, 819:L13.

- Arney, G., Domagal-Goldman, S.D., Meadows, V.S., Wolf, E., **Schwieterman, E.W.**, Charnay, B. & Claire, M.W. (2016) The Pale Orange Dot: The Spectrum and Climate of Hazy Archean Earth. *Astrobiology* in press.

- Krissansen-Totton, J., **Schwieterman, E.W.,** Charnay, B., Arney, G., Robinson, T.D., Meadows, V., Catling, D. 2016. Is the Pale Blue Dot Unique? Optimized photometric bands for identifying Earth-like exoplanets. *The Astrophysical Journal*, 817:31.

- **Schwieterman, E.W.**, Robinson, T.D., Meadows, V.S., Misra, A., Domagal-Goldman, S.D. 2015. Detecting and Constraining N_2 Abundances in Planetary Atmospheres Using Collisional Pairs**.** *The Astrophysical Journal*, 810:57.

- Harman, C.E., **Schwieterman, E.W**., Schottelkotte, J.C., Kasting, J.F. 2015. Abiotic O_2 Levels on Planets around F, G, K, and M Stars: Possible False Positives for Life? *The Astrophysical Journal*, 812:137.

- **Schwieterman, E.W.,** Cockell, C.S., Meadows, V.S. 2015. Nonphotosynthetic Pigments as Potential Biosignatures. *Astrobiology*, 15(5): 341-361.

- Amador, E.S., Cable, M.C, Chaundry, N., Cullen, T., Gentry, D., Jacobsen, M.B., Murukesan, G., **Schwieterman, E.W.**, Stevens, A.H., Stockton, A., Yin, C., Cullen, D.C., Geppert, W. 2015. Synchronous in-field application of life-detection techniques in planetary analog missions. *Planetary and Space Sciences*, 106: 1-10.

- Robinson, T.D.; Ennico, K.; Meadows, V.S.; Sparks, W.; Bussey; D.B.J.; **Schwieterman; E.W**.; Breiner, J. 2014. Detection of Ocean Glint and Ozone Absorption Using LCROSS Earth Observations. *The Astrophysical Journal*, 787:1.

- Knight, M.M., Schleicher, D.G., Farnham, T.L., **Schwieterman, E.W.**, Christensen, S.R. 2012. A Quarter-Century of Observations of Comet 10P/Tempel 2 at Lowell Observatory: Continued Spin-Down, Coma Morphology, Production Rates, and Numerical Modeling. *The Astronomical Journal,* 144:153.

- Meech, K.J., and 191 colleagues (including **Schwieterman, E.W.**) 2011. EPOXI: Observations from a Worldwide Earth-Based Campaign. *The Astrophysical Journal Letters*, 734:L1.

- Knight, M.M., Farnham, T.L., Schleicher, D.G., **Schwieterman, E.W.** 2011. The Increasing Rotation Period of Comet 10P/Tempel 2. *The Astronomical Journal*, 141:2.

- **Schwieterman, E. W.,** Wood, M.A., Piwowar, D., Patterson, J., Rea, R., Monard, B., Krajci, T., Bolt, G., Roberts, G., Foote, J., McCormick, J. 2010. Time-Series

Photometry of GW Librae One Year after Outburst. *Journal of the Southeastern Association for Research in Astronomy,* Vol 3.

- Addison, B. C., Durrance, S.T., Vennes, S., **Schwieterman, E.W.**, Nickerson, D. 2010. Modeling and Observing Extrasolar Planetary Transits. *Journal of the Southeastern Association for Research in Astronomy,* Vol 3.
- Piwowar, D., Wood, M.A., **Schwieterman, E.W.,** Patterson, J., Monard, B., Rea, R., Starkey, D., Roberts, G. 2010. Time-Series Photometry of the Cataclysmic Variable Systems VY Aquarii and V2491 Cygni. *Journal of the Southeastern Association for Research in Astronomy,* Vol 3.

IAU Circulars

- Knight, M., **Schwieterman, E.,** Schleicher, D. 2010. Comet 103P/Hartley. IAU Circ. 9163.

Conference Presentation (Oral)

- **Schwieterman, E.,** et al. 2016. Spectral identification of abiotic O_2 buildup from early runaways and rarefied atmospheres. AAS Meeting #227, #211.04.
- **Schwieterman, E.** Binder, B. 2016. Promoting Inclusivity in STEM through Active Recruiting and Mentoring: The Pre-Major in Astronomy Program (Pre-MAP) at the University of Washington. AAS Meeting #227, #313.04.
- Binder, B., **Schwieterman, E.** 2016. The Pre-Major in Astronomy Program (Pre-MAP): What Makes a Great Research Project? AAS Meeting #227, #313.03.
- **Schwieterman, E.**, et al. 2015. Spectral identification of abiotic O_2 buildup from early runaways and rarefied atmospheres. AAS Division of Planetary Sciences #47, #404.04.
- **Schwieterman, E.** et al. 2015. Promoting Diversity in STEM through Active Recruiting and Mentoring: The Pre-Major in Astronomy Program (Pre-MAP) at the University of Washington. AAS Division of Planetary Sciences Meeting #47, #202.08.
- **Schwieterman, E.W.** 2015. Bridging the Skill Gap from High School to Student Researcher: The Pre-Major in Astronomy Program (Pre-MAP) at the University of Washington. Northwest Astronomy Teaching Exchange (NATE), Center for Astronomy Education (CAE). doi: 10.13140/RG.2.1.2008.9044.
- **Schwieterman, E.W.,** et al. 2015. Using Dimers to Constrain Planetary Habitability and Discriminate Against False Positives for Life. Astrobiology Science Conference 2015 #7486. Talk.

- Domagal-Goldman, S.D., and 17 colleagues (including **Schwieterman, E.W.**) 2015. A Week in the Life: An Astrobiology-Focused Study for a LUVOIR (Large UV-Optical-IR) Telescope. Astrobiology Science Conference 2015 #7703

- **Schwieterman, E.,** et al. Distinguishing True and False Positive Oxygen Signatures with Models and Observations. American Astronomical Society Meeting #225, #224.02. Talk.

- Meadows, V., Robinson, Ty. Misra, A., Ennico, K. Sparks, W.B., Claire, M., Crisp, D., **Schwieterman, E.**, Bussey, D., Breiner, J. 2015. Earth as an Exoplanet: Lessons in Recognizing Planetary Habitability. American Astronomical Society Meeting #225, #406.05.

- Domagal-Goldman, S., Meadows, V., **Schwieterman, E**., Luger, R., Wordsworth, R., Barnes, R., Segura, A., Claire, M. Mechanisms for Generating False Positives for Extrasolar Life. American Astronomical Society Meeting #225, #407.07.

- Arney, G., Meadows, V., Domagal-Goldman, S., Claire, M., **Schwieterman, E.** 2015. Hazy Archean Earth as an Analog for Hazy Earthlike Exoplanets. American Astronomical Society Meeting #225, #224.02.

- Knight, M.M., Schleicher, D.G., Farnham, T.L., **Schwieterman, E.W**., Christensen, S.R. 2012. Production Rates, Jet Modeling, and the Continued Spin-Down of 10P/Tempel 2. Asteroids, Comets, and Meteors 2012. LPI Contribution No. 1667, id.6410.

- Schleicher, D.G., Knight, M.M., Farnham, T.L., **Schwieterman, E.W**., Christensen, S. R. 2012. A Quarter-Century of Observations of Comet 10P/Tempel 2 at Lowell Observatory. American Astronomical Society, DPS Meeting #44, #514.09.

Conference Presentations (Poster)

- **Schwieterman, E.**, Cockell, C., Meadows, V.S. 2014. Non-photosynthetic pigments as potential biosignatures. Exoplanets, Biosignatures, and Instruments #2-40. Poster.

- Gentry, D., Amador, E.S., Cable, M.L., Chaudry, N., Cullen, T., Jacobsen, M., Murusekan, G., **Schwieterman, E**., Stevens, A., Stockton, A., Yin, C., Cullen, D., Geppert, W. 2014. Field Comparisons of Three Biomarker Detection Methods in Icelandic Mars Analogue Environments. American Geophysical Union, Fall Meeting 2014, #P21D-3961.

- **Schwieterman, E.W.,** et al. 2014. Using N_2-N_2 Collisionally-Induced Absorption to Detect N_2 and Determine Pressure in Planetary Atmospheres. American Astronomical Society Meeting #223, #347.18.

- Arney, G., Domagal-Goldman, S., Meadows, V., Claire, M., **Schwieterman, E.** 2014. Pale Orange Dots: Hazy Archean Earth as an Analog for Hazy Earthlike Exoplanets. American Astronomical Society, DPS meeting #46, #210.18.

- Cable, M.L., Amador, E.S., **Schwieterman, E.,** Jacobsen, M.B., Yin, C., Stockton, A.M., Gentry, D.M., Stevens, A., Murukesan, G., Chaundry, N., Cullent, T., Geppert, W., Cullen, D. 2014. Icelandic Lava Fields as a Terrestrial Analog for Mars: Investigating Habitability, Productivity, and Microbial Diversity. 45th Lunar and Planetary Science Conference. LPI contribution No. 1777, p.2721.

- **Schwieterman, E.W.,** et al. 2012. Characterizing Terrestrial Exoplanets: Evaluating Temperature and Albedo Retrieval Methods with Near-IR EPOXI Mars Spectra. Astrobiology Science Conference 2012. #4217.

- **Schwieterman, E.W.**, et al. 2010. Analysis of 10P/Tempel 2's Morphological Features and Pole Orientation. Bull. Am. Astr. Soc. 42, 965.

- **Schwieterman, E.W.**, et al. 2010. Rotational Period Investigation of Comet 10P/Tempel 2 During the 1999 Apparition and Other Results. Bull. Am. Astr. Soc. 42, 454.

- **Schwieterman, E.,** et al. 2009. Time-Series Photometry of GW Librae One Year After Outburst. Bull. Am. Astr. Soc. 41, 469.

- Piwowar, D.T., Wood, M.A., **Schwieterman, E.,** Patterson, J., Monard, B., Rea, R., Starkey, D., Roberts, G. 2009. Time Series Photometry of the Cataclysmic Variable Systems VY Aquarii and V2491 Cygni. Bull. Am. Astr. Soc. 41, 469.

Non-Refereed Articles

- **E. Schwieterman**. "A Report from the FameLab Competition" University of Washington Astrobiology Newsletter, Fall 2015.

- **E. Schwieterman**. "Can Non-photosynthetic Life Be Seen from Space? An Astrobiology Research Rotation Report", University of Washington Astrobiology Program Newsletter, Spring 2014.

- **E. Schwieterman** & E. Amador. "Nordic-UK-USA Astrobiology Field Campaign" for the *Where in the World Are Our Astrobiologists* feature, University of Washington Astrobiology Program Newsletter, Fall 2013.

Invited and Outreach Talks

- "Life Beyond the Solar System: The hunt for habitable worlds and biosignatures in the 2020s and beyond", the Seattle Astronomical Society (Seattle, 2016)
- "Biosignatures and Technosignatures: Finding life outside of the solar system", the Pacific Science Center's Science and a Movie Night at Central Cinema (Seattle, 2016)
- "Lifesigns and Biosignatures: How we'll find life outside the solar system", Astronomy on Tap science outreach talk (Seattle, 2015)
- "Spectrally Identifying Habitable Worlds and Biosignatures", Blue Marble Space Institute of Science (Seattle, 2015)
- "An Astrobiologist in the Land of Eternal Sunsets", NASA Famelab competition (Chicago, 2015)
- "Paper, Glass, and the Greenhouse Effect", NASA Famelab competition (Chicago, 2015)
- UW Astrobiology Science Magazine "Detecting Oxygen False Positives" (UW, 2015)
- Society of Physics Students Internship Seminar, Panel Member (UW, 2015)
- "Planetary Processes as False Positives for Life", General Exam (UW, 2014)
- "Scattering of Light and the Color of Planets", Lakewood High Outreach (UW, 2014)
- "Non-photosynthetic Pigments: Adventures in Microbiology and Spectral Modeling" Astrobiology PhD Program Research Rotation Talk (UW, 2013)
- UW League of Astronomers, "Being a Graduate Student" (UW, 2013)
- "Scattering of Light", Lakewood High Outreach (UW, 2013)